"Felix Qui Potuit Rerum Cognoscere Causas" – Virgil

University of Alberta

Fundamentals of Film Growth by Glancing Angle Deposition for Inorganic and Inorganic/Liquid Crystal Hybrid Optical Systems

by

Nicholas George Wakefield

A thesis submitted to the Faculty of Graduate Studies and Research
in partial fulfillment of the requirements for the degree of

Doctor of Philosophy

in

Micro-Electro-Mechanical Systems (MEMS) and Nanosystems

Electrical and Computer Engineering

Fall 2011
Edmonton, Alberta

Abstract

This thesis investigates two facets of thin film growth via glancing angle deposition. The first half of the work focuses on the fundamentals of film growth with a focus on uniformity and optical design. This portion of the thesis addresses important engineering questions that are relevant to future commercialization of this technology, by investigating issues of scalability and repeatability, which are crucial for large scale manufacturing. This research is also directly applicable to laboratory research as it allows for combinatorial approaches to experimental design, and addresses experimental uncertainty in device performance. This work underscores the importance of film density and column tilt, and the material constants that quantify these parameters. This work illustrates how knowledge of these constants is sufficient to predict a wide variety of important film properties, including thickness, density and column tilt non-uniformities, and can be used to predict and design the anisotropic optical properties of columnar thin films. This design flexibility is illustrated experimentally in the fabrication of a novel, single material, thin film, normal-incidence, reflective linear polarizer. The second half of the thesis investigates the interaction between liquid crystalline molecules and nanoporous metal oxide films. It builds upon prior work by a number of researchers, and contributes a two-dimensional finite element model based on an elastic model of nematic liquid crystals in order to explain molecular alignment in these systems. The model indicates

how film column tilt, film density and columnar aspect ratio contribute to molecular alignment, and suggests methods by which to achieve the desired film alignment. Experimentally, a number of reactive and non-reactive nematic liquid crystals are studied in silica thin films, with both hydrophilic and hydrophobic surface chemistries to examine real-world behaviour of a variety of systems. Finally, a system of fluorescent, reactive liquid crystals embedded in silica thin films placed on top of a transparent substrate is investigated for use as a luminescent solar concentrator, and is found to significantly enhance device performance.

Preface

"Don't Panic." – Douglas Adams

Motivation and History

Though it will (hopefully!) not appear this way to the reader, for quite some time I felt that my research results and progress could be described as, for lack of a better word, backwards. On several (several!) occasions, the results that I obtained were almost exactly opposite to what I had expected to find, and it so happens that the very layout of the material in this thesis is presented in a manner almost exactly opposite to the chronological order in which it was carried out. While the former situation could certainly prove infuriating at times, the act of straightening out the backwardness, and the reason this thesis is laid out in the manner that it is, has ultimately been a very rewarding experience. Writing this thesis, and stitching the many elements of my research together to make a surprisingly cohesive document, has reminded me that science is about asking questions and solving puzzles, and coming to the realization that things were not quite as backwards as they had initially appeared. It is not always clear what impact one's work will have on future work, but I hope the solutions that I try to describe here, in response to the puzzles and situations that I found important, interesting and unanswered are of great help to future scientists trying to straighten out their own small piece of the universe.

Like many before it in the Engineered Nanomaterials Laboratory, this thesis is ultimately about the behaviour of nanocolumnar materials fabricated by glancing angle deposition, and describes my particular story of trying to get them to do interesting things. When I first started my research, the goal of my project was to embed liquid crystalline materials into three-dimensional

photonic band gap materials and to investigate their properties and attempt to fabricate switchable photonic devices. The actual end-result is one decidedly different from that original goal. Though the ultimate story is not best told in this fashion, I feel that a short description of the actual chronological order in which my research proceeded makes an interesting story, and might prove useful to future students interested in how disjointed a thesis' research can actually be. The following describes a basic timeline of my research, and detailed background information and references will be provided in the relevant chapters.

My work in the Engineered Nanomaterials Laboratory with Dr. Sit actually began in December 2004, while I was still an undergraduate in Engineering Physics. My 4th year project was to examine the birefringence of TiO_2 films and how that was affected by thermal annealing. This project represented my first exposure to thin film deposition and optical characterization, which would become commonplace techniques in my graduate research. It also exposed me to the first instance of observed behaviour being directly opposite to the behaviour that I had expected, when I learned that the birefringence of the TiO_2 films had the opposite sign that I had initially expected. Understanding the origin of this behaviour and how to change the sign would end up being a major focus of my research, though I didn't realize it at the time. After continuing some minor research on birefringent TiO_2 as a research assistant in the spring, I formally began my Masters with Dr. Sit in September, 2005. While classes occupied the bulk of my time, I was able to examine the behaviour of liquid crystalline and dichroic materials infiltrated into our nanocolumnar materials. It was my original expectation to be able to get liquid crystals to align in complex three-dimensional GLAD structures in a repeatable manner, and to be able to reproduce and extend previous research on liquid crystals infiltrated into helical structures by combining this with the related three-dimensional photonic crystal project that was ongoing in our group.

However, getting reliable molecular alignment in these films proved to be incredibly challenging; samples were difficult to produce (and reproduce) reliably, and my research yielded few positive results. After struggling with this line of research through the first half of 2006, I changed my focus to try and create an optical filter device. To decide on a direction to pursue, I drew inspiration from the successful research into circular polarizers made from helical

films carried out by colleagues such as Andy van Popta and Kevin Robbie, as well as from the same liquid crystal phases that had much in common with our helical films. I ultimately decided that, in the interest of symmetry, a useful contribution would be to fabricate a linear polarizing film, which led me to examine S-shaped film structures, which form the basis of Chapter 4. I predicted that these S-shaped structures should have linear polarization selectivity based on inspiration from a theoretical liquid crystal molecular alignment known as a periodically bent nematic, and I was curious if our nanostructured films could induce such an alignment, just as our helical structures introduced a type of cholesteric liquid crystal alignment. The result of this was a collaboration spanning late 2006 and early 2007 with the Theory and Modeling Group at the National Institute for Nanotechnology, in particular with Dr. Andriy Kovalenko and Dr. Michael Brett and their student, Viktor Leontyev. Together we realized the successful modeling and creation of an S-shaped polarizer made of TiO_2, but one that passed the opposite polarization than had been expected. The reason for this was identical to the reason behind the earlier observations regarding birefringent TiO_2, and this fact prompted a desire to characterize this behaviour in more detail.

Before undertaking that research direction, I officially transferred into my PhD program in the spring of 2007. Then, in late 2007 and early 2008, I was fortunate to have an opportunity to pursue a collaboration with the Polymers for Information and Communication Technologies group in the Chemistry and Chemical Engineering Department at the Eindhoven University of Technology, under the supervision of Professor Dick Broer and Dr. Cees Bastiaansen. While there, I returned to the idea of infiltrating liquid crystals into GLAD films, but switched materials to reactive liquid crystals, which could be polymerized within our films. This lead to more robust samples and more repeatable experiments. One particular device proved interesting, and is discussed in Chapter 6. The device in question is the luminescent solar concentrator, which is comprised of a layer of fluorescent polymer on a transparent substrate. The layer absorbs incident solar energy and reradiates it into the substrate, where it can be waveguided to the substrate edge, for collection by a photovoltaic cell, for instance. Our initial goal was to orient a fluorescent dye in a polymeric liquid crystal using a GLAD film. This combination resulted in a significant improvement in collected light, but to my great surprise, the light was output in the

opposite direction than I had expected. Additionally, the orientation of the reactive liquid crystals in the system was unclear, and needed to be determined.

Before pursuing that research direction, I instead returned home in the spring of 2008 in order to focus on the detailed optical properties of GLAD films, as described in Chapter 3. I felt that a great deal of existing research ignored a number of important engineering questions that were of critical importance if commercialization could ever be achieved. Most notably, I felt that previous work lacked adequate models to predict optical properties of different film structures which, if present, could significantly improve optical filter design based on GLAD films. Building off of previous work by Ian Hodgkinson and James Gospodyn, I sought to extend our understanding of how deposition algorithms affect film geometry, and how this geometry in turn affects the optical properties of the resultant films. To address this problem, I organized and took part in a significant collaboration in 2008 with members of Professor Brett's group, primarily Michael Taschuk, Jason Sorge and Louis Bezuidenhout. Together, we were able to produce and characterize a significant volume of samples, from which I was able to determine a number of important relationships between the manner in which a film was deposited and its consequent film structure and the relation between structure and optical behaviour.

One major issue that arose during this project was a question of repeatability. Supposedly identical depositions would yield different values for film properties such as thickness density, or refractive index. The origin of this discrepancy was due to non-uniformities that arise over a substrate, during a single deposition, as a result of differing geometry along that substrate. I felt that this process non-uniformity was a crucial, fundamental engineering question, unanswered in the literature, and absolutely essential to answer in order to fully understand scalability and repeatability concerns. As a result, I pursued that line of research during the end of 2008 and the beginning of 2009. The resulting work is a very elementary look at the growth of GLAD films, and unifies the results from a number of previous elementary studies on aspects such as film density and column tilt by researchers such as Poxson, Lichter and Chen. This work forms the basis of Chapter 2 in this thesis. In the end, I feel that this is was the most successful and useful contribution of this thesis, and hope that it proves useful to others in the future.

During the spring and summer of 2009, I was able to return to Eindhoven,

where I was able to more closely look at the material that I had begun my graduate research with, the alignment of liquid crystals in nanoporous materials. While in Eindhoven, I was able to learn much more about liquid crystals from colleagues in the department, and I had access to a much greater variety of materials than was available at the University of Alberta. I was also able to draw heavily on many of the skills and techniques that I had learned in the first year of my graduate studies, during my initial, unsuccessful experiments with liquid crystal infiltration, with much greater success. This work is presented in Chapter 5, and hopefully represents a new step forward in understanding the interaction of liquid crystals in GLAD films, building primarily off previous work by several colleagues, notably Scott Kennedy, Anastasia Elias and my supervisor, Jeremy Sit. I was able to characterize the alignment of a variety of liquid crystals in GLAD films under various conditions, and develop a mathematical model based on the elasticity of liquid crystals to explain the observed behaviour. At the same time, I encountered one final example of observations being counter to my expectations. Liquid crystals in a GLAD film were always assumed to align parallel to the columnar direction of the film. While this turned out to be true for previously investigated non-reactive liquid crystals, in similar non-reactive liquid crystals, it was determined that the molecules aligned perpendicular to the columns. This was an unfortunate fact, however, it led to some interesting experiments with surface functionalization in an attempt to modify molecular alignment.

Finally, throughout 2010, and now into 2011, I have been assembling all of the above research into this thesis and into publications. It has been very rewarding to see different aspects of my research complement each other, with results from certain thesis chapters closely interweaving with that in other chapters. The outline of this thesis is presented below, along with brief descriptions of the motives behind each topic, and their position in the overarching framework of nanomaterials research. These descriptions will be expanded upon in greater detail in the individual chapters.

Thesis Outline

Chapter 1 introduces a few recurrent, background ideas that underpin several focal points of this thesis. This chapter includes a description of oblique angle

deposition, wave propagation in dielectrics, effective medium theories, and optical characterization approaches that were used frequently during the course of this thesis. This chapter is intended to act as a quick reference, primarily for future students in the Nanomaterials laboratory, on a number of topics related primarily to the optics of dielectric, columnar films.

Chapter 2 describes the glancing angle deposition (GLAD) process and emphasizes my work on the uniformity of films fabricated using this method. My goal was to develop a model based on the geometry of the system in order to explain the variations in film thickness, density, and microstructure that are often observed between samples created during the same deposition run. This was an important problem to investigate in order to answer the oft-posed questions regarding the repeatability of devices fabricated using GLAD, as well as to identify what potential limitations or benefits one might encounter in large scale production. The results in this chapter are build on several fundamental studies of GLAD films by prior researchers. The major aim of the work in this chapter is to identify process non-uniformities for the purposes of identifying repeatability concerns in experimental settings, as well as to investigate potential advantages and challenges associated with future scaling in a manufacturing setting.

Chapter 3 focuses on the optical properties of GLAD films made out of SiO_2 and TiO_2. The purpose of this work was to document and explain the changes in porosity and the resultant change in physical properties that arise in slanted post structures fabricated using different substrate motion algorithms. This work culminated in the deposition of a large number of films with the collaborative assistance of several members of our group, and the generation of a unifying model that could capably predict the optical properties of general slanted post structures, requiring prior knowledge of only a few well-known and well-documented material specific properties. The major motivation for this chapter was to provide a framework for future researchers to design optical filters based on GLAD from an a priori standpoint, and to be able to theoretically identify what kinds of materials and material properties are required for specific devices. Ideally this should allow future experimental optical designs to be done less haphazardly, and with more focus and direction.

Chapter 4 applies the results of the previous chapter to create and refine the fabrication of a non-absorbing, reflective linear polarizer for use at normal

incidence. This work illustrates the benefit of the data and model obtained in Chapter 3 and serves as a nice parallel to earlier work on GLAD involving circular polarization filters made using helical GLAD films. The experimental results are supplemented by theoretical models based on matrix methods, as well as simulated finite-difference time-domain results carried out primarily by V. Leontyev. The major thrust of this chapter was to develop an optical filter in conjunction with the results of Chapter 3, and demonstrate the validity the work in the previous chapter through a proof-of-concept device.

Chapter 5 is a rather significant departure from the first half of the thesis. It concerns the physics of liquid crystalline materials, and attempts to explain how these materials interact and can be aligned in porous films made using GLAD. The liquid crystals are treated as an elastic continuum and their alignment can be elucidated by finding the distortion that corresponds to a minimum in the elastic free energy. This is done by solving differential equations using finite elements, and compared to real world results involving a variety of liquid crystalline materials in SiO_2 films. Chemical functionalization of the GLAD films is also employed in an attempt to exert control over the molecular orientation of infiltrated liquid crystals. This chapter builds on significant work by a number of previous researchers, and aimed to investigate the interaction between liquid crystals and GLAD films using methods not previously attempted. The major intent of this work was to provide future researchers with a mathematical model with which to analyze these systems in future experiments, as well as to begin to catalogue the widely different observed behaviours of a variety of liquid crystal materials in different GLAD systems.

Chapter 6 examines an application of liquid crystal-infiltrated GLAD films and examines the fabrication of luminescent and scattering solar concentrators. These consist of a layer of GLAD infiltrated with fluorescent liquid crystalline polymer networks on transparent substrates. The film is capable of redirecting incident solar energy into the substrate itself, where it can be guided to an edge and collected by a photovoltaic cell, for instance. The potential advantage of these devices is to enable the collection of solar energy over large areas, while minimizing the footprint of the photovoltaic cells themselves in an effort to reduce costs. The work in this chapter was based on existing solar concentrators made using fluorescent liquid crystalline materials, and was initially meant to

try and exploit the ease of aligning liquid crystalline materials at oblique angles in GLAD films. Ultimately, the major aims of this research were not met, but a number of interesting phenomena, notably the presence of strong directional scattering in polymer/GLAD hybrid materials, were observed, and should be of interest for future research.

Finally, the major results of this thesis are summarized in Chapter 7, which re-emphasizes the significance of this thesis in the context of related research, the major successes of this thesis and identifies potential directions for future investigation.

Acknowledgments

I'd like to thank a lot of people for helping me get to this point. First and foremost, I'd like to thank my parents and my sister for always being supportive of me, always encouraging me to pursue my education and for helping me out in so many ways. You have my eternal love and thanks. Next, I'd like to convey a huge thank you to my supervisor, Jeremy Sit, who has always been there to discuss ideas and to provide feedback, has always been positive about my results even when I might not have been, and who has been an incredible (and I seriously mean incredible) help during the weeks and months that I have been writing this thesis. I am seriously grateful for that. I'd also like to thank some of the other supervisory figures that I've had the pleasure to know. Mike Brett was always a positive voice, and was one to provide sharp questions and good insight into my many research difficulties. I must thank Dick Broer and Cees Bastiaansen, as well as Michael Debije, for taking me in as one of their own at the TUE in Eindhoven and being patient with me while I complained that none of my experiments were working. I had a wonderful time in the Netherlands during my PhD, and I thank you for the opportunity. To the many postdocs in our group, thanks for keeping me in line, and for providing some structure and organization which I desperately needed at times. And thanks to all my wonderful friends both in and out of the lab, here in Edmonton and elsewhere. You never failed to make me laugh, be there to go on adventures with or to waste copious amounts of time on trivia, puzzles, hockey pools, Rock Band and other mindless distractions. Thanks for making things fun (at the expense of many late nights and narrowly avoided deadlines) and providing me with a wonderful set of memories. Finally, to the women who have come and gone from my life during my studies, you also have my thanks. My time spent with each of you was time well spent, and you each provided a unique perspective and helped shape the way I see the real world outside the lab. So once more,

to each of you who have helped get me to this point, thank you so much for all of your help. I am honoured and deeply grateful to have had friends and family as wonderful you, and can scarcely believe my good fortune.

Table of Contents

List of Tables

List of Figures

List of Symbols and Abbreviations

Symbols

$\bar{\mathbf{b}}$	Average broadening vector 79
$\hat{\mathbf{b}}$	Broadening vector 78
$\mathbf{B}$	Magnetic field 9
$\mathbf{B}_0$	Magnetic field amplitude 10
ξ'	Net orientation angle 40
b	Complex representation of $\hat{\mathbf{b}}$ 79
$\mathbf{C}, \mathbf{G}$	Electromagnetic vectors 109
C	Basis transformation matrix from linearly to circularly polarized light 116
c	Material constant to determine $\bar{\varrho}$ 9
c	Speed of light in vacuum 10
C_χ	$\cos\chi$ 24
Δ	4×4 Berreman matrix 112
δ	Extra film thickness required in certain GLAD algorithms . . 33
$\Delta^j(d)$	Fractional variation in j within $\pm d$ of the substrate center . . . 45
$\Delta_i^j(d)$	Fractional variation in j within $\pm d$ along the i-axis 45
$\mathbf{D}$	Electric displacement field 9
D	LSC substrate thickness 203
D	Tooling factor (deposition ratio) 37
D	Unit cell height 159
d	Column diameter in finite element model 155
D_{norm}	Tooling factor at normal incidence 37
$D_{O'}$	Tooling factor at substrate centre (O') 38
$\Delta\mathbf{E}_0$	Electric field deviation in a dielectric inclusion 15

$\mathbf{E}$	Electric field 9
$\mathbf{E}_0$	Electric field amplitude 10
ε	Dielectric tensor/constant 10
ε_0	Permittivity of free space 10
$\varepsilon_1, \varepsilon_2$	Dielectric constants of components 1 and 2 of a composite material 13
ε_{inc}	Dielectric constants of a dielectric inclusion 13
ε_i	Principal dielectric constant along ith principal axis 10
$\varepsilon_o, \varepsilon_e$	Ordinary and extraordinary dielectric constants 144
E	Material constant for relating α to β 6
$\mathcal{F}$	Total free energy in a nematic 147
ϕ	Azimuthal angle of $\mathbf{n}$ 150
ϕ	Azimuthal rotation angle 25
ϕ_0	PhiSweep growth parameter 83
ϕ_0'	Angle at which $\bar{b}^2$ switches sign for PhiSweep films 85
ϕ_α	Partial derivative of ϕ with respect to α 150
ϕ_{beam}	Angle of input light polarization 186
φ	Polar angle to P measured from x-axis 26
F	Frank-Oseen free energy 146
f	Spin-pause fraction 81
f_m	Spin-pause fraction in layer m 123
$\bar{\Gamma}$	Average vertical growth rate at P 30
Γ	Vertical film growth rate at P 29
γ	$P/(P+\delta)$ 81

γ_1	r/R_{OS}	27
γ_2	z_s/R_{OS}	27
Γ_{QCM}	Deposition rate on the QCM	37
G	Geometric gain	203
$g_{\alpha\beta}$	Partial derivative of n_β with respect to coordinate α	147
$\mathbf{H}$	Auxiliary magnetic field	9
h	Planck's constant	203
I	Identity matrix	113
I	Incident light intensity	19
I_L, I_R	Light intensity measured for left and right circularly polarized light, respectively	19
I_u, I_v	Light intensity measured along u- and v-axes, respectively	19
I_x, I_y	Light intensity measured along x- and y-axes, respectively	19
$I_{\lambda_{\text{in}}}, I_{\lambda_{\text{out}}}$	Input and output irradiance per unit wavelength	203
$\mathbf{J}_f$	Free current density	9
$\mathbf{k}$	Wavevector	10
$\mathbf{k}_i, \mathbf{k}_r, \mathbf{k}_t$	Incident, reflected and transmitted wavevectors	113
K	Elastic constant in the one-constant approximation	146
k	Vapour source proportionality constant	29
K_1, K_2, K_3	Splay, twist and bend elastic constants	146
k_i	Wavevector component along ith axis	10
k_i, k_r, k_t	Incident, reflected and transmitted wavevector amplitudes	113
Λ	S-shaped film period	123
λ	Lagrange multiplier for $\mathbf{R}(\mathbf{n})$	147

λ	Mean free path 2
λ	Wavelength 87
λ_c	Center wavelength 119
L	Differential operator matrix 109
L	LSC edge length 203
μ	Diamagnetic tensor/constant 10
μ_0	Permeability of free space 10
μ_i	Principal diamagnetic constant along ith principal axis 10
dm/dt	Total mass deposited at P 29
M	Combined dielectric and diamagnetic tensor 110
M	Number of layers per period 123
m	Layer number 123
Δn	In-plane birefringence 77
$\Delta n_{\max}$	In-plane birefringence of a serial bideposited film 79
η	Power efficiency 203
η_{EQE}	External quantum efficiency 203
$\mathbf{n}(\mathbf{r})$	Nematic director field 144
N	Refractive index of a film deposited at normal incidence 77
n	Directionality of vapour source 29
n	Refractive index 10
N_1, N_2	Number of dielctric inclusions of type 1 and 2 respectively . 15
n_{avg}	Average of the three principal indices 77
$N_{\mathrm{in}}, N_{\mathrm{out}}$	Input and output number of photons per unit time 203

n_i	Principal index along the ith axis	11
n_o, n_e	Ordinary and extraordinary refractive indices	144
n_x, n_y, n_z	Cartesian components of director field	147
O	Center of rotating substrate	23
O'	Substrate center	26
$\mathbf{P}$	Polarization (dipole moment per unit volume)	14
$\mathbf{p}$	Dipole strength	14
P	Arbitrary point on substrate	25
P	Pressure in Pa	2
P	Transfer matrix	113
p_{helix}	Helical pitch	107
$P_{\text{in}}, P_{\text{out}}$	Total input and output power	203
p_{ribbon}	Twisted ribbon pitch	108
P_i	Components of the electric polarization, $\mathbf{P}$	16
p_v	Vertical post pitch	32
$P_{\lambda_{\text{in}}}, P_{\lambda_{\text{out}}}$	Input and output power per unit wavelength	203
$\hat{\mathbf{q}}$	Columnar growth trajectory (unit vector)	28
$\mathbf{q}$	Columnar growth trajectory	39
θ	Incident light angle	18
θ	Off-axis angle	27
θ	Polar angle of $\mathbf{n}$	150
θ_i^{LC}	Angle between ith molecule and the nematic director	145
θ_α	Partial derivative of θ with respect to α	150

θ_{bulk}	Director orientation in the bulk of a liquid crystal cell 165
$\theta_i, \theta_r, \theta_t$	Incident, reflected and transmitted angles..... 113
θ_k	Angle between wavevector and x' axis 11
$\Theta_O s, \Phi_O$	Polar and azimuthal coordinates of O 23
$\theta_{O'}$	Off-axis angle at substrate centre (O') 31
Q	Alternate 4×4 Berreman matrix..... 112
q	Pitch of a twisted nematic/cholesteric 152
q_0	Natural (chiral) pitch 153
q_0	Natural pitch of a cholesteric nematogen 153
q_i	Depolarization factor along the ith axis 16
$\bar{\rho}$	Average film density 6
$\bar{\varrho}$	Average fractional density 7
$\bar{\varrho}_{\text{scale}}$	Average fractional density measured using microbalance ... 88
$\bar{\varrho}_{\text{VASE}}$	Average fractional density measured using ellipsometry 88
$\bar{\varrho}_{O'}$	Average fractional film density at substrate centre (O') 31
$\mathcal{R}$	Modified free energy with Lagrange constraint 147
ρ	Instantaneous film density 29
ρ_{norm}	Film density at normal incidence..... 7
ρ_f	Free charge density 9
$\rho_{O'}$	Film density at substrate centre (O') 31
ϱ	Instantaneous fractional film density..... 29
R	Radius of a dielectric inclusion..... 13
R	Defect radius 156

R	Reflectance matrix	117
R	Rotation matrix	108
r	Amplitude reflection matrix	116
r	Distance in xy-plane from O to P	26
r	Radial coordinate	14
$R(\mathbf{n})$	Normalization constraint on $\mathbf{n}$	147
R_{ij}	Reflectance coefficients	117
r_{ij}	Amplitude reflection coefficient	116
$\mathbf{R}_{OP}$	Vector from O to P	26
$\hat{\mathbf{R}}_{OS}, \hat{\mathbf{\Theta}}_O, \hat{\mathbf{\Phi}}_O$	Spherical coordinate unit vectors at O	24
$\mathbf{R}_{OS}$	Vector from O to S	26
R_{OS}	Throw distance from source to substrate center	23
$\mathbf{R}_{PS}$	Vector from P to S	26
$\mathbf{S}$	Incident beam polarization state (2-component vector)	117
$\mathbf{S}$	Stokes vector	19
ψ	$\phi + \varphi$	26
S	Evaporation source	22
S	Nematic order parameter	145
S'	Projection of S in the substrate plane	26
S_0, S_1, S_2, S_3	Stokes parameters; elements of $\mathbf{S}$	19
S_χ	$\sin\chi$	24
T	Film thickness at P	29
T	Film thickness	22

T	Transmittance matrix	117
t	Amplitude transmission matrix	116
t	Time	9
T^{total}	Final film thickness at P	30
t^{total}	Total deposition time	30
$T_{O'}^{\text{total}}$	Final film thickness at substrate centre (O')	31
T_{AB}	Transition temperature from phase A to phase B	145
T_{ij}	Transmittance coefficients	117
t_{ij}	Amplitude transmission coefficient	116
$T_{O'}$	Film thickness at O' (substrate center)	29
T_m	Melting temperature	3
T_s	Substrate temperature	3
$\mathbf{u}_i$	Direction of the ith molecule in a nematic system	144
V	Film volume	29
V	Volume of dielectric host	15
v	Phase speed	10
v_1, v_2	Volume fractions of dielctric inclusions of type 1 and 2 respectively	15
V_{inc}	Volume of dielectric inclusion	15
ω	Angular frequency	10
$d\Omega/dA$	Mass flux per unit area at P	29
χ_1, χ_2, χ_3	Rotation angles about x, y and z axes, respectively	24
$\Delta\xi'$	Rotational misalignment	40
$\mathbf{x}$	4-element Berreman field vector	112

ξ	Orientation angle	27
ξ	Zig-zag growth parameter	82
$\xi'_{O'}$	Orientation angle at O'	41
x', y', z'	Principal coordinates	10
$\hat{\mathbf{X}}, \hat{\mathbf{Y}}, \hat{\mathbf{Z}}$	Global coordinate unit vectors	24
X, Y, Z	Global (lab) coordinates	22
X_O, Y_O, Z_O	Global coordinates of O	23
$\mathbf{x}, \mathbf{y}, \mathbf{z}$	Rotated substrate coordinate system unit vectors	24
x, y, z	Rotated substrate coordinate system	24
$\hat{\mathbf{x}}_O, \hat{\mathbf{y}}_O, \hat{\mathbf{z}}_O$	Substrate coordinate system unit vectors	24
x_O, y_O, z_O	Substrate coordinate system	24
z_s	Substrate height above xy-plane at P	26

Abbreviations

FDFD	Finite-difference frequency-domain	131
FDTD	Finite-difference time-domain	127
GLAD	Glancing angle deposition	22
LCD	Liquid crystal display	139
LCP	Liquid crystalline polymer	139
LSC	Luminescent solar concentrator	201
MBBA	N-(4-Methoxybenzylidene)-4-butylaniline	155
PBN	Periodically bent nematic	121
PMMA	Poly(methyl) methacrylate	202
PVD	Physical vapour deposition	2
QCM	Quartz crystal microbalance	22
SBD	Serial bideposition	33

Chapter 1

Preliminaries

"If you want to make an apple pie from scratch, you must first create the universe." – Carl Sagan

This chapter introduces a few important, recurrent topics that are common to several chapters. These include topics such as theoretical models and characterization techniques that are crucial, but not central, to the work in the following chapters. The material in this chapter is primarily aimed at new researchers, focusing on the optical properties of columnar films. It is intended to serve as a quick reference and assembles simple and relevant derivations for a number of topics that this author felt were poorly summarized in the literature. Notably, these topics include the basics of oblique angle deposition as well as the propagation of electromagnetic waves in anisotropic and composite media.

1.1 Oblique Angle Deposition

Today, the fabrication of thin films is at the heart of a staggering number of technologies. Thin films are material coatings, ranging in thickness from single atoms ($\sim 10^{-10}$ m) to several millimetres, and deposited on substrates for various applications. Today, they are found in microprocessors, liquid crystal displays, glasses, photovoltaic cells, batteries, food packaging and a whole host of other applications. They are ubiquitous in modern electronic devices and

will undoubtedly remain so in future technologies.

There are several ways to fabricate thin films. One option is to induce a chemical reaction using the substrate itself as a reactant. An example of this is the oxidation of silicon to form a silicon dioxide gate during the fabrication of transistors in integrated circuits. One can also promote a chemical reaction to occur on a substrate from vapour or liquid precursors. Examples of this include chemical vapour deposition and atomic layer deposition which are capable of generating high-purity solid films. A third option is physical vapour deposition, which will be the most important approach for the purposes of this thesis.

Physical vapour deposition (PVD) is a technique where atoms in the vapour phase impinge on a substrate where they condense and accumulate to form a thin film. The plume can be formed in several ways: sputtering and evaporation by resistive or electron-beam heating of a source material are the most common techniques, but one can also employ more exotic techniques including laser ablation and molecular beams. A variety of materials can be deposited using these techniques, including most metals, as well as both organic and inorganic compounds. Typically, the deposition process takes place in vacuum. This is done largely to maintain control of the ambient atmosphere to ensure a high purity film. Working in vacuum also raises the evaporation rate of the source material, enabling deposition to take place at lower temperatures. Vacuum also provides one additional feature that is of critical importance. Atoms emanating from the source will travel in a straight line for, on average, a distance, λ, called the mean free path, before being scattered into a random direction. For a typical gas such as nitrogen, one can write an expression for λ at room temperature as:

$$\lambda = \frac{0.04}{P}, \tag{1.1}$$

where $P$is the pressure in Pa, and λ is measured in metres. This relationship is shown in Figure 1.1. We can see at the typical deposition pressures listed ($\sim$ 10 μPa - 10 mPa or 0.1 μTorr - 0.1 mTorr), the mean free path is on the order of metres or greater. Typical source-to-substrate distances are on the order of one metre, and so vapour molecules leaving the source travel along straight line trajectories to the substrate. As a result of this behaviour, films fabricated by physical vapour deposition at low pressure result in the formation of a columnar nanostructure.

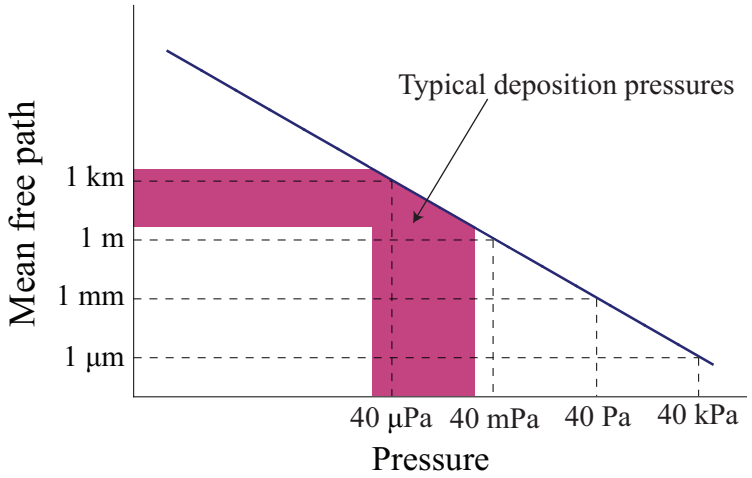

Figure 1.1: Mean free path, λ, as a function of pressure, P, with common deposition conditions identified.

Upon reaching the substrate, incident atoms adsorb onto the surface and are free to diffuse. At this point, the adsorbed atom (adatom) can either desorb from the surface or encounter other adatoms and form a nucleus. As a nucleus grows larger, it becomes more and more likely to capture new adatoms and continues to grow. Eventually, the substrate will be covered by stochastically positioned nuclei, and film growth proceeds as additional vapour adsorbs onto these seeding nuclei. The nature of the film formed as deposition continues depends largely on the ratio of the substrate temperature, T_s, relative to the melting temperature, T_m, of the deposited material, and can be described using the structure zone model [1, 2]. The model explains that at low substrate temperatures ($T_s/T_m \lesssim 0.3$), the diffusion length of the adatoms is small, so incident atoms nucleate close to the initial point of contact with the substrate. This results in a columnar film structure with a high degree of surface roughness. At higher substrate temperatures ($0.3 \lesssim T_s/T_m \lesssim 0.5$), adatoms are able to diffuse greater distances which tends to smooth out the film structure, minimizing surface roughness and eliminating the columnar nature of the film. At the highest temperatures ($0.5 \lesssim T_s/T_m \lesssim 1$), there is sufficient thermal energy to promote bulk diffusion, and crystallization can take place. In this thesis, the substrate is unheated, and remains below about 500 K in all cases [3]. An observational demonstration of this fact is that after the longest and hottest depositions, the substrate temperature was just able to induce PMMA substrates

to melt, which occurs at about 430 K [4]. The deposited materials tend to be metal oxides such as SiO_2 and TiO_2, with melting points of around 1925 K and 2115 K, respectively. The ratio, T_s/T_m, in these cases is less than 0.2, so our films can be understood as being deposited at low temperature, and exhibiting strong columnar features.

When the incident vapour impinges on the substrate at normal incidence, atoms are free to land either on existing nuclei or on the substrate itself, as shown in Figure 1.2a). As the film grows, a columnar film forms at all points on the substrate, as shown in Figure 1.2c), and the film can be considered dense, or non-porous. However, at oblique incidence angles, α, the initial nuclei cause shadowed regions on the substrate, in which vapour flux cannot impinge. This situation is shown in Figure 1.2b). While some atoms will diffuse into these shadowed regions, as the film grows, the vast majority of material will deposit on existing nuclei, forming the slanted columnar structure shown in Figure 1.2d). Physical vapour deposition done in this manner is known as oblique angle deposition.

Oblique angle deposition creates a film of slanted posts, or nanorods, inclined at an angle, β, measured from the substrate normal. This is one of the major features of films fabricated by oblique angle deposition. Having a tilted geometry introduces anisotropy into the film, which can give rise to anisotropy in the film's elastic, electrical, magnetic or optical properties [5–8]. This anisotropy exists even when the film material is completely isotropic; the anisotropy is a result purely of the film's nanostructure. This is a very useful property, as it widens significantly the number of materials one can employ when looking to design a device with anisotropic features. Additionally, standard anisotropic materials are often single crystalline, and require more difficult and expensive fabrication procedures, and can be difficult to interface with planar technologies. These features of oblique angle deposition have been known for over a century; one of the first reports was by Kundt [9], who observed anisotropic optical properties in metals deposited at oblique incidence, though was obviously unable to explain exactly why this was the case.

In all reported cases, $\beta < \alpha$, and several formulae to describe the relationship have been proposed. One proposal is the generalized tangent rule [10],

$$\tan\beta = E\tan\alpha, \tag{1.2}$$

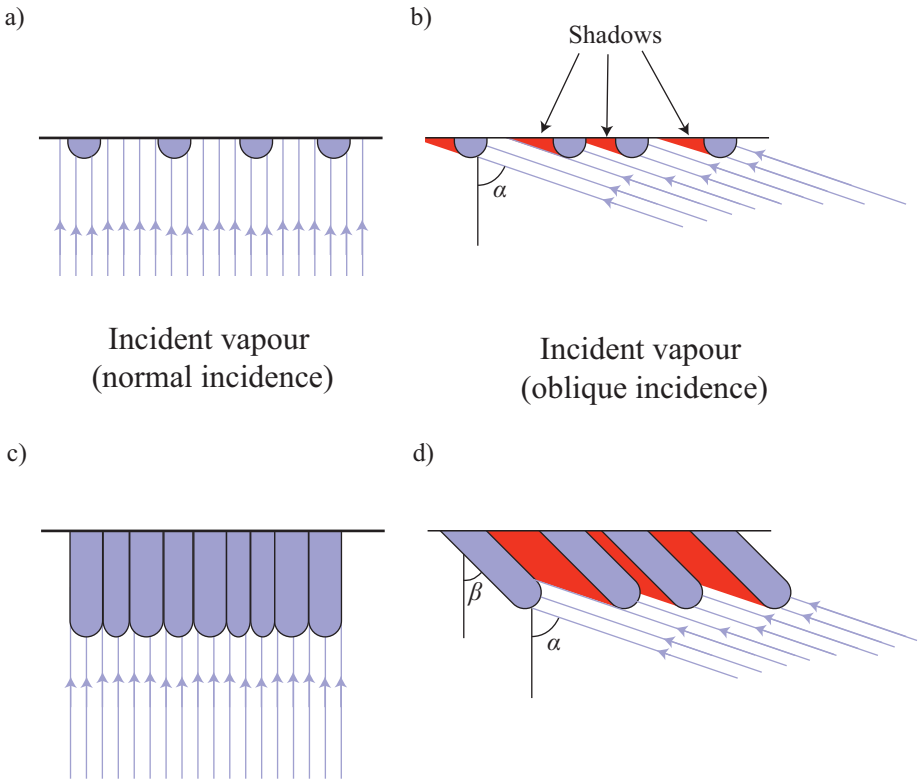

Figure 1.2: Comparison of shadowing and film growth in normal incidence versus oblique angle deposition.

where E is a material specific constant[1.1]. When E is taken to be $1/2$, the rule is simply known as the tangent rule [12], and is one of the oldest rules relating α to β. Other relationships have been suggested, including Tait's rule [13]:

$$\beta = \alpha - \arcsin \frac{1 - \cos \alpha}{2}, \tag{1.3}$$

and another relationship established by Lichter and Chen [14]:

$$\tan \beta = \frac{2}{3} \frac{\tan \alpha}{1 + E \tan \alpha \sin \alpha}, \tag{1.4}$$

where E is once again a material-specific constant, though different from the value used in the tangent rule equation. Notice that the generalized tangent rule predicts that $\beta \to 90^\circ$ as $\alpha \to 90^\circ$, which is not observed. On the other hand, the Lichter-Chen result gives:

$$\tan \beta|_{\alpha=90^\circ} = \frac{2}{3E}. \tag{1.5}$$

This is a much more physically sensible result, and much more applicable at large α.

In general, none of these relationships is completely accurate over the range $0 \leq \alpha \leq 90^\circ$, and it is often best to simply tabulate β as a function of α. However, if one knows β at a particular α, one can fit for E in either equation (1.2) or (1.4) to obtain reasonable predictions of β given small variations in α.

The second important feature of films fabricated by oblique angle deposition is that they are porous; for an equal film thickness, a film fabricated at a higher α will have less mass than one fabricated at a lower α. This implies that the average film density, $\bar{\rho}$, decreases with increasing α. The reasoning for this is quite straightforward, and can be deduced from Figure 1.2d). As the deposition angle increases, the shadowed regions become larger and larger, and the internuclear spacing increases. This decreases the surface coverage of the substrate and reduces the mass of the film in a given thickness. At the same time, the available surface area of the film is greatly increased as compared with that of a solid film. This is because the sides of the columns are also exposed in an obliquely deposited film, as shown in Figure 1.2. It should be noted that while the columns are depicted as being completely isolated in

[1.1] See Poxson [11] for an expression relating c to geometric properties of the film columns.

Figure 1.2d), this situation does not typically occur until $\alpha \gtrsim 80^\circ$. At lower angles, truly isolated columns do not exist, but pores remain throughout the film structure [15]. SEMs of films deposited above and below 80° are shown in Figure 1.3. Considering films with $\alpha \gtrsim 80^\circ$, one has largely isolated columns in a matrix of void. This is especially useful as one can infiltrate gaseous or liquid materials into the void for various purposes. One can use this feature for a number of applications, including templating polymers [16], gas sensing [17], chromatography [18], battery technology [19] and solar cells [20]. Obliquely deposited films have also been used extensively to align liquid crystals [21], which is a subject that will be investigated in detail in Chapter 5. At lower deposition angles, the film is better thought of as a matrix of solid material, in which pores (void) are embedded. The pores in these films remain accessible by sufficiently small gas atoms, and, in principle, remain viable for sensing applications. Interestingly, these films tend to have even greater surface area than films comprised of isolated columns [15], with surface area usually peaking for films deposited with α between about 60° and 70°. Films deposited at these lower deposition angles also tend to scatter light less strongly, have greater optical anisotropy [22] and align liquid crystals in a different manner than films deposited at higher deposition angles [23], and remain of considerable interest, despite the absence of isolated nanocolumnar structures.

As with β, several relationships have been suggested to relate the density to the deposition angle. This is typically done by relating α to $\bar{\varrho}$, the average fractional density, which is related to $\bar{\rho}$ by:

$$\bar{\varrho} = \frac{\bar{\rho}}{\rho_{\text{norm}}}, \tag{1.6}$$

where ρ_{norm} is the density of a film deposited at normal incidence. By this definition, $\bar{\varrho} \equiv 1$ when $\alpha = 0^\circ$. Among the relationships that relate $\bar{\varrho}$ to α are the material-independent relationship obtained by Tait [13]:

$$\bar{\varrho} = \frac{2\cos\alpha}{1+\cos\alpha}, \tag{1.7}$$

and the material-dependent relationship obtained by Poxson [11]:

$$\bar{\varrho} = \frac{c}{c+\alpha\tan\alpha}. \tag{1.8}$$

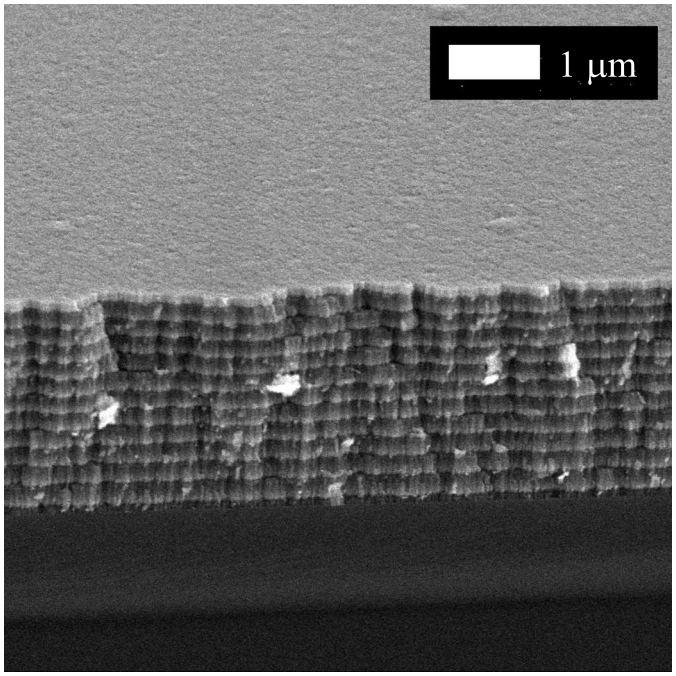

(a) Film deposited at $\alpha = 70°$

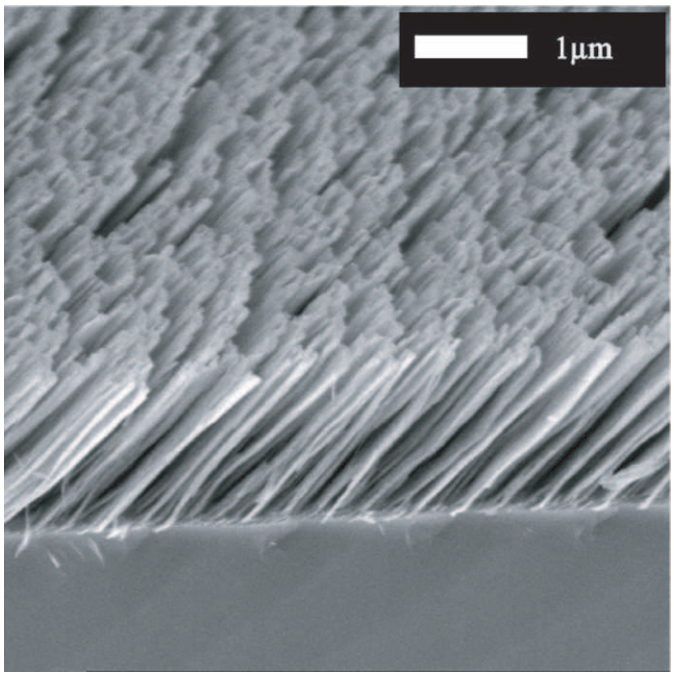

(b) Film deposited at $\alpha = 85°$

Figure 1.3: SEM images of SiO_2 films fabricated at different deposition angles

Here, c is a material specific constant. Both of these relationships illustrate the major features of the fractional density, which are that $\bar{\varrho} = 1$ when $\alpha = 0°$, and $\bar{\varrho} = 0$ when $\alpha = 90°$. However, as with the β relationships, neither is perfectly accurate, and tabulated values are often the best recourse. However, when one knows $\bar{\varrho}$ at some α, the Poxson relationship in particular can be useful for predicting small variations in $\bar{\varrho}$ due to small variations in α.

The films used in this thesis are deposited using a generalized version of oblique angle deposition called glancing angle deposition, which introduces substrate rotation during growth to manipulate the column growth. The main advantage of glancing angle deposition is the ability to modify the shape of the film columns. However, many properties of films made using glancing angle deposition, notably the density and optical constants, can be described using the same models that are applied to films made using oblique angle deposition. The use of the Poxson formula, as in Chapter 2 is one example of this, as is the use of effective medium theories, as presented in the following section.

1.2 Electromagnetic Waves

Classically, we describe the propagation of light as a solution to the wave equation which arises as a result of the interplay between the electric, **E**, and magnetic, **B**, fields as described by Maxwell's equations. In matter, Maxwell's equations are given by the following differential equations, with t denoting time:

$$\nabla \cdot \mathbf{D} = \rho_f, \qquad \text{Gauss}' \text{ law} \tag{1.9}$$

$$\nabla \cdot \mathbf{B} = 0, \qquad \text{Gauss}' \text{ law for magnetism} \tag{1.10}$$

$$\nabla \times \mathbf{E} = -\frac{\partial \mathbf{B}}{\partial t}, \qquad \text{Faraday}'\text{s law} \tag{1.11}$$

$$\nabla \times \mathbf{H} = \mathbf{J}_f + \frac{\partial \mathbf{D}}{\partial t}, \qquad \text{Ampere}'\text{s law} \tag{1.12}$$

Here, **D** is the electric displacement field, **H** is the auxiliary magnetic field and $\mathbf{J}_f$ and ρ_f are the free current density and free charge density. These are supplemented by the constitutive relations:

$$\mathbf{D} = \varepsilon_0 \varepsilon \mathbf{E}, \tag{1.13}$$

$$\mathbf{B} = \mu_0 \mu \mathbf{H}. \tag{1.14}$$

Here, ε and μ are the relative dielectric and diamagnetic tensors, and describe a material's response to external fields. The constants ε_0 and μ_0 are the permittivity and permeability of free space, respectively. As we have seen, in a principal coordinate system, having principal axes, x', y' and z', one can write the dielectric and diamagnetic tensors as:

$$\varepsilon = \begin{pmatrix} \varepsilon_{x'} & 0 & 0 \\ 0 & \varepsilon_{y'} & 0 \\ 0 & 0 & \varepsilon_{z'} \end{pmatrix}, \tag{1.15}$$

$$\mu = \begin{pmatrix} \mu_{x'} & 0 & 0 \\ 0 & \mu_{y'} & 0 \\ 0 & 0 & \mu_{z'} \end{pmatrix}, \tag{1.16}$$

where ε_i and $\mu_i$are the principal dielectric and diamagnetic constants along the ith principal axis, for $i = x', y', z'$. In isotropic materials, the principal constants are all equal, and the tensors can each be replaced by a single scalar value. In non-magnetic materials, as used throughout this thesis, the diamagnetic constant becomes unity.

In a homogeneous, linear dielectric, the free charges and currents are zero, and the dielectric tensor is constant. In such a material we can postulate harmonic plane wave solutions to the electric and magnetic fields:

$$\mathbf{E} = \mathbf{E}_0 e^{i(\mathbf{k}\cdot\mathbf{r}-\omega t)}, \tag{1.17}$$

$$\mathbf{B} = \mathbf{B}_0 e^{i(\mathbf{k}\cdot\mathbf{r}-\omega t)}. \tag{1.18}$$

Here, $\mathbf{E}_0$ and $\mathbf{B}_0$ are the electric and magnetic field amplitudes, $\mathbf{k}$ is the wavevector and ω is the angular frequency. The phase speed of the wave is:

$$v = \frac{\omega}{k} \equiv \frac{c}{n}, \tag{1.19}$$

where k is the amplitude of the wavevector, c is the speed of light in vacuum and n is the refractive index. Substituting the plane wave solutions into

Maxwell's equations and making use of the constitutive relations gives:

$$\mathbf{k} \cdot \varepsilon_0 \varepsilon \mathbf{E}_0 = \mathbf{k} \cdot \mathbf{B}_0 = 0 \tag{1.20}$$

$$\mathbf{k} \times \mathbf{E}_0 = \omega \mathbf{B}_0 \tag{1.21}$$

$$\mathbf{k} \times \mathbf{B}_0 = -\omega \varepsilon_0 \mu_0 \varepsilon \mathbf{E}_0. \tag{1.22}$$

The first of these equations indicate that $\mathbf{D}_0$ and $\mathbf{B}_0$ are perpendicular to the propagation direction, $\hat{\mathbf{k}}$, while the last requires that $\mathbf{D}_0$ and $\mathbf{B}_0$ are also mutually perpendicular. In general, these equations also give a complicated relationship between ω and $\mathbf{k}$ as a result of the dielectric tensor. However, in special cases in which $\mathbf{E}_0$ is parallel to the ith principal axis of the dielectric, so that $\mathbf{E}_0 = E_0 \hat{\mathbf{i}}$, one finds that $\mathbf{D}_0$ is parallel to $\mathbf{E}_0$ and the speed of the wave is given by:

$$v_i = \frac{\omega}{k} = \frac{1}{\sqrt{\varepsilon_0 \mu_0}\sqrt{\varepsilon_i}} = \frac{c}{n_i}. \tag{1.23}$$

Here, we have identified $c = 1/\sqrt{\varepsilon_0 \mu_0}$ as the speed of light in vacuum, and $n_i = \sqrt{\varepsilon_i}$as the refractive index along the ith principal axis. In this situation, light propagates as in an isotropic material.

Another important case is when light is propagating in a direction normal to one of the principal axes. If we take the principal axes as x', y' and z', we will consider propagation in the $x'z'$-plane. In this case, $k_{y'} = 0$ and light can be polarized either along the y' axis, or in the $x'z'$-plane. Light polarized along the y'-axis is described above, upon making the substitution $i \to y'$. For light polarized in the $x'z'$-plane, we have:

$$\mathbf{k} = k_{x'} \hat{\mathbf{x}}' + k_{z'} \hat{\mathbf{z}}' = k(\cos\theta_k \hat{\mathbf{x}}' + \sin\theta_k \hat{\mathbf{z}}'), \tag{1.24}$$

where $\theta_k$is the angle between the wavevector and the x'-axis. Equation (1.20) then gives:

$$\begin{aligned} 0 &= k(\cos\theta_k \varepsilon_{x'} E_{0x'} + \sin\theta_k \varepsilon_{z'} E_{0z'}), \\ \Rightarrow \qquad E_{0z'} &= -\frac{\varepsilon_{x'}}{\varepsilon_{z'}} \cot\theta_k E_{0x'}. \end{aligned} \tag{1.25}$$

Equation (1.21) gives:

$$\mathbf{k} \times \mathbf{E}_0 = \omega \mathbf{B}_0 = k(\sin\theta_k E_{0x'} - \cos\theta_k E_{0z'})\hat{\mathbf{y}}'. \tag{1.26}$$

This can be substituted into equation (1.22) to yield:

$$\begin{aligned}
\mathbf{k} \times \mathbf{B}_0 &= \frac{k^2}{\omega}(\cos\theta_k \hat{\mathbf{x}}' + \sin\theta_k \hat{\mathbf{z}}') \times (\sin\theta_k E_{0x'} - \cos\theta_k E_{0z'})\hat{\mathbf{y}}', \\
&= \frac{k^2}{\omega}(\sin\theta_k E_{0x'} - \cos\theta_k E_{0z'})(\cos\theta_k \hat{\mathbf{z}}' - \sin\theta_k \hat{\mathbf{x}}'), \\
&= -\omega\varepsilon_0\mu_0(\varepsilon_{x'} E_{0x'}\hat{\mathbf{x}}' + \varepsilon_{z'} E_{0z'}\hat{\mathbf{z}}').
\end{aligned} \tag{1.27}$$

Finally, one can eliminate the electric field terms by substituting from equation (1.25). Equating either of the two vector components above gives:

$$\frac{k^2}{\omega}\left(\sin\theta_k + \cos\theta_k \frac{\varepsilon_{x'}}{\varepsilon_{z'}}\cot\theta_k\right)\sin\theta_k = \omega\varepsilon_0\mu_0\varepsilon_{x'}. \tag{1.28}$$

This can be rearranged to yield the dispersion relation:

$$v = \frac{\omega}{k} = c\left(\frac{\sin^2\theta_k}{\varepsilon_{x'}} + \frac{\cos^2\theta_k}{\varepsilon_{z'}}\right)^{\frac{1}{2}}. \tag{1.29}$$

In analogy with equation (1.23), we can identify the square-rooted quantity as the inverse of the refractive index, so upon making the substitutions for the principal refractive indices, $n_i^2 = \varepsilon_i$, we have:

$$\frac{1}{n} = \left(\frac{\sin^2\theta_k}{n_{x'}^2} + \frac{\cos^2\theta_k}{n_{z'}^2}\right)^{\frac{1}{2}}. \tag{1.30}$$

We will return to this equation frequently in this thesis.

1.3 Bruggeman Effective Medium Approximation

As mentioned above, films fabricated using oblique or glancing angle deposition can be thought of as a heterogeneous mixture of the deposited film material and void. As a result, the optical properties of such a film will differ from that of a film that is made up of only the bulk material, with no void.

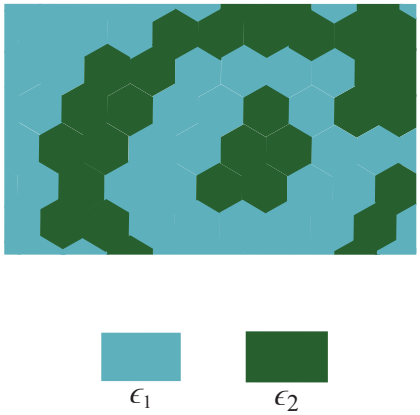

Figure 1.4: Microstructure of a composite medium

Further, the optical properties will naturally be different depending on the percentage of void in the film, so it makes sense to model the optical properties as a function of some related quantity, such as the average fractional density, $\bar{\varrho}$. Finally, if the regions of void or film material, known as inclusions, are sufficiently small, as compared with the wavelength of light, the film will act as a homogeneous film, with an effective refractive index given by some average of the refractive index of the two inclusion materials. Finding this average index is the purview of effective medium theory.

Presented here is a brief derivation of the Bruggeman effective medium theory [24–27], to explain the phenomenon. Figure 1.4 shows a composite structure made up of two materials with dielectric constants ε_1 and ε_2. We seek to describe this material by a single dielectric material, with a dielectric constant equal to ε. We do this by embedding representative inclusions in the effective medium, and solving for the dielectric constant of the material in such a way that the average field that exists in the composite medium is the same as in the effective medium.

We consider the case of a single spherical dielectric inclusion, with dielectric constant, ε_{inc}, and radius, R, embedded in a host material of dielectric constant, ε, as shown in Figure 1.5. We assume that the field far away from the sphere is given by a constant, $\mathbf{E}_0$, and we wish to determine the field inside the sphere. One can solve this problem easily using Laplace's equation [28]. Inside the

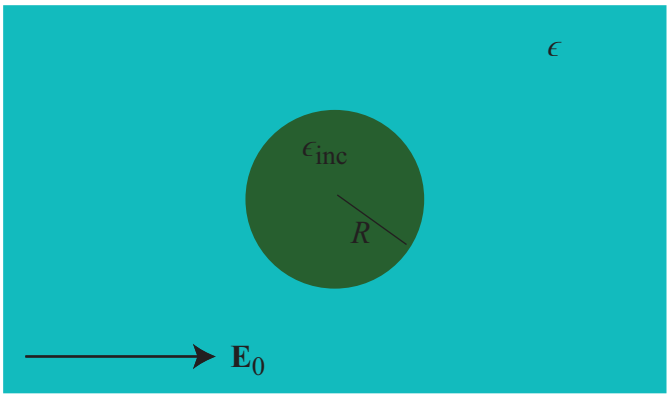

Figure 1.5: Spherical dielectric inclusion embedded in a host dielectric medium

sphere, the field is constant:

$$\mathbf{E} = \frac{3\varepsilon}{\varepsilon_{\text{inc}} + 2\varepsilon}\mathbf{E}_0 = \mathbf{E}_0 - \frac{\varepsilon_{\text{inc}} - \varepsilon}{\varepsilon_{\text{inc}} + 2\varepsilon}\mathbf{E}_0, \qquad r \leq R. \tag{1.31}$$

Outside of the sphere, the field is distorted from $\mathbf{E}_0$ as if there were a perfect dipole located at the center of the sphere:

$$\mathbf{E} = \mathbf{E}_0 - \nabla\left(\frac{\mathbf{p}\cdot\hat{\mathbf{r}}}{4\pi\varepsilon_0 r^2}\right), \qquad r > R, \tag{1.32}$$

where the dipole strength, $\mathbf{p}$, is related to $\mathbf{E}_0$ via:

$$\mathbf{p} = 4\pi\varepsilon_0 R^3 \mathbf{E}_0 \left(\frac{\varepsilon_{\text{inc}} - \varepsilon}{\varepsilon_{\text{inc}} + 2\varepsilon}\right). \tag{1.33}$$

The sphere then acts as a material with a constant dipole moment per unit volume, or polarization, $\mathbf{P}$, given by:

$$\mathbf{P} = \frac{\mathbf{p}}{\frac{4}{3}\pi R^3} = 3\varepsilon_0 \mathbf{E_0}\left(\frac{\varepsilon_{\text{inc}} - \varepsilon}{\varepsilon_{\text{inc}} + 2\varepsilon}\right) \tag{1.34}$$

We can substitute this result into equation (1.31) to rewrite the electric field in the sphere as:

$$\mathbf{E} = \mathbf{E}_0 - \frac{\mathbf{P}}{3\varepsilon_0}. \tag{1.35}$$

The field $-\frac{\mathbf{P}}{3\varepsilon_0}$ is known as the depolarization field. It arises from the polar-

ization of the material, and acts to diminish the applied field, $\mathbf{E}_0$. This field depends strongly on the geometry of the inclusion, and we will return to this point shortly.

We now compute the average field of this system. The average field of a dipole over any spherically symmetric region in which it is centered is zero, so the average field outside of the sphere is simply $\mathbf{E}_0$. Inside the sphere, the field is constant, so the average field is just $\mathbf{E}_0 - \mathbf{P}/3\varepsilon_0$. If we let the volume of the dielectric be V, and the volume of the sphere be $V_{\text{inc}} = \frac{4}{3}\pi R^3$, then the average field in the complete system, due to a single inclusion, is then:

$$\begin{aligned}\mathbf{E}_{\text{avg}} &= \mathbf{E}_0\left(1 - \frac{V_{\text{inc}}}{V}\right) + \left(\mathbf{E}_0 - \frac{\mathbf{P}}{3\varepsilon_0}\right)\frac{V_{\text{inc}}}{V} \\ &= \mathbf{E}_0 - \frac{\mathbf{P}}{3\varepsilon_0}\frac{V_{\text{inc}}}{V} \equiv \mathbf{E}_0 + \Delta\mathbf{E}_0 \end{aligned} \tag{1.36}$$

We see that the action of a single inclusion is to cause a deviation in the electric field from its nominal value of $\mathbf{E}_0$ by a value, $\Delta\mathbf{E}_0$.

The Bruggeman approach assumes that the average field across all the inclusions (the entire composite medium) be equal to the undistorted field, $\mathbf{E}_0$. This means that the total deviation in the average field across all inclusions must vanish. If there are N_1 inclusions of material 1, and N_2inclusions of material 2, with volumes, V_1 and V_2, respectively, then the total deviation in the field across all inclusions, which must vanish, is given by:

$$\Delta\mathbf{E}_{0_{\text{total}}} = \frac{\mathbf{P}_1}{3\varepsilon_0}\frac{N_1 V_1}{V} + \frac{\mathbf{P}_2}{3\varepsilon_0}\frac{N_2 V_2}{V} = 0. \tag{1.37}$$

We recognize the terms $\frac{N_1 V_1}{V}$ and $\frac{N_2 V_2}{V}$ as the volume fractions, v_1 and v_2, of the respective materials. Naturally, we have that $v_1 + v_2 = 1$. We can see then that the total deviation in the average field is simply a weighted sum of the depolarization fields of each inclusion type. We can then substitute the appropriate values for $\mathbf{P}_1$ and $\mathbf{P}_2$ from equation (1.34) to obtain:

$$v_1\frac{\varepsilon_1 - \varepsilon}{\varepsilon_1 + 2\varepsilon} + (1 - v_1)\frac{\varepsilon_2 - \varepsilon}{\varepsilon_2 + 2\varepsilon} = 0. \tag{1.38}$$

This is the famous Bruggeman effective medium approximation [29]. For our purposes, one of the media involved will typically be void. If we set material 1 to the dielectric source material, and material 2 to void, then v_1 becomes equal

to the fractional density, $\bar{\varrho}$, and we have the following:

$$\bar{\varrho}\frac{\varepsilon_1 - \varepsilon}{\varepsilon_1 + 2\varepsilon} + (1 - \bar{\varrho})\frac{1 - \varepsilon}{1 + 2\varepsilon} = 0. \tag{1.39}$$

If one instead considered ellipsoidal inclusions [30], with principal axes x', y' and z', described by the following equation:

$$\frac{x'^2}{a^2} + \frac{y'^2}{b^2} + \frac{z'^2}{c^2} = 1, \tag{1.40}$$

then the inclusions still give rise to a constant polarization, $\mathbf{P}$, and a constant depolarization field. If the principal components of the polarization are $P_{x'}, P_{y'}$ and $P_{z'}$, they are related to the external field by:

$$P_i = \frac{\varepsilon_0 E_{0_i}}{q_i}\left(\frac{\varepsilon_{\text{inc}} - \varepsilon_i}{\varepsilon_{\text{inc}} + (q_i^{-1} - 1)\varepsilon_i}\right), \qquad i = x', y', z', \tag{1.41}$$

where $q_{x'}, q_{y'}$ and $q_{z'}$are known as depolarization factors [31]. The electric field inside the inclusion is given by:

$$\mathbf{E} = \mathbf{E}_0 - \frac{q_{x'}P_{x'}\hat{\mathbf{x}}'}{\varepsilon_0} - \frac{q_{y'}P_{y'}\hat{\mathbf{y}}'}{\varepsilon_0} - \frac{q_{z'}P_{z'}\hat{\mathbf{z}}'}{\varepsilon_0}, \tag{1.42}$$

where the three terms on the right comprise the principal components of the depolarization field. The depolarization factors are given by the integrals:

$$q_{x'} = \frac{abc}{2}\int_0^\infty \frac{ds'}{(a^2 + s')D(s')} \tag{1.43}$$

$$q_{y'} = \frac{abc}{2}\int_0^\infty \frac{ds'}{(b^2 + s')D(s')} \tag{1.44}$$

$$q_{z'} = \frac{abc}{2}\int_0^\infty \frac{ds'}{(c^2 + s')D(s')}, \tag{1.45}$$

where:

$$D(s') = \sqrt{(a^2 + s')(b^2 + s')(c^2 + s')}. \tag{1.46}$$

We usually take the situation where $a \leq b \leq c$, so that the ellipsoid is longest along the z' direction, and narrowest along the x' direction. This results in

Table 1.1: Depolarization factors for several limiting ellipsoidal cases

Shape	a, b, c	$q_{x'}$	$q_{y'}$	$q_{z'}$
Sphere	$a = b = c$	$1/3$	$1/3$	$1/3$
Cylinder	$a = b,\ c = 0$	$1/2$	$1/2$	0
Slab	$b = c = 0$	1	0	0

$q_{z'} \leq q_{y'} \leq q_{x'}$. One can also show that:

$$q_{x'} + q_{y'} + q_{z'} = 1. \tag{1.47}$$

Table 1.1 lists the depolarization factors for several limiting cases of ellipsoidal inclusions [32]. Note that substitution of the spherical case, $q_{x'} = q_{y'} = q_{z'} = 1/3$, into equation (1.41) is consistent with the earlier formula derived for a spherical inclusion given by equation (1.34).

The change in the depolarization field necessitates a change in the expression for the effective medium. In this case, the Bruggeman relationship yields three equations; one effective dielectric constant is obtained for each principal axis, and the medium is biaxial, in general. We know that the Bruggeman formula is obtained by setting the weighted sum of the depolarization fields to zero. So, for a two-component medium, with an external field, $\mathbf{E}_0$, applied along the ith principal axis, with $i = x', y', z'$, setting the weighted sum of the depolarization fields to zero gives:

$$v_1 \frac{q_i P_{i_1}}{\varepsilon_0} + (1 - v_1) \frac{q_i P_{i_2}}{\varepsilon_0} = 0, \qquad i = x', y', z'. \tag{1.48}$$

Substituting the appropriate expressions for P_{i_1} and P_{i_2} from equation (1.41) gives:

$$v_1 \frac{\varepsilon_1 - \varepsilon_i}{\varepsilon_1 + (q_i^{-1} - 1)\varepsilon_i} + (1 - v_1) \frac{\varepsilon_2 - \varepsilon_i}{\varepsilon_2 + (q_i^{-1} - 1)\varepsilon_i} = 0, \qquad i = x', y', z'. \tag{1.49}$$

If material 2 is taken to be void, and material 1 is a simple dielectric, then as with earlier, v_1 becomes equal to the fractional density, $\bar{\varrho}$, and we have the final result:

$$\bar{\varrho} \frac{\varepsilon_1 - \varepsilon_i}{\varepsilon_1 + (q_i^{-1} - 1)\varepsilon_i} + (1 - \bar{\varrho}) \frac{1 - \varepsilon_i}{1 + (q_i^{-1} - 1)\varepsilon_i} = 0, \qquad i = x', y', z'. \tag{1.50}$$

This is the Bruggeman effective medium approximation for ellipsoidal inclusions [29]. It gives the effective dielectric constant, ε, of a material made up of ellipsoidal dielectric inclusions in void. As such, it is highly suitable for use in columnar thin films, such as those produced by oblique angle deposition.

1.4 Variable Angle Mueller-Matrix Ellipsometry

In this thesis, frequent use is made of the variable angle Mueller-matrix ellipsometric measurement technique [33, 34]. This measurement approach allows us to determine the optical properties of a film by examining how the film manipulates polarized light.

The measurement setup is illustrated in Figure 1.6. Input light of a known

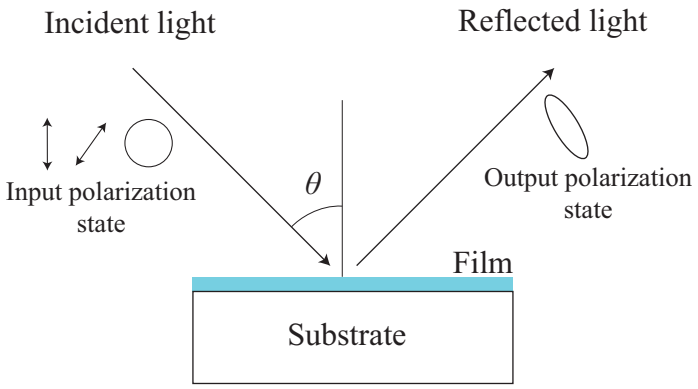

Figure 1.6: Measurement setup for variable angle Mueller-matrix ellipsometry

polarization and a known wavelength is incident on the sample at an angle, θ. The polarization state of the input light is modified by the film, and this change is measured by the measurement tool. Specifically, the measurement tool compares the input and output Stokes parameters [35] by comparing the incident and reflected transmittances of various polarization states.

The polarization state of a beam of light can be described using the 4-element Stokes vector:

$$\mathbf{S} = \begin{pmatrix} S_0 \\ S_1 \\ S_2 \\ S_3 \end{pmatrix}, \tag{1.51}$$

where the individual components, S_0, S_1, S_2 and S_3 are termed the Stokes parameters. The electric field of the light beam is a vector that has two orthogonal components, normal to the direction of propagation. There are several equivalent bases in which to express the electric field, and three are necessary to define the Stokes parameters. The first choice uses two linear polarization states along orthogonal axes, which we label x and y. The second choice is along two new linear states, u and v, which are rotated by $\pi/4$ from the x and y states. Finally, the third choice employs left- and right-circularly polarized states, L and R. The Stokes vectors are then defined by via the intensity, I, of light in each of the basis states:

$$S_0 = I_x + I_y = I_u + I_v = I_L + I_R, \tag{1.52}$$

$$S_1 = I_x - I_y, \tag{1.53}$$

$$S_2 = I_u - I_v, \tag{1.54}$$

$$S_3 = I_L - I_R. \tag{1.55}$$

Often, S_0 is simply set equal to unity, and the other Stokes parameters are scaled accordingly.

The action of a film is to transform light from an incident polarization state, $\mathbf{S}^i$, to a reflected polarization state, $\mathbf{S}^r$. The film therefore acts as a 4 x 4 matrix, known as the Mueller matrix, M. By inputting known polarization states and measuring the output state, one can determine the elements of the Mueller matrix, M, as a function of both wavelength and incidence angle. The tool that we employ for this purpose is the V-VASE (J. A. Woollam Co. Inc.). It is capable of measuring spectral data between $300 - 1700$ nm ($0.7 - 4.1$ eV), for incidence angles from $25^\circ - 90^\circ$. The tool can generate any arbitrary input polarization, but because it possesses only a linear analyzing polarizer but no retardation element on the detection side, it cannot detect S_3. As a result, only the first three rows of the Mueller matrix can be obtained. Typically, this is not a major concern, as the optical properties of most films can be adequately determined using only the first three rows of M. If data from the fourth row is necessary, it can be obtained by inserting a waveplate between the sample and detector of the ellipsometer [36].

To actually obtain the optical properties of the measured sample, the tool employs the WVASE32 software (J. A. Woollam Co. Inc.) to generate a math-

ematical model of the film and substrate. The software then solves for the film thickness (if unknown) and for the optical constants at each wavelength, by modeling the film using physical models such as the Cauchy dispersion model, or the Bruggeman effective medium. From this, modeled values for the Mueller matrix are generated. The software then iteratively changes the model parameters using the Levenburg-Marquardt algorithm [37] until the modeled Mueller matrix values are a best fit solution to the measured ones. The resulting optical constants of the model are then taken to represent the real optical constants of the measured sample. Note that the samples in this thesis are commonly modeled as Bruggeman effective media, as described above, so this approach actually determines the optical constants implicitly, by directly determining the fractional density, $\bar{\varrho}$, as well as the film's depolarization factors, $q_{x'}, q_{y'}$ and $q_{z'}$.

1.5 Conclusions

As indicated earlier, this chapter is meant to be used as a quick reference for understanding a number of principles that recur throughout this thesis, and for future researchers working on the optical properties of anisotropic thin films. While much of this material can be found in various textbooks and papers, often times these resources offer only partial derivations, or employ unnecessarily complex mathematics. As a result, these sources can be difficult to follow and are ineffective at communicating the necessary material to interested parties. It is the author's hope that this chapter helps to explain and consolidate a number of these topics for the use of future scientists, so that they may be learned faster, and with considerably less frustration.

Chapter 2

Uniformity of the Glancing Angle Deposition Process

"It requires a very unusual mind to undertake the analysis of the obvious." – Alfred North Whitehead

2.1 Introduction

The material in this chapter is intended to facilitate future prototyping and manufacturing of devices based on glancing angle deposition technology, which is described herein. This chapter focuses on modeling process uniformities during film growth, and how this affects important properties such as film thickness, film density and columnar structure over large area depositions, which would likely be necessary for commercial manufacturing. The material in this chapter expands upon a number of prior studies on the fundamentals of film growth using glancing angle deposition [39–41], but addresses a number of engineering concerns regarding repeatability, scalability and process uniformity, that have been previously overlooked. Additionally, the results presented below explicitly illustrate and explain the engineering significance of two material parameters, column tilt and film density, and how they affect process variations

[2.0] A version of this chapter has been published. N. Wakefield and J. Sit, Journal of Applied Physics, 109, 084322 (2011) [38]

during substrate rotation. The material in this chapter is of crucial importance for determining device specifications and tolerances for film structures and devices based on glancing angle deposition, and is intended for any researchers or engineers involved with prototyping or manufacturing devices using this technology. The model presented is quite simple, but it will be shown that the experimental results still match the predicted values to a high degree of accuracy, and the model still possesses enough versatility for a variety of film structures, for different materials and for temperature effects.

2.2 Glancing Angle Deposition

The cornerstone of the research in this thesis is the glancing angle deposition (GLAD) technique, a generalized version of the oblique angle deposition technique [40,42–45]. GLAD is an approach capable of creating nanostructured materials with controlled geometry. The structure of the film arises via bottom-up processes, as opposed to being patterned by lithography or other top-down methods. GLAD works by introducing dynamic changes in the substrate orientation during deposition, which has significant effects on the columnar orientation and columnar shape, and can be used to introduce controlled variation into the film's properties. The substrate orientation is usually implemented as a function of film thickness, T, which is usually monitored using a nearby quartz crystal microbalance (QCM). This chapter will describe the GLAD process in detail, with a focus on the uniformity of film properties, how they vary over individual substrates, and how these properties can be altered using different substrate rotation approaches. Typically, the substrate is rotated about two independent axes, but we will present first a general framework handling the case of substrate rotation about three orthogonal axes, before simplifying to the more standard case.

2.2.1 Coordinate systems

The geometry of the GLAD setup requires several right-handed coordinate systems, and is somewhat complicated in the most general case. To start, a fixed, global, XYZ coordinate system is defined, as in Figure 2.1, having its origin at the deposition source, S, which may be the electron-beam evaporation source, for example. The X-axis is chosen to be in the direction normal to S,

while Y- and Z-axes are freely chosen. To be consistent with the geometry of our particular deposition chamber, the Y-axis is chosen to be in the direction normal to the chamber door, pointing out of the plane of the figure, which fixes the Z-axis as well (points to the right). The definition of the XYZ-axes in this manner allows for any point above the source to be unambiguously expressed in spherical coordinates.

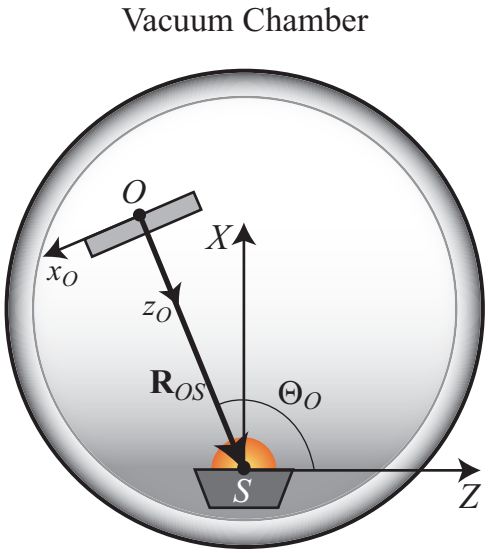

Figure 2.1: Global coordinate system description (not to scale). XYZ is a fixed, global coordinate system whose origin is at source S. The Y-axis points out of the plane of the page. The substrate holder is located at point O, the origin of the $x_O y_O z_O$ coordinate system which describes the home position of the substrate holder.

Of primary interest are those points that coincide with the center of a rotating substrate holder within the chamber. Such a point, labeled O, has the coordinates $(X_O, Y_O, Z_O) = R_{OS}(\sin\Theta_O \cos\Phi_O, \sin\Theta_O \sin\Phi_O, \cos\Theta_O)$, where R_{OS} is the distance from O to S (termed the throw distance), Θ_O is the polar angle measured off the Z-axis, and Φ_O is the azimuthal angle, as measured in the positive sense from the X-axis. The unit vectors of the spherical coordinate system and the XYZ system are related via:

$$\hat{\mathbf{X}} = \sin\Theta_O \cos\Phi_O \hat{\mathbf{R}}_{OS} + \cos\Theta_O \cos\Phi_O \hat{\boldsymbol{\Theta}}_O - \sin\Phi_O \hat{\boldsymbol{\Phi}}_O, \tag{2.1}$$

$$\hat{\mathbf{Y}} = \sin\Theta_O \sin\Phi_O \hat{\mathbf{R}}_{OS} + \cos\Theta_O \sin\Phi_O \hat{\boldsymbol{\Theta}}_O + \cos\Phi_O \hat{\boldsymbol{\Phi}}_O, \tag{2.2}$$

$$\hat{\mathbf{Z}} = \cos\Theta_O \hat{\mathbf{R}}_{OS} - \sin\Theta_O \hat{\boldsymbol{\Theta}}_O. \tag{2.3}$$

Assuming a planar substrate holder, oriented such that the substrate normal is pointed at S, we define a new, $x_O y_O z_O$ coordinate system that is unambiguously generated from the spherical coordinate unit vectors:

$$\hat{\mathbf{x}}_O = \hat{\mathbf{\Theta}}_O, \tag{2.4}$$

$$\hat{\mathbf{y}}_O = -\hat{\mathbf{\Phi}}_O, \tag{2.5}$$

$$\hat{\mathbf{z}}_O = -\hat{\mathbf{R}}_{OS}. \tag{2.6}$$

The z_O-axis corresponds to the substrate normal and points to the deposition source S, while we will see that the x_O- and y_O-axes are chosen to be consistent with the film's principal axes as described in Chapter 3. It is most common for a GLAD apparatus to be designed such that the substrate holder is directly above the source; in such a case $\Theta_O = 90°$, $\Phi_O = 0°$, $\hat{\mathbf{x}}_O = -\hat{\mathbf{Z}}$, $\hat{\mathbf{y}}_O = \hat{\mathbf{Y}}$, and $\hat{\mathbf{z}}_O = -\hat{\mathbf{X}}$.

Finally, one can then define an xyzcoordinate system to handle substrate rotations. The xyz system is defined to be coincident with the $x_O y_O z_O$ system when no rotation has taken place. Rotations are handled by first rotating the xyz system about the x-axis by the angle χ_1, then rotating about the updated y-axis by the angle χ_2, then finally rotating about the updated z-axis by the angle χ_3. Therefore, a vector expressed in $x_O y_O z_O$ coordinates can be expressed in xyz coordinates by multiplying it by the rotation matrix, $A_{\chi_1\chi_2\chi_3}$, where:

$$\begin{aligned} A_{\chi_1\chi_2\chi_3} &= \begin{pmatrix} C_{\chi_3} & S_{\chi_3} & 0 \\ -S_{\chi_3} & C_{\chi_3} & 0 \\ 0 & 0 & 1 \end{pmatrix} \begin{pmatrix} C_{\chi_2} & 0 & S_{\chi_2} \\ 0 & 1 & 0 \\ -S_{\chi_2} & 0 & C_{\chi_2} \end{pmatrix} \begin{pmatrix} 1 & 0 & 0 \\ 0 & C_{\chi_1} & S_{\chi_1} \\ 0 & -S_{\chi_1} & C_{\chi_1} \end{pmatrix} \\ &= \begin{pmatrix} C_{\chi_2}C_{\chi_3} & C_{\chi_1}S_{\chi_3} - S_{\chi_1}S_{\chi_2}C_{\chi_3} & S_{\chi_1}S_{\chi_3} + C_{\chi_1}S_{\chi_2}C_{\chi_3} \\ -C_{\chi_2}S_{\chi_3} & C_{\chi_1}C_{\chi_3} + S_{\chi_1}S_{\chi_2}S_{\chi_3} & S_{\chi_1}C_{\chi_3} - C_{\chi_1}S_{\chi_2}S_{\chi_3} \\ -S_{\chi_2} & -S_{\chi_1}C_{\chi_2} & C_{\chi_1}C_{\chi_2} \end{pmatrix}. \end{aligned} \tag{2.7}$$

Here, we have used the notation $C_\chi \equiv \cos\chi$ and $S_\chi \equiv \sin\chi$. $A_{\chi_1\chi_2\chi_3}$ is a function of χ_1, χ_2 and χ_3 which may vary over the course of the deposition. Also, because of the unitary nature of the underlying matrices, the inverse of $A_{\chi_1\chi_2\chi_3}$ is given by its transpose.

It should be made clear that the decomposition into three rotation matrices,

as shown in equation (2.7), is not unique. There are an infinite number of ways of carrying out a rotation from the $x_O y_O z_O$ system to the xyz system, and the order in which the rotations can be applied is also freely chosen. This means that the breakdown as shown in equation (2.7) may or may not coincide exactly with the actual step-by-step rotations carried out in the experimental setup. This does not matter, so long as the full matrix product, $A_{\chi_1\chi_2\chi_3}$, properly describes the complete real-world rotation. As an example, consider the case in which the experimental setup performs (1) a rotation, α_1, about the y_O axis, followed by (2) a ϕ_1 rotation about the z axis followed by (3) an α_2 rotation about the y_O axis once more. The complete rotation is described simply by a rotation first about y with $\chi_2 = \alpha_1 + \alpha_2$ followed by a rotation about z with $\chi_3 = \phi_1$, with $\chi_1 = 0$. Individually, rotation (1) is given by $\chi_2 = \alpha_1$, with $\chi_1 = \chi_3 = 0$ and rotation (2) is given by $\chi_3 = \phi_1$, with $\chi_1 = \chi_2 = 0$. However, because rotation (2) causes the y and y_O axes to be no longer coincident, rotation (3) is not given simply by $\chi_2 = \alpha_2$, with $\chi_1 = \chi_3 = 0$. Instead, χ_1, χ_2 and χ_3 are all in general non-zero, and the situation is much more complicated than looking at the three rotations as a whole. The point is that it is not necessary to try and match the step-by-step rotations of the experimental setup, so long as the total mathematical and real-world rotations are identical. In particular, it is very common for the experimental setup to rotate only about y_O and z, as in the example outlined above. In this case, it is most straightforward to set $\chi_1 = 0$ always, apply the χ_2 rotation first, and the χ_3 rotation second. In this way, χ_2 and χ_3 line up with the usual literature quantities α, denoting the previously described deposition angle, and ϕ, the azimuthal rotation angle. Making the appropriate substitutions, one obtains the following rotation matrix:

$$A_{\alpha\phi} = \begin{pmatrix} \cos\alpha\cos\phi & \sin\phi & \sin\alpha\cos\phi \\ -\cos\alpha\sin\phi & \cos\phi & -\sin\alpha\sin\phi \\ -\sin\alpha & 0 & \cos\alpha \end{pmatrix}. \tag{2.8}$$

2.2.2 Points and Vectors of Interest

We now wish to determine the incident material flux at P , an arbitrary point of interest on the substrate. The applicable geometry is shown in Figure 2.2. P is located by the static xyz coordinates $\mathbf{R}_{OP}^{xyz} = (r\cos\varphi, r\sin\varphi, z_s)$. In other

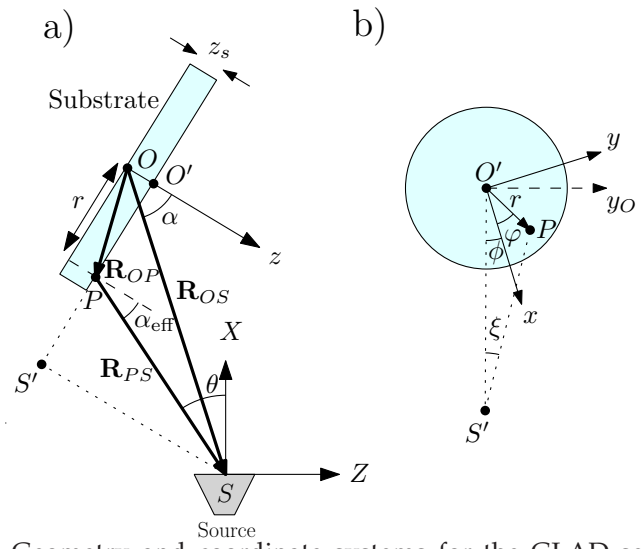

Figure 2.2: Geometry and coordinate systems for the GLAD setup (not to scale). (a) As seen from front of chamber. Points O, O', S, and S' are in the plane of the page, while point of interest P is behind the plane of the page. (b) Looking at the substrate, in the $-z$ direction.

words, P is a real-world point on the substrate surface with z_s representing the thickness of the substrate or height above the xy plane. We now look to describe the geometric orientation at P at a single instant of time.

The evaporation source is located at the position $\mathbf{R}_{OS} = R_{OS}\hat{\mathbf{z}}_O$, regardless of the position of O within the deposition chamber. The position vector $\mathbf{R}_{OP}$ locates the point P. Given its coordinates above, expressed in the xyz coordinate system, it can be expressed in the $x_O y_O z_O$ system using the matrix, $A^{-1}_{\alpha\phi}$:

$$\mathbf{R}_{OP}^{x_O y_O z_O} = A^{-1}_{\alpha\phi}\mathbf{R}_{OP}^{xyz} = \begin{pmatrix} r\cos\alpha\cos\psi - z_s\sin\alpha \\ r\sin\psi \\ r\sin\alpha\cos\psi + z_s\cos\alpha \end{pmatrix}, \tag{2.9}$$

where we introduce the quantity $\psi \equiv \phi + \varphi$. Of primary interest is the vector, $\mathbf{R}_{PS}$, which points from the substrate point of interest, P, to the source point S.

In $x_O y_O z_O$ coordinates, $\mathbf{R}_{PS}$ can be obtained from $\mathbf{R}_{OS}^{x_O y_O z_O}$ and $\mathbf{R}_{OP}^{x_O y_O z_O}$:

$$\begin{aligned}\mathbf{R}_{PS}^{x_O y_O z_O} &= \mathbf{R}_{OS}^{x_O y_O z_O} - \mathbf{R}_{OP}^{x_O y_O z_O} \\ &= \begin{pmatrix} -r\cos\alpha\cos\psi + z_s\sin\alpha \\ -r\sin\psi \\ R_{OS} - r\sin\alpha\cos\psi - z_s\cos\alpha \end{pmatrix}, \end{aligned} \tag{2.10}$$

The magnitude of $\mathbf{R}_{PS}$ gives the source-to-substrate separation for the given point of interest P, and the direction of $\mathbf{R}_{PS}$ can be used to determine (1) the local deposition angle, α_{eff}, defined as the angle between the substrate normal $\hat{\mathbf{z}}$ and $\mathbf{R}_{PS}$; and (2) the off-axis angle, θ, given as the angle between the negative of the source normal $-\hat{\mathbf{X}}$ and $\mathbf{R}_{PS}$. R_{PS}, α_{eff}, and θ can be computed from:

$$\begin{aligned} R_{PS} &= |\mathbf{R}_{PS}| \\ &= R_{OS}\sqrt{1+\gamma_1^2+\gamma_2^2-2\gamma_1\sin\alpha\cos\psi-2\gamma_2\cos\alpha}, \end{aligned} \tag{2.11}$$

$$\begin{aligned} R_{PS}\cos\alpha_{\text{eff}} &= \mathbf{R}_{PS}\cdot\hat{\mathbf{z}} \\ &= R_{OS}(\cos\alpha-\gamma_2), \end{aligned} \tag{2.12}$$

$$\begin{aligned} R_{PS}\cos\theta &= -\mathbf{R}_{PS}\cdot\hat{\mathbf{X}} \\ &= R_{OS}\cos\Phi_O(\sin\Theta_O+\gamma_1(\cos\psi\cos(\alpha+\Theta_O)+\sin\psi\tan\Phi_O) \\ &\quad -\gamma_2\sin(\alpha+\Theta_O)), \end{aligned} \tag{2.13}$$

where $\gamma_1 \equiv \frac{r}{R_{OS}}$ and $\gamma_2 \equiv \frac{z_s}{R_{OS}}$. At the point P, the film behaves as though it were deposited at an angle α_{eff}, even though the substrate is inclined at an angle α. Since α_{eff} varies across the substrate, this has important ramifications on the density and column tilt, that will be discussed shortly. The off-axis angle is important for quantifying the behaviour of the vapour plume at P, and will also be addressed shortly. Note also that the off-axis angle is the only parameter exhibiting a dependence on the angular location of O, as a result of its dependence on the orientation of the source. Finally, while the explicit forms of equations (2.11) to (2.13) apply to the case where only α and ϕ rotations are present, the vector forms of these equations apply regardless of the chamber's geometry. The quantities above all vary dynamically during deposition, whenever substrate motion is present.

There is one final parameter of interest, the orientation angle, ξ, which

is the angle between the global deposition plane (containing the vectors $\mathbf{R}_{OS}$ and $\hat{\mathbf{z}}$) and the local deposition plane (containing $\mathbf{R}_{PS}$ and $\hat{\mathbf{z}}$). This angle is important because the columns that make up a GLAD film grow toward the source, and in general they grow in the local deposition plane, as opposed to the global one. ξ is defined to be negative when $0^\circ < \psi < 180^\circ$, and positive for $180^\circ < \psi < 360^\circ$. Using the cross-product to determine the magnitude of $\sin\xi$ and choosing signs appropriately yields:

$$\begin{aligned}\sin\xi &= \pm\frac{|(\mathbf{R}_{OS}\times\hat{\mathbf{z}})\times(\mathbf{R}_{PS}\times\hat{\mathbf{z}})|}{|\mathbf{R}_{OS}\times\hat{\mathbf{z}}||\mathbf{R}_{PS}\times\hat{\mathbf{z}}|}\\ &= \pm\frac{|\hat{\mathbf{y}}_O\times(\mathbf{R}_{PS}\times\hat{\mathbf{z}})|}{|\mathbf{R}_{PS}\times\hat{\mathbf{z}}|}\\ &= -\frac{\gamma_1\sin\psi}{\sqrt{\sin^2\alpha+\gamma_1^2-2\gamma_1\sin\alpha\cos\psi}}.\end{aligned} \tag{2.14}$$

The top-most expression is true in general, while replacing $\frac{\mathbf{R}_{OS}\times\hat{\mathbf{z}}}{|\mathbf{R}_{OS}\times\hat{\mathbf{z}}|}$ with $\hat{\mathbf{y}}_O$, and the subsequent formulae, hold when only α and ϕ rotations are present.

ξ is shown schematically in Figure 2.2 as the angle $O'S'P$, where S' is z_s above the projection of S onto the xy-plane. Knowing ξ allows one to write the trajectory of columns growing off the substrate. Columns grow in the local deposition plane, characterized by ξ, at an angle β, as measured from the substrate normal. We choose to relate β to α_{eff} using the relationship obtained by Lichter and Chen, equation (1.4), but making the substitution $\alpha \to \alpha_{\text{eff}}$:

$$\tan\beta = \frac{2}{3}\frac{\tan\alpha_{\text{eff}}}{1+E\tan\alpha_{\text{eff}}\sin\alpha_{\text{eff}}}, \tag{2.15}$$

where, as before, E is a material specific parameter.

The unit vector, $\hat{\mathbf{q}}$, expressing the columnar growth trajectory in the xyz coordinate system is given by:

$$\hat{\mathbf{q}}^{xyz} = \begin{pmatrix}\sin\beta\cos(\xi-\phi)\\ \sin\beta\sin(\xi-\phi)\\ \cos\beta\end{pmatrix}. \tag{2.16}$$

As the substrate rotates over the course of the deposition, this trajectory also changes. The net trajectory of the film columns is determined by the way in which this vector changes, but also requires an understanding of the different

rates of growth across the substrate. This point will be addressed shortly.

In the GLAD technique, α and ϕ are specified as functions of the film thickness at O', denoted $T_{O'}$, and in general can vary dynamically leading to complex non-uniformities in film thickness, density, and columnar tilt angle. Typically, α is held constant while ϕ is free to vary; the latter may be a continuous rotation, stepped rotation, or some combination thereof. Section 2.2.4 describes the structures of interest in this study.

2.2.3 Deposited Material

To examine the uniformity of film properties across a substrate, we need to calculate the amount of material deposited at each point on the substrate. This depends directly on the geometry outlined above as well as the nature of the source. For this work, the source is assumed to be a differential source at S. The incident flux (mass per unit time) due to this source on an area $d\mathbf{A}$ located at point P is given by $d\Omega$ [46]:

$$d\Omega = \frac{k\cos^n\theta}{R_{PS}^2}\left(\frac{\mathbf{R}_{PS}}{R_{PS}}\cdot d\mathbf{A}\right), \tag{2.17}$$

where k is a proportionality constant indicating the amount of mass given off by the source. The $\cos^n\theta$ dependence describes the directionality of the source element, with larger values of n indicating increased directionality along the $\hat{\mathbf{X}}$ direction. A value of $n = 0$ implies that the flux from S is isotropic. In the GLAD setup, an area element at point P has the form $d\mathbf{A} = dA\hat{\mathbf{z}}$. Substituting this into equation (2.17) gives the flux per unit area on the substrate:

$$\frac{d\Omega}{dA} = \frac{k\cos^n\theta}{R_{PS}^2}\left(\frac{\mathbf{R}_{PS}}{R_{PS}}\cdot\hat{\mathbf{z}}\right) = \frac{k\cos^n\theta\cos\alpha_{\text{eff}}}{R_{PS}^2}. \tag{2.18}$$

The total mass deposited in a time, dt, at point P is simply:

$$dm = \frac{k\cos^n\theta\cos\alpha_{\text{eff}}dAdt}{R_{PS}^2}. \tag{2.19}$$

In this time, the film will grow by a thickness, $dT = \Gamma dt$, where Γ is the instantaneous vertical rate of film growth at P. Thus, the film deposited in dt occupies a volume $dV = dAdT = \Gamma dAdt$. dm and dV are related by the instantaneous density at point P, denoted ρ, according to $\rho = \frac{dm}{dV}$. Note that $\rho \neq$

$\bar{\rho}$, the average film density, introduced earlier. The relationship between these quantities is explained below. We will also define the instantaneous fractional density, ϱ, according to $\varrho \equiv \rho/\rho_{\text{norm}}$, similar to equation (1.6). With these definitions in place:

$$\rho = \varrho\rho_{\text{norm}} = \frac{dm}{dV} = \frac{k\cos^n\theta\cos\alpha_{\text{eff}}}{\Gamma R_{PS}^2} = \frac{1}{\Gamma}\frac{d\Omega}{dA}. \tag{2.20}$$

Solving this for k yields:

$$k = \frac{\Gamma\rho R_{PS}^2}{\cos^n\theta\cos\alpha_{\text{eff}}}. \tag{2.21}$$

k does not need to be directly evaluated in order to continue the analysis, but, if needed, convenient points at which to make measurements to determine k are the center of the substrate, O', or on a nearby QCM.

For a GLAD film, it can be difficult, in general, to actually measure instantaneous quantities such as ρ, ϱ or Γ, which vary during deposition, and consequently throughout the thickness of the films. There are ways to do this *in situ*, using ellipsometry, for example [47], but we do not treat that case here. In contrast, the average quantities, $\bar{\rho}$, $\bar{\varrho}$ and $\bar{\Gamma}$, can be determined readily. For instance, $\bar{\rho}$ can be determined experimentally through direct mass measurements on small substrate samples while $\bar{\varrho}$ can be determined using optical measurements of refractive index in combination with optical models such as the Bruggeman effective medium approximation introduced in the previous chapter. Likewise, experimental values for the average growth rate, $\bar{\Gamma}$, can be found using measurements of the total film thickness. Average density and growth rate at a given point P are defined through the following relationships:

$$\bar{\Gamma}t^{\text{total}} = T^{\text{total}}, \tag{2.22}$$

$$\bar{\rho}T^{\text{total}} = \int_0^{T^{\text{total}}} \rho(T)dT, \tag{2.23}$$

where T^{total} is the final film thickness at P and $t^{\text{total}}$is the total deposition time. With these definitions in mind, the total mass per unit area deposited at P is

given by:

$$\begin{aligned}\frac{dm}{dA} &= \int_0^{t^{\text{total}}} \frac{d\Omega}{dA} dt \int_0^{T^{\text{total}}} \frac{1}{\Gamma} \frac{d\Omega}{dA} dT \\ &= \int_0^{T^{\text{total}}} \rho(T) dT = \bar{\rho} T^{\text{total}} \\ &= \rho_{\text{norm}} \bar{\varrho} T^{\text{total}}. \end{aligned} \tag{2.24}$$

In other words, the mass deposited per unit area at any point on the substrate is equal to the product of the average density and the thickness, which are both important, measurable quantities. Additionally, because $d\Omega/dA$ is independent of ϕ rotation at the point O' (the center of the substrate), the quantity $\bar{\varrho}_{O'} T_{O'}^{\text{total}}$ must be the same for all film structures deposited at a constant α, grown to the same nominal thickness, as measured by a fixed, external QCM.

According to equation (2.24), $\frac{dm}{dA}$ is related to the measurable quantities $\bar{\varrho}$ and T^{total} at every point on the substrate. As a result, examining the uniformity in $\frac{dm}{dA}$ over a substrate is of great utility. In general, the mass deposited per unit area is:

$$\frac{dm}{dA} = \int_0^{T^{\text{total}}} \frac{1}{\Gamma} \frac{d\Omega}{dA} dT = \int_0^{T^{\text{total}}} \frac{k}{\Gamma} \frac{\cos^n \theta \cos \alpha_{\text{eff}}}{R_{PS}^2} dT. \tag{2.25}$$

Substituting for $\frac{k}{\Gamma}$ from equation (2.21) using values at the particular point of O' gives the following key result, which can be used directly to compute the deposited mass per unit area of any film structure:

$$\frac{dm}{dA} = \int_0^{T_{O'}^{\text{total}}} \rho_{O'} \left(\frac{R_{O'S}^2 \cos^n \theta \cos \alpha_{\text{eff}}}{R_{PS}^2 \cos^n \theta_{O'} \cos \alpha_{\text{eff}_{O'}}} \right) dT_{O'}. \tag{2.26}$$

For obliquely deposited films, there is no substrate rotation. Therefore, the term in brackets is constant so one obtains the result that:

$$\frac{dm}{dA} = \rho_{\text{norm}} \bar{\varrho}_{O'} T_{O'}^{\text{total}} \left(\frac{R_{O'S}^2 \cos^n \theta \cos \alpha_{\text{eff}}}{R_{PS}^2 \cos^n \theta_{O'} \cos \alpha_{\text{eff}_{O'}}} \right). \tag{2.27}$$

Therefore, for deposition in which no rotation is present, $\frac{dm}{dA}$ and $\frac{d\Omega}{dA}$, given by equations (2.27) and (2.18) are identical, up to a constant multiplicative factor. For films done at constant α, equation (2.26) can also be normalized so that $\left.\frac{dm}{dA}\right|_{O'}$ is unity by setting $\rho_{O'} T_{O'}^{\text{total}} = 1$. This assumption allows one to compute

the mass deposited per unit area of any film, normalized to the value at O', based only on the geometry of the system and the directionality of the source.

Cases in which the substrate rotates during deposition can be thought of as being made up of infinitesimal obliquely deposited segments. A particularly important case is where ϕ is a linear function of $T_{O'}$: $\phi = \frac{2\pi T_{O'}}{p_v}$. Here, p_v is the film thickness required for ϕ to increment (or decrement, if $p_v < 0$) by 2π. This algorithm leads to vertically oriented columns, hence the v subscript. In the general case, the substrate will make N complete rotations, and then rotate an extra amount, $\Delta\phi < 2\pi$. In this case one can integrate easily over either $T_{O'}$ or ϕ:

$$\begin{aligned}\frac{dm}{dA} &= \left(\frac{R_{O'S}^2}{\cos^n\theta_{O'}\cos\alpha_{\mathrm{eff}_{O'}}}\right)\int_0^{T_{O'}^{\mathrm{total}}}\frac{\rho_{O'}\cos^n\theta\cos\alpha_{\mathrm{eff}}}{R_{PS}^2}dT_{O'} \\ &= \left(\frac{pR_{O'S}^2}{2\pi\cos^n\theta_{O'}\cos\alpha_{\mathrm{eff}_{O'}}}\right)\int_0^{2\pi N+\Delta\phi}\frac{\rho_{O'}\cos^n\theta\cos\alpha_{\mathrm{eff}}}{R_{PS}^2}d\phi, \qquad (2.28)\end{aligned}$$

Notice that at the point O', equation (2.28) is indeed equivalent to $\bar{\rho}_{O'}T_{O'}^{\mathrm{total}}$, as the terms depending on the geometry of the system are constant. Again, if one sets $\rho_{O'}T_{O'}^{\mathrm{total}} = 1$, the result is normalized so that the deposited mass per unit area is unity at O'. Virtually all film structures possible with GLAD can be thought of as made up of sections of slanted and vertical growth segments, so the net deposited mass per unit area at the substrate for any film structure can be obtained by summing terms in the form of (2.27) and (2.28). In the particular case in which $\Delta\phi = 0$, then one has $Np = T_{O'}^{\mathrm{total}}$ so:

$$\begin{aligned}\frac{dm}{dA} &= \left(\frac{NpR_{O'S}^2}{2\pi\cos^n\theta_{O'}\cos\alpha_{\mathrm{eff}_{O'}}}\right)\int_0^{2\pi}\frac{\rho_{O'}\cos^n\theta\cos\alpha_{\mathrm{eff}}}{R_{PS}^2}d\phi, \\ &= \left(\frac{T_{O'}^{\mathrm{total}}R_{O'S}^2}{2\pi\cos^n\theta_{O'}\cos\alpha_{\mathrm{eff}_{O'}}}\right)\int_0^{2\pi}\frac{\rho_{O'}\cos^n\theta\cos\alpha_{\mathrm{eff}}}{R_{PS}^2}d\phi, \qquad (2.29)\end{aligned}$$

which reduces the problem to integration over a single rotational period, which may be computationally simpler to implement.

2.2.4 Basic Film Structures

In the GLAD technique, there are numerous substrate motion algorithms possible involving various combinations of motion in the tilt and rotation axes (α and ϕ, respectively) described in the literature [48–54]. These affect the resultant columnar film structure and will be brought into much greater focus in the following chapter, but for the time being, the discussion in here is simplified and restricted to the following four structures, each at fixed α:

(A) Slanted posts, for which ϕ is kept constant at 0. This is the standard oblique angle evaporation case. As discussed previously, the resultant film will have columns tilted in the direction of the source at an angle β, measured from the normal, if the measurement is made in the local deposition plane. Columns not on the central axis of the wafer will also tilt slightly inward toward the x-axis, at an angle of ξ.

(B) Vertical posts, for which $\phi = \frac{2\pi T_{O'}}{p_v}$, where p_v is the pitch, as described earlier. For a truly vertical post structure, empirical results indicate that a sufficiently rapid ϕ rotation is required such that the pitch is smaller than the column diameter; slow rotation causes a helical columnar morphology. A typical range of values for the pitch that yields vertical posts is 5 to 10 nm. This algorithm results in vertically oriented columns, similar to those shown in Figure 1.2c), but where the constraint $\alpha = 0$ is not required. We now introduce the notation β', which represents the columnar tilt angle for any general growth algorithm, and reserve the notation β for the column tilt of a pure slanted post, as in (A). Vertical posts can then be described as having columns with $\beta' \sim 0$.

(C) Spin-pause, which consists of alternating slanted post and vertical post segments. In the spin-pause method, ϕ is first held constant at 0 over a thickness $T' << T_{O'}^{\text{total}}$, then rotated for the same thickness with a pitch, p_v. In general, a rapid, third segment with a thickness, δ, on the order of 2 nm must be included in order to return ϕ to an integer multiple of 2π. This introduces a slight asymmetry in film growth[2.1]. This cycle is repeated several times in order to generate the film. The resultant film has a column angle $\beta' < \beta$.

(D) Serial bideposition (SBD), which involves ϕ being held constant at 0° for a thickness $T' << T_{O'}^{\text{total}}$, then held constant at π for the same thickness. Again, this cycle is repeated to build up the film. The resultant columnar

[2.1] Though it was not done in this research, one possible way to eliminate the asymmetry would be to rotate in opposite directions during alternating deposition cycles.

structure is often assumed to be vertical, but in reality, individual columns possess significant tilt.

In this study, the growth algorithms described work in a fashion such that there will be an integer number of rotations in ϕ over the course of the complete deposition. Graphs of these ϕ against $T_{O'}$ are given in Figure 2.3.

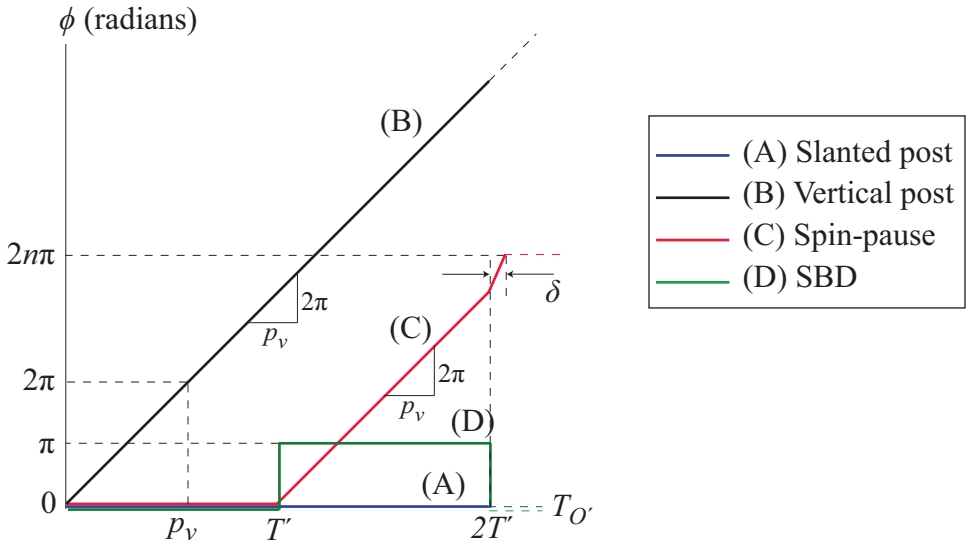

Figure 2.3: Basic film growth algorithms

We now use the equations developed above are used to make predictions of the incident mass per unit area for these four film structures. A 10 cm diameter substrate with a thickness of $z_s = 2$ mm is assumed. The substrate holder is assumed to be directly above the source, as is typically the case for GLAD, with $\Theta_O = \pi/2$, $\Phi_O = 0$ and $R_{OS} = 40$ cm. A deposition angle of $\alpha = 70°$ is employed. For the films involving constant rotation, a pitch, $p_v = 5$ nm is used, and $T' = 12.5$ nm for both the spin-pause and SBD cases.

Figure 2.4 shows the predicted incident mass per unit area for each of the four film structures under consideration, normalized so that $\bar{\rho}_{O'} T_{O'}^{\text{total}} = 1$. Notice the huge variation in uniformity between the different structures. The deposited mass per unit area for the pure slanted post varies by more than 40% in the positive x direction and more than 20% in the negative x direction, but less than 5% in the symmetric $\pm y$ directions. Meanwhile, the non-uniformity in the vertical post is only about 1% in all directions. The spin-pause structure has a non-uniformity that is about half as severe as the pure slanted case, while the

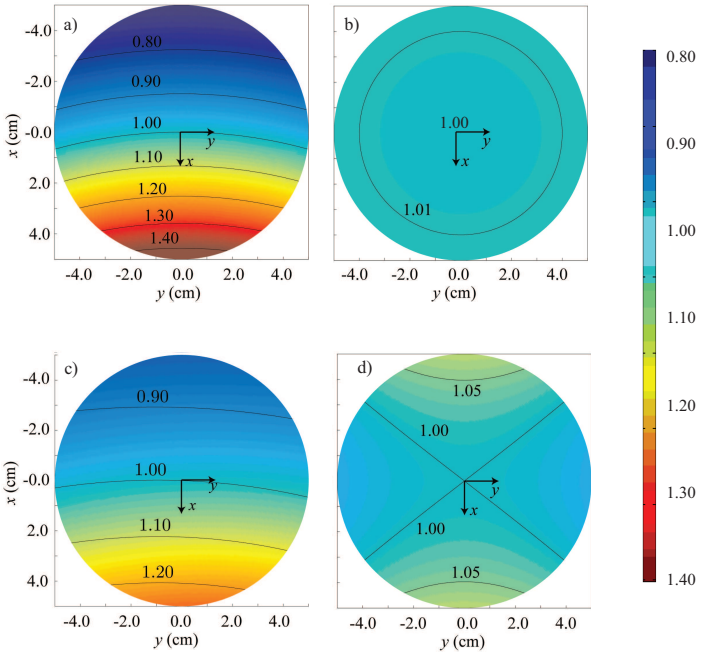

Figure 2.4: Predicted $\frac{dm}{dA}$ over a 10 cm diameter substrate for a) slanted post, b) vertical post, c) spin-pause and d) serially bideposited GLAD film structures deposited at $\alpha = 70°$ (normalized such that $\bar{\rho}_{O'} T_{O'}^{\text{total}} = 1$).

SBD case exhibits a maximum non-uniformity under about 5%, but with strong differences along x and y. As mentioned earlier, there is a slight asymmetry in the deposited mass per unit area distribution for the spin-pause case due to the particulars of that growth algorithm. The asymmetry is very small; there is less than a 1% difference between values at ± 4 cm along the y-axis. Note that all figures in the set were plotted to the same color scale which emphasizes that the structures involving short-pitch rotations in ϕ have much better uniformity.

2.2.5 Thickness and Density Non-uniformities

We have now demonstrated that it is easy to calculate the deposited mass per unit area for any arbitrary film growth algorithm. However, while this gives some insight into the non-uniformity that occurs during deposition, it would be far more useful to be able to be able to discuss the density and the thickness separately, rather than just their product. To start, an expression for the total thickness at P is required. Since $dt = dT/\Gamma = dT_{O'}/\Gamma_{O'}$, we can write:

$$T^{\text{total}} = \int_0^{T^{\text{total}}} dT = \int_0^{T^{\text{total}}_{O'}} \frac{\Gamma}{\Gamma_{O'}} dT_{O'}. \tag{2.30}$$

In order to eliminate the $\Gamma/\Gamma_{O'}$ term, we use equation (2.20), which gives the relation that $\varrho\Gamma \propto d\Omega/dA$. Taking a ratio of this relationship at point P and point O', and using equation (2.18) gives:

$$T^{\text{total}} = \int_O^{T^{\text{total}}_{O'}} \frac{\varrho_{O'}}{\varrho} \frac{\cos^n\theta \cos\alpha_{\text{eff}} R^2_{O'S}}{\cos^n\theta_{O'} \cos\alpha_{\text{eff}_{O'}} R^2_{PS}} dT_{O'}. \tag{2.31}$$

To evaluate this integral, an expression for ϱ is required. Finding such an expression is a complicated question, as density has been found to vary with the deposition geometry, the deposited material, the substrate material, and the rotation of the substrate itself [43, 55]. However, it is a reasonable approximation to neglect many of these complications and simply model the density as a function of the effective deposition angle, α_{eff}, using one of the formulae developed for obliquely evaporated films mentioned earlier. We earlier identified many potential models, and for the case at hand we choose to use Poxson's formula given in equation (1.8) since it captures material dependence and does so simply, using only a single parameter. Since ρ is now the density of an in-

finitesimal obliquely deposited segment, with deposition angle, α_{eff}, we take Poxson's result and make the substitutions $\bar{\varrho} \to \varrho$ and $\alpha \to \alpha_{\text{eff}}$ to obtain:

$$\varrho = \frac{c}{c + \alpha_{\text{eff}} \tan(\alpha_{\text{eff}})}. \tag{2.32}$$

Under this model, and for constant α depositions, notice that $\varrho_{O'}$ is constant since $\alpha_{\text{eff}_{O'}}$ is constant, implying also that $\varrho_{O'} = \bar{\varrho}_{O'}$. In Poxson's derivation, c is treated as a material-specific fitting parameter, independent of α_{eff}. In reality, due to the factors listed above, c can not be strictly constant, but it often can be approximately so over a substrate, as long as α_{eff} does not vary by more than about 10 degrees. Most GLAD depositions at angles greater than $\alpha = 50^\circ$ on typical substrates (1" to 6" diameter) meet this requirement. As a result, while published values can be somewhat useful, perhaps the best way to obtain a value for c is to measure the density at O' and solve equation (2.32) directly for c, as this introduces the fewest sources of error. Solving for c via this approach gives the following equation:

$$c = \frac{\bar{\varrho}_{O'} \alpha_{\text{eff}_{O'}} \tan(\alpha_{\text{eff}_{O'}})}{1 - \bar{\varrho}_{O'}} \tag{2.33}$$

Alternatively, one can use the method of tooling factors [56] (also known as deposition ratios). During deposition, thickness is typically monitored by a nearby quartz crystal microbalance (QCM). The deposition rate at the QCM, Γ_{QCM}, is related to the rate of growth at P by the tooling factor, $D = \frac{\Gamma}{\Gamma_{\text{QCM}}}$. Like c, D depends on the geometry of the chamber, the motion of the substrate and the deposited material. To first order, for a given chamber geometry and film material, D is treated as a constant and catalogued as a function of α_{eff}. Considering the behaviour at O' in particular, from equation (2.24) we know that $\left.\frac{dm}{dA}\right|_{O'} = \rho_{\text{norm}} \bar{\varrho}_{O'} T^{\text{total}}_{O'}$ always. An alternate expression can be obtained from equation (2.25) by substituting in the appropriate values at O':

$$\left.\frac{dm}{dA}\right|_{O'} = \frac{\cos^n \theta_{O'} \cos \alpha_{\text{eff}_{O'}}}{R^2_{O'S}} \int_0^{T^{\text{total}}_{O'}} \frac{k}{\Gamma_{O'}} dT_{O'}. \tag{2.34}$$

Now, consider a deposition done at normal incidence to one at a non-zero α, both to the same final thickness at O'. Recalling that the effective deposition angle at O' is $\alpha_{\text{eff}_{O'}}$, and letting D_{norm} denote the tooling factor at normal inci-

dence and $D_{O'}$ denote the tooling factor at O', we can then write:

$$\rho_{\text{norm}}\bar{\varrho}_{O'}(\alpha_{\text{eff}_{O'}})T_{O'}^{\text{total}} = \frac{\cos^n\theta_{O'}\cos\alpha_{\text{eff}_{O'}}}{R_{O'S}^2}\Bigg|_{\alpha}\int_0^{T_{O'}^{\text{total}}}\frac{k}{D_{O'}(\alpha_{\text{eff}_{O'}})\Gamma_{\text{QCM}}}dT_{O'}, \quad (2.35)$$

$$\rho_{\text{norm}}T_{O'}^{\text{total}} = \frac{\cos^n\theta_{O'}\cos\alpha_{\text{eff}_{O'}}}{R_{O'S}^2}\Bigg|_{0^\circ}\int_0^{T_{O'}^{\text{total}}}\frac{k}{D_{\text{norm}}\Gamma_{\text{QCM}}}dT_{O'}. \quad (2.36)$$

Taking the ratio of these two equations yields a relation between the deposition angle and the normalized density, given by the following unwieldy expression:

$$\bar{\varrho} = \frac{D_{\text{norm}}}{D_{O'}(\alpha_{\text{eff}_{O'}})}\frac{(\sin\Theta_O - \gamma_2\sin(\alpha+\Theta_O))^n(1-\gamma_2)^2(\cos\alpha-\gamma_2)}{\sin^n\Theta_O(1+\gamma_2^2-2\gamma_2\cos\alpha)^{\frac{n+3}{2}}}. \quad (2.37)$$

This can be simplified in two ways. First, in the limit of thin substrates, for which $\gamma_2 \ll 1$, one obtains:

$$\bar{\varrho} = \frac{D_{\text{norm}}}{D_{O'}(\alpha_{\text{eff}_{O'}})}\frac{(\sin\Theta_O - \gamma_2\sin(\alpha+\Theta_O))^n(\cos\alpha-\gamma_2)}{\sin^n\Theta_O}. \quad (2.38)$$

Second, consider the common case in which $\Theta_O = \pi/2$, where O is directly above the source, S. In this case, again with $\gamma_2 \ll 1$, equation (2.37) simplifies to:

$$\begin{aligned}\bar{\varrho} &= \frac{D_{\text{norm}}}{D_{O'}(\alpha_{\text{eff}_{O'}})}(\cos\alpha-\gamma_2),\\ &= \frac{D_{\text{norm}}}{D_{O'}(\alpha_{\text{eff}_{O'}})}\cos\alpha_{\text{eff}_{O'}}.\end{aligned} \quad (2.39)$$

This result was also obtained by Poxson, with α instead of $\alpha_{\text{eff}_{O'}}$. For small α, $\alpha \sim \alpha_{\text{eff}_{O'}}$ and the difference can be ignored. For large α, this is not necessarily true. For instance, if $\alpha = 85^\circ$ and $\gamma_2 = 0.01$, then $\cos\alpha = 0.087$ while $\cos\alpha_{\text{eff}_{O'}} = 0.077$, which is a roughly 12% difference. We now make the approximation that equation (2.39) holds not only at O', but at any point, so the equation can be applied without the O' subscripts. Then we can find c by substituting equation (2.39) into equation (2.33) and simplifying:

$$c = \frac{\alpha_{\text{eff}}\tan(\alpha_{\text{eff}})}{\frac{D(\alpha_{\text{eff}})}{D_{\text{norm}}}\sec\alpha_{\text{eff}} - 1}. \quad (2.40)$$

Note that this equation implies that the density and the tooling factor are linked, which is not surprising given their coupled relationship in the deposited mass per unit area. However, the two are often thought of as being independent, which is false. Equation (2.39) provides a method to obtain either the density or the tooling factors for a given material, given knowledge of the other quantity.

The tooling factor approach is sometimes more convenient than solving for c directly, as it uses thickness measurements, which are often simpler and more common. We will also show in the following section that c varies slightly between different growth algorithms. As a result, the tooling factors will also be different for different film growth algorithms; films having a larger c value will have a smaller tooling factor and vice versa. This fact should be kept in mind if film thickness accuracy is especially crucial. Regardless of the approach, once a value for c has been obtained, equation (2.31) can be evaluated to determine film thickness. Then one can find the average film density by simply dividing the deposited mass per unit area, $\frac{dm}{dA} = \bar{\rho} T^{\text{total}}$, by this result. To find the average fractional film density, one must then also divide out ρ_{norm}.

2.2.6 Growth Trajectory of GLAD Columns

The final topic of interest is the trajectory of columns growing at P, which controls the principal coordinates for any tensorial film properties, including dielectric [36] or diamagnetic [57] tensors, for instance. For slanted posts, the situation is fairly straightforward. As described earlier, the posts grow along the constant trajectory, $\hat{\mathbf{q}}$, given by equation (2.16). During the deposition, the film grows to a vertical (z) thickness of T^{total}, so the net trajectory of a slanted post grown at P is given by, with all parameters constant:

$$\mathbf{q}^{xyz} = \begin{pmatrix} \tan\beta\cos(\xi - \phi) \\ \tan\beta\sin(\xi - \phi) \\ 1 \end{pmatrix} T^{\text{total}}. \tag{2.41}$$

This is a vector that makes an angle, β, with the substrate normal, and is oriented at an angle, $\xi - \phi$, in the xy-plane. Recall that β varies with α_{eff}, according to equation (2.15), so β will not be constant over the entire substrate. In order to properly model the variation in β across the substrate, one must

know the parameter, E, from equation (2.15), which can either be obtained from literature values, or by a direct measurement of β at a known α_{eff}. Typically, the point O' is a convenient point to choose.

For depositions in which substrate rotation is present, we treat the deposition as a series of slanted post depositions of thickness dT along trajectories $d\mathbf{q}$. To find the net trajectory, one must simply integrate over $d\mathbf{q}$:

$$\begin{aligned}\mathbf{q}^{xyz} &= \int d\mathbf{q}^{xyz} = \int_0^{T^{\text{total}}} \begin{pmatrix} \tan\beta\cos(\xi-\phi) \\ \tan\beta\sin(\xi-\phi) \\ 1 \end{pmatrix} dT \\ &= \int_0^{T_{O'}^{\text{total}}} \begin{pmatrix} \tan\beta\cos(\xi-\phi) \\ \tan\beta\sin(\xi-\phi) \\ 1 \end{pmatrix} \frac{\Gamma}{\Gamma_{O'}} dT_{O'}. \end{aligned} \tag{2.42}$$

As in equation (2.31), the $\frac{\Gamma}{\Gamma_{O'}}$ term can be dealt with by employing Poxson's formula for density, and the above integral can be computed. Once obtained, $\mathbf{q}^{xyz}$ can be put into the following general form:

$$\mathbf{q}^{xyz} = \begin{pmatrix} \tan\beta'\cos\xi' \\ \tan\beta'\sin\xi' \\ 1 \end{pmatrix} T^{\text{total}}, \tag{2.43}$$

where the net column tilt, β', and the net orientation angle, ξ', can be found via the following relationships:

$$\cos\beta' = \frac{\mathbf{q}\cdot\hat{\mathbf{z}}}{q} = \frac{q_z}{\sqrt{q_x^2+q_y^2+q_z^2}}. \tag{2.44}$$

$$\sin\xi' = \pm\frac{|(\mathbf{q}\times\hat{\mathbf{z}})\times\hat{\mathbf{y}}|}{|(\mathbf{q}\times\hat{\mathbf{z}})|} = \frac{q_y}{\sqrt{q_x^2+q_y^2}}. \tag{2.45}$$

In analogy to the slanted post case, ξ' indicates the net direction that a column grows in the xy-plane. It can also be a useful quantity for identifying the alignment of a sample. For alignment purposes, the quantity of interest at a given point is $\Delta\xi' \equiv \xi'_{\text{measured}} - \xi'_{\text{expected}}$. Any non-zero measurement obtained for $\Delta\xi'$ indicates a rotational misalignment (typically 0-3°) between the x- and y-axes of the substrate, and the coordinate system of the measurement device.

This can be an important issue for reducing uncertainty in measured film parameters, and ensuring they are being measured along appropriate axes. The behavior at O' is often especially simple. At O', equation (2.42) reduces to:

$$\mathbf{q}_{O'}^{xyz} = \int_0^{T_{\text{total}}^{O'}} \begin{pmatrix} \tan\beta_{O'}\cos\phi \\ -\tan\beta_{O'}\sin\phi \\ 1 \end{pmatrix} dT_{O'}. \tag{2.46}$$

In cases where $\sin\phi$ integrates to zero over $T_{O'}$, $q_{O'y}$ will be zero, and consequently, so will $\xi'_{O'}$, regardless of $\beta_{O'}$. This is the case in slanted post films with $\phi = 0$, as well as serially bideposited films, so long as ϕ undergoes an integer number of rotations. Both situations are the case for the films described in this paper. In these cases, $\xi'_{O'_{\text{measured}}}$ is a direct measure of the rotational misalignment, and one need not be concerned about predicted values. In the case of vertical post films, $\xi'_{O'}$ is undefined since $\beta'_{O'} = 0$, but this is not problematic, as the film is radially symmetric, and rotational misalignment does not exist. Finally, for spin-pause films, $\xi'_{O'}$ is in general expected to be non-zero, so one must examine $\Delta\xi'$ to determine rotational misalignment.

2.3 Experimental Results

2.3.1 Experimental Details

TiO_2 (3-6 mm pieces, 99.9% purity, from Cerac, Inc.) films were fabricated on Si wafers (10 cm diameter, p-doped, {100} orientation, from University Wafer) using electron beam evaporation. O is located directly above S, such that $\Phi_O = 0$, $\Theta_O = \pi/2$, with $R_{OS} = 40$ cm. The films were deposited with $\alpha = 70°$ at a rate of $\Gamma_{\text{QCM}} = 0.6$ nm/s as measured by a nearby QCM[2.2]. The slanted post column tilt angle at O' is measured to be $\beta = 39 \pm 5°$, yielding $E = 0.49 \pm 0.16$. The target QCM thickness was $T_{\text{QCM}}^{\text{total}} = 1060$ nm in all cases. z_s was measured to be 2 mm, including the substrate holder, giving $\alpha_{\text{eff}_{O'}} = 70.3°$. The deposition pressure was maintained between 8.0 and 12.0 mPa by flowing in O_2 gas during deposition. Samples were annealed in atmosphere at 100°C for 24 hr following deposition to obtain stoichiometric samples. At normal incidence, we measure

[2.2]Films were deposited at $\alpha = 70°$ since films fabricated with this deposition angle are simple to measure using ellipsometry, but still exhibit significant column tilt, high porosity (¿0.5) and low optical scattering.

TiO_2 to have a density of $\rho_{\text{norm}} = 3.7 \pm 0.3$ g/cm^3 and a tooling factor of $D_{\text{norm}} = 1.5 \pm 0.1$.

Optical characterization was performed using variable-angle, Mueller-matrix, spectroscopic ellipsometry as outlined in the previous chapter and the films were modeled as a biaxial Bruggeman effective medium [36] using the iterative software approach. Spectral data was collected in reflection over the range 0.75-4.10 eV (1650 - 302 nm) in 0.05 eV steps at angles of incidence of 45°, 55° and 65°. The area of the beam spot is dependent on the incident angle, and attains a maximum size of approximately 1×3 mm at 65°. As discussed in the previous chapter, the ellipsometric approach allows for the determination of T^{total}, β', ξ' and $\bar{\varrho}$.

Table 2.1 shows average fractional density, $\bar{\varrho}_{O'}$, thickness, $T^{\text{total}}_{O'}$, and deposited mass per unit area ($\left.\frac{dm}{dA}\right|_{O'} = \bar{\rho}_{O'} T^{\text{total}}_{O'}$), measured for each of the four film structures at O', as well as the value obtained for c obtained using equation (2.33). The deposited mass per unit area is remarkably consistent across each architecture. Even the most extreme value, obtained for the spin-pause case, is within 4% of the other three. Given that the deposited mass per unit area can vary by over 60% across a 10 cm diameter wafer, the agreement is quite remarkable. These results strongly support the prediction that $\bar{\rho}_{O'} T_{O'}$ is indeed independent of film structure. However, the individual thicknesses and densities are certainly not invariant. It is apparent that as more substrate rotation is present, the density decreases, while the thickness increases. As a result, c is smaller for films with increased substrate rotation. The magnitude of these changes is only a few percent, but this can translate to appreciable differences in thickness for thick films and for larger diameter substrates. The difference in thickness implies that $\bar{\Gamma}$, the vertical film growth rate, increases with additional substrate rotation. A possible explanation of this could be that shadowing caused by rotation leads to a preferential exposure of the peaks of existing columns, leading to an increased accumulation of material in the vertical direction.

We first need to determine n, the directionality of the source. The principal effect of increased n is to increase the downward curvature in the contour lines seen in Figure 2.4 a). To estimate the value of n, the normalized $\bar{\rho} T^{\text{total}}$ for a slanted post structure was measured along the x-axis, and compared to predicted values with varying n. The results for $n = 2, 3$ and 4 are shown in

Table 2.1: Density, thickness and c values at O' for different GLAD architectures ($\rho_{\text{norm}} = 3.70$ g/cm^3)

Film structure	$\bar{\varrho}_{O'}$	$T_{O'}^{\text{total}}$ (nm)	$\bar{\rho}_{O'} T_{O'}^{\text{total}}$ (g/cm^2)	c
Slanted post	0.59±0.01	887±5	0.194±0.003	4.9±0.2
Vertical post	0.55±0.01	943±5	0.192±0.003	4.2±0.2
Spin-pause	0.58±0.01	928±5	0.199±0.003	4.7±0.2
SBD	0.54±0.01	935±5	0.187±0.003	4.1±0.2

Figure 2.5. We see that each of the plots shown exhibit good agreement with

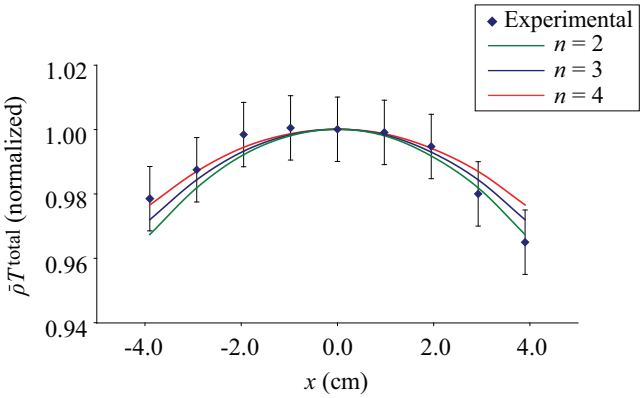

Figure 2.5: The effect of n on the predicted mass flux per unit area

a model, so we use a least-squares approach to determine the best choice, and that can be shown to be $n = 3$. As a result, a $\cos^3\theta$ dependence is assumed in equation (2.17) and for all of the results presented in this thesis.

2.3.2 Deposited Mass per Unit Area

We can now examine the behavior of the four film structures described earlier. Figure 2.6(a) shows the effective deposition angle for the pure slanted post case, where $\alpha = 70°$, $R_{OS} = 40$ cm and $z_s = 2$ mm. The non-zero z_s causes the effective deposition angle to be 70.3° at O', which is a fairly small change. However, the much more notable effect is the non-uniformity in α_{eff} across the substrate. The non-uniformity is about ±2°, which amounts to about a 6% variation in α_{eff}. Given $E = 0.49$ and $c = 4.9$, we can compute the non-uniformity in $\bar{\varrho}$ and β, as shown in Figures 2.6(b) and 2.6(c). The non-uniformity in the fractional

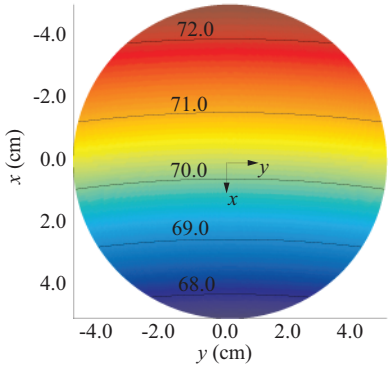

(a) Effective deposition angle, α_{eff}.

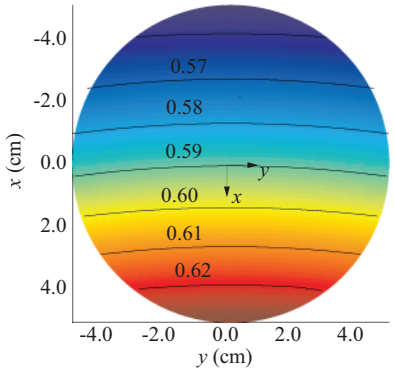

(b) Average fractional density, $\bar{\varrho}$.

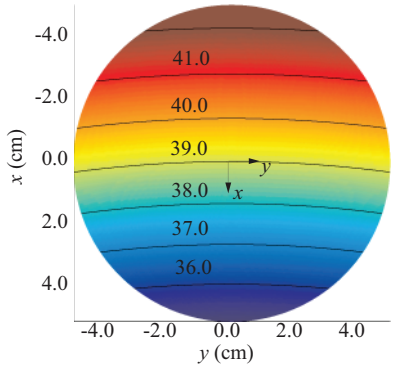

(c) Column tilt angle, β.

Figure 2.6: Calculated values for pure slanted post deposition with $\alpha = 70°$, $R_{OS} = 40$, $z_s = 2$ mm, $E = 0.49$ and $c = 4.9$.

density as a result of the variation in α_{eff} is a fairly significant 10%,while the non-uniformity in β only about 2° total. It is clear, however, that even a relatively small variation in α_{eff} can have significant effects on the physical properties of the resultant film. Since all films can be treated as a sum of infinitesimal slanted post segments, the non-uniformities present here will underlie the resultant properties of any arbitrary film structure.

Figure 2.7 shows the normalized $\bar{\rho}T^{\text{total}}$ measured along the x-axis for all

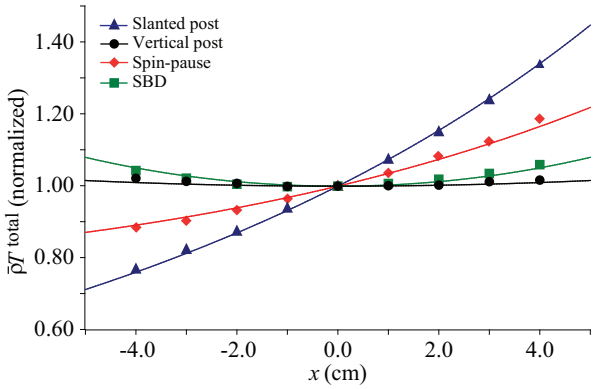

Figure 2.7: Experimental (points) and predicted (solid lines) deposited mass per unit area along the x-axis for different GLAD architectures (normalized).

four structures. $\Delta\xi' = 0°$ is measured for all cases, other than the vertical post case, for which ξ' is undefined. The agreement between the measured data and the model predictions is very good; on the scale shown, the error in the measured data is equivalent to the size of the data points. As expected, GLAD films fabricated with increased rotation during deposition exhibit much better uniformity in $\bar{\rho}T^{\text{total}}$, with the SBD and vertical post films exhibiting 10% and 4% uniformity, respectively, within 4 cm of the center of the substrate. For the slanted and spin-pause cases, the magnitude of the $\bar{\rho}T^{\text{total}}$ non-uniformity is greater on the half of the substrate closest to the source, while for the vertical post and SBD cases, the deposited mass per unit area is at a minimum at the center of the wafer and increases with $|x|$. We can define a unitless measure of the uniformity, $\Delta_i^j(d)$, as the difference between the maximum and minimum values of the quantity j (which can be thickness, density, etc.) along the $i = x, y$-axis, over a $\pm d$ range, divided by the average of those two values. Likewise, $\Delta^j(d)$ can be defined as the variation in j within a radius, d, of the center of

Table 2.2: Measured decimal non-uniformity in deposited mass per unit area, average density and total thickness for the four film structures (predicted values in brackets)

	Non-uniformity			
Variable	Slanted post	Vertical post	Spin-pause	SBD
$\Delta_x^{\bar{\rho}^{T^{\text{total}}}}(4\text{ cm})$	0.54 (0.55)	0.02 (0.01)	0.30 (0.27)	0.05 (0.05)
$\Delta_y^{\bar{\rho}^{T^{\text{total}}}}(4\text{ cm})$	0.04 (0.03)	0.02 (0.01)	0.02 (0.01)	0.02 (0.03)
$\Delta^{\bar{\rho}^{T^{\text{total}}}}(4\text{ cm})$	0.54 (0.55)	0.02 (0.01)	0.30 (0.27)	0.08 (0.08)
$\Delta_x^{T^{\text{total}}}(4\text{ cm})$	0.45 (0.45)	0.01 (0.00)	0.22 (0.22)	0.03 (0.03)
$\Delta_y^{T^{\text{total}}}(4\text{ cm})$	0.02 (0.03)	0.00 (0.00)	0.03 (0.01)	0.02 (0.03)
$\Delta^{T^{\text{total}}}(4\text{ cm})$	0.45 (0.45)	0.01 (0.00)	0.22 (0.22)	0.05 (0.06)
$\Delta_x^{\bar{\rho}}(4\text{ cm})$	0.10 (0.11)	0.02 (0.01)	0.09 (0.05)	0.02 (0.02)
$\Delta_y^{\bar{\rho}}(4\text{ cm})$	0.03 (0.00)	0.02 (0.01)	0.02 (0.00)	0.02 (0.00)
$\Delta^{\bar{\rho}}(4\text{ cm})$	0.10 (0.11)	0.02 (0.01)	0.09 (0.05)	0.03 (0.02)

the substrate. Typically, most of the non-uniformity is contributed along the x-axis, so that $\Delta^j = \Delta_x^j$. This is not always true, however; SBD films in particular do not follow this rule. To first order, Δ values are proportional to d, so one can predict the non-uniformity for a variety of substrate sizes, if one knows the non-uniformity of a substrate having a particular d. Table 2.2 tracks Δ values for deposited mass per unit area, average density and total thickness for each film structure, with $d = 4$ cm, which covers the measurable area of the substrate.

Figure 2.8 shows the results measured along the y-axis for the same samples. For clarity, error bars are shown only for the spin-pause case, but are of comparable magnitude (± 0.01) for each data point. Again, the data is in very good agreement with the model, and it is clear that along the y-axis, uniformity is very good for each film structure, with even the worst-case slanted post film exhibiting $\Delta_y^{\bar{\rho}^{T^{\text{total}}}}(4\text{ cm}) < 5\%$. There are two interesting observations to make. The first is that the deposited mass per unit area is indeed asymmetric in the spin-pause case as a result of the asymmetry of the deposition algorithm. More interesting, however, is the fact that the deposited mass per unit area for a vertical post film exhibits the opposite curvature as compared to the other algorithms, with the spin-pause result intermediate between slanted post and

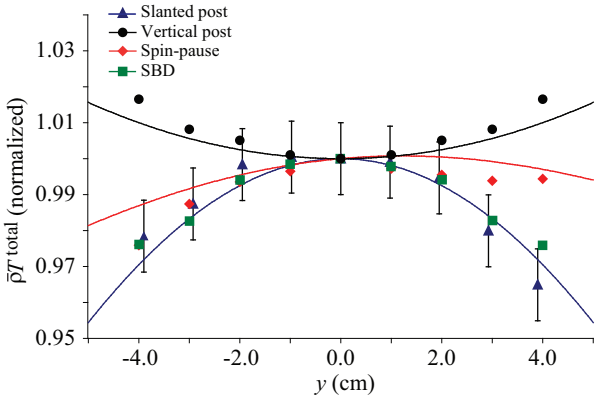

Figure 2.8: Experimental (points) and predicted (solid lines) deposited mass per unit area along the y-axis for different GLAD architectures (normalized).

SBD films. This suggests an approach for obtaining a film with almost no variation in the deposited mass per unit area along the y-axis of the wafer. The spin-pause films discussed so far all have equal amounts of both spinning and paused growth, but this ratio is flexible. Additional spinning growth should flatten the deposited mass per unit area along the y-axis. One can find that for a spinning to paused growth ratio of 3.55, $\Delta_y^{\bar{\rho}T^{\text{total}}}$ is minimized to less than 0.3%, which is about three times less than the already highly uniform vertical post case.

2.3.3 Thickness and Average Fractional Density

We have now established that the deposited mass per unit area given in equation (2.18) leads to highly accurate predictions for the deposited mass per unit area in GLAD films which can include substrate rotation. Thickness is obtained via equation (2.31), using the c values from Table 2.1, and average fractional density is obtained by dividing the predicted deposited mass per unit area by the product of this result and the density at normal incidence, ρ_{norm}. We first examine the measured and predicted thickness values along the x- and y-axes for the four film structures as shown in Figures 2.9(a) and 2.9(b). Along the x-axis, the agreement between predicted and measured values is quite good in each case. The predicted and measured values are within 0.01 in each case. Agreement is also quite good along the y-axis, with all predicted values being within 0.02 of the observed values. Just as with the deposited mass per unit

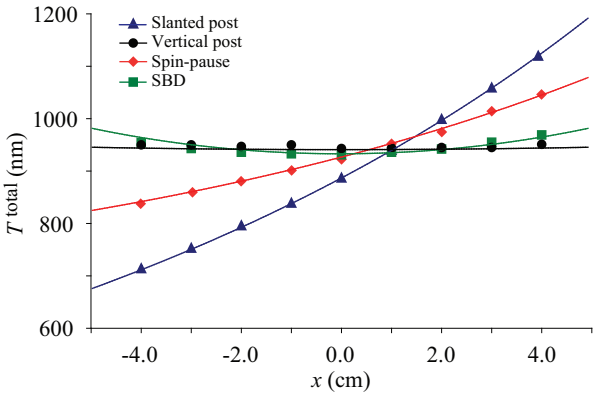

(a) Along x

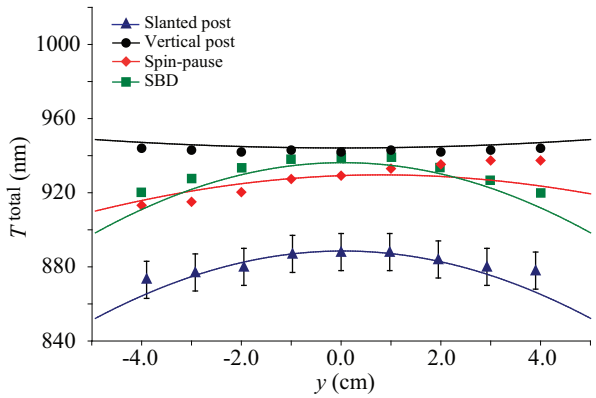

(b) Along y

Figure 2.9: Experimental (points) and predicted (solid lines) thickness (T^{total}) along the x-and y-axes for all four GLAD structures.

area, the magnitude of the thickness non-uniformity is far more significant in the x-direction as compared with the y-direction. In particular, for the pure slanted post case, the thickness non-uniformity is quite large, exhibiting a difference in thickness of greater than 400 nm across the substrate. Meanwhile, for the vertical post and SBD cases, the thickness non-uniformity is quite good, exhibiting differences of only 3 nm and 30 nm respectively.

Having determined T^{total}, we can then look at the predicted fractional density, $\bar{\varrho}$ by dividing the deposited mass per unit area by $\rho_{\text{norm}} T^{\text{total}}$ and comparing to measured results. This data is shown in Figures 2.10(a) and 2.10(b). Error bars are shown only for the slanted post results, but should be assumed as having the same ± 0.01 value for all measurements. Again, the model yields excellent results when compared to measured values. We observe that the percent variation in density is not as significant as that in thickness, which can also be seen from the Δ values in Table 2.2. As with the previous cases, the most significant non-uniformities are found along the x-axis, in those films that possess the least amount of substrate rotation. In the slanted post case in particular, the percent variation in density can be as high as about 10%, as mentioned earlier. This can in turn lead to significant variations in material properties such as the refractive index, or electrical conductivity. For instance, using the Bruggeman model for the refractive index, the effective index will change from 1.6 to 1.7 as $\bar{\varrho}$ changes from 0.56 to 0.63, assuming TiO_2 film material, with a bulk index of 2.2. This can be a significant difference over a single substrate, and needs to be taken into consideration when making density, refractive index or other measurements. In contrast, for vertical post and SBD films along the x-axis, and along the y-axis for all film structures, the observed and predicted variation in density is very low (less than the uncertainty of the measurement, in fact). This is a very nice result as it indicates that film properties dependent on density will be more or less invariant along y, which can be important for fabricating repeatable samples, or for the placement of witness samples.

2.3.4 Columnar Trajectory

We first compare the measured and predicted column tilts, β', along the x-axis for the four film structures. The result is shown in Figure 2.11. The ability to predict the column tilt angle across the substrate is one of the major features of the model presented here. As usual, error bars are only shown for the

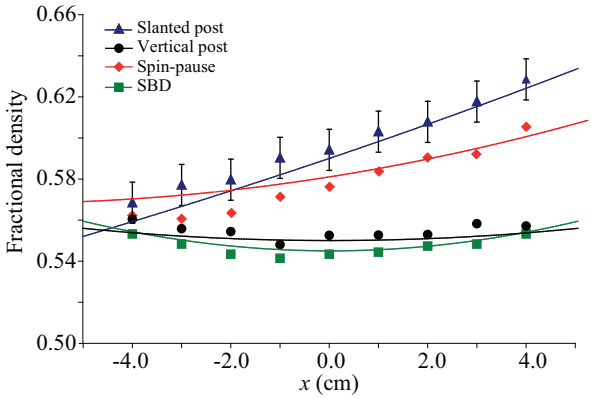

(a) Along x

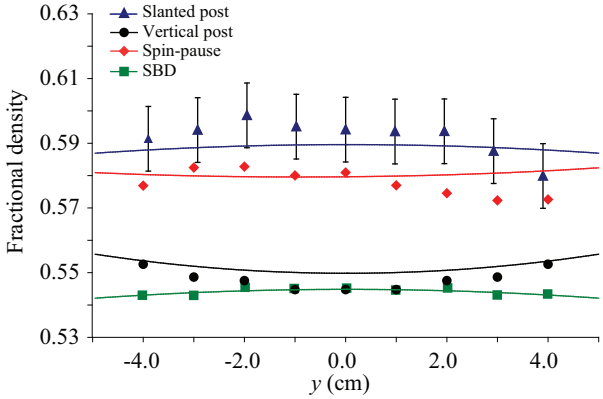

(b) Along y

Figure 2.10: Experimental (points) and predicted (solid lines) average fractional density ($\bar{\varrho}$) along the x-and y-axes for all four GLAD structures.

slanted post case, but can be assumed to be the same ($\pm 5^\circ$) for all measured data. The model does a very good job of predicting column tilt particularly for the slanted post as well as for the SBD case. The SBD measurements exhibit some slight asymmetry, which is likely due to a systematic uncertainty in the measurement location, in both the x- and y- directions. This uncertainty is actually present in all four datasets, but is most noticeable for the SBD case, because of the large variation in column tilt. Within experimental error, the vertical post column tilt is also relatively well predicted, however the measured data is slightly noisy. The only major discrepancy is what appears to be a relatively constant offset in the spin-pause case. The model correctly predicts a nearly constant β', with only a slight increase with x. It is not clear why the modeled data is offset from the measured data in this case, but it is possible that the presence of vertical growth segments makes it so that equation (2.15) is not applicable without a slight modification. Analogous effects have been observed in chevron films [48], where deposition on the reverse side of a pure slanted post results in a different column angle than that obtained when deposited on a bare substrate.

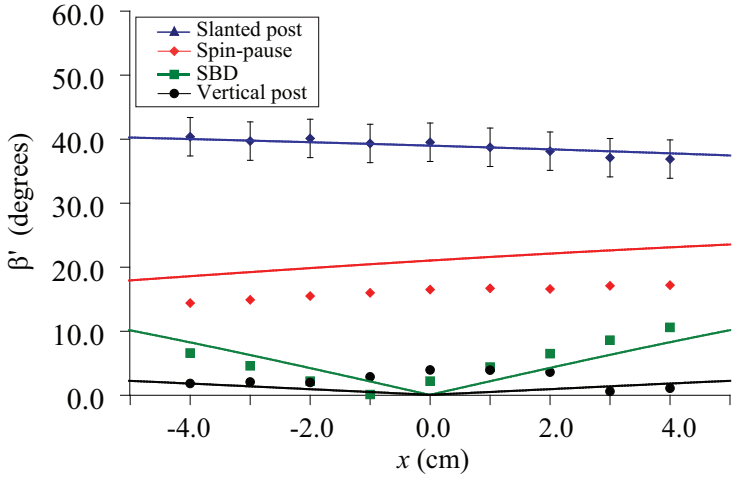

Figure 2.11: Experimental (points) and predicted (solid lines) column tilt angle (β') in degrees along the x-axis for all four GLAD structures

We can also examine the trajectory of the columnar posts grown for each of the four film structures. Figure 2.12 shows β', the predicted tilt of the film columns given by equation (2.44), across the entire substrate for each of the

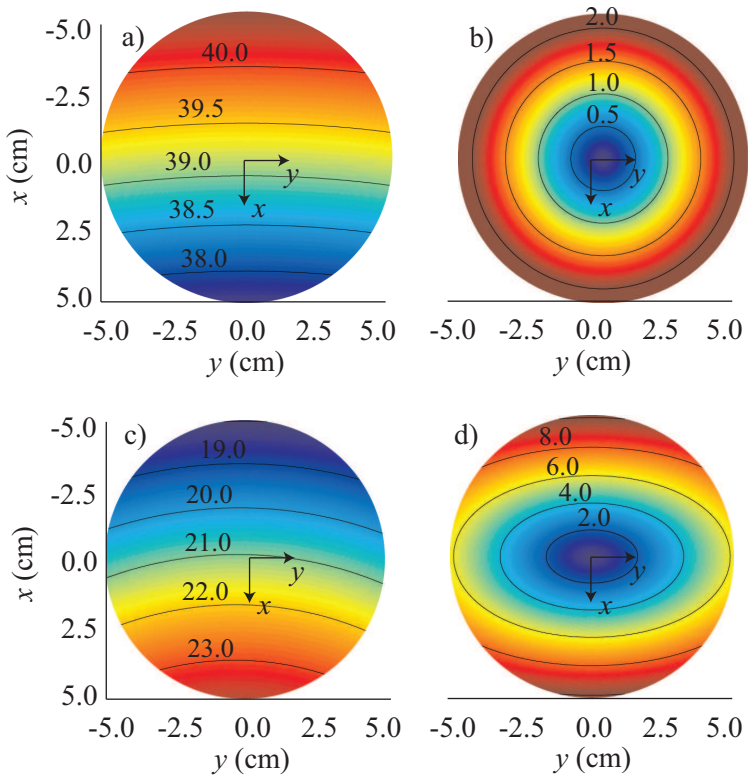

Figure 2.12: The simulated net column tilt, β', in degrees for a) slanted post, b) vertical post, c) spin-pause and d) serially bideposited GLAD film structures deposited at $\alpha = 70°$.

four film structures, while Figure 2.13 shows the direction in which columnar

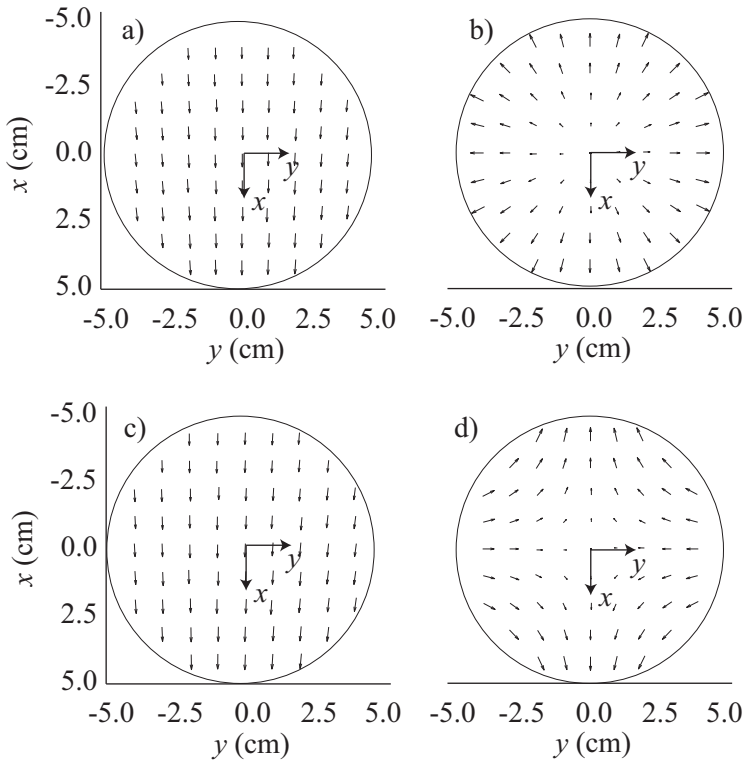

Figure 2.13: The simulated columnar growth trajectory in the xy-plane for a) slanted post, b) vertical post, c) spin-pause and d) serially bideposited GLAD film structures deposited at $\alpha = 70°$.

growth takes place, projected onto the xy-plane. The arrows in Figure 2.13 are oriented at an angle of ξ', given by equation (2.45), relative to the x-axis, and shorter arrows indicate more vertical (smaller β') columns. These two figures show how different the columnar growth of these different films are. The slanted post and spin-pause films are fairly similar. Both grow predominantly toward the source, along the x-axis. The slanted post columns all point inward, toward the x-axis, in the local deposition plane. By virtue of the asymmetry of the spin-pause growth algorithm, the majority of the columns have a small component along the y-direction, which corresponds to the non-zero $\xi_{O'}$ discussed earlier. Figure 2.12 also indicates what kind of variation in the column tilt can be expected for these two film structures. As with the deposited mass per unit area, thickness and density, column tilt varies strongly along the x-axis, and more weakly along the y-axis. Of note is only a small 2° total variation in

the column tilt over the substrate in the slanted post case. In the spin-pause case, $\beta'_{O'}$ is about half that of the slanted post case, but the variation in β' has doubled to 4°. Additionally, in the slanted post case, the column tilt decreases along x, but it increases along x in the spin-pause case. This implies that there exists a ratio of spinning to paused growth at which the column tilt is highly uniform across the substrate. This is in fact true, and occurs for a ratio of spinning to paused growth of about 1:10.

The vertical post and SBD cases are quite different. In the vertical post case, it is found that the columns are almost vertical. Technically, they are not strictly vertical, but rather grow radially outward from O', but β' attains a maximum of about 2°, which is effectively zero. However, this effect is a function of α, and will be discussed later. The presence of non-verticality can introduce optical or magnetic biaxiality into a vertical post film, which is usually regarded as being uniaxial [58, 59]. The SBD case also presents a number of interesting features. One feature of note is that columns point away from O' along the x-axis, but inward along the y-axis. Elsewhere, the columns grow in various diagonal directions. However, during growth, the columns always broaden along the y-axis [54]. This means that columns along the x-axis broaden in a direction orthogonal to their tilting direction, while columns along the y-axis broaden in the same plane as their tilt. This is important for an application such as chromatography [18], which relies on both columnar broadening and column tilt to achieve molecular separation. It is also important from an optical point of view, as the change in columnar growth direction relative to the broadening direction causes a rotation in the local principal axes, and a corresponding change in the optical properties. Finally, SBD films are often assumed to be vertical, but this is clearly not the case. The model shows that film columns near the edge of the substrate can have a significant column tilt. Along the y-axis, this tilt is not too severe, attaining a value of about 5° at ± 4 cm, while at ± 4 cm along the x-axis, the columnar tilt is predicted to be about 8°. Additionally, because the columns point in opposite directions along $\pm x$ or $\pm y$, in a way the variation in column tilt can be thought of as twice these values. As with the vertical post film, this effect is a strong function of deposition angle. For all four film structures described, the measured β' corresponds quite well with the model's predictions.

2.3.5 Review

The primary goal of this chapter has been to outline a procedure that enables one to compute the distribution of deposited mass per unit area, density, thickness as well as the growth trajectory (ξ' and β') for arbitrary GLAD films, focusing on those done with constant α. The method is reviewed below:

1. Compute the normalized $\frac{dm}{dA}$ using equation (2.26) with $\rho_{O'} = T^{\text{total}}_{O'} = 1$. This requires knowledge of only the geometry of the system, and the directionality of the source, n.

2. Determine $T^{\text{total}}_{O'}$ and $\bar{\rho}_{O'}$. $T^{\text{total}}_{O'}$ is often a design variable, while $\bar{\rho}_{O'}$ can often be determined by direct measurement, or through knowledge of ρ_{norm} and $\bar{\varrho}_{O'}$, for example. Multiply the normalized $\frac{dm}{dA}$ by $\bar{\rho}_{O'} T^{\text{total}}_{O'}$ to scale it appropriately.

3. Determine c. This may be a tabulated value, or may be accomplished by measuring $\bar{\varrho}_{O'}$ and solving for c using equation (2.33), or through one of the other methods outlined above. Evaluate equation (2.31) to determine T^{total}.

4. Divide the appropriately scaled $\frac{dm}{dA}$ by T^{total} to obtain $\bar{\rho}$. Divide $\bar{\rho}$ by ρ_{norm} to obtain $\bar{\varrho}$.

5. Compute $\mathbf{q}_{xyz}$ from equation (2.42), then compute β' and ξ' from equations (2.44) and (2.45). This requires knowledge of E in equation (2.15), which may be a known quantity, or may require a separate measurement.

By and large, this procedure is applicable to any system geometry involving flat substrates and sufficiently low deposition pressures. It should also be useful in estimating the effects of non-uniformity on other related thin film parameters, such as a film's effective refractive index or conductivity. Finally, this procedure should be useful in designing new deposition systems concerned primarily with film uniformity. This is particularly relevant for large scale manufacturing of devices based on GLAD films.

2.4 Additional Modeled Results

A major convenience of the model presented above is that a number of questions regarding non-uniformity can now be answered confidently without the need to actually deposit multiple films, or, more significantly, physically change the geometry of the system. This section addresses a number of those questions.

2.4.1 Geometric Effects

We can identify a number of potential geometric variables that can be changed in a given GLAD setup. Most notably, these include the deposition angle, α, the throw distance, $\mathbf{R}_{OS}$, the substrate thickness, z_s and the substrate size. Some of these parameters, such as α, are under the user's direct control, and the variation of film properties is potentially of interest if one is attempting to optimize some performance metric. Other parameters, such as the throw distance, are often fixed by a given chamber. In this case, it is interesting to know how different chamber geometries would affect the resultant films.

There are a number of results, and the different film structures have very different characteristics. The analysis will proceed in three sections. We will first investigate the pure slanted post and spin-pause cases, which have similar properties, followed by the SBD case and finally the vertical post case. In all cases, we employ a throw distance of 40 cm, as before, but we assume a substrate thickness of zero, for simplicity. We assume $E = 0.49$, and use the same c values as previously, taken from Table 2.1.

Pure Slanted Posts and Spin-Pause

To begin, we examine the effect of α on non-uniformity. We first look at the quantity, α_{eff}, given by equation (2.13) at the points $d = \pm 4$ cm along the x-axis for a pure slanted posts. The result is shown in Figure 2.14, for a throw distance of $R_{OS} = 40$ cm, and zero substrate thickness. We see that at small α, the two values diverge from a small, non-zero value, with α_{eff} at $x = +4$ cm going to zero at the value $\alpha_c = 5.5°$before monotonically increasing toward 90°. During the latter phase, the difference in α_{eff} decreases with increasing α, while in the former phase, the difference increases with increasing α. Note also that for $\alpha < \alpha_c$ slanted columns with $x < d$ have $\xi = 0°$ along the x-axis, while columns with

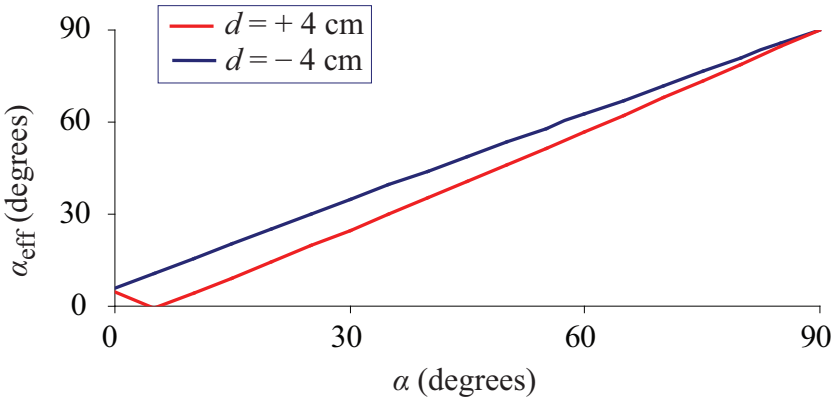

Figure 2.14: α_{eff} as a function of α at $d = \pm 4$ cm for pure slanted posts

$x > d$ have $\xi = 180^\circ$. This means that columns on opposite sides of the point $x = d$ point toward d. The value of α_c increases if the ratio d/R_{OS} increases. If this is done by making the throw distance small, one could potentially obtain a large α_c for a small d, leading to potentially interesting gradients in the overall film properties, over relatively small distances. However, this requires one to maintain a point-like evaporation source, which could prove difficult. It may, however, be possible using something analogous to a pinhole aperture, commonly seen in optical setups.

We now look to describe the non-uniformity of the deposited mass per unit area, the density, the thickness and the column tilt angle, for the same four structures described above. For the pure slanted post structure, Figure 2.15(a) shows $\Delta_x^{\bar{\rho}T^{\text{total}}}(4\text{ cm})$, $\Delta_x^{\bar{\rho}}(4\text{ cm})$ and $\Delta_x^{T^{\text{total}}}(4\text{ cm})$ as a function of α, and Figure 2.15(b) shows the difference, in degrees, between the maximum and minimum values for β on the x-axis with $-4\text{ cm} < x < 4\text{ cm}$. Figures 2.15(c) and (d) show the same results, but for the y-axis. Finally, Figure 2.15(e) shows the value of β' at O. Figure 2.16 shows the same results for the spin-pause structure. We see that these two structures have a number of similar features with regards to non-uniformity, but there are some notable differences has well. Both structures exhibit monotonically increasing $\Delta_x^{\bar{\rho}T^{\text{total}}}$ and $\Delta_x^{\bar{\rho}}$ with deposition angle. However, $\Delta_x^{T^{\text{total}}}$ is not monotonic. It reaches a peak value at $\alpha = 75^\circ$ in both

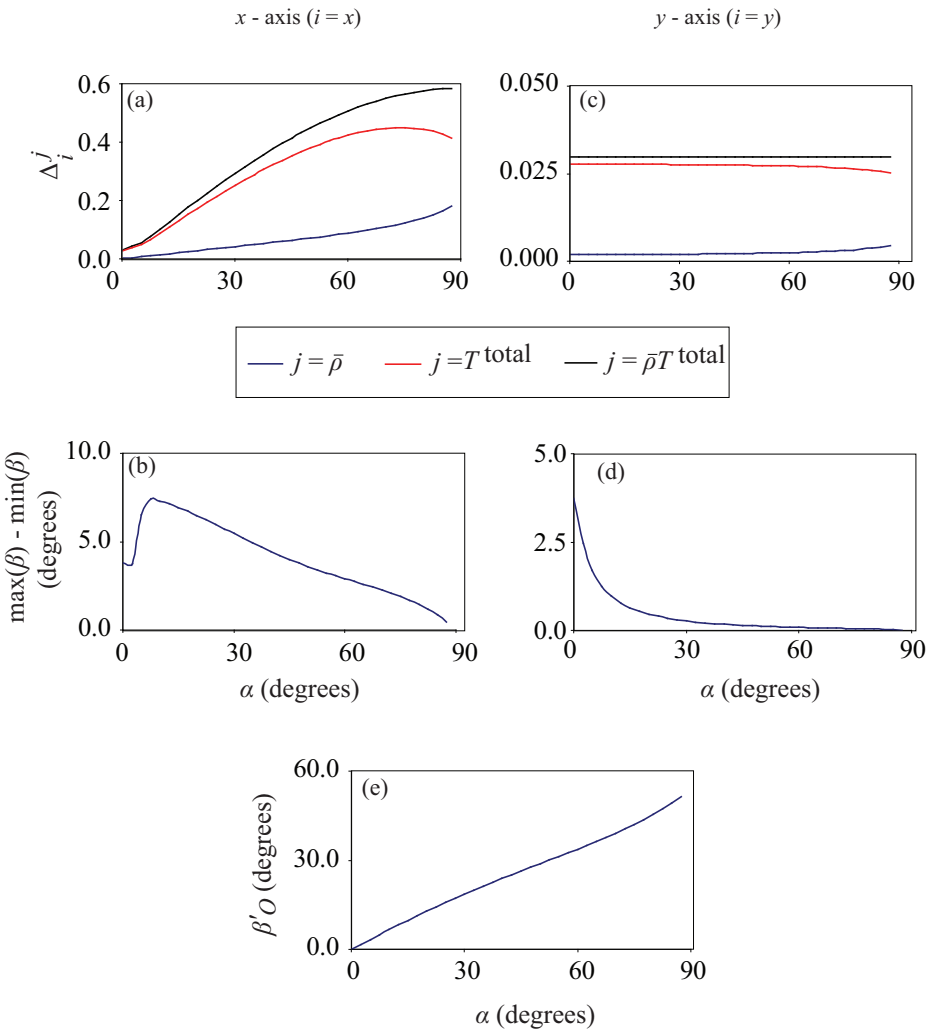

Figure 2.15: Pure slanted post non-uniformity data as a function of α. (a) $\Delta_x^{\bar{\rho}T^{\text{total}}}(4\text{ cm})$, $\Delta_x^{\bar{\rho}}(4\text{ cm})$ and $\Delta_x^{T^{\text{total}}}(4\text{ cm})$; (b) Difference in maximum values of β' for $-4\text{ cm} < x < 4\text{ cm}$; (c) $\Delta_y^{\bar{\rho}T^{\text{total}}}(4\text{ cm})$, $\Delta_y^{\bar{\rho}}(4\text{ cm})$ and $\Delta_y^{T^{\text{total}}}(4\text{ cm})$; (d) Difference in maximum values of β' for $-4\text{ cm} < y < 4\text{ cm}$; (e) β' at substrate center (O).

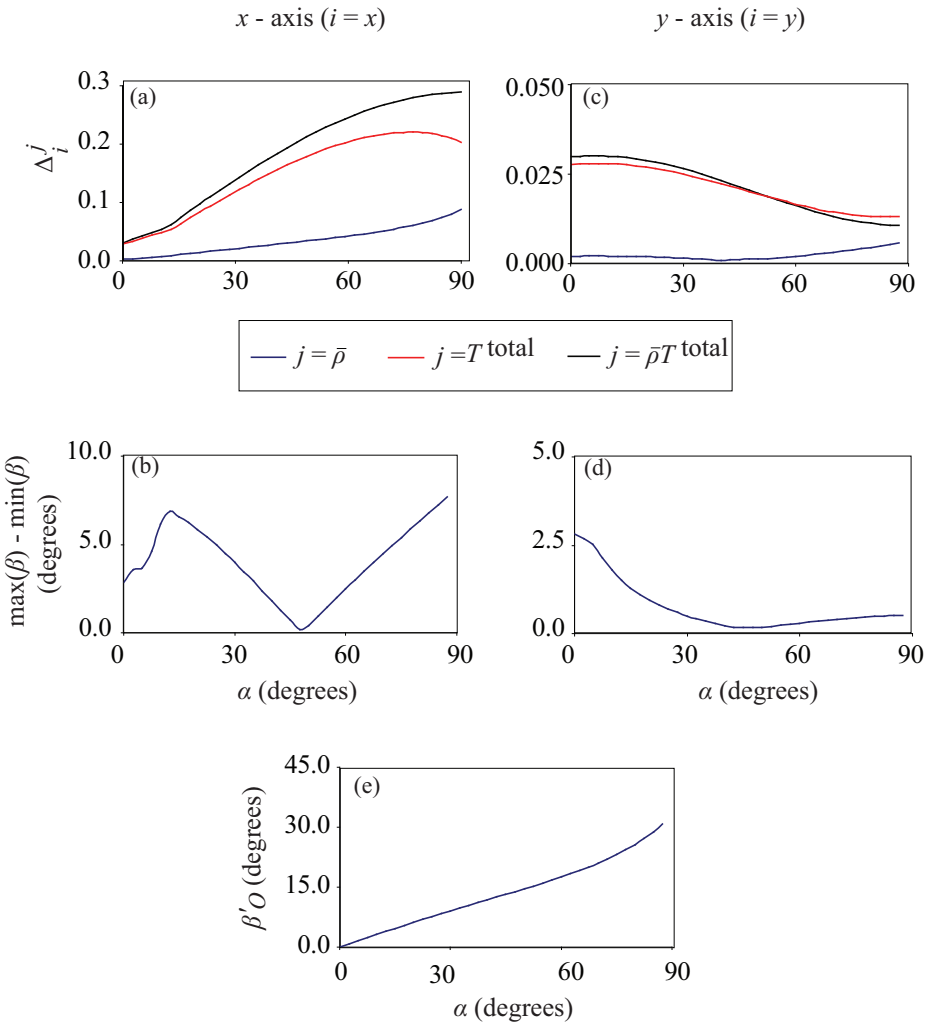

Figure 2.16: Spin-pause non-uniformity data as a function of α. (a) $\Delta_x^{\bar{\rho}T^{\text{total}}}(4\text{ cm})$, $\Delta_x^{\bar{\rho}}(4\text{ cm})$ and $\Delta_x^{T^{\text{total}}}(4\text{ cm})$; (b) Difference in maximum values of β' for $-4\text{ cm} < x < 4\text{ cm}$; (c) $\Delta_y^{\bar{\rho}T^{\text{total}}}(4\text{ cm})$, $\Delta_y^{\bar{\rho}}(4\text{ cm})$ and $\Delta_y^{T^{\text{total}}}(4\text{ cm})$; (d) Difference in maximum values of β' for $-4\text{ cm} < y < 4\text{ cm}$; (e) β' at substrate center (O).

cases, before decreasing slightly at large α. Therefore, it could be expected that thickness uniformity along x actually improves with deposition angle, beyond a certain point. Along the y-axis, the two structures are considerably different. The pure slanted post has a constant $\Delta_y^{\bar{\rho}T^{\text{total}}}$, across all α. This is because ρT^{total} is independent of α along the y-axis, which can be deduced from equation (2.27). The thickness and density non-uniformities are also roughly constant. $\Delta_y^{\bar{\rho}}$ tends to increase with α meaning that $\Delta_y^{T^{\text{total}}}$ must then decrease, in order to keep $\Delta_y^{\bar{\rho}T^{\text{total}}}$ constant. In the spin-pause case, by contrast, $\Delta_y^{\bar{\rho}T^{\text{total}}}$ decreases with α. This leads to a decreasing $\Delta_y^{T^{\text{total}}}$, while $\Delta_y^{\bar{\rho}}$ has a similar behaviour to that of the pure slanted case.

The behaviour of β'_O for both cases is relatively similar, with the value obtained in the spin-pause case being roughly half of the slanted post value across most of the range. The maximum difference in β' along the two axes, however, is quite different between the two cases, and both feature some interesting characteristics. In the slanted post case, the variation in β decreases with α along both the x- and y-axes, other than for an anomalous section at small α along the x-axis. This is due to the strange behaviour observed below α_c, as discussed above. Again, if one could move α_c to larger values, while still maintaining conditions suitable for GLAD, this could result in interestingly shaped film structures. For the spin-pause case, we find behaviour to the slanted post case at low α, but as α increases we find a point around $\alpha = 48^\circ$ at which the difference in β' vanishes along the x-axis. The reason this occurs is similar to the situation encountered when varying the ratio of paused growth to spinning growth discussed earlier. For α less than 48°, β' decreases with increasing x, while for α above 48°, β' and x increase together. The variation in β' along the y-axis is similar to that along the x-axis, but not nearly as dramatic. It should be noted that the variation in β' also approaches zero at $\alpha = 48^\circ$.

These examples indicate the utility of this model, in identifying conditions leading to highly uniform properties. We will see even greater examples of this in the SBD and vertical post cases.

SBD and Vertical Posts

The SBD and vertical post cases exhibit many more interesting features than the slanted post and spin-pause cases. For the SBD case, Figure 2.17(a) shows $\Delta_x^{\bar{\rho}T^{\text{total}}}(4\text{ cm})$, $\Delta_x^{\bar{\rho}}(4\text{ cm})$ and $\Delta_x^{T^{\text{total}}}(4\text{ cm})$ as a function of α, and Figure 2.17(b)

shows the difference, in degrees, between the maximum and minimum values for β on the x-axis with -4 cm $< x <$ 4 cm. Figures 2.17(c) and (d) show the same results, but for the y-axis. Finally, Figure 2.17(e) shows the value of β' at O. Figure 2.18 shows the same results for the vertical post structure along any radial direction, since they are all equivalent.

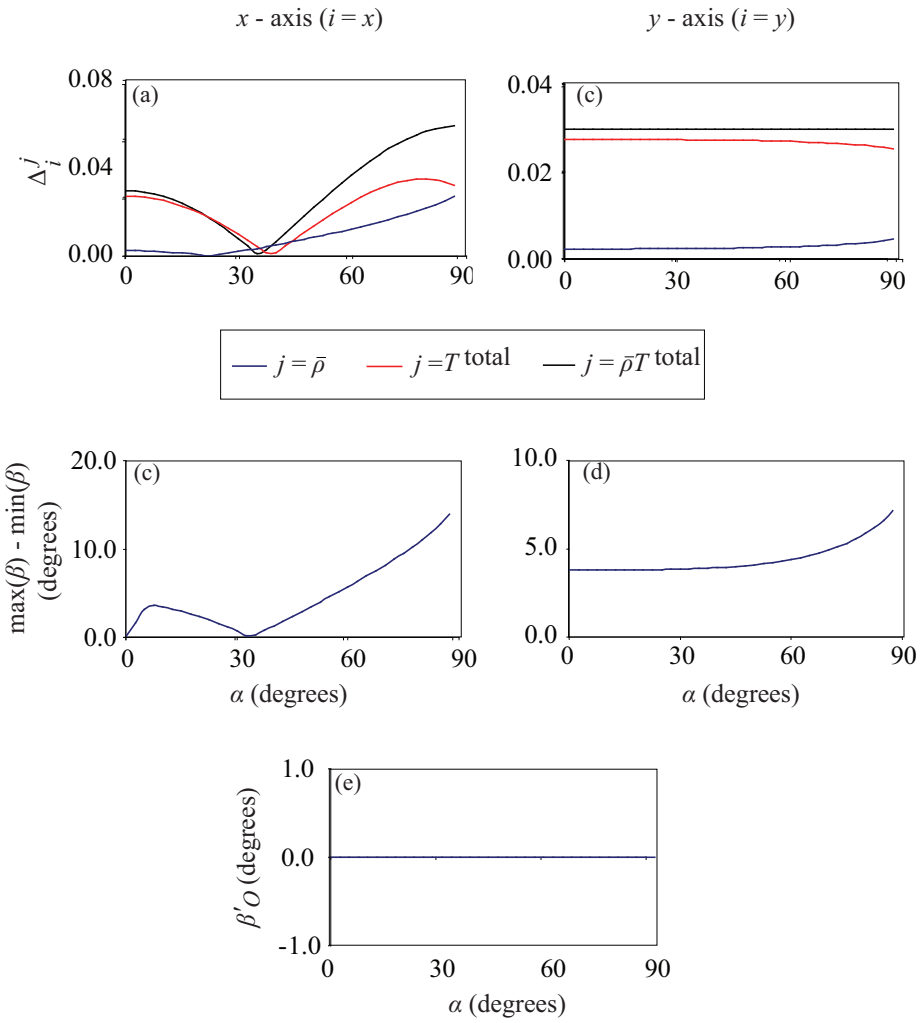

Figure 2.17: SBD non-uniformity data as a function of α. (a) $\Delta_x^{\bar{\rho}T^{\text{total}}}(4\text{ cm})$, $\Delta_x^{\bar{\rho}}(4\text{ cm})$ and $\Delta_x^{T^{\text{total}}}(4\text{ cm})$; (b) Difference in maximum values of β' for -4 cm $< x <$ 4 cm; (c) $\Delta_y^{\bar{\rho}T^{\text{total}}}(4\text{ cm})$, $\Delta_y^{\bar{\rho}}(4\text{ cm})$ and $\Delta_y^{T^{\text{total}}}(4\text{ cm})$; (d) Difference in maximum values of β' for -4 cm $< y <$ 4 cm; (e) β' at substrate center (O).

Both of these structures have the same qualitative behaviour in $\Delta_x^{\bar{\rho}T^{\text{total}}}$, $\Delta_x^{\bar{\rho}}$

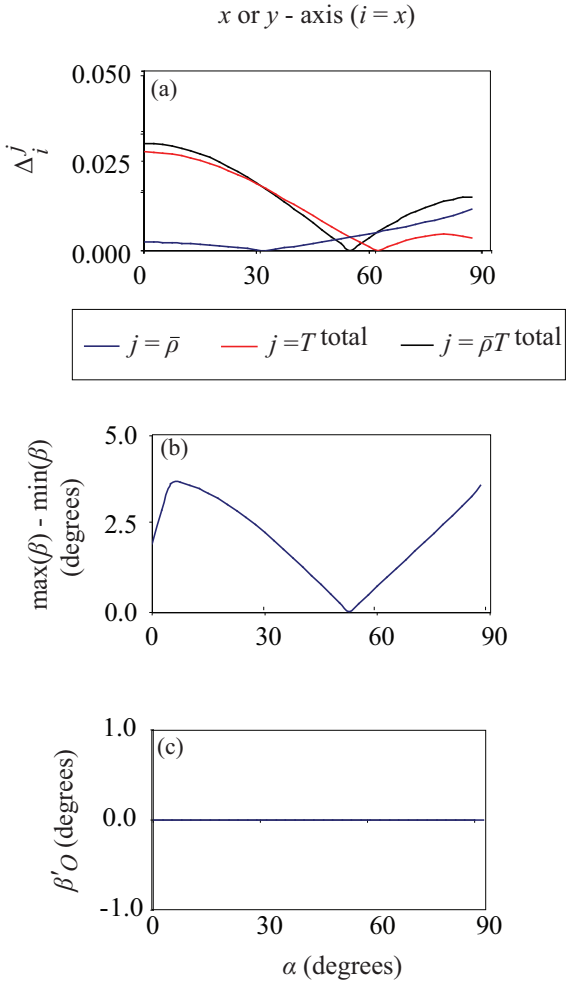

Figure 2.18: Vertical post non-uniformity data as a function of α. (a) $\Delta^{\bar{\rho}T^{\text{total}}}(4\text{ cm}), \Delta^{\bar{\rho}}(4\text{ cm})$ and $\Delta^{T^{\text{total}}}(4\text{ cm})$; (b) Difference in maximum values of β' for $-4\text{ cm} < x, y < 4\text{ cm}$; (c) β' at substrate center (O).

and $\Delta_x^{T^{\text{total}}}$. Each of these starts at some finite value at normal incidence, then decreases to zero at a particular α. Beyond this point, $\Delta_x^{\bar{\rho}T^{\text{total}}}$ and $\Delta_x^{\bar{\rho}}$ increase monotonically with α, as in the slanted post case. However $\Delta_x^{T^{\text{total}}}$ first reaches a local maximum, whereupon it decreases as $\alpha \to 90^\circ$. In both cases, the non-uniformity in density is zero at the lowest value of α, followed by the non-uniformity in the deposited mass per unit area, then finally in the thickness. For the SBD film, the behaviour of the non-uniformity in density, thickness and deposited mass along the y-axis is identical to the behaviour in the pure slanted post case, and possesses no significant features.

The behaviour of the column tilt is quite similar in both cases as well. The column tilt at O is zero in both cases, for all α, which is expected due to the symmetry of deposition at O. The difference between the maximum and minimum values for β along the x-axis for the SBD films, and for the vertical posts in general, follows a very similar pattern to that observed in the spin pause case. In both cases, the difference in β increases from its value at zero degrees to a local maximum at low α, before decreasing to zero at an intermediate value of α. Here, the variation in β along the x-axis effectively vanishes. This occurs at $\alpha = 33^\circ$ for SBD films and $\alpha = 51^\circ$ for vertical posts. Beyond this point, the variation in β increases as $\alpha \to 90^\circ$. For SBD films along the y-axis, the variation in β is monotonically increasing with α, and is never zero. Thus, unlike in the spin-pause case, the column tilt variation across the entire wafer never approaches zero. The SBD case always retains some non-uniformity in the column tilt along the y-axis.

These examples show that the variation in certain quantities tends to zero at certain deposition angles, dependent on the film structure. It is obvious that these points of zero variation depend on the deposition algorithm and one could investigate the dependence of those points on differing algorithms, such as the ones outlined in the following chapter. We will not do that here, however. Another interesting question is the dependence of the non-uniformities on the throw distance. This is an interesting question because it is not easily answered experimentally, as throw distance is often a fixed parameter for a given deposition system. It is also an important question for system design, if one wished to build a system favoring a uniform thickness for a particular film structure. Generally, it is interesting to determine what conditions give uniform film structures at large $\alpha (\gtrsim 70^\circ)$, since this is where the most interesting

film properties emerge.

Figure 2.19 shows α_{eff} at the points $d = \pm 4$ cm as a function of the throw distance, R_{OS}, for a film deposited at $\alpha = 70^\circ$ along the x-axis. At large throw

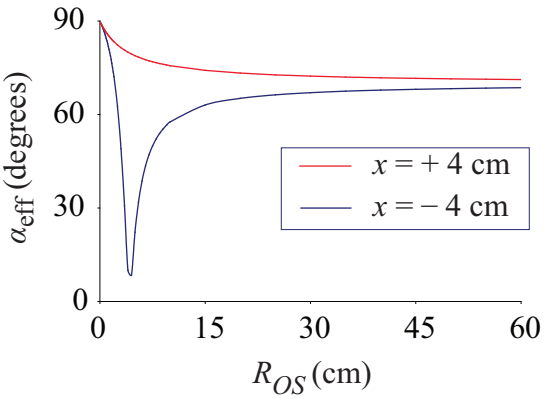

Figure 2.19: Dependence of α_{eff} at $d = \pm 4$ cm on throw distance, R_{OS} for a slanted post film

distances, as one expects, there is only a slight difference in α_{eff} at the opposing edges of the substrate, though we know that this translates into significant changes in film density and film thickness. As the throw distance is reduced, we see some very interesting behaviour. For the point on the substrate farther from the source, the effective deposition angle actually increases monotonically as R_{OS} decreases. By contrast, the point closer to the source experiences a decreasing effective deposition angle that tends to normal incidence as $R_{OS} \sim d$. At this point, there is an enormous gradient in the deposition conditions along the x-axis, which leads to large gradients in film density, thickness, and column tilt. This again suggests that very interesting film behaviour could be obtained if it were possible to engineer a suitably point-like vapour source located within a distance similar to the substrate size.

Qualitatively, the behaviour of the non-uniformity quantities is very similar as a function of throw distance, for all variables and for all film structures. Very broadly, the non-uniformities tend toward zero as the throw distance tends to infinity, and grow very large at small distances. The data for $\Delta_x^{\rho^{T^{\text{total}}}}(4\text{ cm})$, $\Delta_x^{\rho}(4\text{ cm})$ and $\Delta_x^{T^{\text{total}}}(4\text{ cm})$ for both slanted and vertical posts is shown in Figure 2.20, for $\alpha = 0^\circ, 30^\circ, 70^\circ$ and 85°. The exact results are relatively unsurprising, especially for large throw distances. At short throw distances, comparable to the radius of the substrate, the non-uniformities become very large, and have

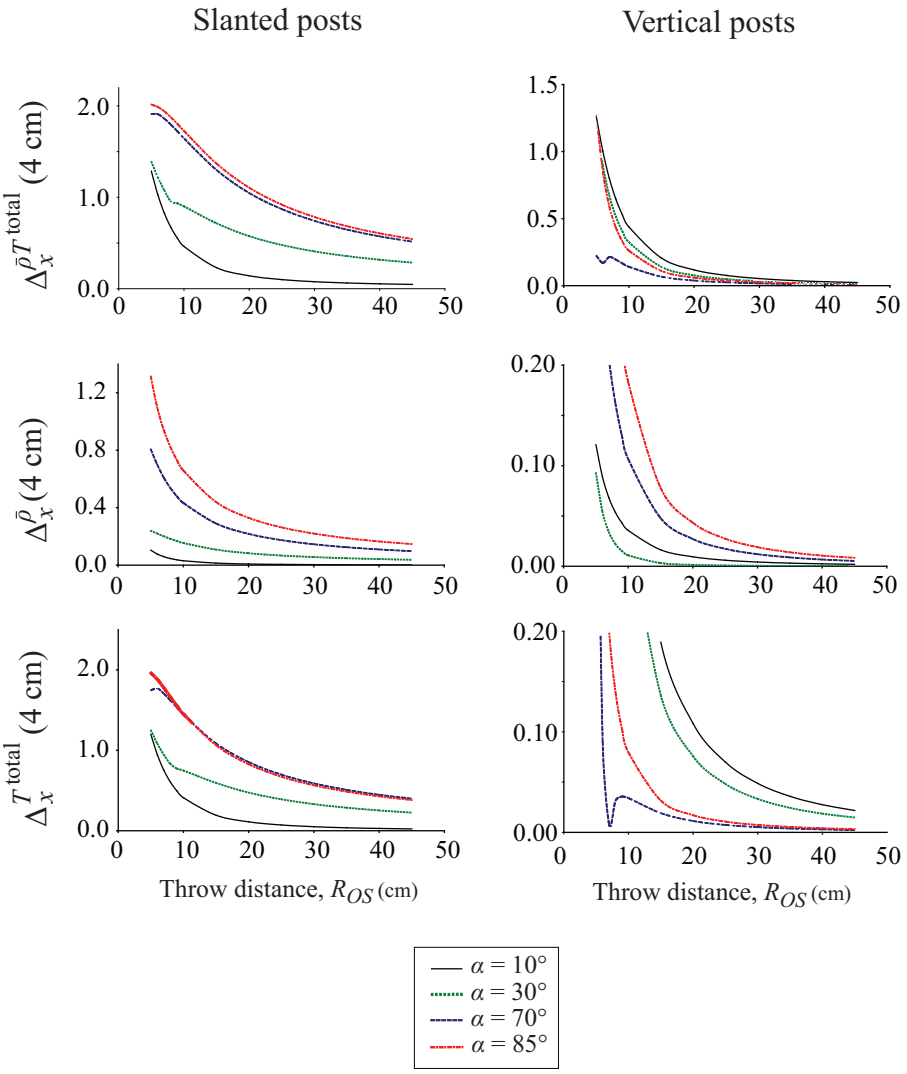

Figure 2.20: $\Delta_x^{\rho T^{\text{total}}}(4\text{ cm})$, $\Delta_x^{\rho}(4\text{ cm})$ and $\Delta_x^{T^{\text{total}}}(4\text{ cm})$ as a function of throw distance, R_{OS}, for slanted and vertical posts at various deposition angles

Table 2.3: Values of c and E for different materials

Material	c	E
TiO_2	$4.2 - 4.9$	0.49
SiO_2	3.2 [11]	0.84 (next chapter)
ITO	3.6 [11], 4.1 (next chapter)	N/A
Ge	N/A	0.4 [14]
Al (293 K)	N/A	0.2 [14]
Al (623 K)	N/A	1.5 [14]

a complex dependence on R_{OS}. This occurs because of behaviour described in Figure 2.19. Outside of this case, the general rule is clear and unsurprising: film uniformity improves significantly with increasing throw distance.

2.4.2 Material effects

Finally, we might be curious as to how the uniformity in things such as density or column tilt are affected by different materials. In our model, material effects are captured by the constants c and E for density and column tilt as implemented by the Poxson and Lichter-Chen models, respectively[2.3]. Table 2.3 show how values of E and c can vary from material to material. Presently though, the two values are not well tabulated, which is a major shortcoming for engineering and design purposes. Future work should endeavour to better characterize these two parameters for as many materials as possible.

Figures 2.21 and 2.22 shows the effect of c on the uniformity in the deposited mass per unit area, the density and the thickness, for each of the four film structures, deposited at $\alpha = 70^\circ$ and 85° respectively, along the x-axis. Note that the horizontal axis of the graph indicates the numerical value of c, as well as the corresponding fractional density, $\bar{\varrho}$. It is immediately important that $\Delta_x^{\bar{\rho}T^{\text{total}}}$ is constant for all film structures, regardless of c. This is entirely expected as the deposited mass flux per unit area is independent of the fractional density. However, the general behaviour of $\Delta_x^{\bar{\rho}}$ and $\Delta_x^{T^{\text{total}}}$ is clearly dependent on c, as well as the specific film growth algorithm. Materials with larger values of c imply that for a given deposition angle, the given material will produce a film whose fractional density is larger than that of a material with a smaller c value. We see under most circumstances, as c decreases, and the film material deposits

[2.3] See references [11, 39, 40] for additional data on density and c, and references [10, 14] for additional data related to column tilt and E.

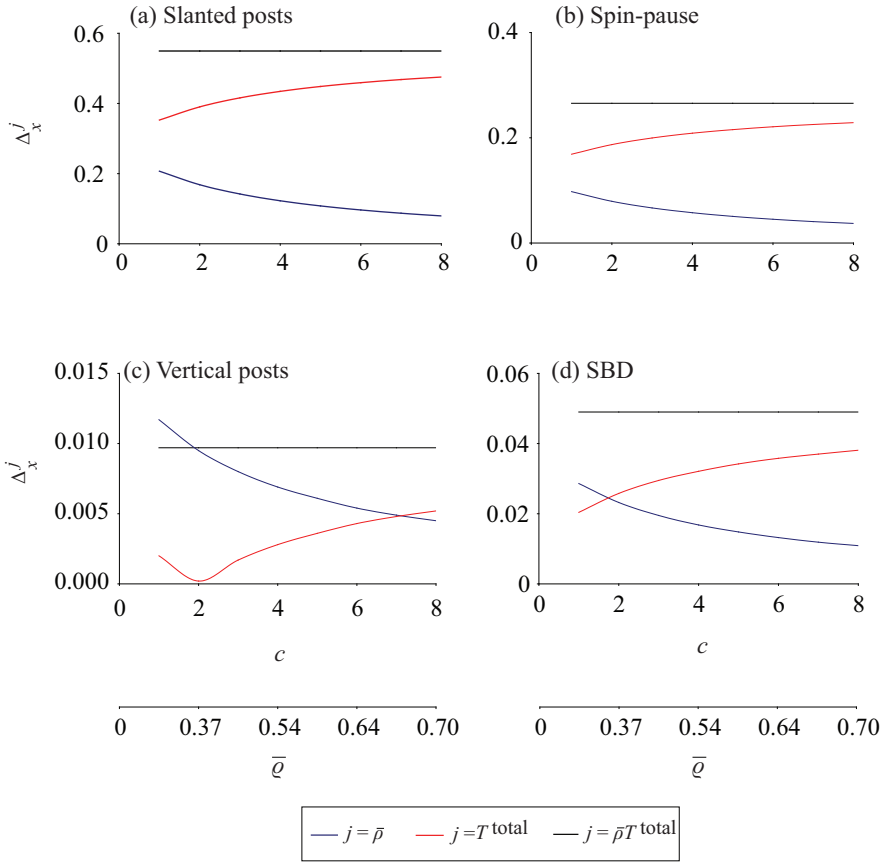

Figure 2.21: $\Delta_x^{\bar{\rho}\Delta_x^{T^{\text{total}}}}(4\text{ cm}), \Delta_x^{\bar{\rho}}(4\text{ cm}$ and $\Delta_x^{T^{\text{total}}}(4\text{ cm})$ as a function of c for (a) slanted posts, (b) spin-pause films, (c) vertical posts and (d) SBD films. All depositions simulated for $\alpha = 70°$.

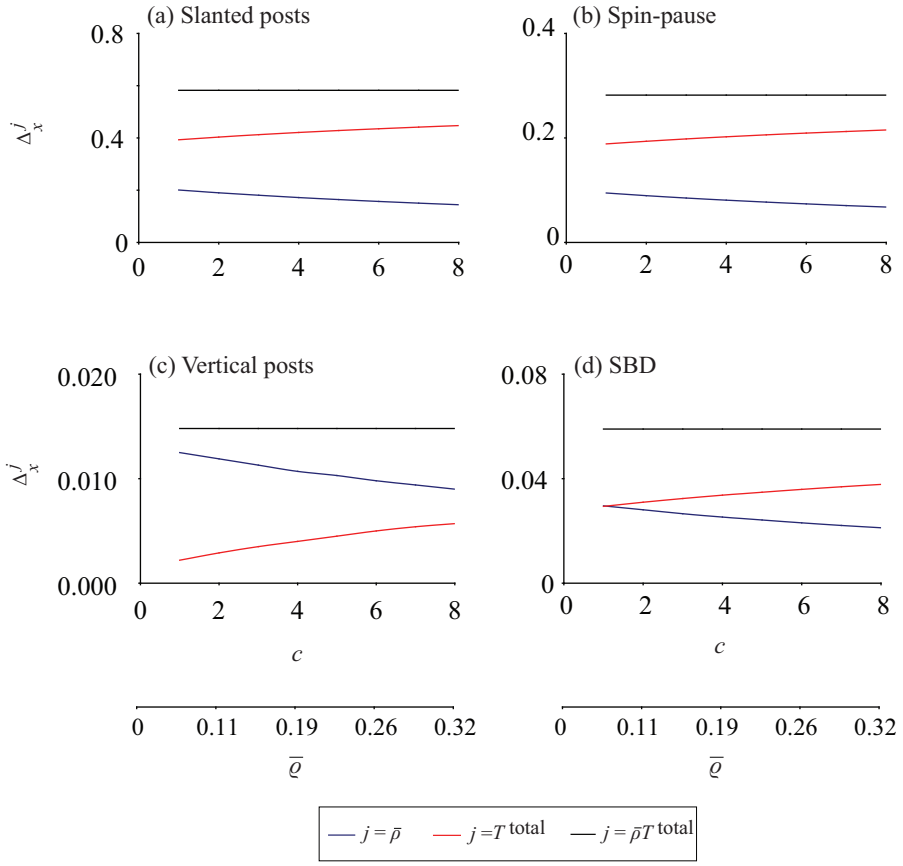

Figure 2.22: $\Delta_x^{\bar{\rho}\Delta_x^{T^{\text{total}}}}(4\text{ cm}), \Delta_x^{\bar{\rho}}(4\text{ cm}$ and $\Delta_x^{T^{\text{total}}}(4\text{ cm})$ as a function of c for (a) slanted posts, (b) spin-pause films, (c) vertical posts and (d) SBD films. All depositions simulated for $\alpha = 85°$.

with a smaller fractional density, then the non-uniformity associated with the density increases, while the non-uniformity associated with the thickness decreases. It is then a general rule that if one wants to improve the uniformity in thickness, one should lower c, and if one wishes to improve the uniformity in density, one should increase c. One obvious way to do this is by changing materials, but if a particular material is desired, it is reasonable to presume that one could effect a change in c through a change in deposition temperature [60], or potentially other deposition conditions. There is not a great difference in the non-uniformities at the different deposition angles, other than the fact that the variation in these quantities with c seems to be slightly less in the $\alpha = 85^\circ$ case as compared with the $\alpha = 70^\circ$ case.

We also note that under certain conditions in the vertical post and SBD cases, the non-uniformity in density is greater than the non-uniformity in thickness. This is actually the common situation in vertical post films deposited at 70°, but is also expected in SBD films with low c. However, since these films have relatively low non-uniformities, these effects are not especially noticeable. Finally, we notice that for $c \lesssim 2$ in the vertical post case, the non-uniformity in thickness and density both increase with decreasing c. This occurs because under normal circumstances the curvature of the density and thickness profiles as a function of x, for instance as shown in Figures 2.9 and 2.10, is in the same direction. For $c \lesssim 2$ in the vertical post case under these conditions, the curvature of the thickness and the density are opposite. It is apparent that it is the curvature of the thickness that changes direction, as $\Delta_x^{T^{\text{total}}}$ vanishes at $c \sim 2$.

As the final topic of interest in this chapter, we examine the effect of E on the variation in β' over a substrate. Figure 2.23 shows the difference between the maximum and minimum values for β', in degrees, along the x-axis, for all four film structures as a function of E in the range -4 cm $< x < +4$ cm. Simulations are carried out for deposition at 70° and 85° with the same parameters as used in Section 2.3, but now allowing E to vary. Note that the horizontal axis of the figure also indicates the natural β at this deposition angle. Most film materials have a value of E between about 0.5 and 1, so the data on the left-hand side of the figure is the most relevant. The results for the two deposition angles are fairly similar. Materials with a larger E have a smaller natural column tilt, β, and as is not too surprising, have a smaller overall variation in β'. We see that SBD films have the largest variation in β', regardless of E, and this increases

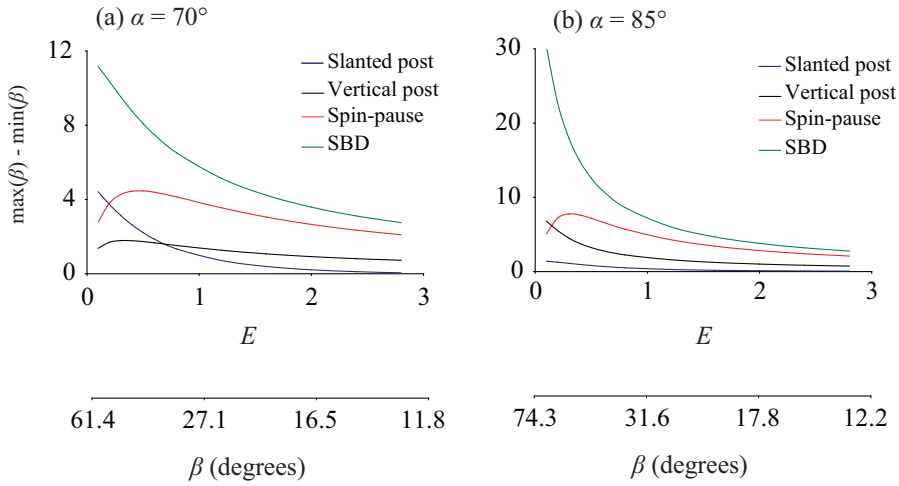

Figure 2.23: The variation in β' along the x-axis for all four film structures on the domain, -4 cm $< x <$ + 4 cm. (a) $\alpha = 70°$; (b) $\alpha = 85°$

significantly as E decreases. This is especially true at the higher deposition angle. Vertical posts and slanted posts have relatively low variation in column tilt, with slanted posts surprisingly exhibiting the smallest overall variation in β. Finally, we see that spin-pause films exhibit a moderate amount of column tilt variation. Interestingly, this variation is found to decrease with decreasing values of E, as E tends to 0. Broadly speaking, one finds that materials with a smaller natural column tilt will exhibit less overall variation in β' over a substrate, and that unlike in the case of thickness and density, substrate rotation can either worsen or improve column tilt uniformity.

2.5 Conclusions

This chapter covered a great deal of material and it is somewhat difficult to concisely summarize all the results. The major focus of this work was to build a model from a few very basic concepts in order to be able to predict useful parameters about films fabricated by glancing angle deposition. Being able to identify the variation in film thickness, or in column tilt is incredibly important for engineering purposes and relates to the feasibility of future manufacturing. In the near-term, it is hoped that the results in this chapter can be used by researchers to identify the repeatability and expected variation in GLAD de-

vice performance. In the long-term, it is hoped that the work described here will allow engineers to understand the possible limitations (or lack thereof) for GLAD film growth in larger scale commercial applications. Understanding the limits of the technology will hopefully allow engineers to comprehend what types of GLAD film structures are suitable for large scale production, or to identify alternative chamber geometries and substrates that will accommodate large scale processing.

The model presented here is relatively simple. Ultimately, it required knowledge of two material specific variables, the density and the column tilt, which turn out to be quite crucial indeed, and should be well (and better) characterized for all materials used in GLAD. Despite the simplicity of the model, it was capable of generating very accurate predictions of real world results, and could be modified to make predictions of a number of situations that are not easy to investigate experimentally. Future researchers should be able to expand upon the model given here to address more sophisticated situations including substrate temperature control [61] and macroscopic geometric shadowing [62]. Additional locations for improvement on the model include the ability to handle non-pointlike deposition sources and higher pressure deposition (sputtering included) as well as the ability to handle deposition on non-planar substrates. Ultimately, this chapter indicates the power of simple models and the importance of identifying the small handful of key parameters in any given problem.

Chapter 3

Controlling the Principal Indices in Slanted Columnar Films

"Research is what I'm doing when I don't know what I'm doing." – Werner Von Braun

3.1 Introduction

The previous chapter dealt with the basics of film growth in the GLAD approach, with a focus on examining the variation in film thickness and density across a substrate, due to varying deposition conditions. This chapter focuses on physical properties of GLAD films, with an aim to illustrate the tunability of the optical properties for optical filter design, and is intended for researchers and engineers attempting to design optical filters and sensors that exploit the specific properties of GLAD films. It expands upon a significant amount of prior research on optically anisotropic GLAD films and effective media by a number of groups [10, 22, 36, 49] as well as advanced GLAD film growth algorithms presented by several groups [52, 63, 64]. The major contribution presented here is to provide a framework for engineers to be able to reliably predict optical film properties *a priori* for a wide variety of structures

[3.0] A version of this chapter has been published. N. Wakefield *et al.*, Journal of the Optical Society of America A, 28, 1830 (2011) [84]

and materials, rather than having to always fabricate and measure device behaviour *a posteriori*. It is hoped that this will enable accurate modeling and rational design of optical filters based on GLAD, as described in Chapter 4.

The use and design of optical coatings is essential in many high technology areas, including both imaging and display technologies, photovoltaic cells and optical telecommunications. These coatings are typically made of multilayer stacks of two or more materials of negligible porosity. One alternative approach is to use material layers with varying porosity. The introduction of pores into the constituent layers has several useful properties. A single material can be used to generate layers of widely different refractive index, and the refractive index profile can be easily changed continuously or discretely during fabrication. The shape of the pores is also controllable during fabrication, and by controlling the pore shape in a known fashion, one can introduce uniaxial or biaxial anisotropy into one or more layers, even if the base material is completely anisotropic. This allows one to introduce polarization selective effects or to compensate for off-axis propagation, for instance, without having to resort to traditional anisotropic materials. Finally, the presence of porosity allows one to infiltrate liquid or gaseous material in order to modify the properties of the optical filter. This allows for the fabrication of several very interesting devices, including optical gas sensors, [17] liquid crystal alignment layers, [65] or as dynamic scattering layers for electrophoretic (e-paper) devices. [66] In this chapter, we employ glancing angle deposition (GLAD), which is a physical vapour technology that can produce optical thin films with controlled anisotropy and porosity that can be modified in real-time during deposition. The optical properties of a film layer can be varied through rotation of the substrate during deposition, as this affects the nucleating conditions experienced by incoming vapor, and results in controllable variations in film morphology. Recent examples of innovations using this approach include normally incident reflective polarizers, [67] anti-reflection coatings for solar cells, [68] highly absorbing films, [69] and both one- and three-dimensional photonic crystals. [59, 70, 71] These devices all make use of both the anisotropy and the porosity inherent in GLAD films and would not be possible using bulk thin films alone.

3.2 Film Fabrication

As described in the previous chapter, we know that GLAD results in the fabrication of nanostructured thin films oriented at an angle, β', from the substrate normal and at an angle, ξ', with respect to the x-axis of the substrate. In addition to this formation of tilted columns, the columnar structures themselves exhibit broadening, as shown in Figure 3.1. Broadening takes place in all di-

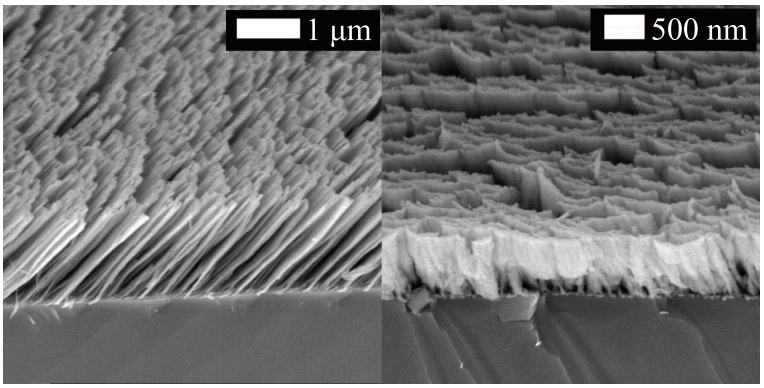

Figure 3.1: Illustration of broadening in a GLAD film. Notice the broadening in the direction normal to the plane in which the column is tilted; this anisotropic growth is often termed "second anisotropy" [43]. Second anisotropy often has a crescent moon shape, as seen in the image above; in optical modeling, this subtlety is often ignored in favour of simpler models.

rections, but is favored in the direction normal to the deposition plane. The net effect of this is that the columns of a GLAD film can be approximated by ellipsoidal shapes. Ultimately, we wish to describe the film as an effective medium. Recalling then the discussion from Chapter 1 regarding ellipsoidal inclusions in the Bruggeman effective medium approximation, we understand that as a result of the columnar broadening, films fabricated using GLAD will in general be biaxial [72], meaning that the films can be described by a constant dielectric tensor, with three distinct eigenvalues. The principal coordinate system, $x'y'z'$, of the resultant films is shown in Figure 3.2. The labels are chosen such that $n_{x'} < n_{y'} < n_{z'}$, a convention that holds for the vast majority of GLAD film structures. The dielectric tensor, ε, of the film in the xyz frame can be written

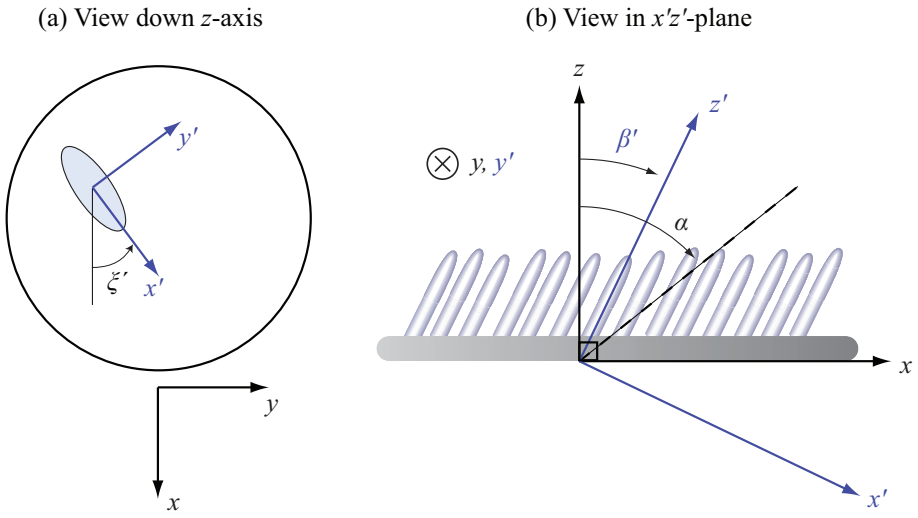

Figure 3.2: Principal coordinate system for a slanted post GLAD film: (a) Looking straight down on the substrate along the -z-axis; (b) Cross-section in the $x'z'$-plane.

as:

$$\varepsilon = R^{-1}\begin{pmatrix} n_{x'}^2 & 0 & 0 \\ 0 & n_{y'}^2 & 0 \\ 0 & 0 & n_{z'}^2 \end{pmatrix} R = R^{-1}\begin{pmatrix} \varepsilon_{x'} & 0 & 0 \\ 0 & \varepsilon_{y'} & 0 \\ 0 & 0 & \varepsilon_{z'} \end{pmatrix} R, \tag{3.1}$$

where the ε_i's are the principal dielectric constants. R is the rotation matrix from the xyz frame to the principal frame, given by:

$$R = \begin{pmatrix} \cos\beta' & 0 & \sin\beta' \\ 0 & 1 & 0 \\ -\sin\beta' & 0 & \cos\beta' \end{pmatrix}\begin{pmatrix} \cos\xi' & \sin\xi' & 0 \\ -\sin\xi' & \cos\xi' & 0 \\ 0 & 0 & 1 \end{pmatrix}. \tag{3.2}$$

For the films in this chapter, we will absorb any non-uniformities into measurement uncertainties, and we will always assume $\xi' = 0$, so the second term in the rotation matrix is simply the identity matrix. We are interested primarily in determining the refractive index seen by light normally incident on the film, along the $-z$-axis. There are two cases to consider: light polarized along the x-axis, and light polarized along the y-axis. Because the y- and y'-axes are

parallel, the latter case is straightforward:

$$n_y = n_{y'}. \tag{3.3}$$

For x-polarized light, we have light polarized normal to one of the principal axes. This situation is described by equation (1.30). In this case the incident wavevector makes an angle $\beta' - \pi/2$ with the x' axis, so the refractive index seen by light polarized along x is:

$$\frac{1}{n_x^2} = \frac{\cos^2\beta'}{n_{x'}^2} + \frac{\sin^2\beta'}{n_{z'}^2}. \tag{3.4}$$

Finally, the in-plane birefringence, defined as $\Delta n = n_y - n_x$, is a useful practical measure of the film's optical anisotropy, as it pertains to light normally incident on the film, as opposed to along one of its principal axes.

As mentioned earlier, the anisotropy in columnar shape and inclination arises due to the geometry of the film's nanoscale architecture [10]. Per the material in Chapter 1, we may model the film as an effective medium consisting of a mixture of void and isotropic dielectric material. Writing Bruggeman's formula with ellipsoidal inclusions in terms of the refractive index gives:

$$\bar{\varrho}\left(\frac{N^2 - n_i^2}{N^2 + (q_i^{-1} - 1)\varepsilon_i}\right) + (1 - \bar{\varrho})\left(\frac{1 - n_i^2}{1 + (q_i^{-1} - 1)n_i^2}\right) = 0, \qquad i = x', y', z'. \tag{3.5}$$

We recall that $\bar{\varrho}$ is the average fractional density, $N$is the refractive index of a film deposited at normal incidence ($\bar{\varrho} = 1$), and the q_i's are depolarization factors described in Chapter 1. A useful parameter turns out to be the average index:

$$n_{\text{avg}} = (n'_x + n'_y + n'_z)/3, \tag{3.6}$$

To a good approximation, the average index is a function of only $\bar{\varrho}$ and N, and can be determined using the following empirical result:

$$\frac{n_{\text{avg}} - 1}{N - 1} = \bar{\varrho}\left(1 - \frac{N - 1}{10}(1 - \bar{\varrho})\right). \tag{3.7}$$

This illustrates that the average index is best thought of as quadratic in the density, and is not linear. The above result is accurate to within a few percent

for $N < 2.5$, and especially accurate as $N \to 1$.

One could obtain the principal indices themselves from Bruggeman's equation by knowing the depolarization factors, which can be determined from the lengths of the ellipsoidal axes. We recall that a small depolarization factor is obtained when the ellipsoidal dielectric inclusion is extruded along a given axis. For instance, a depolarization factor approaching zero represents a long, needle-like shape along the associated axis. Smaller depolarization factors lead to larger values for the principal index. However, one can not measure depolarization factors directly without performing the difficult task of measuring the dimensions of the film columns, and determining the q_i's directly. One exception is in the case of $q_{z'}$, which describes extrusion along the columnar axis. In this case, because of the substantial elongation of the ellipsoidal inclusion along z', $q_{z'}$ tends toward zero. However, it is usually best described by a small, non-zero value around 0.10. [73] Given such a value for $q_{z'}$ one can then solve equation (3.5) directly for $n_{z'}$. As a result, for a given film density, $n_{z'}$ is typically relatively constant and independent of substrate rotation.

In contrast, $n_{x'}$ and $n_{y'}$, and their associated depolarization factors $q_{x'}$ and $q_{y'}$, vary significantly with substrate motion. This behaviour arises because of the competing effects of atomic shadowing and columnar broadening. One can quantify this behavior by examining the motion of the deposition plane during growth. We restrict our discussion to the behaviour at the center of the substrate, and ignore substrate thickness effects. As in the previous chapter, we define $\hat{\mathbf{R}}_{OS}$ as the unit vector from the center of the substrate to the source:

$$\hat{\mathbf{R}}_{OS} = \sin\alpha\cos\phi\hat{\mathbf{x}} - \sin\alpha\sin\phi\hat{\mathbf{y}} + \cos\alpha\hat{\mathbf{z}}. \tag{3.8}$$

Also as mentioned in the previous chapter, the global deposition plane is the plane containing $\hat{\mathbf{R}}_{OS}$ and $\hat{\mathbf{z}}$. In the lab frame, this plane is stationary, but in the xyz coordinate system, the unit normal to the deposition plane, termed the instantaneous broadening vector, $\hat{\mathbf{b}}$, is given by:

$$\hat{\mathbf{b}} = \frac{\hat{\mathbf{z}} \times \hat{\mathbf{R}}_{OS}}{|\hat{\mathbf{z}} \times \hat{\mathbf{R}}_{OS}|} = \sin\phi\hat{\mathbf{x}} + \cos\phi\hat{\mathbf{y}} = \cos\left(\frac{\pi}{2} - \phi\right)\hat{\mathbf{x}} + \sin\left(\frac{\pi}{2} - \phi\right)\hat{\mathbf{y}}. \tag{3.9}$$

The shadowing that leads to the formation of the columnar film structure in GLAD only takes place in the deposition plane. Normal to that plane, incident

atoms have a higher diffusivity and the film columns broaden significantly. [63] For instance, in the slanted post case, $\phi \equiv 0$ and $\hat{\mathbf{b}} = \hat{\mathbf{y}}$, leading to preferred broadening and extension along the y-axis. This preferred broadening can be seen in the SEM micrograph of Figure 3.2. This in turn leads to a longer ellipsoidal inclusion size in the y direction. Since the y- and y'-axes are parallel in the slanted post case, this leads to a smaller $q_{y'}$ and a larger $n_y = n_{y'}$. As a way to quantify the maximal broadening direction for a general deposition, we need to determine the average of $\hat{\mathbf{b}}$ over a deposition. However, the averaging must be done carefully, so that broadening contributions from $\hat{\mathbf{b}}$ and $-\hat{\mathbf{b}}$ are additive and not subtractive. This can be done by treating $\hat{\mathbf{b}}$ as the complex number $b = e^{i\pi/2}e^{-i\phi}$, where the real and imaginary parts of b correspond to the $\hat{\mathbf{x}}$ and $\hat{\mathbf{y}}$ components of the broadening vector. We then compute the root mean squared average of b over the deposition, labeled $\bar{b}$. This can be interpreted as a new vector, $\bar{\mathbf{b}}$, that points in the direction of maximum broadening, and whose length indicates the relative magnitude of broadening parallel to $\bar{\mathbf{b}}$ as compared with the direction orthogonal to $\bar{\mathbf{b}}$.

For the films identified in this work, $\bar{\mathbf{b}}$ is always along either $\hat{\mathbf{x}}$ or $\hat{\mathbf{y}}$. This means that $\bar{b}^2$is positive or negative in the two respective cases. We postulate that the in-plane birefringence, Δn, is linearly proportional to $\bar{b}^2$, according to the following:

$$\Delta n = n_y - n_x = -\bar{b}^2 \Delta n_{\max}, \tag{3.10}$$

where $\Delta n_{\max}$ is the maximum attainable in-plane birefringence for any film structure at the same α. We will demonstrate later that this maximum is observed in serially bideposited films. Therefore, if one knows $\bar{\varrho}$, $q_{z'}$, $\Delta n_{\max}$, and β', one can predict the principal indices of any slanted post GLAD film. Of these, $\bar{\varrho}$ and $\Delta n_{\max}$ are often tabulated as functions of α. [15,63,74] As discussed above, $q_{z'}$ is often set to the constant value 0.10. Finally, as was shown in the previous chapter, for a given substrate motion algorithm, knowledge of β' can be deduced from knowledge of β alone. In the next section, we will present a simplified formula for calculating β' that does not require the complete machination of the previous chapter. This is useful since β is often tabulated as a function of α. [13,75]

3.3 Advanced GLAD Algorithms

The previous chapter gave an indication of how azimuthal substrate rotation implemented as a function of film thickness allows for the formation of different columnar film structures. During our consideration of film uniformity issues we dealt with four specific structures: the pure slanted post, the vertical post, the spin-pause structure which is a combination of the former two structures, and the serial bideposited architecture. The films described in this work make use of three advanced GLAD growth algorithms, known as spin-pause, zig-zag and PhiSweep. [52, 76] These algorithms all lead to tilted columnar structures with new principal axes and principal refractive indices. Each structure can be considered as a combination of vertical and naturally slanted post segments, which provides the basis of our simplified model for predicting column tilts. The four structures of the previous chapter are each a particular case of one of the following three algorithms.

Spin-pause

The spin-pause algorithm as a function of the thickness at the substrate center, T_O, is shown schematically in Figure 3.3(a). A single period of the algorithm

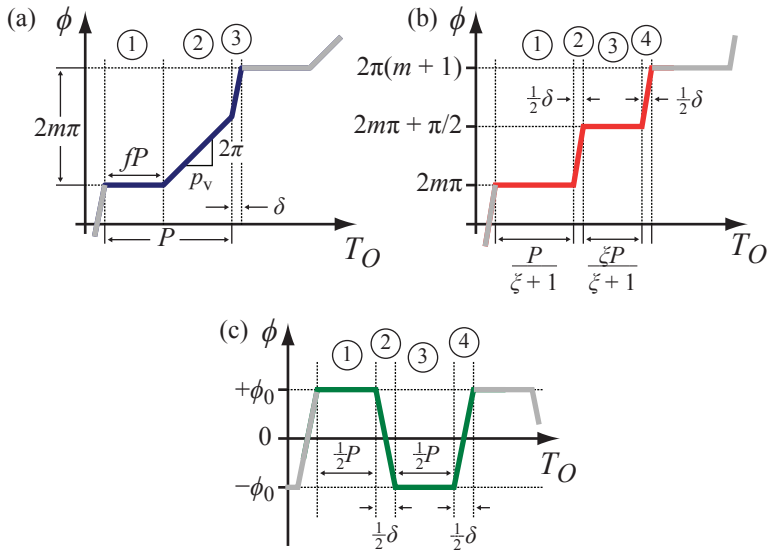

Figure 3.3: Substrate motion algorithms for the three film structures under consideration: (a) spin-pause, (b) zig-zag, (c) PhiSweep. The period of the algorithm is $P + \delta$ in all cases.

is broken into three regions and is characterized by four parameters, P, f, p_v and δ. To create the film, this algorithm uses alternating naturally slanted posts (region 1), vertical posts (region 2) with a combined thickness, P, and a short step of thickness δ used to rotate ϕ to the next largest integer multiple of 2π (region 3). $P + \delta$ is the period of the algorithm, which is repeated until the desired thickness is achieved. The parameter $f$is the spin-pause fraction, and is defined as the ratio of slanted growth to P. In the limit as $\delta \to 0$, films with $f = 0$ are vertical posts, while films with $f = 1$ are naturally slanted posts. Finally, p_v is the pitch of the spinning section and is typically about 5 nm. This parameter is present so that samples grown for varying f have similar vertical post segments.

In order to estimate the column tilt as a function of f, we could use the procedure outlined in Chapter 2. However, a simplified approach provides a very reasonable estimate. We seek the column tilt at the center of the substrate, and we do this by modeling growth as either purely vertical, when the substrate is rotating, or purely slanted, when the substrate is stationary. We also neglect the effect of mildly different growth rates for different structures.

For the spin-pause algorithm, the structure can be modeled as the resultant, $\mathbf{R}_{sp}$, of a naturally slanted post growing along a trajectory, $\mathbf{r}_1$ and two vertical post segments growing along trajectories, $\mathbf{r}_2$ and $\mathbf{r}_3$.

$$\begin{aligned} \mathbf{r}_1 &= fP(\tan\beta\hat{\mathbf{x}} + \hat{\mathbf{z}}), \\ \mathbf{r}_2 &= (1-f)P\hat{\mathbf{z}}, \\ \mathbf{r}_3 &= \delta\hat{\mathbf{z}}, \\ \mathbf{R}_{\text{sp}} = \mathbf{r}_1 + \mathbf{r}_2 + \mathbf{r}_3 &= Pf\tan\beta\hat{\mathbf{x}} + (P+\delta)\hat{\mathbf{z}}. \end{aligned} \tag{3.11}$$

The resultant column angle, β'_{sp} is the angle between $\mathbf{R}_{sp}$ and $\hat{\mathbf{z}}$, given by:

$$\tan\beta'_{\text{sp}} = \frac{Pf\tan\beta}{P+\delta} = \gamma f\tan\beta, \tag{3.12}$$

where $\gamma \equiv \frac{P}{P+\delta}$. The broadening vector now rotates at certain points during growth. We compute $\bar{b}^2_{\text{sp}}$ by forming the broadening vector as in equation (3.9), translating that to its complex number analog and taking its mean square. The

result is as follows:

$$\bar{b}_{sp}^2 = \frac{-1}{P+\delta}\left(fP + \frac{e^{-i\phi_1}}{2\pi}(p_v - p_\delta)\sin\phi_1\right), \qquad \text{where} \tag{3.13}$$

$$\phi_1 = \frac{2\pi P(1-f)}{p_v}, \tag{3.14}$$

$$p_\delta = \frac{2\pi\delta}{2m\pi - \phi_1}, \tag{3.15}$$

$$m = \left\lceil \frac{P(1-f)}{p_v} \right\rceil. \tag{3.16}$$

In most cases, the $\sin\phi_1$ term can be ignored[3.1]. In this case, $\bar{b}_{sp}^2$ is negative, meaning that $\bar{b}_{sp}$ is purely imaginary, and we can write the average broadening vector as:

$$\bar{\mathbf{b}}_{sp} = \sqrt{\gamma f}\hat{\mathbf{y}}. \tag{3.17}$$

Therefore, the broadening direction is along the y-axis and proportional to $\sqrt{f}$. Commonly, $\gamma \to 1$, so we can write $\bar{\mathbf{b}}_{sp} = \sqrt{f}\hat{\mathbf{y}}$.

So, as expected, for fully vertical posts ($f = 0$), $\bar{b} = 0$ and there is no preferred broadening direction. More slanted posts, with larger values of f, lead to larger (imaginary) values of $\bar{b}$, implying increased broadening along the y-axis. It is therefore expected that for small f, n_x and n_y will be similar, Δn will be small and positive and β' will be small. At large f, n_x and n_y will diverge, Δn will approach Δn_{max} and β' will approach β.

Zig-zag

The zig-zag algorithm is shown schematically in Figure 3.3(b). The algorithm involves four regions and is characterized by three parameters, P, ξ, and δ. The algorithm involves two slanted 'zig' and 'zag' growth segments, respectively (regions 1 and 3) offset by π radians and two rapid rotation segments of thickness $\delta/2$ needed to rotate between the slanted growth segments. $P + \delta$ is once again the period of the algorithm and $\xi$is the ratio of 'zag' growth to 'zig' growth. Films with $\xi = 0$ are naturally slanted posts, while films with $\xi = 1$

[3.1] For those cases where $\phi_1 \lesssim 2m\pi$, one should instead approximate $\sin\phi_1$ by the third order Taylor series, $\sin\phi_1 \approx 2(\phi_1 - 2m\pi) - \frac{(2(\phi_1-2m\pi)^3)}{3!}$. This is still a small correction, and $\bar{b}^2$ can still be approximated as real and negative, so that the broadening is still predominantly along the y-axis. This approximation can be used for $0.8 < \frac{\phi_1}{2m\pi} < 1$.

fall under the class of serial bideposition. [63] We can model this algorithm once again as a combination of vertical and slanted posts:

$$\begin{aligned}
\mathbf{r}_1 &= \frac{P}{\xi+1}(\tan\beta\hat{\mathbf{x}} + \hat{\mathbf{z}}),\\
\mathbf{r}_2 &= \frac{\delta}{2}\hat{\mathbf{z}},\\
\mathbf{r}_3 &= \frac{\xi P}{\xi+1}(-\tan\beta\hat{\mathbf{x}} + \hat{\mathbf{z}}),\\
\mathbf{r}_4 &= \frac{\delta}{2}\hat{\mathbf{z}},\\
\mathbf{R}_{zz} = \mathbf{r}_1 + \mathbf{r}_2 + \mathbf{r}_3 + \mathbf{r}_4 &= P\left(\frac{1-\xi}{1+\xi}\right)\tan\beta\hat{\mathbf{x}} + (P+\delta)\hat{\mathbf{z}}. \qquad (3.18)
\end{aligned}$$

This is the same result as equation (3.11) with $f \to \frac{1-\xi}{1+\xi}$, so the following can be written immediately:

$$\tan\beta'_{zz} = \gamma\left(\frac{1-\xi}{1+\xi}\right)\tan\beta. \qquad (3.19)$$

In this case, one can easily calculate $\bar{b}^2_{zz}$ as $-P/(P+\delta)$, so the average broadening vector is:

$$\bar{\mathbf{b}}_{zz} = \sqrt{\gamma}\hat{\mathbf{y}}. \qquad (3.20)$$

We find that the broadening vector is entirely independent of the zig-zag growth parameter, ξ, and always along the y-axis. Further, in the common limit $\gamma \to 1$, $\bar{\mathbf{b}}_{zz}$ simply becomes $\hat{\mathbf{y}}$, representing a high degree of broadening along the y-axis. This suggests that Δn will be constant and roughly equal to $\Delta n_{\max}$ for all ξ. Previous experimental results have shown that this is not strictly true, as the in-plane birefringence of films with $\xi = 1$ ($\beta' \sim 0$) has typically been found to be greater than films with $\xi = 0$ ($\beta' \sim \beta$). [77] This will be addressed in a later section.

PhiSweep

The PhiSweep algorithm is illustrated in Figure 3.3(c), and is characterized by three parameters, P, ϕ_0 and δ. The algorithm is broken into four regions. Regions 1 and 3 are slanted post segments, each of length $P/2$, held at angles of $\pm\phi_0$. Regions 2 and 4 are rapid spinning sections of length $\delta/2$ similar to regions 2 and 4 in the zig-zag algorithm. Films with $\phi_0 = 0$ are naturally slanted

posts, while films with $\phi_0 = \pi/2$ are serially bideposited, but, importantly, they broaden in a direction normal to that of the serially bideposited zig-zag films. As with the prior two cases, the film can be modeled as a combination of vertical and slanted sections:

$$\begin{aligned}
\mathbf{r}_1 &= \frac{P}{2}(\tan\beta\cos\phi_0\hat{\mathbf{x}} + \tan\beta\sin\phi_0\hat{\mathbf{y}} + \hat{\mathbf{z}}),\\
\mathbf{r}_2 &= \frac{\delta}{2}\hat{\mathbf{z}},\\
\mathbf{r}_3 &= \frac{P}{2}(\tan\beta\cos\phi_0\hat{\mathbf{x}} - \tan\beta\sin\phi_0\hat{\mathbf{y}} + \hat{\mathbf{z}}),\\
\mathbf{r}_4 &= \frac{\delta}{2}\hat{\mathbf{z}}.\\
\mathbf{R}_{\text{Œ}} = \mathbf{r}_1 + \mathbf{r}_2 + \mathbf{r}_3 + \mathbf{r}_4 &= P\tan\beta\cos\phi_0\hat{\mathbf{x}} + (P+\delta)\hat{\mathbf{z}}. \qquad (3.21)
\end{aligned}$$

Once again, this is identical to equation (3.11), with $f \to \cos\phi_0$, yielding;

$$\tan\beta'_\phi = \gamma\cos\phi_0\tan\beta. \qquad (3.22)$$

This result has been obtained previously by Gish for the case $\gamma = 1$. [78] Working out $\bar{b}_\phi^2$ gives the following:

$$\bar{b}_\phi^2 = -\gamma\left(\cos 2\phi_0 + \frac{\delta}{2P\phi_0}\sin 2\phi_0\right). \qquad (3.23)$$

This is actually a very interesting result. Consider first the case where δ/P is negligible. Then we obtain the result that $\bar{b}_\phi^2 = -\gamma\cos 2\phi_0$. For $\phi_0 \le \pi/2$, $\bar{b}_\phi^2$ is negative, implying that $\bar{b}_\phi$ is imaginary, and we obtain

$$\bar{\mathbf{b}}_\phi = \sqrt{\gamma\cos 2\phi_0}\hat{\mathbf{y}}, \qquad 0 \le \phi_0 \le \frac{\pi}{2}. \qquad (3.24)$$

However, for $\phi_0 > \pi/2$, $\bar{b}_\phi^2$ is actually positive, meaning that $\bar{b}_\phi$ is real, and we obtain:

$$\bar{\mathbf{b}}_\phi = \sqrt{-\gamma\cos 2\phi_0}\hat{\mathbf{x}}, \qquad \frac{\pi}{2} \le \phi_0 \le \pi. \qquad (3.25)$$

For the case where the contribution due to a non-zero δ/P is retained, the only change is that the transition into broadening along the x-axis occurs at a

slightly larger ϕ_0. This occurs at the angle ϕ_0'given implicitly by:

$$\cos 2\phi_0' + \frac{\delta}{2P\phi_0'} \sin 2\phi_0' = 0. \tag{3.26}$$

This overall result means that the PhiSweep algorithm can cause broadening along either the x- or y-axes, which is an important distinction from the spin-pause and zig-zag cases, which only broaden along the y-axis. For cases in which broadening along the x-axis is preferred ($\phi_0 > \phi_0'$), this implies that $n_x > n_y$, meaning negative in-plane birefringence. Generally speaking, this behavior is rare, though it is observed in certain organic films. [79] Physically, it is characterized by broadening in the same direction as column tilt. Consequently, we find that for $\phi_0 = \phi_0'$, $\bar{\mathbf{b}}_\phi$ vanishes, and the in-plane birefringence is expected to vanish. Additionally, one also expects a point at which $n_{x'} = n_{y'}$ at which the film degenerates from a biaxial film into a uniaxial one.

Notice that each of the three algorithms produces a resultant trajectory in the xz-plane, as in the natural slanted post case. Notice also that each of equations (3.12), (3.19) and (3.22) have the same form:

$$\tan\beta' = a\gamma \tan\beta, \tag{3.27}$$

with $a = f, \frac{1-\xi}{1+\xi}, \cos\phi_0$for each of the three cases, and a continuously variable from 0 to 1. This means that all three algorithms can access the same range of tilt angles, from 0 to $\tan^{-1}(\gamma \tan\beta)$, for appropriate choices of the relevant growth parameter. This is a very nice result, as it unifies all three slanted post algorithms (and presumably, any number of other possible slanted post algorithms) under a single parameter, allowing for a direct comparison of the results. Additionally, because the broadening conditions are different in each case, films fabricated with the same tilt angle (same a) are expected to have significantly different optical constants. The important results of this section are tabulated in Table 3.1.

If we now put together the results of the previous sections, we see that for a given material, and a given deposition angle, if we know the refractive index at normal incidence, N, the natural column tilt, β, the fractional density, $\bar{\varrho}$, as well as the maximum in-plane birefringence, $\Delta n_{\max}$, then we can then determine $\beta', n_{x'}, n_{y'}, n_{z'}$ as well as n_x and Δn using the following procedure:

Table 3.1: Characteristics of films grown by different algorithms

	Spin-pause	Zig-zag	PhiSweep
Growth parameter	f	ξ	ϕ_0
a	f	$\frac{1-\xi}{1+\xi}$	$\cos\phi_0$
$\bar{b}^2$	$-\gamma f$	$-\gamma$	$-\gamma\left(\cos 2\phi_0 + \frac{\delta}{2P\phi_0}\sin 2\phi_0\right)$
$\bar{\mathbf{b}}/\lvert\bar{\mathbf{b}}\rvert$	$\hat{\mathbf{y}}$	$\hat{\mathbf{y}}$	$\hat{\mathbf{y}}$, $0 \le \phi_0 \le \phi_0'$ $\hat{\mathbf{x}}$, $\phi_0' \le \phi_0 \le \frac{\pi}{2}$

1. Determine a, $\bar{b}$ and γ for the algorithm in question.
2. Obtain $n_{z'}$ from equation (3.5) using the known value for $\bar{\varrho}$ and by setting $q_{z'} = 0.1$.
3. Obtain n_{avg} from equation (3.7) using the known value for $\bar{\varrho}$.
4. Obtain β' from equation (3.27) using the known values of a and γ.
5. Solve for n_x, $n_{x'}$ and $n_{y'}$ by simultaneously solving equations (3.4), (3.6) and (3.10).

This procedure is very powerful, and as the next section illustrates, it is capable of making accurate predictions of both the column tilt and the refractive indices. We will also demonstrate that the model is capable of predicting certain unique properties that are relatively uncommon in metal-oxide columnar films.

3.4 Experimental Results

3.4.1 Experimental Details

TiO_2 and SiO_2 (Cerac Inc., 99.9% pure) films were fabricated with electron-beam evaporation on Si substrates (p-doped, {100} orientation, from University Wafer) with a source-to-substrate throw distance of 40 cm. SiO_2 films ($N_{SiO_2} = 1.46$ at 500 nm) were fabricated at a deposition pressure of 0.3 mPa to 0.7 mPa, with no gases added during deposition. TiO_2 films ($N_{TiO_2} = 2.43$

at 500 nm) were fabricated reactively with oxygen added to the chamber to maintain a deposition pressure of 9.3 mPa to 12.0 mPa. TiO_2 samples were annealed post-deposition at 100°C for 24 hours to ensure stoichiometric films. The algorithms were implemented at constant α according to the prescriptions in the previous section. In all cases, films were grown with $P = 23$ nm, $\delta = 2$ nm ($\gamma = 0.92, \phi_0' = 46.5°$) and to a target thickness of $T_0^{\text{total}} = 1000$ nm. Vertical post sections in spin-pause films were grown with a pitch, $p_v = 5$ nm. T_{total} and β' were obtained via SEM measurement[3.2]. The film density was determined by weighing substrates before and after deposition. Knowing the area of the substrate and the film thickness allows one to estimate the film density. However, because the worst-case thickness non-uniformity in GLAD films can be larger than 40% across a 10 cm diameter substrate, [38] one must take care to obtain a thickness measurement of the film at a location close to the location of the refractive index measurement.

To determine the principal refractive indices, variable angle Mueller matrix ellipsometry was performed as outlined in Chapter 1. Measurements were taken in reflection at three angles of incidence (45°, 55° and 65°) over the range 400 nm to 1700 nm. In order to examine the validity of the Bruggeman model, the film was modeled as a biaxial thin film with each of the principal indices having a Cauchy dispersion:

$$n_i = A_i + \frac{B_i}{\lambda^2} + \frac{C_i}{\lambda^4}, \qquad i = x', y', z'. \tag{3.29}$$

The values of T^{total} and β' obtained from SEM measurements are input to the model. In this approach, there are ten free parameters: three each of the A_i's, B_i's and C_i's, as well as T^{total}. The thickness is allowed to vary since the combined uncertainty from the SEM measurement itself, and from taking the SEM measurement and the optical measurement at different points on the substrate can be very high, and because small variations in T^{total} can affect the model fit significantly. Small changes in β' do not strongly affect the model fit, but can significantly affect the principal indices, so β' is held fixed at the value ob-

[3.2] Column tilt angle was obtained by taking two column tilt measurements, β_1' and β_2' along non-parallel cleaved edges. The true column tilt, β', can then be found from the following:

$$\tan\beta' = \frac{1}{\sin\psi}\sqrt{\tan^2\beta_1' + \tan^2\beta_2' - 2\tan\beta_1'\tan\beta_2'\cos\psi}, \tag{3.28}$$

where ψ is the angle between the two edges.

tained from microscopy. The films fabricated for this study are listed in Table 3.2 along with a summary of their measured properties.

The column tilt angle, β' is plotted in Figure 3.4 as a function of the nor-

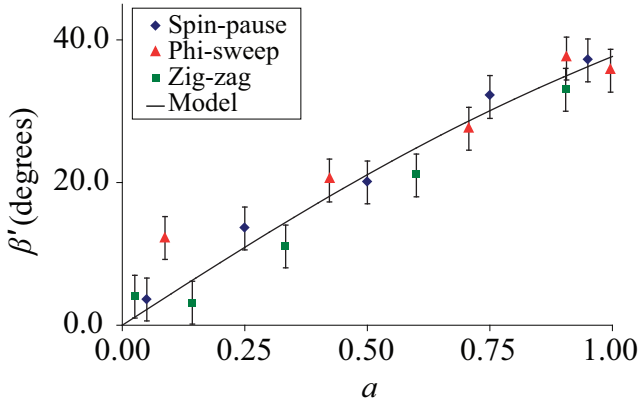

Figure 3.4: Column tilt angle, β', as a function of the structure parameter, a

malized structure parameter, a, for TiO_2 and SiO_2 films of all three types of films, grown at $\alpha = 70°$ (samples M to AA and AF to AJ). The relations $\beta' = \tan^{-1}(a\gamma \tan\beta)$ have also been plotted, for $\beta = 40.0°$ and $\beta = 35.0°$ as the measured natural column angles for TiO_2 and SiO_2 at this deposition angle. The model does a reasonable job of predicting the column tilt angles, though there is some discrepancy. There also appear to be some structure-dependent trends; for instance zig-zag films have β' values that are consistently measured to be less than the predicted value, while PhiSweep films tend to have values somewhat above those predicted. It is not immediately clear what causes these discrepancies, but it is likely that it has to do with the fact that nucleating on the backside of tilted columns leads to differences in β' as a result of a lower effective deposition angle for material arriving on the column itself. [48] This behaviour also explains why films with sudden changes in ϕ, including all zig-zag structures and PhiSweep films with large a, have a slightly higher density than expected.

We also compared the densities given by direct mass measurements to densities obtained by using the Bruggeman model in the ellipsometric approach. Figure 3.5 shows a comparison of the fractional density obtained from the ellipsometric approach, $\bar{\varrho}_{\text{VASE}}$, and from directly measuring the density by measuring the mass and volume of the film, $\bar{\varrho}_{\text{scale}}$. The figure plots the negative

Table 3.2: Film samples and their measured properties (optical constants given at 500 nm)

Label	Structure	Material	α (°)	a	b^2	β' (°)	n'_x	n'_y	n'_z	n_x	Δn	n_{avg}
A	Spin-pause	TiO_2	60	0.50	0.46	16.8	1.80	1.88	1.95	1.81	0.07	1.88
B	Spin-pause	TiO_2	70	0.50	0.46	22.7	1.60	1.70	1.82	1.63	0.07	1.71
C	Spin-pause	TiO_2	80	0.50	0.46	30.2	1.36	1.46	1.58	1.41	0.05	1.47
D	Spin-pause	TiO_2	85	0.50	0.46	33.2	1.25	1.33	1.43	1.29	0.03	1.34
E	Zig-zag	TiO_2	60	0.50	0.92	18.0	1.90	1.99	2.04	1.92	0.08	1.98
F	Zig-zag	TiO_2	70	0.50	0.92	13.0	1.64	1.78	1.82	1.65	0.13	1.75
G	Zig-zag	TiO_2	80	0.50	0.92	21.0	1.35	1.47	1.59	1.37	0.10	1.47
H	Zig-zag	TiO_2	85	0.50	0.92	26.0	1.26	1.38	1.41	1.29	0.09	1.35
I	PhiSweep	TiO_2	60	45.0	0.05	20.0	1.81	1.86	2.04	1.84	0.02	1.90
J	PhiSweep	TiO_2	70	45.0	0.05	33.0	1.61	1.69	1.84	1.67	0.02	1.71
K	PhiSweep	TiO_2	80	45.0	0.05	38.0	1.47	1.48	1.63	1.53	-0.05	1.53
L	PhiSweep	TiO_2	85	45.0	0.05	45.1	1.28	1.34	1.51	1.38	-0.05	1.38
M	Spin-pause	TiO_2	70	0.05	0.05	3.6	1.66	1.68	1.90	1.66	0.02	1.75
N	Spin-pause	TiO_2	70	0.25	0.23	13.6	1.64	1.70	1.89	1.65	0.05	1.74
O	Spin-pause	TiO_2	70	0.50	0.46	20.0	1.62	1.71	1.87	1.64	0.07	1.73
P	Spin-pause	TiO_2	70	0.75	0.69	32.0	1.59	1.72	1.90	1.66	0.06	1.74
Q	Spin-pause	TiO_2	70	0.95	0.87	37.1	1.57	1.73	1.89	1.67	0.06	1.73
R	Zig-zag	TiO_2	70	0.90	0.92	33.0	1.63	1.80	1.92	1.70	0.10	1.78
S	Zig-zag	TiO_2	70	0.60	0.92	21.0	1.63	1.77	1.90	1.66	0.11	1.77
T	Zig-zag	TiO_2	70	0.33	0.92	11.0	1.65	1.76	1.87	1.66	0.10	1.76
U	Zig-zag	TiO_2	70	0.14	0.92	3.2	1.64	1.76	1.87	1.64	0.12	1.76
V	Zig-zag	TiO_2	70	0.03	0.92	4.0	1.64	1.77	1.81	1.64	0.13	1.74
W	PhiSweep	TiO_2	70	1.00	0.99	35.7	1.55	1.72	1.88	1.64	0.08	1.72
X	PhiSweep	TiO_2	70	0.91	0.66	37.4	1.55	1.73	1.86	1.65	0.08	1.71
Y	PhiSweep	TiO_2	70	0.71	0.05	27.5	1.65	1.70	1.96	1.70	0.00	1.77
Z	PhiSweep	TiO_2	70	0.42	-0.56	20.3	1.79	1.72	1.89	1.80	-0.08	1.80
AA	PhiSweep	TiO_2	70	0.09	-0.90	12.2	1.79	1.66	1.90	1.79	-0.13	1.78
AB	PhiSweep	SiO_2	60	0.71	0.05	16.0	1.33	1.33	1.34	1.33	0.01	1.33
AC	PhiSweep	SiO_2	70	0.71	0.05	22.3	1.25	1.25	1.28	1.25	0.00	1.26
AD	PhiSweep	SiO_2	80	0.71	0.05	31.0	1.13	1.13	1.16	1.14	-0.01	1.14
AE	PhiSweep	SiO_2	85	0.71	0.05	31.0	1.08	1.08	1.10	1.08	0.00	1.09
AF	PhiSweep	SiO_2	70	1.00	0.99	33.0	1.21	1.25	1.26	1.22	0.03	1.24
AG	PhiSweep	SiO_2	70	0.91	0.66	32.0	1.22	1.26	1.26	1.23	0.03	1.25
AH	PhiSweep	SiO_2	70	0.71	0.05	27.0	1.23	1.24	1.27	1.24	0.00	1.25
AI	PhiSweep	SiO_2	70	0.42	-0.56	17.7	1.26	1.24	1.27	1.26	-0.02	1.26
AJ	PhiSweep	SiO_2	70	0.09	-0.90	4.1	1.25	1.22	1.26	1.25	-0.03	1.24

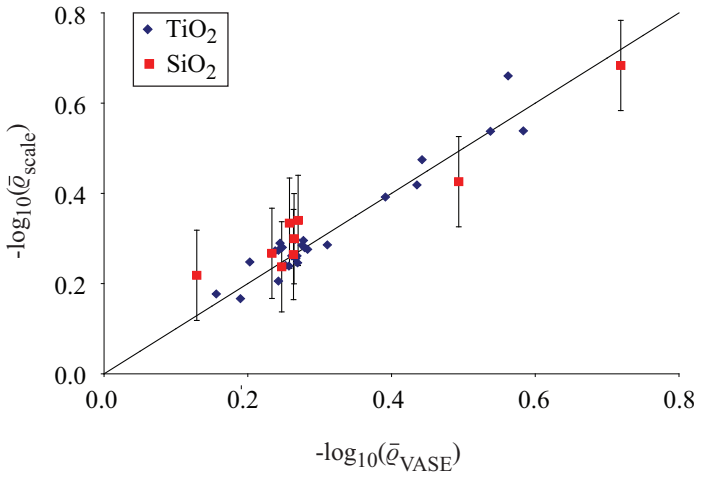

Figure 3.5: Comparison of the fractional density measured using ellipsometry, $\bar{\varrho}_{\text{VASE}}$, and measured directly, $\bar{\varrho}_{\text{scale}}$ for both TiO_2 and SiO_2 samples

base-10 logarithm of the two quantities so that the slope of the line relating two variables gives the exponent of the relationship. Error bars are shown only for the SiO_2 data, but are comparable for both datasets, and represent a measurement uncertainty of 10%. This uncertainty arises primarily because of the uncertainty in measuring the film thickness. The line $\bar{\varrho}_{\text{VASE}} = \bar{\varrho}_{\text{scale}}$ is also drawn as a comparison. We see that, qualitatively, the value returned by the VASE measurement is in agreement with the value obtained through direct measurement, for all data points, within experimental uncertainty. Quantitatively, the equation of the best-fit line through the SiO_2 set is given by $\bar{\varrho}_{\text{scale}} = (0.78 \pm 0.08)\bar{\varrho}_{\text{VASE}} + (0.09 \pm 0.03)$ with $R^2 = 0.93$, but this improves significantly when one forces a zero intercept to $\bar{\varrho}_{\text{scale}} = (1.00 \pm 0.05)\bar{\varrho}_{\text{VASE}}$, but with a slightly worse $R^2 = 0.84$. The best-fit line to the TiO_2 dataset is much better, and gives $\bar{\varrho}_{\text{scale}} = (1.01 \pm 0.06)\bar{\varrho}_{\text{VASE}} + (0.00 \pm 0.02)$ with $R^2 = 0.93$, even without constraining the intercept to zero. Since the slope of the line is equal to unity within error, it is quite clear that the two approaches yield statistically equivalent values in the TiO_2 case, and this appears to be true in the SiO_2 case as well, but the dataset is simply too small to conclude this definitively. These results provide significant evidence for the fact that ellipsometric measurements of fractional density are as valid as direct mass measurements.

Figure 3.6 shows the average index, n_{avg}, plotted against the fractional density, $\bar{\varrho}$ for all film samples, separated by material. Also plotted is n_{avg}, as

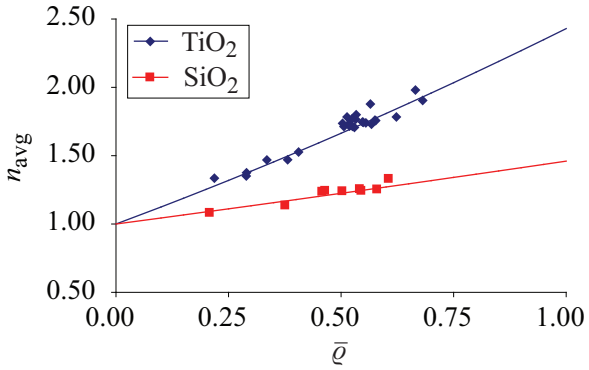

Figure 3.6: Modeled (lines) and experimental (points) n_{avg} vs. $\bar{\varrho}$ for TiO_2 and SiO_2 films of all types. Modeled data obtained from equation (3.7)

obtained from equation (3.7), for both materials. As one can see, equation (3.7) does well to predict n_{avg} through knowledge of $\bar{\varrho}$ and N alone. As predicted, there is no first-order change in the average index due to variation in the q_i's. Consequently, since $\bar{\varrho}$ is itself controlled primarily by α, [80] these observations emphasize the general rule that for a film of a single material, large changes in n_{avg} during deposition can only be obtained by changing the deposition angle.

Figure 3.7 shows the predicted and measured principal indices for TiO_2 and SiO_2 films of varying structure type, with varying a (samples M-AA and AF-AJ). The predicted values were obtained by simultaneously solving equations (3.5), (3.7) and (3.10) with $q_{z'} = 0.1$ for both materials. For TiO_2, $\Delta n_{max} = 0.13$ and $\bar{\varrho} = 0.54 \pm 0.03, 0.57 \pm 0.03$ and 0.55 ± 0.03 were used for spin-pause, zig-zag and PhiSweep films respectively. This corresponds to c values in the Poxson formula equal to 3.9 ± 0.5, 4.4 ± 0.5 and 4.1 ± 0.5. For the SiO_2 PhiSweep films, we used $\Delta n_{max} = 0.03$ and $\bar{\varrho} = 0.55 \pm 0.01$, corresponding to $c = 4.1 \pm 0.2$. These numbers are in broad agreement with the c values obtained in the previous chapter, but there is too much uncertainty in the measurement to conclude anything definitive. As mentioned earlier, note that the maximum values for Δn_{max} come from limiting cases of the algorithms that produce serially bideposited structures. The values for $\bar{\varrho}$ represent the measured average density and standard deviation for each film set. In Figure 3.7, the solid lines represent the predicted index for the mean value of $\bar{\varrho}$, while the highlighted bands represents the predicted range in the index due to the uncertainty in the density measurement. Figure 3.8 shows the measured birefringence for the same TiO_2

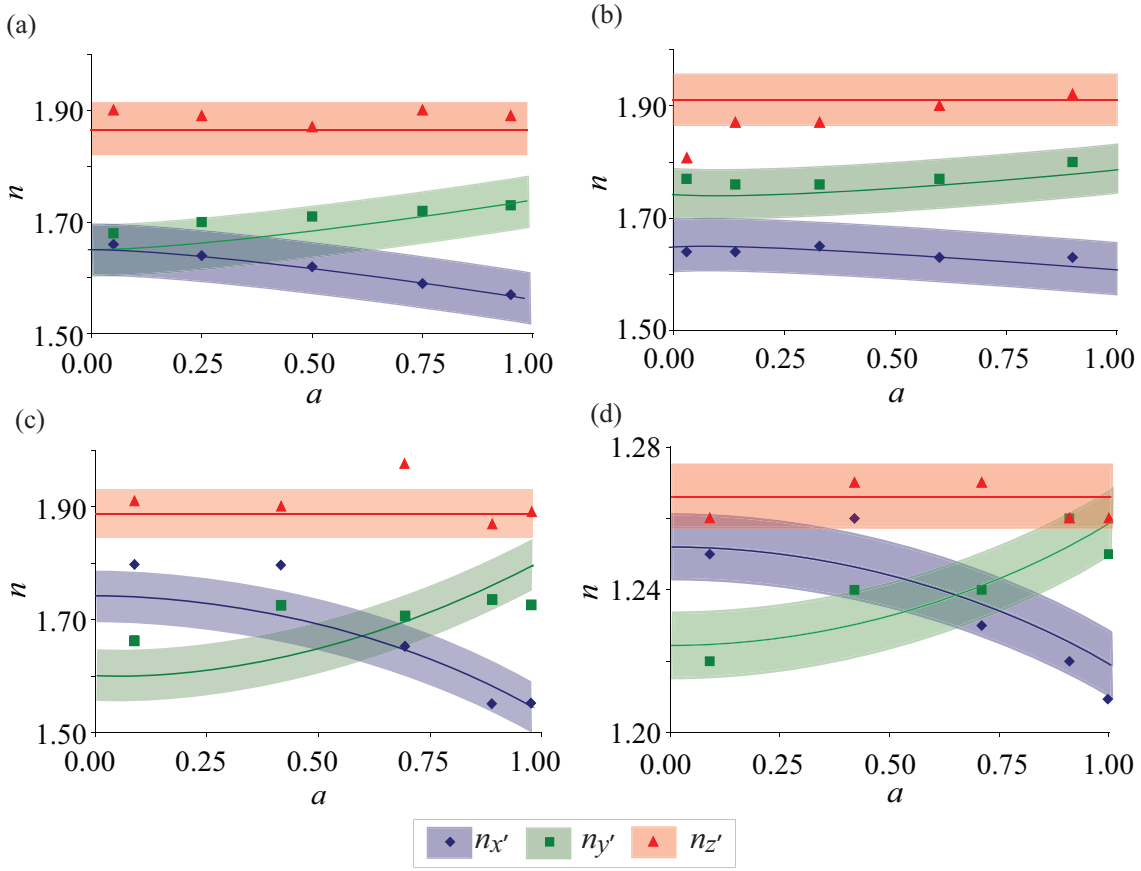

Figure 3.7: Modeled (lines) and experimental (points) principal indices, $n_{x'}$, $n_{y'}$ and $n_{z'}$ for (a) TiO_2 spin-pause, (b) TiO_2 zig-zag, (c) TiO_2 PhiSweep and (d) SiO_2 PhiSweep films with $\alpha = 70°$. Solid lines indicate predicted values for the mean value of $\bar{\varrho}$; the bands encompass the uncertainty in the prediction due to the uncertainty in the measurement of $\bar{\varrho}$.

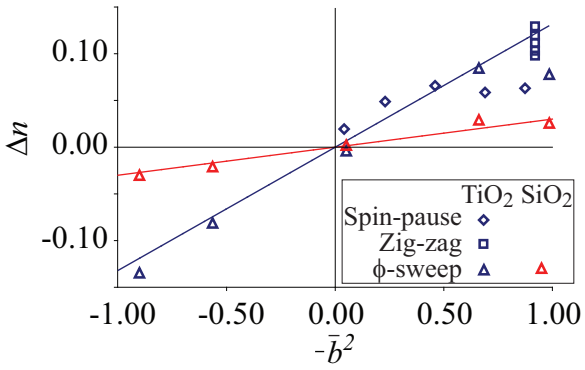

Figure 3.8: Modeled (lines) and experimental (points) values for the in-plane birefringence, Δn, for SiO_2 and TiO_2 films of all types.

and SiO_2 films, plotted alongside equation (3.10) for both materials.

It is clear that the model provides an accurate prediction of the principal indices. This is particularly true for the spin-pause films at all values of a. In this case we see uniaxial behaviour at $a = 0$ as predicted, and the relation $n_{x'} < n_{y'} < n_{z'}$ holds everywhere. As expected, $n_{z'}$ is approximately constant, and is well-modeled by a constant $q_{z'}$. We also observe fairly significant changes in $n_{x'}$ and $n_{y'}$ as the structure varies. However, despite the large changes in $n_{x'}$ and $n_{y'}$, one can see from Table 3.2 that the in-plane index, n_x, is remarkably constant. This is likely a coincidence for this particular deposition angle, but it implies that for TiO_2 at $\alpha = 70°$, spin-pause films are approximately index-matched to each other for x-polarized light. This is a nice result from a design point of view, as it allows one to focus only on designing for $n_y = n_{y'}$ if one restricts themselves to devices consisting of layers made of this class of film.

The zig-zag samples exhibit significantly different results. Again, the experimental results are well-predicted by the model, particularly at large a. The overall change in $n_{x'}$ and $n_{y'}$ is much smaller than in the spin-pause case, though they trend in the same manner as a function of a. $n_{z'}$ is again seen to be roughly constant, as expected. The most defining characteristics of the zig-zag films are the slow change in $n_{x'}$ and $n_{y'}$ and the large birefringence seen at all a. In fact, as Table 3.2 shows, Δn actually increases as the film transitions from a purely slanted structure toward an SBD structure. This is consistent with previous research and the earlier comments indicating that Δn is highest in SBD films. As a result, even though Figure 3.8 shows that equation (3.10) does a very good job at predicting Δn, we must conclude that Δn can not be a

function of b alone. Clearly, Δn also correlates with decreasing a, independent of $\bar{b}^2$, and this should be accounted for if more accurate predictions are necessary. Zig-zag films are then best characterized as films whose principal indices exhibit minimal variation, and who retain a large in-plane birefringence at all column tilt angles. As an approximation, this algorithm decouples the principle indices and Δn from the column tilt angle.

As expected, the PhiSweep films exhibit by far the most distinct behavior. Out of the algorithms considered, this is the only one for which the standard rule $n_{x'} < n_{y'}$ fails, and this is true of both the TiO_2 and SiO_2 films[3.3]. We note first that, as seen in Figure 3.8, we do in fact see that for both film materials the in-plane birefringence vanishes for $\bar{b}^2 = 0$. We also observe that for $-\bar{b}^2 < 0$, the in-plane birefringence does indeed become negative, as broadening is preferred in the direction of column tilt. This further confirms the utility of $\bar{b}$ in identifying both the broadening direction in GLAD films, as well as in identifying the resultant optical properties. The model does underestimate the magnitude of the negative birefringence as $-\bar{b}^2 \to -1$. This is the same behaviour that is observed with the zig-zag films as $-\bar{b}^2 \to 1$, as these two situations both represent serially bideposited films, which tend to have higher Δn, as discussed previously.

The model also predicts uniaxial behavior ($n_{x'} = n_{y'}$) at $a = 0.57$ ($\phi_0 = 55.2^\circ$) for TiO_2 and at $a = 0.64$ ($\phi_0 = 50.2^\circ$) for SiO_2, both of which are fairly consistent with the observed behavior. For TiO_2 we predict ordinary and extraordinary indices of $n_o = 1.66$ and $n_e = 1.88$ at the uniaxial point, while for SiO_2 we predict $n_o = 1.24$ and $n_e = 1.27$. At the uniaxial point, the predicted column tilt, β', is 23.8° and 22.4° for the TiO_2 and SiO_2 cases, respectively, indicating that a tilted, uniaxial film is indeed realizable using the GLAD process. Using higher α should enable the formation of tilted uniaxial films with even larger columnar tilts. Notice also that the ordinary index of the PhiSweep film is not the same as in a vertical post fabricated at the same α, meaning that these two uniaxial films are not index matched for a given deposition angle.

The uniaxial nature obtainable through PhiSweep is quite advantageous as one can more easily match the film's ordinary index to that of another isotropic or uniaxial layer. Additionally, calculating the propagation constant of modes

[3.3] One could relabel $n_{x'}$ and $n_{y'}$ in this case, but we choose not to in order to retain continuity of slope in the principal indices, as in Figures 3.7(c) and (d).

in uniaxial films is far simpler than in biaxial films, and this can simplify design choices. Additionally, the formation of a negative birefringent sample is potentially useful for nematic liquid crystal infiltration. [65, 81] Certain calamitic liquid crystals have been found to align along the columns of porous GLAD films, but due to the typical positive uniaxial nature of these molecules, they contribute an effective negative birefringence upon infiltration, reducing the anisotropy of the hybrid film, and limiting the performance of the system. By switching to a film with negative birefringence, it is possible that this effect will be mitigated. Finally, it must be noted that in $n_{x'}$, the PhiSweep algorithm exhibits the greatest peak-to-peak variation in any principal index. The variation is measured at more than 0.25 for PhiSweep, compared to maximum variations of about 0.10 in the other two algorithms. This translates, to a slightly lesser extent, into n_x, which also sees the greatest variation in PhiSweep. By contrast, the observed variation in n_y is no greater than in the other algorithms. Thus, to achieve the greatest modulation in the in-plane indices, one should focus on the PhiSweep algorithm, with an eye to modulating n_x.

3.5 Additional Modeled Results

We now understand that, for a given material, if one knows the refractive index of a normal incidence film, N, as well as the column tilt, β, the density, $\bar{\varrho}$ and the maximum birefringence, $\Delta n_{\max}$, as functions of α, we can predict the principal indices for any film structure presented here. Knowing β and $\bar{\varrho}$ is equivalent to knowing the material parameters, E and c, from the Lichter-Chen (equation (1.4)) and Poxson (equation (1.8)) relationships, which we have found here for TiO_2 and SiO_2, and are often tabulated in the literature. If we can then obtain $\Delta n_{\max}$ as a function of α, we could calculate the optical properties of any of the three film structures outlined in this chapter for all deposition angles, which is of major utility for optical filter design. We will see a direct application of this in the next chapter, but for the time being we will present modeled data for the optical properties of TiO_2 films across all deposition angles.

To accomplish this, we need $\Delta n_{\max}$. We choose to adapt the results given by van Popta *et al* [74]. The results therein demonstrate that $\Delta n_{\max}$ increases from zero at low α to a maximum value of 0.14 ± 0.01 at $\alpha = 70^\circ$ (for a wavelength of approximately 500 nm), which is consistent with our measurements. Beyond

$\alpha = 70^\circ$, the birefringence decreases, presumably to zero at $\alpha = 90^\circ$. This is a commonly encountered phenomenon, and the presence of a peak birefringence value arises because increasing the deposition angle increases the absolute amount of columnar broadening which tends to increase birefringence, but decreases the average refractive index of the film, which tends to reduce birefringence. With this in mind, we model the system as a piecewise linear system given the three known points: $\Delta n_{\max} = 0$ at $\alpha = 0^\circ, 90^\circ$, and $\Delta n_{\max} = 0.14$ at $\alpha = 70^\circ$:

$$\Delta n_{\max}(\alpha) = \begin{cases} 0.14\dfrac{\alpha}{70^\circ}, & \alpha \leq 70^\circ \\ 0.14\left(1 - \dfrac{\alpha - 70^\circ}{20^\circ}\right), & \alpha > 70^\circ \end{cases} \tag{3.30}$$

Figure 3.9 shows the assumed $\Delta n_{\max}$ as a function of α, at 500 nm.

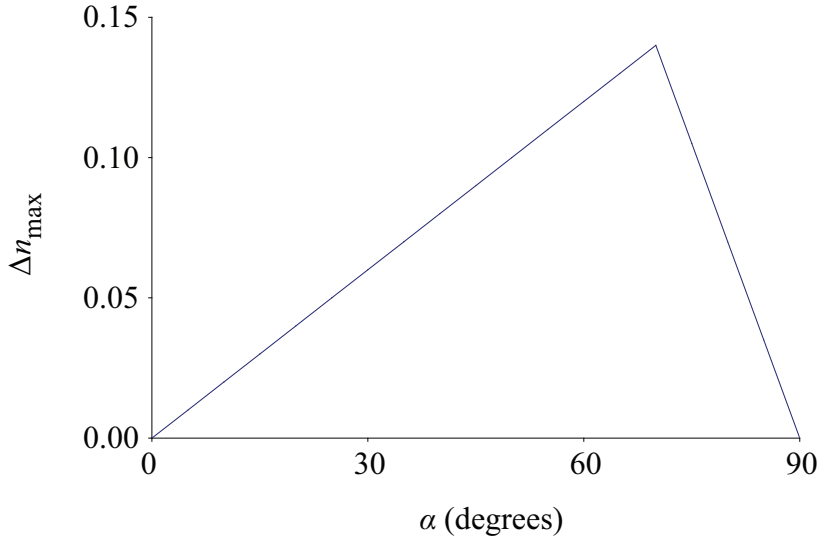

Figure 3.9: $\Delta n_{\max}$ for TiO_2 films as a function of deposition angle, α, at 500 nm

If we now assume representative values $E = 0.49$ and $c = 4.1$ for TiO_2, we can determine the optical constants for all film structures, and at all deposition angles. Since we are interested primarily in normally incident light, we focus on the in-plane indices, n_x and n_y. Figure 3.10 shows n_x and n_y for the spin-pause, zig-zag and PhiSweep structures, as functions of a for deposition angles of $0^\circ, 25^\circ, 50^\circ, 70^\circ$ and 85°. We see that the primary effect of α is to change the magnitude of n_x and n_y, with films deposited at higher α having lower index

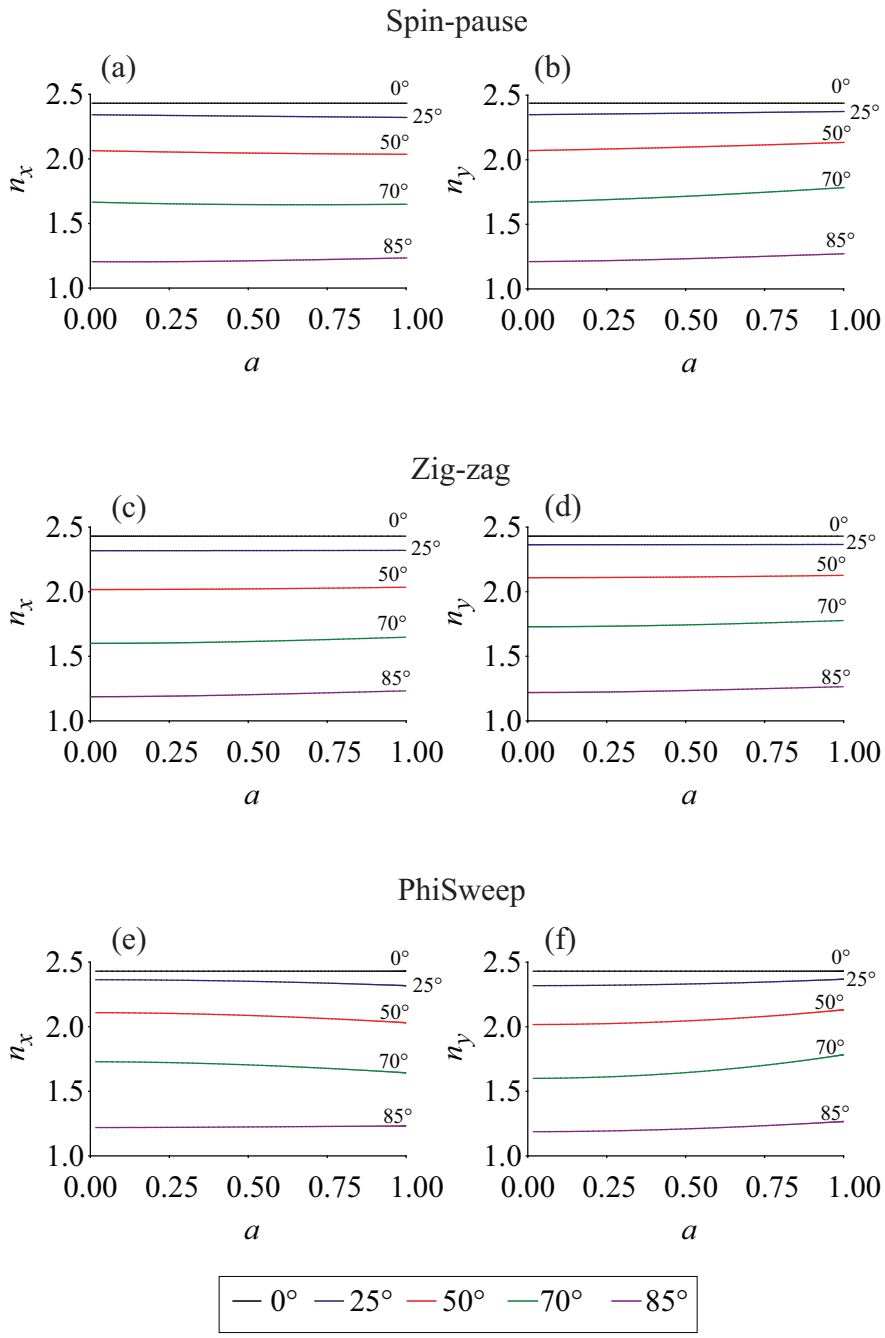

Figure 3.10: In-plane indices, n_x and n_y as functions of a, for $\alpha = 0°, 25°, 50°, 70°$ and $85°$. (a) and (b) Spin-pause; (c) and (d) Zig-zag; (e) and (f) PhiSweep

values. This is unsurprising, since we know that α directly controls the density of the film, which in turn controls the average index of the film. This ultimately controls the relative size of the individual refractive indices. It is also difficult to see in the Figure, but the curvature of the individual index profiles is affected slightly by α. Films with α corresponding to larger values of $\Delta n_{\max}$ exhibit greater variability with a then those with smaller $\Delta n_{\max}$. Thus, if one desires greater index variability for a constant α, one should choose a deposition angle corresponding to the maximum in $\Delta n_{\max}$, typically around 70°. On the other hand, if one desires small variability in index at a constant deposition angle, one should seek to deposit as far away from the above maximum as possible.

Figure 3.11 shows the predicted Δn for the three film structures as functions of a, for the same range of deposition angles as above. The in-plane birefringence is given by equation (3.10), which states that $\Delta n = -\bar{b}^2 \Delta n_{\max}$. Since $\bar{b}$ is independent of deposition angle, the only place α enters the relationship is through $\Delta n_{\max}$. As a result, the functional form of Δn for a given film algorithm is the same regardless of deposition angle, up to the $\Delta n_{\max}$ scale factor. As a result, we see clearly that the in-plane birefringence peaks when $\Delta n_{\max}$ is a maximum at $\alpha = 70°$. One important consequence of this fact is that in the PhiSweep case, for a given material, the value of a (or the corresponding value of $\phi_0 = \phi_0'$) at which $\Delta n = 0$ is expected to be independent of α. This means that one should not expect to be able to adjust the location of ϕ_0' for a particular material by a simple change in deposition angle.

Though the point at which the in-plane birefringence vanishes in the PhiSweep case is independent of α, this is not true of the point at which $n_{x'} = n_{y'}$, where the film behaves uniaxially. Figure 3.12 shows the difference, $n_{y'} - n_{x'}$ for PhiSweep films as a function of a for a range of deposition angles. In this case, we see that the uniaxial point occurs at smaller values of a for increasing values of α. Since smaller values of a imply larger values of ϕ_0, we find that as the deposition angle increases, the uniaxial point moves along the PhiSweep spectrum from the pure slanted post extreme toward the SBD extreme. Smaller values of a tend to imply smaller values of β' as well, but this is only true at constant α. If one computes β' at which one obtains uniaxial behaviour, one obtains the result shown in Figure 3.13. We see that despite the lessening values of a, the column tilt at the uniaxial point actually increases with α, up until the highest deposition angles, where it plateaus around 25°, before decreasing

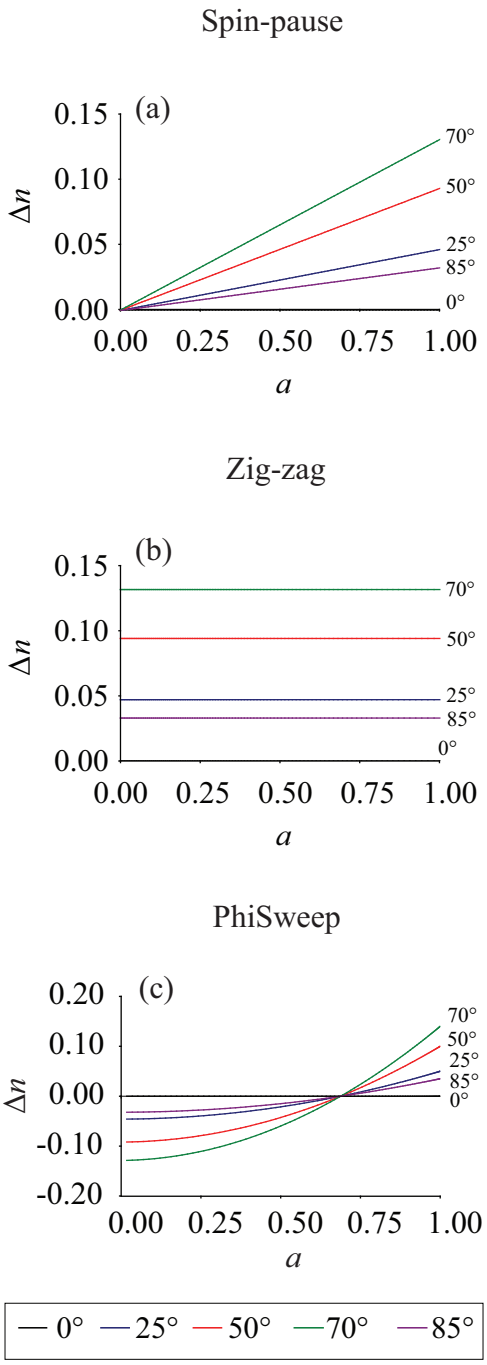

Figure 3.11: In-plane birefringence, Δn as a function of a, for $\alpha = 0°, 25°, 50°, 70°$ and $85°$. (a) Spin-pause; (b) Zig-zag; (c) PhiSweep

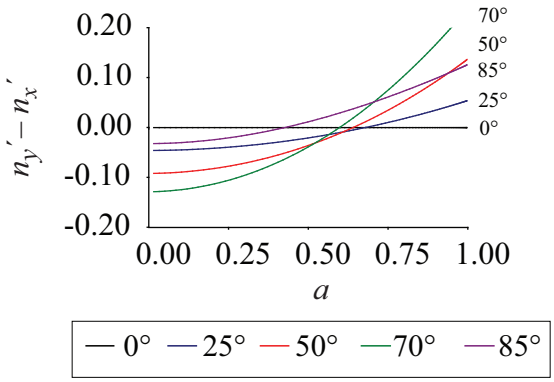

Figure 3.12: The difference, $n_{y'} - n_{x'}$, for PhiSweep films as a function of a, for $\alpha = 0°, 25°, 50°, 70°$ and $85°$.

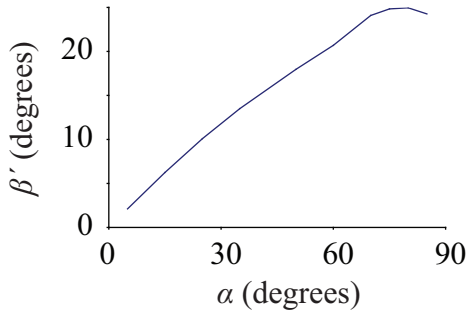

Figure 3.13: The column tilt of TiO_2, β', PhiSweep films at which uniaxial behaviour is obtained as a function of α

slightly as $\alpha \rightarrow 90^\circ$. This behaviour arises because in the case of TiO_2, the tendency of the column tilt to increase with α outweighs the tendency of the column tilt to decrease with decreasing a. This behaviour is expected to be material specific, in general.

We can also examine the effect of material parameters on the modeled results. In particular, changing the column tilt parameter, E, yields fairly interesting results. Figure 3.14 shows the behaviour of the principal indices as a function of a for the three film structures as E takes on the values $0.1, 0.3, 0.8$ and 1.6. The results are shown for $\alpha = 70^\circ$ and 85°. The values of E imply column tilts of $55.5^\circ, 45.9^\circ, 30.9^\circ$ and 19.6° at $\alpha = 70^\circ$ and column tilts of $74.3^\circ, 59.9^\circ, 37.0^\circ$ and 27.5° at $\alpha = 85^\circ$. We first note that $n_{z'}$ is constant as E changes, which is expected behaviour. We also find as E decreases, implying that the natural column tilt is increasing, that the variation between $n_{x'}$ and $n_{y'}$ increases significantly. This is true for every film structure, and the relative effect is more apparent at both larger a and larger α. These results strongly support the idea that in order to promote greater anisotropy between the principal indices of a film, one should endeavor to increase the natural column angle of the film as much as possible, perhaps through controlling the substrate temperature or deposition pressure [82] or by employing ion-assisted deposition [83].

We also see from Figure 3.14(e) and (f) that when one changes E, the value of a, or ϕ_0, at which one obtains uniaxial behaviour moves. As E decreases, the uniaxial point moves to lower values of a, which might initially suggest that the uniaxial point occurs at a lower β'. However, if we actually compute the column tilt angle of the uniaxial structure, one obtains the results shown in Figure 3.15. We observe two interesting facts. The first is that despite the uniaxial point moving to smaller a with decreasing E, one still expects that the column tilt of the uniaxial structure is larger. This means that it is a viable option to obtain a uniaxial film with a higher column tilt by decreasing E. Secondly, we see that the effect seems relatively independent of α, as the results obtained at $\alpha = 70^\circ$ and at $\alpha = 85^\circ$ appear to be nearly identical.

3.6 Conclusions

This chapter has tabulated the principal refractive indices for a number of TiO_2 and SiO_2 films made using a variety of advanced GLAD algorithms and out-

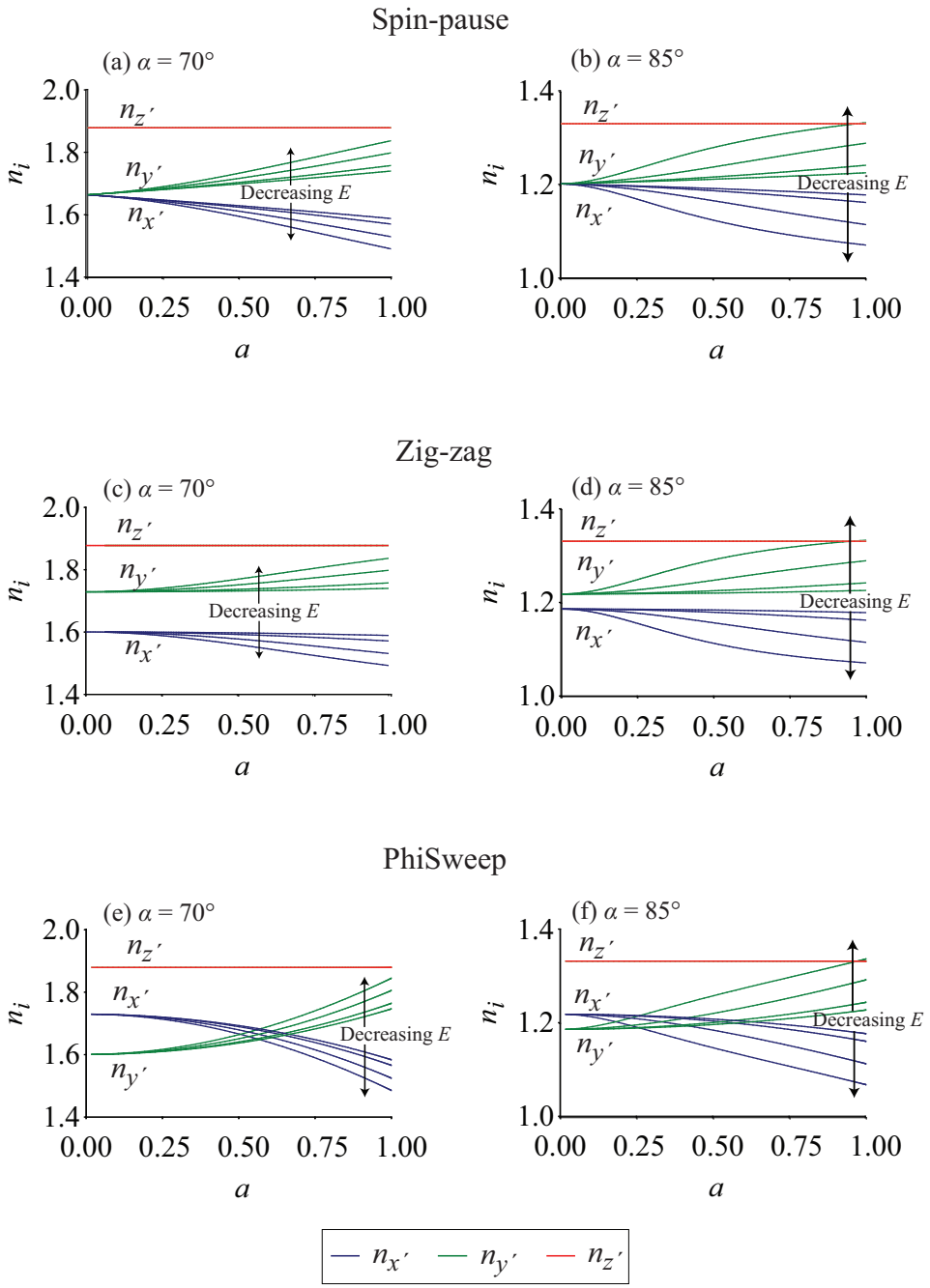

Figure 3.14: The behaviour of $n_{x'}, n_{y'}$ and $n_{z'}$ as functions of a, for $E = 0.1, 0.3, 0.8$ and 1.6. (a) Spin-pause, $\alpha = 70°$; (b) Spin-pause, $\alpha = 85°$; (c) Zig-zag, $\alpha = 70°$; (d) Zig-zag, $\alpha = 85°$; (e) PhiSweep, $\alpha = 70°$; (f) PhiSweep, $\alpha = 85°$;

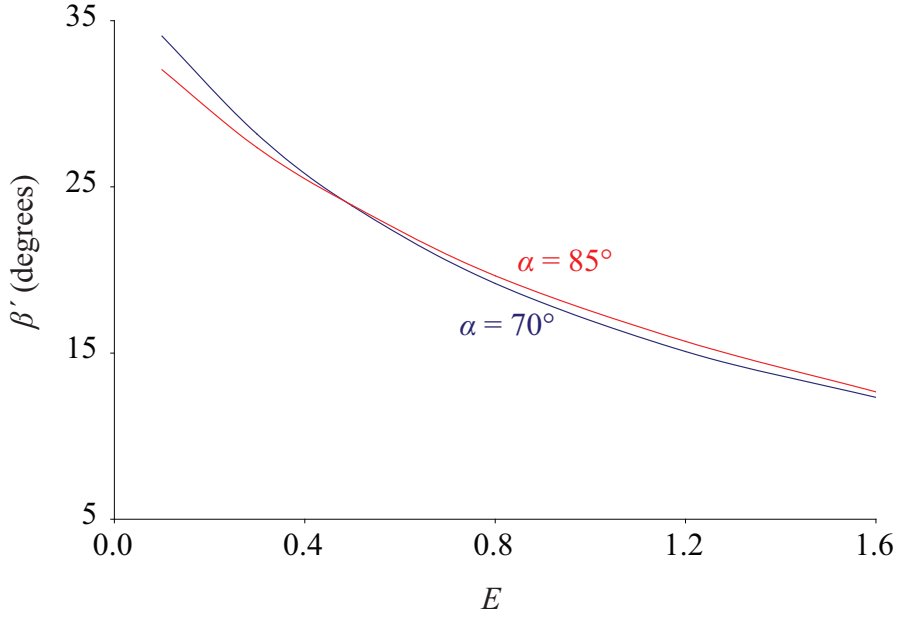

Figure 3.15: Column tilt angle, β', at which uniaxial behaviour is obtained in PhiSweep films as a function of E, for $\alpha = 70°$ and $\alpha = 85°$

lined a model that can accurately predict the refractive indices for any arbitrary film material and structure. This echoes the message from the previous chapter, that advocated the utility of simple models which can be applied in a wide range of scenarios. For a particular algorithm and deposition angle, the model requires only four commonly tabulated empirical data points:

1. The film material's refractive index at normal incidence, N;

2. The in-plane birefringence, $\Delta n_{\max}$ of a slanted post;

3. The column tilt, β;

4. The fractional density, $\bar{\varrho}$.

Items 3) and 4), as noted in the previous chapter, are very important for properly characterizing a film, and ideally one should know these values prior to doing extensive work on any particular material. These variables are often known as functions of α, and many authors have provided a variety of formula

to calculate them. [11, 13, 43] The use of this model and the tabulated values are intended for aiding researchers predict and design GLAD films for the purposes of anisotropic optical filter design, as will be illustrated in the following chapter.

This chapter also predicted and experimentally demonstrated several interesting possibilities, including the fabrication of samples with negative in-plane birefringence as well as the fabrication of uniaxial samples with non-zero column tilt. Both of these results were accomplished using the PhiSweep algorithm, which can suppress broadening normal to the columnar growth direction. These features are rare in metal-oxide films fabricated using GLAD, but their existence was correctly predicted by the simple model presented here. This clearly demonstrates the utility of our model in predicting unique optical behaviour in GLAD films and reinforces the idea that one can learn a tremendous amount about a system, given knowledge of even the most basic rules that govern it. The results of this chapter build upon the significant contributions of prior researchers in understanding the optical behaviour of GLAD films, and will hopefully contribute to the design of useful optical devices, as outlined in the next chapter.

Chapter 4

Linear Polarization Filters

"Science progresses best when observations force us to alter our preconceptions" – Vera Rubin

4.1 Introduction

The work presented in this chapter concerns the fabrication of non-absorbing, normal-incidence reflective linear polarizers made using GLAD. Fabricating a thin-film polarizer for use at normal incidence is non-trivial, and the ability to make it non-absorbing is important for high-power laser applications, where absorbing polarizers could be damaged by excess heat. This work was inspired largely in part by previous work on GLAD films concerning helical films exhibiting circular polarization selectivity [58,74,85] and also builds off a number of other related studies that examined the use of GLAD films in optical filter design. These latter studies include linear polarization filters made from serially bideposited films [86] as well as one- and three-dimensional photonic crystal devices [70,71] that exploit the variable density and geometry of GLAD films. The major innovation of the work presented here is to demonstrate a film structure that exhibits linear polarization selectivity in a directly analogous way to the circular polarization selectivity exhibited by helical films. This

[4.0] A version of this chapter has been published. V. Leontyev *et al.*, Journal of Applied Physics, 104, 104302 (2008) [67] and N. Wakefield *et al.*, Journal of the Optical Society of America A, 28, 1830 (2011) [84]

means that the final film structure is composed of a single material, and that the columnar structure is retained throughout the film, which is relevant to liquid crystal alignment, to be discussed in Chapter 5. Finally, optical filter design in this chapter is accomplished by applying the results of the model presented in the previous chapter to real-world film structures.

We begin this chapter with a brief discussion of the fabrication of these films, and relate their optical properties to the results of the previous chapter, using a 4×4 matrix method to simulate optical transmittance. From there, the discussion turns to the design of linear polarization filters, which, similar to the origin of GLAD-based circular polarization filters, are inspired by their own liquid crystal phase, which we will learn about in much greater detail in the following chapter.

4.2 Helical Films and Circular Polarizers

4.2.1 Film Structures

GLAD films exhibiting circular polarization selectivity come in two distinct forms. The first type is a helical structure, as shown in Figure 4.5. A GLAD

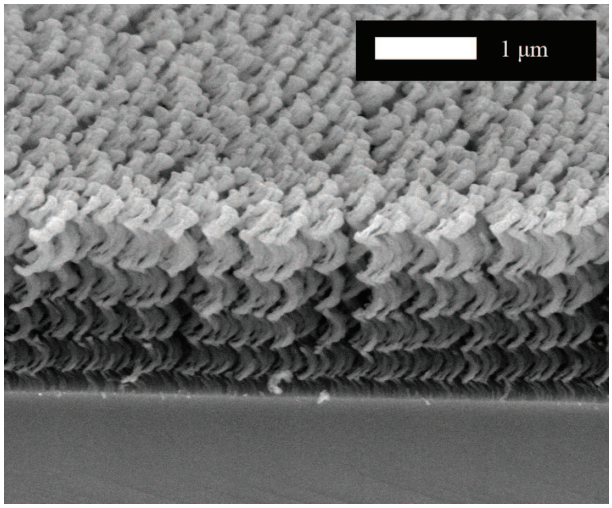

Figure 4.1: Helical GLAD film (SiO_2)

helix is fabricated in the exact same way as a vertical post, as described in

Chapter 2:

$$\phi = \frac{2\pi T_{O'}}{p_{\text{helix}}}, \tag{4.1}$$

except that in the helical case, p_{helix} is much larger than the pitch in the vertical post case. Typical values are anywhere from 100 to 1000 nm. Locally, one can envision the dielectric tensor as that of a slanted post. The principal axes, however, rotate through the thickness of the film. We recall from equation (3.1) that we can express the dielectric tensor in any frame given the principal dielectric tensor and the rotation matrix from the substrate frame to the principal frame, provided in equation (3.2). For a helix, we assume that the principal dielectric tensor is constant, and that the column tilt angle of the helix is constant with film thickness equal to the tilt of a pure slanted post ($\beta'(z) = \beta$). The angle ξ', however, is a function of z. In general, ξ' at an arbitrary point on a substrate can be calculated using the methods of Chapter 2. However, we can easily compute ξ' at the substrate center. We know that the orientation angle, ξ, is zero at the substrate center from equation (2.14). Then, equation (2.41) tells us that $\xi' = -\phi$ for $z - z_s < z < z_s + T^{\text{total}}$. We can understand this result by examining the helical trajectory as shown in Figure 4.2. Notice that the helix

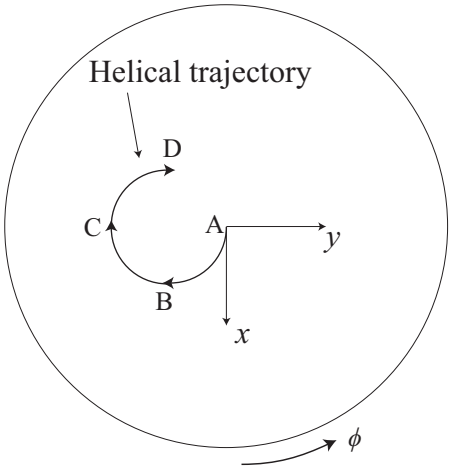

Figure 4.2: Trajectory for a helical GLAD film

rotates in the opposite sense as the substrate rotation which is why ξ' has the opposite sign as ϕ. If the helical pitch is positive, so that $\phi > 0$ and $\xi' < 0$, as shown in Figure 4.2, then the helix is left-handed. Conversely, if the pitch is negative, then the helix is right-handed. If we assume that the helix has a

constant tilt angle, β, and that the initial segment of the helix is a slanted post in the xz-plane of the substrate, then the rotation matrix from the substrate coordinate system (x, y, z) to the principal coordinate system (x', y', z') is:

$$R = \begin{pmatrix} C_{\beta'} & 0 & S_{\beta'} \\ 0 & 1 & 0 \\ -S_{\beta'} & 0 & C_{\beta'} \end{pmatrix} \begin{pmatrix} C_\phi & -S_\phi & 0 \\ S_\phi & C_\phi & 0 \\ 0 & 0 & 1 \end{pmatrix}. \tag{4.2}$$

If one carries out the matrix multiplication to obtain the relative dielectric tensor, ϵ, in the substrate frame, one obtains:

$$\epsilon = \begin{pmatrix} C_\phi^2 C_\beta^2 n_{x'}^2 + C_\beta S_\phi^2 n_{y'}^2 + S_\beta^2 C_\phi^2 n_{z'}^2 & C_\phi S_\phi C_\beta n_{x'}^2 - C_\phi S_\phi n_{y'}^2 & \\ C_\beta^2 C_\phi S_\phi n_{x'}^2 - C_\beta C_\phi S_\phi n_{y'}^2 + S_\beta^2 S_\phi n_{z'}^2 & S_\phi^2 C_\beta n_{x'}^2 + C_\phi^2 n_{y'}^2 & \cdots \\ -S_\beta C_\phi C_\beta n_{x'}^2 - C_\beta S_\beta n_{z'}^2 & -S_\beta S_\phi n_{x'}^2 & \end{pmatrix}$$
$$\begin{pmatrix} -C_\phi^2 S_\beta C_\beta n_{x'}^2 - S_\beta S_\phi^2 n_{y'}^2 + S_\beta C_\beta n_{z'}^2 \\ \cdots \quad -S_\beta C_\phi C_\beta S_\phi n_{x'}^2 + S_\beta S_\phi C_\phi n_{y'}^2 + S_\beta S_\phi C_\beta n_{z'}^2 \\ -S_\beta^2 C_\phi n_{x'}^2 + C_\beta^2 n_{z'}^2 \end{pmatrix}. \tag{4.3}$$

The relative dielectric tensor is seen to vary as a function of film thickness, since ϕ is a function of thickness given equation (4.1). It does not vary in the plane of the film, so the film comprises what is known as a stratified medium. In practice, it is often more practical to specify the principal indices and the rotation angles of the principal axes, and use a computer to calculate the resultant tensor.

The second type of circularly selective film is a twisted ribbon [87]. This type of structure is essentially an SBD structure, as discussed in Chapters 2 and 3, that twists about the z-axis. Normally an SBD structure is achieved by repeatedly modulating ϕ between 0 and π. To form a twisted ribbon, during the nth modulation, the structure instead modulates between $0 + \phi_n$ and $\pi + \phi_n$, where $\phi_n = \frac{2\pi(n-1)p_{\text{SBD}}}{p_{\text{ribbon}}}$, where p_{SBD} is much less than p_{ribbon}. For an SBD, ξ' at the substrate center is undefined, but one can find a suitable value by calculating ξ' for zig-zag films, and taking the limit as the zig-zag becomes an SBD structure. One finds that in this case $\xi' = -\phi$, just as with the helical structure, so structures with $\phi > 0$ (positive pitch) are left-handed, while structures with $\phi < 0$ (negative pitch) are right-handed. We also know for an SBD

at the substrate center that $\beta' = 0$ so we find that a twisted ribbon acts like a helical film, with opposite handedness and zero column tilt. One can then find the dielectric tensor in the substrate coordinates by making the substitutions $\beta' \to 0$ and $\xi' \to -\phi$:

$$\epsilon = \begin{pmatrix} C_\phi^2 n_{x'}^2 + S_\phi^2 n_{y'}^2 & -C_\phi S_\phi (n_{x'}^2 - n_{y'}^2) & 0 \\ -C_\phi S_\phi (n_{x'}^2 - n_{y'}^2) & S_\phi^2 n_{x'}^2 + C_\phi^2 n_{y'}^2 & 0 \\ 0 & 0 & n_{z'}^2 \end{pmatrix}, \tag{4.4}$$

$$= \begin{pmatrix} \frac{1}{2}(n_{x'}^2 + n_{y'}^2) + \frac{1}{2}(n_{x'}^2 - n_{y'}^2) C_{2\phi} & S_{2\phi}(n_{y'}^2 - n_{x'}^2) & 0 \\ S_{2\phi}(n_{y'}^2 - n_{x'}^2) & \frac{1}{2}(n_{x'}^2 + n_{y'}^2) + \frac{1}{2}(n_{y'}^2 - n_{x'}^2) C_{2\phi} & 0 \\ 0 & 0 & n_{z'}^2 \end{pmatrix} \tag{4.5}$$

4.2.2 Berreman Calculus

In order to determine the transmission of light through an anisotropic, stratified medium, one can use the method outlined by Berreman [88]. Berreman used a 4×4 matrix approach as opposed to the commonly encountered 2×2 matrix method put forth by Born and Wolf [89], that applies only to isotropic, stratified materials. In the Berreman approach, and assuming an $e^{-i\omega t}$ harmonic time-dependence, we write Faraday's law and Ampere's law in matrix form as:

$$\begin{pmatrix} 0 & 0 & 0 & 0 & -\frac{\partial}{\partial z} & \frac{\partial}{\partial y} \\ 0 & 0 & 0 & \frac{\partial}{\partial z} & 0 & -\frac{\partial}{\partial x} \\ 0 & 0 & 0 & -\frac{\partial}{\partial y} & \frac{\partial}{\partial x} & 0 \\ 0 & \frac{\partial}{\partial z} & -\frac{\partial}{\partial y} & 0 & 0 & 0 \\ -\frac{\partial}{\partial z} & 0 & \frac{\partial}{\partial x} & 0 & 0 & 0 \\ \frac{\partial}{\partial y} & -\frac{\partial}{\partial x} & 0 & 0 & 0 & 0 \end{pmatrix} \begin{pmatrix} E_x \\ E_y \\ E_z \\ H_x \\ H_y \\ H_z \end{pmatrix} = -i\omega \begin{pmatrix} D_x \\ D_y \\ D_z \\ B_x \\ B_y \\ B_z \end{pmatrix}$$

$$L\mathbf{G} = -i\omega\mathbf{C}, \tag{4.6}$$

where the last line implicitly defines the matrix, L, and the vectors $\mathbf{G}$ and $\mathbf{C}$. The vectors $\mathbf{G}$ and $\mathbf{C}$ are related through the constitutive relations. If we take linear, non-magnetic materials, with no coupling between $\mathbf{D}$ and $\mathbf{H}$ or $\mathbf{E}$ and $\mathbf{B}$,

we have:

$$\begin{pmatrix} D_x \\ D_y \\ D_z \\ B_x \\ B_y \\ B_z \end{pmatrix} = \begin{pmatrix} \epsilon_0\epsilon_{xx} & \epsilon_0\epsilon_{xy} & \epsilon_0\epsilon_{xz} & 0 & 0 & 0 \\ \epsilon_0\epsilon_{yx} & \epsilon_0\epsilon_{yy} & \epsilon_0\epsilon_{yz} & 0 & 0 & 0 \\ \epsilon_0\epsilon_{zx} & \epsilon_0\epsilon_{zy} & \epsilon_0\epsilon_{zz} & 0 & 0 & 0 \\ 0 & 0 & 0 & \mu_0 & 0 & 0 \\ 0 & 0 & 0 & 0 & \mu_0 & 0 \\ 0 & 0 & 0 & 0 & 0 & \mu_0 \end{pmatrix} \begin{pmatrix} E_x \\ E_y \\ E_z \\ H_x \\ H_y \\ H_z \end{pmatrix}$$

$$\mathbf{C} = M\mathbf{G}. \tag{4.7}$$

The upper-left quadrant of $M$is simply ϵ_0 times the dielectric tensor, while the bottom right quadrant is μ_0 times the identity matrix.

If one assumes, as Berreman did, propagation in the xz-plane, then our waves have the form $e^{i(k_x x + k_z z)}$, where k_x is constant and k_z is a function of thickness. The partial derivatives $\partial/\partial y$ and $\partial/\partial x$ then become 0 and ik_x respectively. Substituting equation (4.7) into equation (4.6) gives:

$$\begin{pmatrix} 0 & 0 & 0 & 0 & -\frac{\partial}{\partial z} & 0 \\ 0 & 0 & 0 & \frac{\partial}{\partial z} & 0 & -ik_x \\ 0 & 0 & 0 & 0 & ik_x & 0 \\ 0 & \frac{\partial}{\partial z} & 0 & 0 & 0 & 0 \\ -\frac{\partial}{\partial z} & 0 & ik_x & 0 & 0 & 0 \\ 0 & -ik_x & 0 & 0 & 0 & 0 \end{pmatrix} \begin{pmatrix} E_x \\ E_y \\ E_z \\ H_x \\ H_y \\ H_z \end{pmatrix} =$$

$$-i\omega \begin{pmatrix} \epsilon_0\epsilon_{xx} & \epsilon_0\epsilon_{xy} & \epsilon_0\epsilon_{xz} & 0 & 0 & 0 \\ \epsilon_0\epsilon_{yx} & \epsilon_0\epsilon_{yy} & \epsilon_0\epsilon_{yz} & 0 & 0 & 0 \\ \epsilon_0\epsilon_{zx} & \epsilon_0\epsilon_{zy} & \epsilon_0\epsilon_{zz} & 0 & 0 & 0 \\ 0 & 0 & 0 & \mu_0 & 0 & 0 \\ 0 & 0 & 0 & 0 & \mu_0 & 0 \\ 0 & 0 & 0 & 0 & 0 & \mu_0 \end{pmatrix} \begin{pmatrix} E_x \\ E_y \\ E_z \\ H_x \\ H_y \\ H_z \end{pmatrix} \tag{4.8}$$

Expanding the equations out gives two algebraic equations:

$$ik_x H_y = -i\epsilon_0\omega(\epsilon_{zx}E_x + \epsilon_{zy}E_y + \epsilon_{zz}E_z) \tag{4.9}$$

$$k_x E_y = \omega\mu_0 H_z. \tag{4.10}$$

These can be solved to isolate E_z and H_z:

$$E_z = -\frac{k_x}{\epsilon_0 \epsilon_{zz} \omega} H_y - \frac{\epsilon_{zx}}{\epsilon_{zz}} E_x - \frac{\epsilon_{zy}}{\epsilon_{zz}} E_y, \tag{4.11}$$

$$H_z = \frac{k_x}{\omega \mu_0} E_y. \tag{4.12}$$

Equation (4.8) also provides four differential equations:

$$-\frac{\partial H_y}{\partial z} = -i\omega\epsilon_0(\epsilon_{xx}E_x + \epsilon_{xy}E_y + \epsilon_{xz}E_z), \tag{4.13}$$

$$\frac{\partial H_x}{\partial z} - ik_x H_z = -i\omega\epsilon_0(\epsilon_{yx}E_x + \epsilon_{yy}E_y + \epsilon_{yz}E_z), \tag{4.14}$$

$$\frac{\partial E_y}{\partial z} = -i\omega\mu_0 H_x, \tag{4.15}$$

$$-\frac{\partial E_x}{\partial z} + ik_x E_z = -i\omega\mu_0 H_y. \tag{4.16}$$

Isolating the derivatives on the left-hand side and using equations (4.11) and (4.12) to eliminate E_z and H_z gives:

$$\begin{aligned}
\frac{\partial E_x}{\partial z} &= i\omega\epsilon_0 \left(-\frac{k_x \epsilon_{zx}}{\omega \epsilon_0 \epsilon_{zz}} E_x - \frac{k_x \epsilon_{zy}}{\omega \epsilon_0 \epsilon_{zz}} E_y + \left(\frac{1}{\epsilon_0 c} - \frac{k_x^2}{\omega^2 \epsilon_0^2 \mu_0 c \epsilon_{zz}} \right) \mu_0 c H_y \right), \\
&= i\omega\epsilon_0(\Delta_{11}E_x + \Delta_{12}\mu_0 c H_y + \Delta_{13}E_y + \Delta_{14}\mu_0 c H_x). \qquad (4.17) \\
\frac{\partial(\mu_0 c H_y)}{\partial z} &= i\omega\epsilon_0 \left(\mu_0 c \left(\epsilon_{xx} - \frac{\epsilon_{xz}\epsilon_{zx}}{\epsilon_{zz}} \right) E_x + \mu_0 c \left(\epsilon_{xy} - \frac{\epsilon_{xz}\epsilon_{zy}}{\epsilon_{zz}} \right) E_y \cdots \right. \\
&\qquad \left. - \frac{k_x \epsilon_{xz}}{\epsilon_0 \epsilon_{zz} \omega} \mu_0 c H_y \right), \\
&= i\omega\epsilon_0(\Delta_{21}E_x + \Delta_{22}\mu_0 c H_y + \Delta_{23}E_y + \Delta_{24}\mu_0 c H_x). \qquad (4.18) \\
\frac{\partial E_y}{\partial z} &= -i\omega\epsilon_0 \left(\frac{1}{\epsilon_0 c} (\mu_0 c H_x) \right), \\
&= i\omega\epsilon_0(\Delta_{31}E_x + \Delta_{32}\mu_0 c H_y + \Delta_{33}E_y + \Delta_{34}\mu_0 c H_x). \qquad (4.19) \\
-\frac{\partial(\mu_0 c H_x)}{\partial z} &= -i\omega\epsilon_0 \left(\mu_0 c \left(\epsilon_{yx} - \frac{\epsilon_{yz}\epsilon_{zx}}{\epsilon_{zz}} \right) E_x + \mu_0 c \left(\epsilon_{yy} - \frac{\epsilon_{yz}\epsilon_{zy}}{\epsilon_{zz}} - \frac{k_x^2}{\omega^2 \epsilon_0 \mu_0} \right) E_y \right. \\
&\qquad \left. - \frac{k_x \epsilon_{yz}}{\omega \epsilon_0 \epsilon_{zz}} \mu_0 c H_y \right), \\
&= i\omega\epsilon_0(\Delta_{41}E_x + \Delta_{42}\mu_0 c H_y + \Delta_{43}E_y + \Delta_{44}\mu_0 c H_x). \qquad (4.20)
\end{aligned}$$

This can be rewritten in matrix form:

$$\frac{\partial}{\partial z}\begin{pmatrix} E_x \\ \mu_0 c H_y \\ E_y \\ \mu_0 c H_x \end{pmatrix} = i\omega\epsilon_0 \begin{pmatrix} \Delta_{11} & \Delta_{12} & \Delta_{13} & \Delta_{14} \\ \Delta_{21} & \Delta_{22} & \Delta_{23} & \Delta_{24} \\ \Delta_{31} & \Delta_{32} & \Delta_{33} & \Delta_{34} \\ \Delta_{41} & \Delta_{42} & \Delta_{43} & \Delta_{44} \end{pmatrix} \begin{pmatrix} E_x \\ \mu_0 c H_y \\ E_y \\ \mu_0 c H_x \end{pmatrix},$$

$$\frac{\partial}{\partial z}\mathbf{x} = i\omega\epsilon_0 \Delta \mathbf{x}. \tag{4.21}$$

Δ is a matrix whose coefficients are given implicitly above, and we want to use this equation to determine the electric and magnetic fields contained in $\mathbf{x}$. We scale the magnetic fields by $\mu_0 c$ so that the numerical values of the vector $\mathbf{x}$ are of the same magnitude. This ensures that the components of Δ are also of the same magnitude, which is important for computational purposes. The solution for $\mathbf{x}$ is an exponential. Since we are usually given the incident fields at the top of the film ($z = z_s + T^{\text{total}}$), we can write:

$$\mathbf{x}(z) = e^{i\omega\epsilon_0(z - z_s - T^{\text{total}})\Delta(z)}\mathbf{x}(z_s + T^{\text{total}}). \tag{4.22}$$

This equation tells us how to transform from the fields at the top of the film to the fields at any point z inside the film. If we seek the fields at the bottom of the film ($z = z_s$) in particular, we find:

$$\mathbf{x}(z_s) = e^{-i\omega\epsilon_0 T^{\text{total}}\Delta(z_s)}\mathbf{x}(z_s + T^{\text{total}}) \equiv Q\mathbf{x}(z_s + T^{\text{total}}). \tag{4.23}$$

The matrix Q transforms the fields from their value at the top of the film to their value at the bottom of the film. Computing Q directly is often difficult, and an indirect approach is often necessary. We begin by finding the value of $\mathbf{x}$ at $z - dz$. If we assume that Δ is approximately constant on $[z - dz, z]$, then:

$$\begin{aligned} \mathbf{x}(z - dz) &= e^{i\omega\epsilon_0(z - dz - z_s - T^{\text{total}})\Delta(z)}\mathbf{x}(z_s + T^{\text{total}}) \\ &= e^{-i\omega\epsilon_0 dz\Delta(z)}\mathbf{x}(z). \end{aligned} \tag{4.24}$$

To second order, we can expand the exponential to obtain:

$$\mathbf{x}(z - dz) = \left(I - i\omega\epsilon_0 dz\Delta(z) - \frac{\omega^2\epsilon_0^2 dz^2\Delta^2(z)}{2}\right)\mathbf{x}(z) \equiv P(z, -dz)\mathbf{x}(z), \tag{4.25}$$

where I is the identity matrix and $P(z, -dz)$ is a transfer matrix that takes known field values at z and generates field values at $z - dz$. Therefore, given the fields at $z = z_s + T^{\text{total}}$, one can find the fields at $z = z_s$ by successive applications of P. If the differential thicknesses, dz, are taken to be identical:

$$\begin{aligned}\mathbf{x}(z_s) &= P(z_s + dz, dz)...P(z_s + T^{\text{total}} - dz, dz)P(z_s + T^{\text{total}}, -dz)\mathbf{x}(z_s + T^{\text{total}}) \\ &\equiv Q\mathbf{x}(z_s + T^{\text{total}}),\end{aligned} \tag{4.26}$$

and we have found a method to calculate Q. Berreman indicates that a first order approximation to P does not converge to the actual value of P, no matter how small dz is, and this is why we took a second order approximation earlier. We can now use Q to determine the reflectance and transmittance of light incident on our film.

As mentioned earlier, we presume light incident in the xz-plane, as shown in Figure 4.3. We consider light incident from an isotropic medium, with index, n_1, and exiting the film into another isotropic medium of index, n_2. The field at the top of the film ($z = 0$) is equal to the sum of an incident wave plus a reflected wave. The field at the end of the film, $z = T^{\text{total}}$ is equal to the field of the transmitted wave.

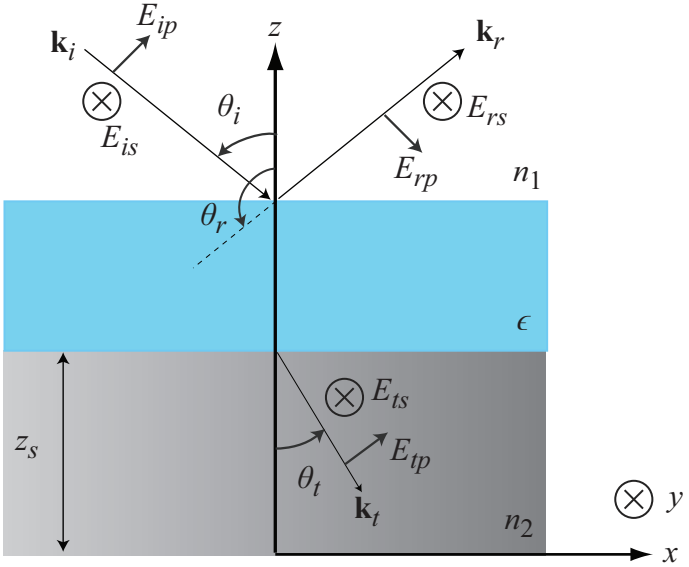

Figure 4.3: Schematic of light incident on an anisotropic, stratified medium

The incident wave has wavevector $\mathbf{k}_i = k_i(\sin\theta_i\hat{\mathbf{x}} - \cos\theta_i\hat{\mathbf{z}})$and can be polar-

ized such either that the electric field or the magnetic field is along the y-axis. These are known as transverse electric or s-polarized and transverse magnetic or p-polarized states, respectively. At normal incidence, these reduce in turn polarization along the y-axis and the x-axis. In the transverse electric case, we then have:

$$\mathbf{E}_i = E_{iy}\hat{\mathbf{y}} \tag{4.27}$$

$$\begin{aligned}\mu_0 c\mathbf{H}_i = c\mathbf{B}_i &= \frac{c\mathbf{k}_i \times \mathbf{E}_i}{\omega} = \frac{ck_i E_{iy}}{\omega}(\cos\theta_i\hat{\mathbf{x}} + \sin\theta_i\hat{\mathbf{z}}) \\ &= n_1 E_{iy}(\cos\theta_i\hat{\mathbf{x}} + \sin\theta_i\hat{\mathbf{z}}) = \mu_0 cH_{ix}\hat{\mathbf{x}} + \mu_0 cH_{iz}\hat{\mathbf{z}}\end{aligned} \tag{4.28}$$

where we have employed equations (1.19) and (1.21). The transverse magnetic case is the same, with the orientation of the electric and magnetic fields reversed:

$$\mathbf{E}_i = E_i(\cos\theta_i\hat{\mathbf{x}} + \sin\theta_i\hat{\mathbf{z}}) = E_{ix}\hat{\mathbf{x}} + E_{iz}\hat{\mathbf{z}} \tag{4.29}$$

$$\mu_0 c\mathbf{H}_i = -n_1 E_i\hat{\mathbf{y}} = -\frac{n_1 E_{ix}}{\cos\theta_i}\hat{\mathbf{y}} = \mu_0 cH_{iy}\hat{\mathbf{y}} \tag{4.30}$$

We see that we can choose one of E_{iy}, H_{ix} and H_{iy} freely, as well as one of E_{ix}, E_{iz} and H_{iz} freely, and the other components can be determined from these free parameters. If we choose to specify E_{ix} and E_{iy}, we find these expressions for H_{ix} and H_{iy}:

$$\mu_0 cH_{ix} = n_1 E_{iy}\cos\theta_i \tag{4.31}$$

$$\mu_0 cH_{iy} = -\frac{n_1 E_{ix}}{\cos\theta_i}. \tag{4.32}$$

The reflected wave is identical to the incident wave, except that the electric field amplitudes are now E_{rx} and E_{ry}, and the $\mathbf{z}$ component of the wavevector is reversed, which can be achieved by replacing θ_i by $\theta_r = \pi - \theta_i$. This yields:

$$\mu_0 cH_{rx} = -n_1 E_{ry}\cos\theta_i \tag{4.33}$$

$$\mu_0 cH_{ry} = \frac{n_1 E_{rx}}{\cos\theta_i}. \tag{4.34}$$

The transmitted wave is also identical to the incident wave, but with electric field amplitudes E_{tx} and E_{ty}. One must also replace θ_i by θ_t, which can be

obtained by Snell's law:

$$n_1 \sin\theta_i = n_2 \sin\theta_t. \tag{4.35}$$

For the transmitted magnetic fields we obtain:

$$\mu_0 c H_{tx} = n_2 E_{ry} \cos\theta_t \tag{4.36}$$

$$\mu_0 c H_{ty} = -\frac{n_2 E_{rx}}{\cos\theta_t}. \tag{4.37}$$

Finally then, we have expressions for the incident and exiting waves:

$$\mathbf{x}(z_s + T^{\text{total}}) = \begin{pmatrix} E_{ix} + E_{rx} \\ \mu_0 c(H_{iy} + H_{ry}) \\ E_{iy} + E_{ry} \\ \mu_0 c(H_{ix} + H_{rx}) \end{pmatrix} = \begin{pmatrix} E_{ix} + E_{rx} \\ -\frac{n_1}{\cos\theta_i}(E_{ix} - E_{rx}) \\ E_{iy} + E_{ry} \\ n_1 \cos\theta_i (E_{iy} - E_{ry}) \end{pmatrix} \tag{4.38}$$

$$\mathbf{x}(z_s) = \begin{pmatrix} E_{tx} \\ \mu_0 c H_{ty} \\ E_{ty} \\ \mu_0 c H_{tx} \end{pmatrix} = \begin{pmatrix} E_{tx} \\ -\frac{n_2 E_{tx}}{\cos\theta_t} \\ E_{ty} \\ n_2 E_{ty} \cos\theta_t \end{pmatrix}. \tag{4.39}$$

These are connected via the matrix, Q, through equation (4.26). We can rewrite that equation as $\mathbf{x}(z_s + T^{\text{total}}) = Q^{-1}\mathbf{x}(z_s)$ and expand in terms of the components to obtain:

$$\begin{aligned} E_{ix} &= \left(Q_{11}^{-1} - Q_{12}^{-1}\frac{n_2}{\cos\theta_t}\right) E_{tx} \\ &\quad + \left(Q_{13}^{-1} + Q_{14}^{-1} n_2 \cos\theta_t\right) E_{ty} - E_{rx} \end{aligned} \tag{4.40}$$

$$\begin{aligned} -\frac{E_{ix} n_1}{\cos\theta_i} &= \left(Q_{21}^{-1} - Q_{22}^{-1}\frac{n_2}{\cos\theta_t}\right) E_{tx} \\ &\quad + \left(Q_{23}^{-1} + Q_{24}^{-1} n_2 \cos\theta_t\right) E_{ty} - \frac{E_{rx} n_1}{\cos\theta_i} \end{aligned} \tag{4.41}$$

$$\begin{aligned} E_{iy} &= \left(Q_{31}^{-1} - Q_{32}^{-1}\frac{n_2}{\cos\theta_t}\right) E_{tx} \\ &\quad + \left(Q_{33}^{-1} + Q_{34}^{-1} n_2 \cos\theta_t\right) E_{ty} - E_{ry} \end{aligned} \tag{4.42}$$

$$\begin{aligned} E_{iy} n_1 \cos\theta_i &= \left(Q_{41}^{-1} - Q_{42}^{-1}\frac{n_2}{\cos\theta_t}\right) E_{tx} \\ &\quad + \left(Q_{43}^{-1} + Q_{44}^{-1} n_2 \cos\theta_t\right) E_{ty} + n_1 \cos\theta_i E_{ry}. \end{aligned} \tag{4.43}$$

This can be written as a matrix equation in the four unknowns, E_{rx}, E_{ry}, E_{tx} and E_{ty}, which can be inverted and solved. One can then obtain the z components of the electric fields as $E_{iz} = -E_{ix}\tan\theta_i$, $E_{rz} = E_{rx}\tan\theta_i$ and $E_{tz} = -E_{tx}\tan\theta_t$. We can then write the incident, reflected and transmitted beams in terms of their s- and p-polarized amplitudes:

$$E_{ip} = \sqrt{E_{ix}^2 + E_{iz}^2} = E_{ix}\sqrt{1+\tan^2\theta_i} = E_{ix}\sec\theta_i \tag{4.44}$$

$$E_{is} = E_{iy} \tag{4.45}$$

$$E_{rp} = \sqrt{E_{rx}^2 + E_{rz}^2} = E_{rx}\sqrt{1+\tan^2\theta_i} = E_{rx}\sec\theta_i \tag{4.46}$$

$$E_{rs} = E_{ry} \tag{4.47}$$

$$E_{tp} = \sqrt{E_{tx}^2 + E_{tz}^2} = E_{tx}\sqrt{1+\tan^2\theta_t} = E_{tx}\sec\theta_t \tag{4.48}$$

$$E_{ts} = E_{ty}. \tag{4.49}$$

The reflected and transmitted components are related to the incident components by way of the amplitude reflection and transmission coefficients, r_{ij} and t_{ij}, which are defined according to:

$$\begin{pmatrix} E_{rs} \\ E_{rp} \end{pmatrix} = \begin{pmatrix} r_{ss} & r_{sp} \\ r_{ps} & r_{pp} \end{pmatrix} \begin{pmatrix} E_{is} \\ E_{ip} \end{pmatrix} \equiv r_{\text{lin}} \begin{pmatrix} E_{is} \\ E_{ip} \end{pmatrix} \tag{4.50}$$

$$\begin{pmatrix} E_{ts} \\ E_{tp} \end{pmatrix} = \begin{pmatrix} t_{ss} & t_{sp} \\ t_{ps} & t_{pp} \end{pmatrix} \begin{pmatrix} E_{is} \\ E_{ip} \end{pmatrix} \equiv t_{\text{lin}} \begin{pmatrix} E_{is} \\ E_{ip} \end{pmatrix}, \tag{4.51}$$

where r_{lin} and $t_{\text{lin}}$are the reflection and transmission matrices for s- and p-polarized light, respectively. Note that if we have s-polarized light such that $E_{is} = 1$ and $E_{ip} = 0$, then $E_{rs} = r_{ss}$ and $E_{rp} = r_{ps}$. Similar relations hold for the transmission coefficients and for p-polarized light. We can also write expressions for incident circularly polarized light. For any beam, if $E_s = 1$, and $E_p = i$ one has right circular light, while one has left circular light if $E_s = 1$, and $E_p = -i$. We can use vectors having right and left circular components instead of s- and p-components by applying the transformation:

$$\begin{pmatrix} E_R \\ E_L \end{pmatrix} = \frac{1}{2}\begin{pmatrix} 1 & -i \\ 1 & i \end{pmatrix} \begin{pmatrix} E_s \\ E_p \end{pmatrix} \equiv C \begin{pmatrix} E_s \\ E_p \end{pmatrix}, \tag{4.52}$$

where we have defined Cas a matrix which transforms from an s- and p-

polarized representation to a right and left circularly polarized representation. We can then find the reflection and transmission matrices for circularly polarized light, r_{circ} and t_{circ}, as:

$$r_{\text{circ}} = \begin{pmatrix} r_{RR} & r_{RL} \\ r_{LR} & r_{LL} \end{pmatrix} = C r_{\text{lin}} C^{-1} \tag{4.53}$$

$$t_{\text{circ}} = \begin{pmatrix} t_{RR} & t_{RL} \\ t_{LR} & t_{LL} \end{pmatrix} = C t_{\text{lin}} C^{-1}. \tag{4.54}$$

Finally, we can compute the reflectance and transmittance coefficients, R and T. The reflectance and transmittance indicate the ratio of reflected and transmitted power to the incident power. They can be obtained from the amplitude reflection and transmission coefficients in the exact same way as is commonly seen when deriving the Fresnel coefficients between two interfaces:

$$R_{\text{lin}} = \begin{pmatrix} R_{ss} & R_{sp} \\ R_{ps} & R_{pp} \end{pmatrix} = \begin{pmatrix} |r_{ss}|^2 & |r_{sp}|^2 \\ |r_{ps}|^2 & |r_{pp}|^2 \end{pmatrix} \tag{4.55}$$

$$T_{\text{lin}} = \begin{pmatrix} T_{ss} & T_{sp} \\ T_{ps} & T_{pp} \end{pmatrix} = \frac{n_2 \cos\theta_t}{n_1 \cos\theta_i} \begin{pmatrix} |t_{ss}|^2 & |t_{sp}|^2 \\ |t_{ps}|^2 & |t_{pp}|^2 \end{pmatrix} \tag{4.56}$$

$$R_{\text{circ}} = \begin{pmatrix} R_{RR} & R_{RL} \\ R_{LR} & R_{LL} \end{pmatrix} = \begin{pmatrix} |r_{RR}|^2 & |r_{RL}|^2 \\ |r_{LR}|^2 & |r_{LL}|^2 \end{pmatrix} \tag{4.57}$$

$$T_{\text{circ}} \begin{pmatrix} T_{RR} & T_{RL} \\ T_{LR} & T_{LL} \end{pmatrix} = \frac{n_2 \cos\theta_t}{n_1 \cos\theta_i} \begin{pmatrix} |t_{RR}|^2 & |t_{RL}|^2 \\ |t_{LR}|^2 & |t_{LL}|^2 \end{pmatrix}. \tag{4.58}$$

The reflectance and transmittance coefficients must satisfy:

$$R_{ss} + R_{ps} + T_{ss} + T_{ps} = 1 \tag{4.59}$$

$$R_{sp} + R_{pp} + T_{sp} + T_{pp} = 1, \tag{4.60}$$

by conservation of energy. These are the reflectance and transmittance coefficients from an incident medium into a transmitted medium. Typically the incident medium will be air ($n_1 = 1$), and the transmitted medium will be a substrate. Usually we are interested in the transmittance from air, through the substrate, and into air again. Computing the transmittance in such a case can be done with the aid of Figure 4.4. Given an incident beam $\mathbf{S}$, with components indicating the initial power in orthogonal linear or circular components, we see

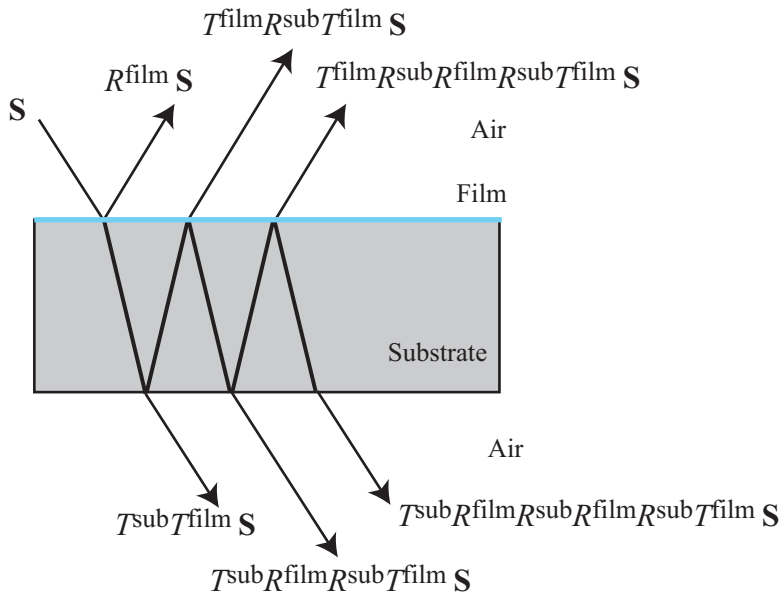

Figure 4.4: Transmittance of a thin film through a substrate

that the transmitted power is given by:

$$T^{\text{sub}}(I + R^{\text{film}}R^{\text{sub}} + R^{\text{film}}R^{\text{sub}}R^{\text{film}}R^{\text{sub}} + ...)T^{\text{film}}\mathbf{S} \equiv T^{\text{system}}\mathbf{S}, \tag{4.61}$$

where we have defined the transmittance matrix of the whole system, T^{system}. The individual components of T^{system} are the quantities T_{ss}, T_{sp} and so on, for the system as a whole, and what are typically measured in spectrophotometry, for instance. The bracketed quantity is a matrix geometric series, so we can write down a closed expression for T^{system}:

$$T^{\text{system}} = T^{\text{sub}}(I - R^{\text{film}}R^{\text{sub}})^{-1}T^{\text{film}}. \tag{4.62}$$

The transmittance and reflectance matrices for the film were derived earlier, while the transmittance and reflectance matrices for the substrate back into air are simple diagonal matrices, with the usual Fresnel coefficients as components. The linear forms of the matrices are given below; the circular forms can

be obtained by the matrix transformation given earlier:

$$R_{\text{lin}}^{\text{sub}} = \begin{pmatrix} \frac{\sin^2(\theta_t-\theta_i)}{\sin^2(\theta_t+\theta_i)} & 0 \\ 0 & \frac{\tan^2(\theta_t-\theta_i)}{\tan^2(\theta_t+\theta_i)} \end{pmatrix} \tag{4.63}$$

$$T_{\text{lin}}^{\text{sub}} = \begin{pmatrix} \frac{4\sin^2\theta_i\cos^2\theta_t}{\sin^2(\theta_t+\theta_i)} & 0 \\ 0 & \frac{4\sin^2\theta_i\cos^2\theta_t}{\sin^2(\theta_t+\theta_i)\cos^2(\theta_t-\theta_i)} \end{pmatrix}. \tag{4.64}$$

We can now apply this to the helical and twisted ribbon structures. For the helix, we consider TiO_2 deposition at $\alpha = 70°$, on a glass substrate with $n_2 = 1.5$, and a thickness of $z_s = 0$. We take the helical pitch to be $p_{\text{helix}} = 350$ nm. From Chapter 3 we have the principal indices of a TiO_2 slanted post at 70° as $n_{x'} = 1.57$, $n_{y'} = n_y = 1.73$ and $n_{z'} = 1.89$, ignoring film dispersion, with $\beta' = 37°$. This gives $n_x = 1.67$. Considering the behaviour at the substrate center, we have $\xi'(z) = -\phi = -\frac{2\pi z}{p_{\text{helix}}}$, resulting in a left-handed helix. We consider a 10-period film, so that $T^{\text{total}} = 3500$ nm. With these numbers we have all the values necessary to carry out the Berreman approach. The results for normally incident circularly polarized light are shown in Figure 4.5. Consistent with prior work [58], we see that the left-handed helix has a strong reflection band for right-circular light, centered around $\lambda_c = 590$nm. This is expected since right-handed light experiences a refractive index that modulates evenly between n_x and n'_y. This modulation has a period equal to half the helical pitch, so the predicted center wavelength would be given by the Bragg formula [90] as:

$$\lambda_c = 2\frac{n_x + n_y}{2}\frac{p_{\text{helix}}}{2} = 585 \text{ nm}, \tag{4.65}$$

which is consistent with our result. It is also apparent that most of the reflected light in the reflection band switches handedness, while most of the transmitted light retains the same handedness. Finally, we also find that left-circular light passes through the film as if the film were isotropic with an index $n_{y'}$. This is because left circular light experiences a constant index of n_y as it travels through the film.

We can carry out the same analysis for the twisted ribbon structure. Again, using the results from the previous chapter for a TiO_2 SBD film deposited at 70°, we have $n_{x'} = n_x = 1.72$, $n_{y'} = n_y = 1.62$ and $n_{z'} = 1.89$, with $\beta' = 0$. At the substrate center we again have $\xi' = -\phi = -\frac{2\pi z}{p_{\text{ribbon}}}$. The results for normally

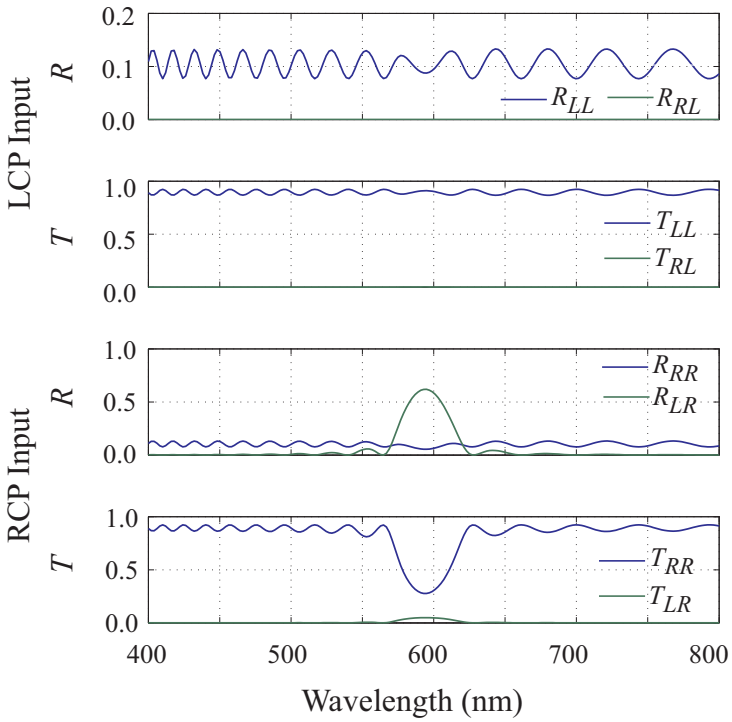

Figure 4.5: Circularly polarized reflectance and transmittance for a left-handed helical GLAD structure

incident circularly polarized light on a 10-period film, with $p_{\text{ribbon}} = 350$ nm, so that $T^{\text{total}} = 3500$ nm are shown in Figure 4.6. The results for the twisted

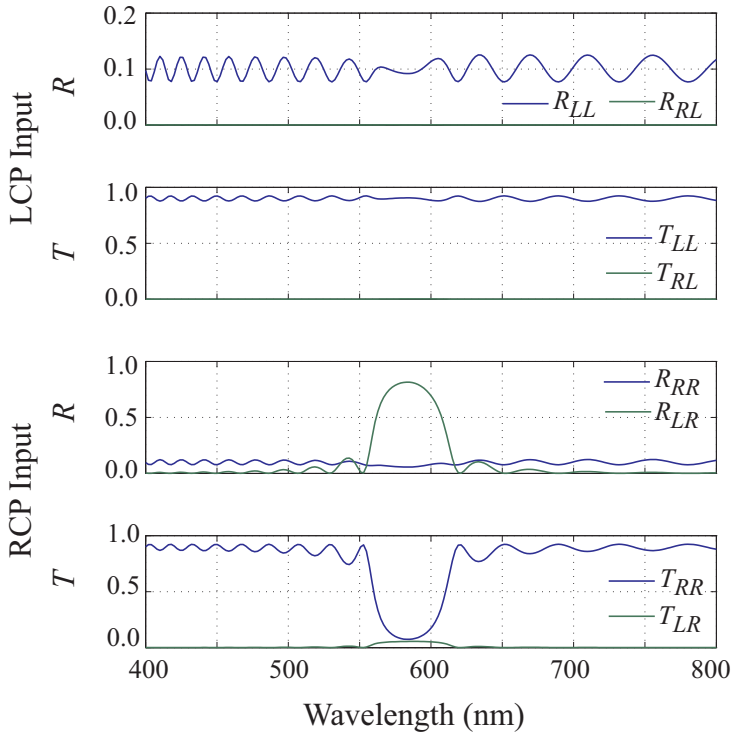

Figure 4.6: Circularly polarized reflectance and transmittance for a left-handed GLAD structure

ribbon are qualitatively very similar. There is again a large reflection band for right-circular light, which gets predominantly reflected as left-circular light. The reflection band has a similar λ_c, but is deeper on account of the greater index modulation present in the film. Finally, left-circular light is again mostly unaffected by the film. These results are all expected, and well-documented in the literature. These do illustrate the utility of the model to predict real-world optical properties, and identify important features of a given film design. We now proceed to investigate the optical properties of S-shaped films, in which we allow β' to vary throughout the thickness of a film.

4.3 S-shaped Structures

In order to create a polarizing film, we took inspiration from the periodically bent nematic (PBN)liquid crystal phase [91]. We will return to a more thor-

ough description of liquid crystal phases in the next chapter, but for the time being, the PBN phase can be described as a state of matter in which elongated molecules are arranged in the shape of an 'S'. Since the molecules are uniaxial, this arrangement produces an index modulation for light polarized parallel to the molecular long-axis, resulting in linear polarization selective transmittance.

We chose to attempt to replicate this structure using GLAD films for several reasons. First, previous results on helical films and circularly polarized selective transmittance were inspired by helical, or cholesteric liquid crystal phases, so it was thought that similar successes could be obtained with linear polarized light. Secondly, the helical GLAD films could also be used to induce cholesteric liquid crystal phases [92–94], in liquid crystal materials that don't normally exhibit cholesteric phases. While the PBN phase has been described in the literature [91, 95, 96], there is no way to achieve the structure through conventional alignment techniques. We were interested in whether or not this could be accomplished using GLAD. Third, S-shaped film fabrication had been clearly described by Robbie and Sit [52], building off previous work by Messier [50], who used a less flexible approach. Finally, the S-shaped approach is distinct from the approach presented by Hodgkinson [86]. In their approach, they use multiple materials, and rely on SBD structures alone to achieve linear polarization selectivity. Our method remains single-material, and has the potential for liquid crystal infiltration. We will return to the applications of GLAD films regarding liquid crystals in the next chapter, and focus exclusively on design and optical properties in this chapter.

4.3.1 Initial Design

The original films were fabricated with an aim simply to create S-shaped structures, with no appeal to the specific optical properties of the layers making up the films. Ultimately, as discussed in the Preface, the need to refine the structure and correct undesired behaviour provided the impetus for the material of Chapter 3.

To make an S-shaped film, initially we employed individual layers of spin-pause structures, as described in Section 3.3, with parameters f, P, p_v and δ. Deposition was done at a constant deposition angle, α. The algorithm is repeated below in Figure 4.7 for convenience. We repeat this spin-pause algorithm M times in order to create one period of the S-shaped film, and allow f

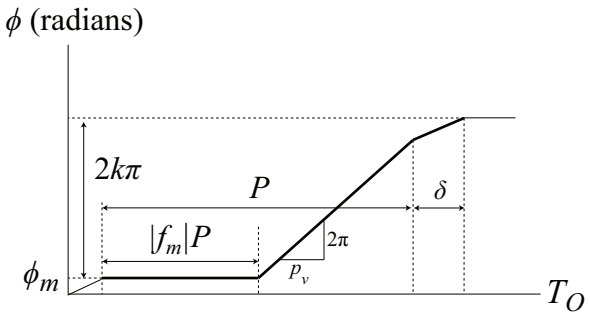

Figure 4.7: Spin-pause algorithm used to generate S-shaped structures

to vary from layer to layer. We call the spin-pause fraction in the mth layer as f_m, where $m = 1, 2...M$. We must add one complication to the algorithm by allowing for $f < 0$. When f is positive, the mth repetition of the algorithm begins at ϕ_m, which is presumed to be an integer multiple of 2π. However, when f is negative, we begin the mth section of the algorithm at an integer multiple of 2π, plus another half rotation of π radians. This allows for the growth of columnar structures in both directions, with $\xi' = 0$ and $\xi' = \pi$. Given these rules, one can obtain the entire algorithm by specifying f_m, along with P, p_v and δ. The thickness of a single period of the S-shaped film is $\Lambda = M(P + \delta)$, and one can repeat this N times to build up the film to the desired thickness. Typically, M and Λ are design choices, and δ is usually set to about 2 nm. This constrains P to the value $\Lambda/M - \delta$.

Initially, we considered two types of structures. The first is a very simple structure that alternates slanted post and vertical post structures to form a discrete type of structure. To obtain such a structure, one can simply set $M = 4$ and define:

$$f_m = \begin{cases} 1 & m = 1 \quad \text{Slanted posts} \\ 0 & m = 2, 4 \quad \text{Vertical posts} \\ -1 & m = 3 \text{Opposite direction slanted posts} \end{cases} \tag{4.66}$$

Along with suitable values for Λ, δ and p_v, this defines the algorithm entirely. There are two slanted segments, $m = 1$ and 3, resulting in columns slanted at an angle, $\beta' = \beta$, but pointing in opposite directions. In the language of Chapter 2, we say that these two segments have $\xi' = 0$ and $\xi' = \pi$. Segments $m = 2$ and 4 are vertical post segments, with $\beta' = 0$. An SEM of an 8-period

TiO_2 film made using this approach and deposited at $\alpha = 70°$, with $\Lambda = 295$ nm is shown in Figure 4.8.

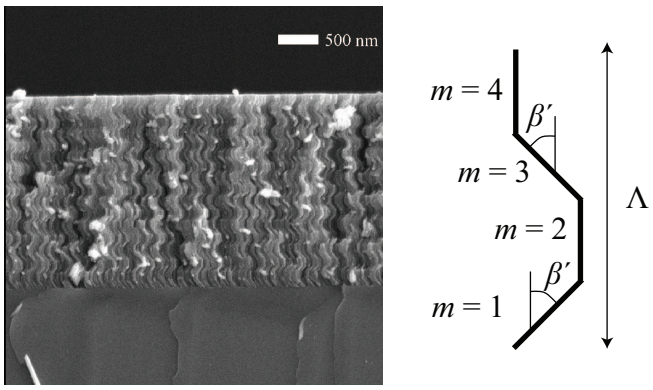

Figure 4.8: SEM and schematic of discrete type S-shaped film structure (TiO_2, $\alpha = 70°$)

The second type of structure we considered uses more layers, and a more continuous form of f_m:

$$f_m = \cos\left(\frac{360(m-1)}{M}\right), \qquad m = [1, M]. \tag{4.67}$$

For a typical value, $M = 16$, this results in a film whose column tilt as a function of m is shown in Figure 4.9(a), for a TiO_2 film deposited at 70°, with the usual Lichter-Chen parameter, $E = 0.49$. An SEM of a 6-period TiO_2 film fabricated

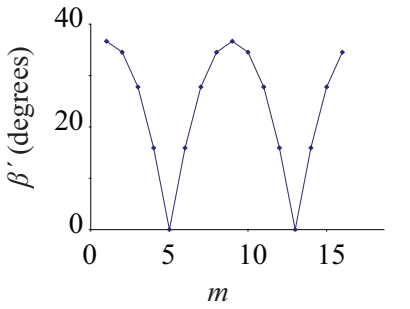

(a) Column tilt, β', as a function of m for a continuous S-shaped film

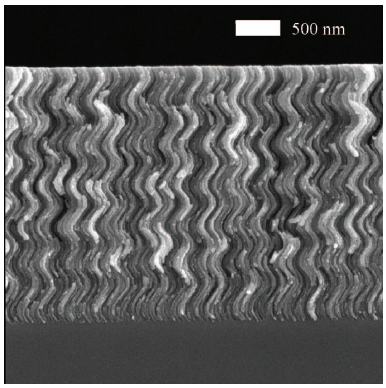

(b) SEM of continuous type S-shaped film (TiO_2, $\alpha = 70°$)

Figure 4.9: Continuous S-shaped film structure

at $\alpha = 70^\circ$ using this continuous approach, with $M = 16$ and $\Lambda = 470$ nm is shown in Figure 4.9(b).

To demonstrate the polarizing nature of such films, fourteen films with a varying number of periods, N, were fabricated out of TiO_2, with $\Lambda = 300 \pm 10$ nm, $p_v = 5$ nm and $\delta = 2$ nm using the discrete approach for f_m. Figure 4.10 shows the experimentally measured transmittance of incident light polarized along the x- and y-axes of a 24 period film. We see that both polarizations ex-

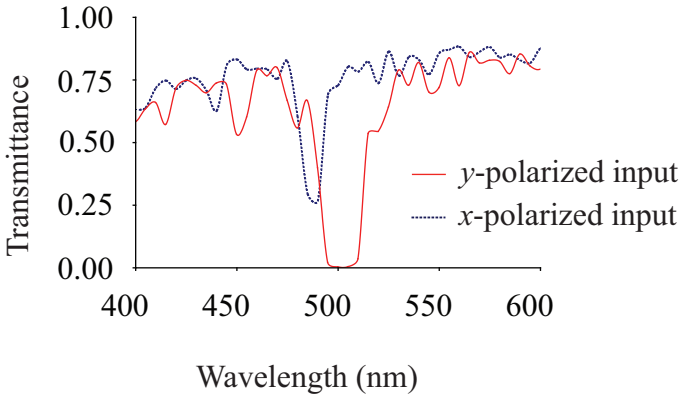

Figure 4.10: Experimentally measured transmittance of a 24 period, TiO_2 discrete, S-shaped film ($\Lambda = 300 \pm 10$ nm, $\alpha = 70^\circ$)

perience selective reflection bands. Input x-polarized light is weakly reflected in a narrow reflection band centered at about 490 nm, while y-polarized light is strongly reflected in a band centered at about 505 nm. At the time of fabrication, however, we were seeking a film that yielded a strong x-polarization reflection band, and left y-polarized light unaffected, as one would obtain for a PBN liquid crystal film. We recognize, with the benefit of the results of the previous chapter, that the y-polarization band gap happens because the slanted post sections exhibit negative birefringence, and consequently the index modulation for y-polarized light is more significant than for x-polarized light. We will return to this issue at the end of the chapter. However, despite the fact that our film reflected the opposite polarization as initially desired, this discrete S-shaped film does indeed fully reflect one linear polarization state of light at 505 nm, transmitting only x-polarized light.

We can simulate this structure using the Berreman approach, using the results of the previous chapter. We ignore dispersion, for simplicity, and use

the refractive index values at 500 nm as representative of the visible spectrum. Since all of our sublayers are spin-pause films, if we deposit at $\alpha = 70°$, all of our structures have principal indices as shown in Figure 3.7(a). The column tilt, β', is controlled by the spin-pause factor, f, according to (3.27), where we can substitute $a = |f|$. The orientation angle, ξ', is either 0 or π, for $f \geq 0$ and $f < 0$, respectively. For spin-pause TiO_2, we also have $E = 0.49 \pm 0.16$, $c = 3.9 \pm 0.5$ and $\Delta n_{\max}$ as given in Figure 3.9. Finally, we limit ourselves to normally incident light only.

The simulated results for a 24-period film with $\Lambda = 300$ nm, $c = 3.7$ and $E = 0.64$ are shown in Figure 4.11(a) and 4.11(b). They are compared to the measured results for input light polarized along both the x- and y-axes. We

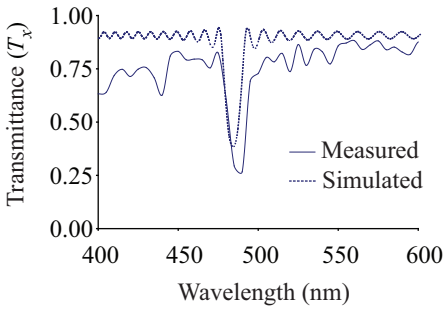

(a) Transmittance, T_x, of input x-polarized light (simulated results obtained using the Berreman approach, with $\Lambda = 300$ nm, $c = 3.7$ and $E = 0.64$)

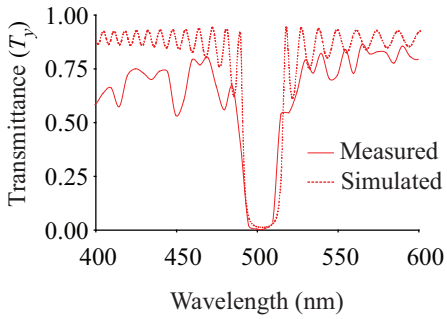

(b) Transmittance, T_y, of input y-polarized light (simulated results obtained using the Berreman approach, with $\Lambda = 300$ nm, $c = 3.7$ and $E = 0.64$)

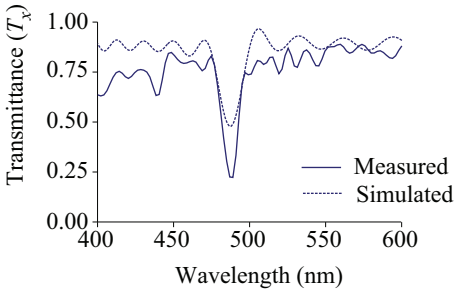

(c) Transmittance, T_x, of input x-polarized light (simulated results obtained using the FDTD approach)

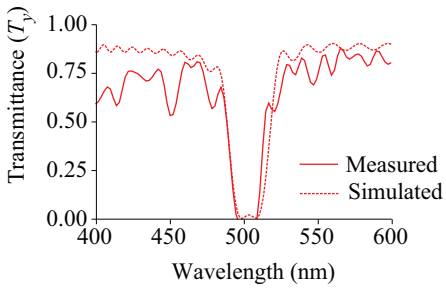

(d) Transmittance, T_y, of input y-polarized light (simulated results obtained using the FDTD approach)

Figure 4.11: Measured and simulated transmittance of a 24-period discrete S-shaped film.

see that, within the experimental uncertainty of the parameters E and c, the

major features of the measured film can be well predicted using the Berreman approach, using the model described in the previous chapter. Many non-ideal features of the film's transmittance are not well captured by the model, notably the aperiodic interference maxima and minima, likely due to non-uniform layer thicknesses as well as the lower overall value for the transmittance, which is likely due to scattering losses. However the two reflection bands for x- and y-polarized light are accurately predicted, with the simulated x-polarized reflection band occurring at a slightly lower wavelength than the measured one.

One can also simulate the transmittance of the film structure by solving Maxwell's equations directly, using a finite difference time domain (FDTD)approach. This was carried out in collaboration with Leontyev *et al.* [67] and the results are shown in Figure 4.11(c) and 4.11(d). This approach models the film using 3-dimensional dielectric structures matched to the real world film structure, as opposed to relying on effective medium approximations. We can see that this approach generates simulated spectra that are also in good agreement with the measured data. Certain features are better predicted by the FDTD approach; notably the position of the reflection band for x-polarized light and the overall magnitude of the transmittance are more accurate in this approach as compared with the Berreman approach. However, the depth of the x-polarized reflection band is better predicted using the Berreman approach. It is apparent that both simulation methods are capable of generating accurate predictions for the optical properties of the film. The Berreman approach has the major advantage of being much quicker. Running a simulation for a 24-period film requires only about one minute on a regular computer. Simulating the same structure using the FDTD approach requires either a much longer simulation time (on the order of 24 hours on a powerful desktop) or a much more powerful machine, dedicated to carrying out these types of computations. The FDTD approach is a more complete approach, however, as it can be applied to structures which are not simply layered in the z-direction, and accommodates features that may be masked by applying the Bruggeman effective medium approximation to the individual film layers. Both approaches could be further improved by introducing material dispersion, or by modeling scattering losses, which can be significant at lower wavelengths, especially for high-index materials, such as TiO_2.

We can quantify the quality of the polarizing effect by examining the degree

of polarization of light transmitted by the film as a function of the number of periods. The degree of polarization is given by the Stokes parameter, S_1:

$$S_1 = \frac{T_x - T_y}{T_x + T_y}, \tag{4.68}$$

where T_x and T_y are the transmittances given incident x- and y-polarized light respectively. We see that when both polarizations are transmitted equally, $S_1 = 0$, while when y-polarized light is strongly reflected, $S_1 \to 1$. Figure 4.12 shows the measured and modeled S_1 for the discrete film as a function of N, using both the Berreman and FDTD approaches (FDTD data taken from Leontyev *et al.*). In this case, we see that the FDTD approach matches the experimental

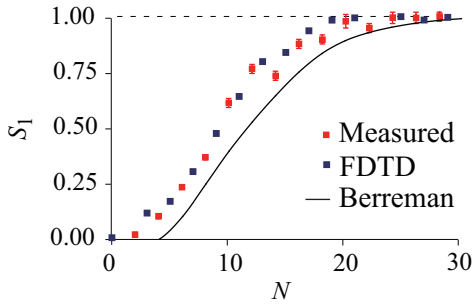

Figure 4.12: Measured and simulated degree of polarization for the discrete S-shaped film.

results very well, while the Berreman approach tends to underestimate the degree of polarization by about 0.1, until N is greater than about 22, where both the experimental and simulated results tend toward 1. The Berreman results are still fairly reasonable, and could potentially be improved if the material parameters of the film were known to greater precision. Experimentally, we see that the output light is completely polarized along x for films thicker than about 20 periods. For thicker films, S_1 still increases slightly, but the overall transmittance of x-polarized light decreases, because of the influence of the nearby x-polarization reflection band. This is an important consideration if wants to use these films in real world applications. Practically speaking, for any film thicker than about 6 periods, one can see the polarization effect with the naked eye. This can be done in a single deposition run, and represents a good film thickness for checking proof of concept film structures, which we will apply here.

Naturally, one can control the position of the reflection band center by changing the layer thickness, Λ. The Bragg formula predicts that the center wavelength, λ_c, is given by:

$$\lambda_c = n_{\text{avg}}\Lambda, \tag{4.69}$$

where n_{avg} is the average index experienced by the polarization state in question. Figure 4.13 shows the dependence of the center wavelength on Λ, for y-polarized light. A linear best-fit is also shown, given by the equation $\lambda_c =$

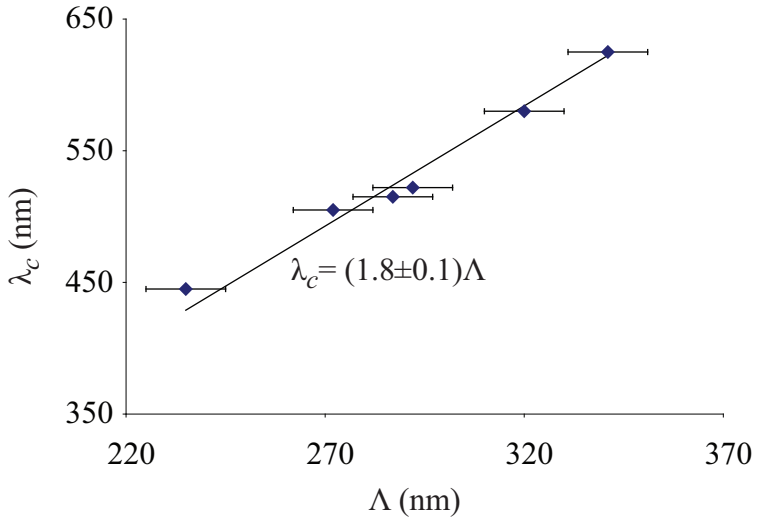

Figure 4.13: Measured dependence of the y-polarized reflection band on the layer thickness, Λ

$(1.8 \pm 0.1)\Lambda$. This implies that the average index experienced by y-polarized light is $n_{\text{avg}} = 1.8 \pm 0.1$. Taking the results from the previous chapter, we find that TiO_2 vertical posts deposited at $\alpha = 70^\circ$ have $n_y = 1.67 \pm 0.05$ and slanted posts have $n_y = 1.77 \pm 0.05$. Since the vertical and slanted sections have the same thickness, we obtain an average index of $n_{\text{avg}} = 1.72 \pm 0.07$, in good agreement with the above result. Since these values for n_y, obtained using the effective medium approach, yield a result consistent with the measured spectra, this provides additional evidence for the validity of the Berreman simulation approach, since that method depends on the acceptability of modeling individual layers as effective media.

It is also of interest to examine the behaviour of S-shaped films fabricated at varying α. Figure 4.14 shows both the degree of polarization, S_1, as well as the value of the transmittance of x-polarized light, T_x, at the center of the y-

polarization reflection band for several 6-period, discrete TiO_2 S-shaped films, deposited with $\Lambda = 265$ nm, at various α. The local maximum between 70° and 75° corresponds to the maximum in the in-plane birefringence, Δn_{max}, as illustrated in Figure 3.9. At these deposition angles, one obtains the largest refractive index modulations for normally incident light, and films fabricated at these α would be expected to have good polarizing properties. We also see that the degree of polarization increases strongly at large α. However, this is not due to the S-shaped nature of the film structure, but is a consequence of scattering. We can see this by noticing that the transmittance of x-polarized light is relatively constant around 0.8 - 0.9 until α is increased beyond 80°, whereupon T_x drops significantly. Above 80°, scattering effects start to dominate the optical properties of GLAD films. This is because the void inclusions in the film grow much larger as the film separates into individual columns. This creates a large number of interfaces between void and dielectric, leading to significant optical scattering. Because n_y is greater than n_x, scattering is stronger for y-polarized light, so the output light is dominantly x-polarized, similar to the behaviour at lower α. However, this behaviour occurs at all wavelengths and transmits light diffusely, which are not typically useful properties for thin film polarizers. As a result, optimal polarizing films should be fabricated around $\alpha = 70°$.

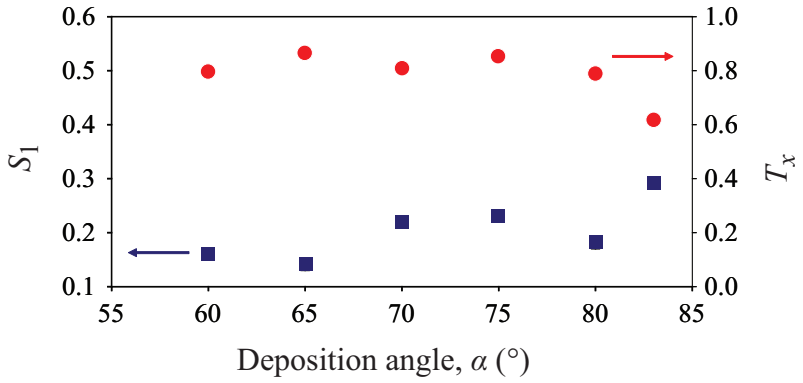

Figure 4.14: Measured S_1 and T_x at the center of the y-polarized reflection band, for discrete S-shaped films fabricated at various α. The uncertainty in the data is less than the size of the data points.

We also find that using the continuous form for f_m given in equation (4.67) yields films exhibiting the same type of polarization selectivity as the discrete structure. Figure 4.15 shows the measured transmission spectrum for a 6-period film fabricated at $\alpha = 70°$ using TiO_2, with $M = 16$. In this case we

employed $\Lambda = 510$ nm, with $p_v = 10$ nm and $\delta = 2$ nm. The optical spectrum of the film was simulated using the same material parameters as previously, $c = 3.7$ and $E = 0.64$.

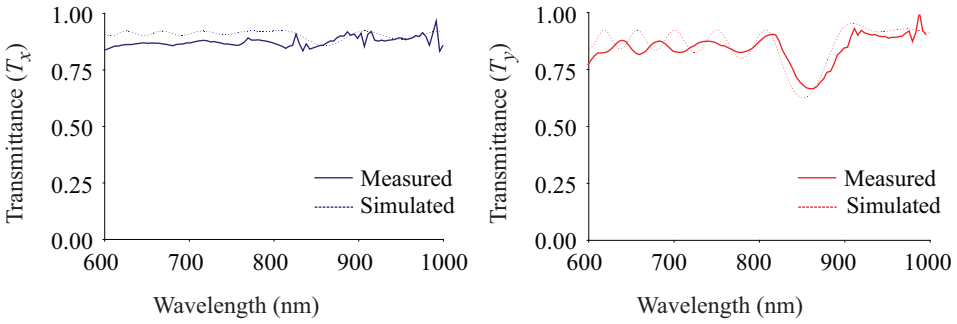

(a) Transmittance, T_x, of input x-polarized light (simulated results obtained using the Berreman approach)

(b) Transmittance, T_y, of input y-polarized light (simulated results obtained using the Berreman approach)

Figure 4.15: Measured and simulated transmittance of a 6-period continuous S-shaped film.

We see that the Berreman approach yields very accurate predictions for the film transmittance, and closely matches both the position and depth of the y-polarization reflection band. Though not shown here, in this case, the Berreman method actually yields significantly more accurate results that the FDTD approach. The predicted transmittance for a 20-period film is shown in Figure 4.16. It has a very similar behaviour to the discrete version, with a deep y-polarized reflection band, and a shallow, blue-shifted x-polarized reflection band. One major difference is that the x-polarized reflection band is predicted to be much weaker than in the discrete case, which is a nice feature as the film acts much more like an ideal reflective linear polarizer.

4.3.2 Refining the Design

In order to refine the design, there are two approaches that one can follow. First, using a finite difference frequency domain (FDFD) approach, one can determine the location of the polarization selective reflection bands as a function of the geometry of the film columns. This includes geometric aspects such as the column tilt angle, or cross-sectional dimensions. This approach was carried out by Leontyev *et al.*, where the ability to separate or close the various reflection bands was demonstrated theoretically. One shortcoming of this approach

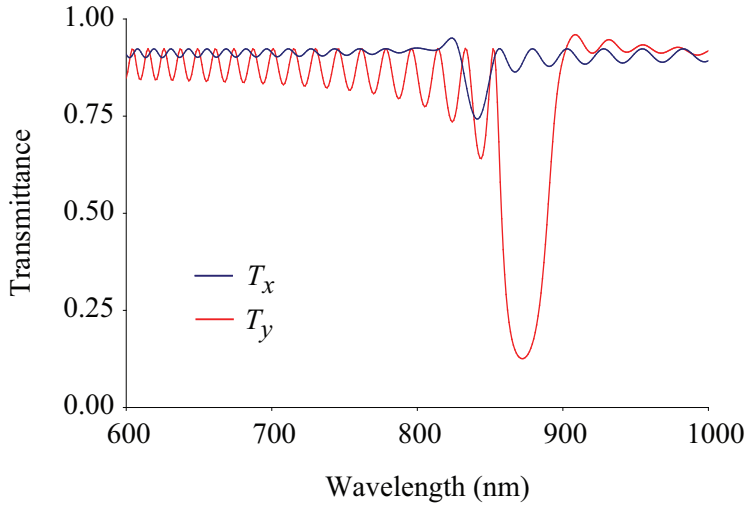

Figure 4.16: Simulated (Berreman approach) transmittance of a 20-period TiO_2, continuous, S-shaped TiO_2 film, deposited at $\alpha = 70°$

is that controlling the geometric parameters involved in the model by changing deposition conditions is not well-characterized. This is one reason why the Berreman approach is potentially more useful, as it relies on the optical properties of individual film layers, which are more straightforward to measure and tabulate, as illustrated in the previous chapter. We examine an application of this approach here.

The film structure described above possesses a strong y-polarized reflection band, and a weaker, neighbouring x-polarized reflection band. We now desire to modify the film structure such that the main reflection band be for x-polarized light, so that light polarized in the plane of the S-shaped columns would be reflected. Second, we wish to eliminate any secondary reflection band for the orthogonal y-polarization state that could arise as a result of inadequate index matching in n_y between layers. We desire that the polarization state orthogonal to that possessing the main reflection band to be unaffected by the film.

In order to obtain these results, using the findings in the previous chapter, we designed a new proof-of-concept structure, created using alternating layers of PhiSweep and vertical post TiO_2. For the first layer, an 80 ± 8 nm PhiSweep film was used, with $\alpha = 70°$ and $\phi_0 = 65°$ ($a = 0.42$). From the previous chapter, we found $c = 4.1 \pm 0.5$ for PhiSweep films, and we will continue to use $c = 3.7$ for spin-pause (and vertical post) films. As discussed in the

previous chapter, we know that the refractive index model underestimates n_x and n_y in PhiSweep films for smaller values of a, so we use $c = 4.6$ to yield the largest values for n_x and n_y as 1.75 and 1.68, respectively. We now need choose a vertical post for the second layer that will be index matched to the first layer for y-polarized light. For vertical posts, at 70°, we have $n_y = 1.64$, which is not index matched to the PhiSweep layer. We now use the model of the previous chapter to determine the deposition angle at which index matching occurs. Using the model, one finds that by simply lowering α to 68°, one can obtain vertical posts with $n_x = n_y = 1.68$. This results in an index modulation of 0.07 for x-polarized light, and perfect index matching for y-polarized light. If we again choose an 80 ± 8 nm thickness for the vertical post layer, then, using the Bragg condition, the x-polarized reflection band is predicted to be centered at $\lambda_c = 549 \pm 40$ nm.

Figure 4.17 shows the simulated transmittance of a 20-period version of this

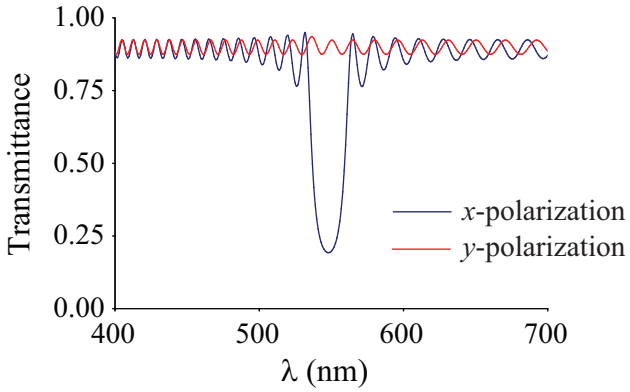

Figure 4.17: Calculated normalized transmittance, $\frac{T_x - T_y}{T_x + T_y}$, of S-shaped films

design, calculated using the Berreman approach. We see that the simulation indicates a strong reflection band for x-polarized light, and no reflection band for y-polarized light. Experimentally, a 6-period version of this film design was fabricated and Figure 4.18 shows the resultant transmittance for input x- and y-polarized light. Consistent with the simulated result, we observe that in the redesigned film, the x-polarization reflection band is indeed fairly large, while the y-polarized light is unaffected, as intended. These results indicate the power of combining the results of Chapter 3 with the Berreman approach outlined in this chapter for the purposes of optical filter design. Here we have illustrated their application with regards to normally incident, reflective linear

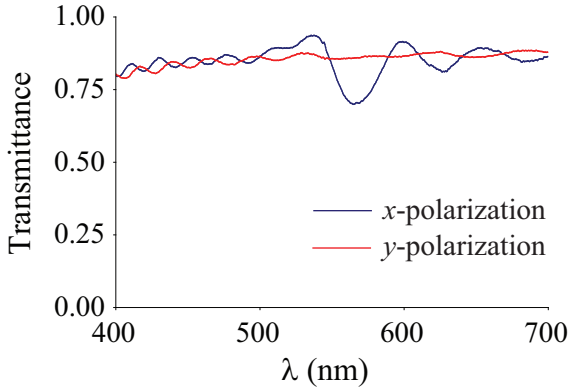

Figure 4.18: Measured x- and y-polarized transmittance of a 6-period redesigned S-shaped film

polarizers, but the method is applicable to any optical filter design amenable to fabrication using GLAD film structures.

4.4 Conclusions

This chapter tells a relatively simple story about an interesting engineering problem and different ways to quantify a system and attempt to refine it. It also indicates a number of nice features of the GLAD process, notably the potentially huge variety in creating optically anisotropic layers. While optical films of great sophistication can be obtained through standard deposition techniques, this chapter shows the creation of an optical filter that relies on the special features inherent to GLAD, and is a nice example of a unique device that would be difficult to fabricate any other way. This chapter also provides a very nice venue for applying the results of the previous chapter in order to confirm the validity and the utility of the model described therein. On a somewhat disappointing note, the motivation for this structure was to ultimately use a porous version of the structure to align liquid crystals, which are discussed in detail in the next chapter. Unfortunately, that goal was never realized, but as a result of attempting it, we were able to develop a potentially useful device here in this chapter, and when the need came to refine the design, that led to a great deal of the material researched in the previous two chapters. The lasting legacy of this chapter is the demonstration of a reflective, thin-film polarizer for use at normal incidence. Such a device is impossible to fabricate

using planar, isotropic film layers, but relatively straightforward using GLAD. Future research should focus on improving device performance, perhaps through annealing, and on identifying large scale viability by examining process non-uniformities by applying the results of Chapter 2.

Chapter 5

Liquid Crystal Alignment in GLAD Films

"Science is always wrong. It never solves a problem without creating ten more." – George Bernard Shaw

5.1 Introduction

The work presented here is a fairly significant departure from the first half of this thesis. It is an extension of a long line of research that traces its origins to the beginnings of modern research into both liquid crystals and oblique angle deposition. The properties and history of liquid crystals will be discussed in greater detail below, but it is worth mentioning here that early technological applications involving liquid crystals relied on obliquely deposited films to induce the crucial single domain alignment required for proper device performance. However, film structures were limited to only slanted post structures and the only major variable of interest was the deposition angle, α. Over time, this method of inducing liquid crystal alignment was largely replaced by other techniques more suitable in manufacturing[5.1]. With the advent of GLAD, there was a resurgence of interest in liquid crystal alignment in these films; one early

[5.1] The potential of using GLAD films for commercial liquid crystal alignment illustrates a good example of a potential application for the material in Chapter 2.

and notable result was the demonstration of chiral liquid crystalline behaviour induced by helical films, in non-chiral liquid crystal molecules, and the ability to switch this behaviour using applied electric fields [81,97,98]. This result indicated that GLAD films, with their three-dimensional structure, could induce alignment of liquid crystal molecules through the bulk of a sample, rather than simply exerting influence at a surface. Due to the variety of possible structures that can be fabricated with GLAD, this opens up possibilities for a number of interesting applications, such as templating liquid crystalline polymer networks [99], or the fabrication of switchable optical filters, including circular polarizers made by infiltrating liquid crystals into the helical films mentioned above, or linear polarizers which would instead make use of S-shaped films, as described in the previous chapter.

To date, however, research into the fundamentals of the interaction between liquid crystalline materials and GLAD film structures has been rather sparse. One notable exception is a nuclear magnetic resonance study carried out by Elias *et. al.* [100], that examined the alignment of a cyanobiphenyl-based liquid crystal in a helical film. It was observed there that the liquid crystal molecule tended to line up along the helical structure of the film, contributing to the notion that molecular alignment could be controlled far from the substrate surface. And while research has continued on the alignment of liquid crystals in other confined geometries, often comprised of not too dissimilar microporous materials [101–104], work related specifically to GLAD films has not extended beyond many of the early studies confined to obliquely deposited films. The purpose of the material in this chapter is to extend that research into the realm of GLAD films, and to introduce a mathematical picture with which to better view and understand alignment in these systems. To date, much of the research on liquid crystal alignment in GLAD films has focused primarily on achieving interesting empirical results, while not paying enough attention to the fundamental interactions that are driving those results. The material in this chapter is intended to start to shift the balance back in the other direction.

5.2 Liquid Crystals

5.2.1 A Brief History of Liquid Crystals

It is traditionally held that liquid crystals were first observed, though not properly understood, in 1888 by Friedrich Reinitzer, in Prague [105]. Reinitzer was studying cholesteryl benzoate, a derivative of cholesterol, and observed strange melting behaviour. Reinitzer reported that cholesteryl benzoate had, in fact, two melting points. The first, at 145.5 °C marked the transition from solid into a cloudy liquid. Then, at 178.5 °C, the cloudy liquid underwent a transition into a clear liquid. Additionally, on cooling the material, dramatic blue and purple colours were seen near both transition points. Reinitzer's research soon gave way to that of his colleague, Otto Lehmann, who definitively showed that while the clear liquid had all the properties of a normal liquid, the cloudy phase had anisotropic properties and other properties then thought of as exclusive to solid crystals [106]. Given that the cloudy phase shared properties characteristic of both liquids and crystals, materials that had similar phases were given the name of liquid crystals (LCs). Over the course of the early 20th century, the physics regarding liquid crystals were well-investigated, however the field remained primarily an academic curiosity. It would take until the 1960s for liquid crystals to transform into a major focus of scientific and commercial research [107]. In the early part of the decade, RCA developed forerunners to the modern-day liquid crystal display (LCD), ultimately developing the first material with room-temperature liquid crystalline behaviour[5.2]. This technology was eventually implemented by Sharp in the first pocket calculators in 1973 to great commercial success. During the same time, Pierre-Gilles de Gennes had completed a framework explaining the liquid crystal phase change as a general principle [108], applicable to systems of all kinds, including magnets, superconductors and polymers. For this work, he was ultimately awarded the Nobel Prize in Physics in 1991[5.3]. In particular, his work concerning liquid crystals and polymers has led to the development of a myriad of liquid crystalline polymer (LCP) materials, which are the focus of a great deal of current

[5.2] Technically, this was the first room-temperature nematic liquid crystal, which will be described in short order.

[5.3] "The Royal Swedish Academy of Sciences has awarded this year's Nobel Prize in Physics to Pierre-Gilles de Gennes (College de France, Paris) for discovering that methods developed for studying order phenomena in simple systems can be generalized to more complex forms of matter, in particular to liquid crystals and polymers."

research. Today, the market dominance of LCDs is the most prevalent example of the commercial application of liquid crystals. LCs are also being used for spatial light modulators [109], mechanical actuators [110, 111], chemical sensors [112], electo-optic windows [113] and in unusually strong plastics [114], such as Kevlar.

5.2.2 Types of Liquid Crystals

Liquid crystal phases [108], or mesophases, are phases of matter in which the constituent liquid crystalline molecules, or mesogens, exhibit positional and orientational order intermediate between traditional liquid and crystalline phases. Solid crystals are characterized as having a microscopic structure that is arranged in a periodic lattice extending for lengths much larger than the period in all three spatial dimensions. If the crystal is composed of anisotropic molecules, the orientation of these molecules also repeats in a predictable manner. This positional and orientational order allows crystals to have anisotropic properties, such as optical birefringence or anisotropic elasticity. Liquids, by contrast, exhibit no such long range order. The constituent particles of a liquid are not arranged with any predictable positional or orientational order, and macroscopic liquid properties are completely isotropic. It is also true that solid crystals exhibit discrete translational and rotational symmetries, whereas liquids exhibit continuous translational and rotational symmetries. As a result, one can say that liquids have a higher symmetry, or lower order, than crystals.

One can first distinguish two types of liquid crystals based on the parameter that affects phase transitions: thermotropic and lyotropic. Lyotropic liquid crystals exhibit mesophases that are controlled by the concentration of the mesogenic species in solvent. These systems are often composed of amphiphilic molecules such as soap, dissolved in water. At low soap molecule concentrations, they are simply randomly dispersed in the mixture. As the concentration increases, the soap molecules arrange into randomly dispersed micelles, with the hydrophobic heads of the molecules at the center of the micelles isolated from the water, and the hydrophilic tails forming the surface of the micelle. As the soap concentration increases further, these micelles will self-organize into periodic structures, similar to those of solid crystals. However, individual molecules remain mobile and can flow, as in a liquid. This behaviour is also prevalent in diblock copolymer systems [115].

(a) Nematic Phase (b) Smectic Phase (c) Columnar Phase

Figure 5.1: Illustration of nematic, smectic and columnar liquid crystal phases. Images taken from [116].

While lyotropic phases are controlled primarily by the concentration of the different species in the mixture, thermotropic liquid crystals have mesophases whose transitions are controlled primarily by temperature. In general, the increased thermal energy at higher temperatures tends to reduce the order of the system, just as in the usual crystalline to liquid to gaseous phase transitions. Thermotropic liquid crystals are characterized by the presence of mesophases that exist at temperatures intermediate between the crystalline and liquid phases. Materials can have more than one mesophase, and these phases can be stable over large temperature ranges, with working temperatures below, at or above room temperature.

One can identify three broad classes of thermotropic liquid crystal phases, based on their degree of order: nematics, smectics and columnar phases. These are shown schematically in Figure 5.1. As with the liquid phase, molecules in a nematic phase possess no long range positional order. Given the position of one molecule in a nematic phase, one cannot predict the position of a distant molecule. Unlike the liquid phase, however, the nematic phase does possess orientational order. This implies that molecules in a nematic phase, and indeed all liquid crystalline phases, are necessarily anisotropic [108]. Typically, nematic molecules are elongated and, in a material with high nematic order, far away molecules are usually aligned such that their long axes are roughly parallel. In addition to orientational order, smectic phases also exhibit positional order in one dimension. Figure 5.1(b) depicts a smectic phase, illustrating periodic, layered spacing of the molecular positioning in the z-direction. Within the individual layers, there is no positional order, and the molecules act as a

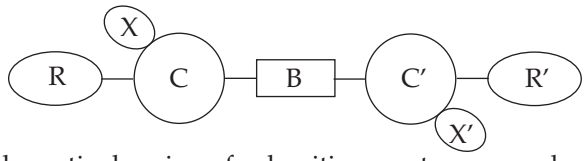

Figure 5.2: Schematic drawing of calamitic nematogens made up of two core groups (C, C′), one bridging group (B), two (optional) substituents (X, X′) and two terminal groups (R, R′). After [119]

two-dimensional liquid. Smectic liquid crystals exhibit Bragg diffraction peaks characteristic of this layer spacing. Finally, columnar phases exhibit positional order in two dimensions. In Figure 5.1(c), this periodicity occurs along the x- and y-direction. Along the z-direction, molecules are free to move; columnar liquid crystals act as an array of one-dimensional liquid tubes. Within each of these three groups, there is a host of exotic subclasses, well-catalogued in reference [117]. The focus of the remainder of this thesis will be on nematic liquid crystals.

5.2.3 Nematic Materials

As mentioned earlier, nematic mesogens are necessarily anisotropic in shape. Commonly, they tend to be elongated rods, as shown in Figures 5.1(a) and 5.1(b), but more exotic shapes, including discotic molecules such as in Figure 5.1(c) or banana-shaped molecules [118] are not excluded. We will focus on rod-like, or calamitic, nematics, which give rise to uniaxial nematic behaviour. A schematic depiction of calamitic nematogens is shown in Figure 5.2. All the materials encountered in this thesis have the above form. In many liquid crystals, including the ones in this thesis, the core groups (C and C′) are identical aromatic rings. These provide rigidity and steric repulsion that contribute to nematic ordering[5.4], and provide strong magnetic anisotropy, due to the different response to magnetic fields aligned perpendicular to the benzene rings as compared to fields in the plane of the rings. The bridging group (B) has a large effect on mesophase formation. If benzene rings form the core groups, then in the absence of any bridging group, the mesogen is termed a biphenyl. If a third benzene ring forms the bridging group it is called terphenyl. Other common bridging groups include −C-C− (diphenylethane), −C=C− (stilbene),

[5.4] Steric repulsion is simply the notion that two objects can not occupy the same space. Due to a competition between orientational and positional entropy, one can show that under certain conditions, it is energetically favorable for long, rod-like objects to align [120].

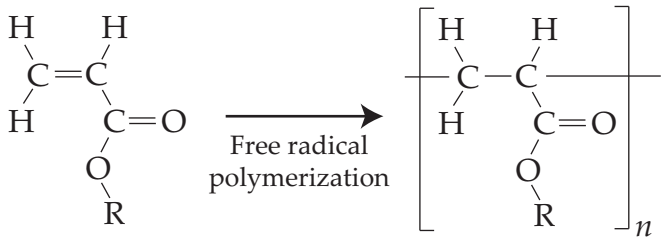

Figure 5.3: Free radical polymerization of an acrylate end group.

−C≡C− (tolane), −N=N− (azobenzene), −CH=N− (Schiff's base) and COO (phenylbenzoate, ester) [121]. Changing the bonding can have drastic effects on the transition temperatures of the liquid crystal. However, bridging groups are often unstable in response to ultraviolet exposure or high temperature, and mesogens can break apart, introducing impurities into the liquid crystal, and changing its behaviour. Many modern compounds use diphenyl mesogens to avoid these problems. Various types of terminal groups (R, R′) exist. Group R is usually an alkyl chain of the form C_nH_{2n+1}, but can also commonly be an alkoxy chain, $C_nH_{2n+1}O$. Short chains actually inhibit mesophases, as the molecules are too rigid to rearrange into ordered states. Longer chains admit mesophases, with larger carbon numbers promoting lower transition temperatures and more ordered phases (e.g. smectic phases preferred over nematic ones), though this is only a rough guideline. For the purposes of creating polymeric liquid crystals, the chains are often terminated by reactive end groups such as acrylates. An acrylate group has a double bond that can be broken by a free radical to form a polymer chain, as shown in Figure 5.3. Polymeric liquid crystals will be described in greater detail shortly. R′ terminal groups can be similar to the R group, but groups not composed of hydrocarbons are also common. The most notable example is the cyano (C≡N) group. The cyano group is easily polarized along its bond axis, which is collinear with the average molecular axis. This implies that the dielectric constant is higher for light polarized along the axis of the molecule, as compared to light polarized perpendicular to it. Cyano-terminated nematogens are also usually uniaxial, and have isotropic polarizability normal to the molecular axis. These molecules can have very high birefringence values ($\Delta n \sim 0.2$), and this is one of the major reasons for their applicability in LCDs. Additionally, this dielectric anisotropy remains present at much lower frequencies. Therefore, an applied electric field will generate a torque on the liquid crystal in such a way that the field experiences the largest

possible dielectric constant. For cyano-terminated nematogens, this means that the molecular axis will align with an externally applied electric field. The presence of a cyano group can also enhance the liquid crystal characteristics of a material by encouraging the formation of dimer pairs, effectively doubling the length of the nematogen. The linking groups (L,L′) are not especially crucial to liquid crystal behaviour, and will typically be composed of single oxygen atoms, or not be present at all. Finally, the substituent groups (X, X′) tend to break molecular symmetry, and this tends to promote smectic phases. These groups will not be encountered in this thesis. The materials used in this thesis will be described in Section 5.4

5.2.4 The Physics of Nematic Liquid Crystals

The orientation of an individual mesogen can be described by a unit vector, $\mathbf{u}_i$, that is parallel to the long axis of the mesogen. In a small neighbourhood around $\mathbf{r}$, these $\mathbf{u}_i$ are parallel, on average, to some common axis, distinguished by the unit vector, $\mathbf{n}(\mathbf{r})$, which is termed the nematic director field. Nematics also have the property that the states $\mathbf{n}(\mathbf{r})$ and $-\mathbf{n}(\mathbf{r})$ are indistinguishable. Note that this does not imply that nematic molecules are symmetric. It does, however, imply that there are an equal number of mesogens with $\mathbf{u}$ roughly parallel to $\mathbf{n}$ as are anti-parallel to $\mathbf{n}$. In the absence of external forces, and for non-chiral molecules, the equilibrium state of a nematic is to have $\mathbf{n}(\mathbf{r}) =$ constant. In this case, the nematic system behaves as a uniaxial crystal, with one principal axis along $\mathbf{n}$, and two degenerate principal axes in the plane normal to $\mathbf{n}$. The dielectric tensor in a principle coordinate frame is:

$$\varepsilon = \begin{pmatrix} \varepsilon_o & 0 & 0 \\ 0 & \varepsilon_o & 0 \\ 0 & 0 & \varepsilon_e \end{pmatrix} = \begin{pmatrix} n_o^2 & 0 & 0 \\ 0 & n_o^2 & 0 \\ 0 & 0 & n_e^2 \end{pmatrix}, \tag{5.1}$$

where ε_o (n_o) and ε_e (n_e) are the ordinary and extraordinary dielectric constants (refractive indices). However, this situation is rarely seen in practice. Typically, external forces, which can include surface interactions generated at the walls of the sample [122], or dopants to introduce chirality, will deform the director field. If the surface interactions promote a single value of $\mathbf{n}$, the liquid crystal is said to be aligned, or monodomain. However, if the surface interactions

promote degenerate values for $\mathbf{n}$, the liquid crystal will be polydomain, where the mesogens assemble into many small domains, each locally aligned, but largely uncorrelated with its neighbors.

In order to quantify the degree of order in the nematic mesophase, we introduce S, the nematic order parameter [108]. We want S to increase as the individual mesogens become increasingly parallel to the director and we want S to vanish in the liquid (disordered) phase. Given these constraints, one might expect the average $\langle \mathbf{u}_i \cdot \mathbf{n} \rangle = \langle \cos \theta_i^{LC} \rangle$ over all solid angles, where θ_i^{LC} is the angle between $\mathbf{u}_i$ and $\mathbf{n}$, to be an appropriate choice. However, we know that there are as many mesogens parallel to $\mathbf{n}$ as there are anti-parallel to it, so $\langle \cos \theta_i^{LC} \rangle$ vanishes. To obtain a non-zero value, one must average over $\cos^2 \theta_i^{LC}$. Choosing an appropriate form for normalization give:

$$S = \frac{1}{2} \langle 3 \cos^2 \theta_i^{LC} - 1 \rangle \tag{5.2}$$

When the system is fully aligned, mesogens can only be found with $\theta_i^{LC} = 0$ or π, and $S = 1$. When the system is completely disordered, mesogens are oriented in all directions with equal probability; the average of $\cos^2 \theta_i^{LC}$ over all solid angles is $1/3$, so that $S = 0$ as desired.

As described above, different mesophases in a thermotropic liquid crystal are accessed by varying temperature. The phase behaviour of a typical thermotropic liquid crystal is shown in Figure 5.4, which illustrates the transition from the crystalline (K) phase through potential smectic (S) and nematic (N) phases before finally passing into the liquid, or isotropic (I) phase. We label the temperature at which the phase transition occurs as T_{AB} , where A is the lower temperature phase, and B is the higher temperature phase. For the research presented here, only nematic phases are observed, so only T_{KN} and T_{NI} are encountered. T_{NI} is also often referred to as the clearing point. This is because a polydomain nematic scatters light strongly [119] and appears as a cloudy liquid. As the temperature rises beyond T_{NI}, the domains vanish and the liquid appears clear. The order parameter is discontinuous at T_{NI}. It will jump from 0 in the isotropic state to some finite value as the liquid crystal cools and enters the nematic phase. The values of the ε_o and ε_e are also functions of S. Larger values of S promote larger anisotropy between the ordinary and extraordinary directions.

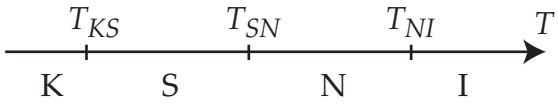

Figure 5.4: Thermotropic phase transitions for a typical liquid crystal.

As mentioned earlier, in the nematic phase, external forces may deform the director field from the ideal state, $\mathbf{n}$ = constant. However, these deformations are usually large compared to the molecular dimension so locally, the liquid crystal still acts as a nematic single crystal. The principal axes of the nematic rotate in accordance with the distortion, but the principle dielectric tensor remains unchanged by these distortions. The director field can be modeled as an elastic continuum, where deformations of the field cost energy. It is assumed that the director field will take on the configuration that minimizes the total free energy of the system. This elastic description was originally proposed by Oseen [123] and expanded upon by Frank [124], and has been widely successful in predicting and modeling nematic behaviour.

Frank and Oseen realized that the free energy of the system must vanish if $\nabla\mathbf{n} = 0$ and therefore chose to expand the free energy as a power series in $\nabla\mathbf{n}$. Terms with odd exponents are inadmissible since the energy must be invariant to a sign change in $\mathbf{n}$, so only terms in $(\nabla\mathbf{n})^2$ and higher even powers can be kept. If one ignores all powers higher than the quadratic ones, expands the vector gradient and collects terms, then the famous Frank-Oseen free energy density for nematic liquid crystals can be written as:

$$F = \frac{K_1}{2}(\nabla \cdot \mathbf{n})^2 + \frac{K_2}{2}(\mathbf{n} \cdot (\nabla \times \mathbf{n}))^2 + \frac{K_3}{2}(\mathbf{n} \times (\nabla \times \mathbf{n}))^2. \tag{5.3}$$

Each of the three terms in the expansion describes one of the three fundamental distortions of a nematic system. These are splay ($\nabla \cdot \mathbf{n} \neq 0$), twist ($\mathbf{n} \cdot (\nabla \times \mathbf{n}) \neq 0$) and bend (($\mathbf{n} \times (\nabla \times \mathbf{n}) \neq 0$), as illustrated in Figure 5.5. Naturally, the K's (sometimes denoted K_{11}, K_{22} and K_{33} to emphasize their underlying tensorial nature) are called the splay, twist and bend elastic constants. Notice that, as expected, the free energy density is zero if $\mathbf{n}$ is constant, which represents the equilibrium state of a nematic in the absence of external forces.

The three elastic constants are often very similar in magnitude, so it is common to make the one-constant approximation [108], $K_1 = K_2 = K_3 \equiv K$, and use the vector identity that $(\mathbf{a} \cdot \mathbf{b})^2 + (\mathbf{a} \times \mathbf{b})^2 = a^2b^2$ to simplify equation (5.3).

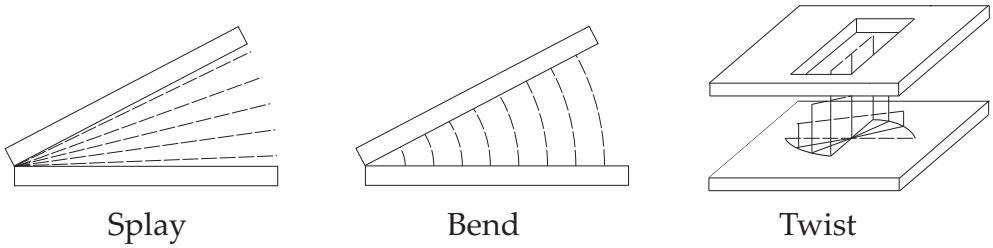

Figure 5.5: Basic deformations in nematic liquid crystals

Recalling that $\mathbf{n}$ is a unit vector, so that $n = 1$, we follow DeGennes to find:

$$\begin{aligned}\frac{2F}{K} &= (\nabla \cdot \mathbf{n})^2 + (\nabla \times \mathbf{n})^2, \\ &= n_{x,x}^2 + n_{y,y}^2 + n_{z,z}^2 + n_{x,y}^2 + n_{x,z}^2 + n_{y,x}^2 + n_{y,z}^2 + n_{z,x}^2 + n_{z,y}^2 \\ &\quad + 2(n_{x,x}n_{y,y} + n_{x,x}n_{z,z} + n_{y,y}n_{z,z} - n_{x,y}n_{y,x} - n_{x,z}n_{z,x} - n_{y,z}n_{z,y}). \end{aligned} \tag{5.4}$$

The total free energy, $\mathcal{F}$, in the nematic system is then given by the integral of F over the volume of the system:

$$\mathcal{F} = \frac{K}{2}\iiint_V ((\nabla \cdot \mathbf{n})^2 + (\nabla \times \mathbf{n})^2) dV. \tag{5.5}$$

The solution for $\mathbf{n}$ is that which provides a stationary value for $\mathcal{F}$ for all variations that leave $\mathbf{n}$ a unit vector. In other words, we need to minimize $\mathcal{F}$ subject to the constraint:

$$R(\mathbf{n}) = n_x^2 + n_y^2 + n_z^2 - 1 = 0. \tag{5.6}$$

This amounts to finding a stationary value for the modified free energy, $\mathcal{R}$, where:

$$\mathcal{R} = \frac{K}{2}\iiint_V ((\nabla \cdot \mathbf{n})^2 + (\nabla \times \mathbf{n})^2 + \lambda R(\mathbf{n})) dV, \tag{5.7}$$

and λ is a Lagrange multiplier.

We now label the derivatives of $\mathbf{n}$ as $g_{\alpha\beta} = \partial n_\beta / \partial \alpha$, with $\alpha, \beta = x, y, z$. Using

Einstein notation to denote summation over repeated indices, we can write:

$$\begin{aligned}\delta\mathcal{R} &= \frac{K}{2}\iiint_V \left[\frac{\partial F}{\partial g_{\alpha\beta}}\delta g_{\alpha\beta} + \lambda\frac{\partial R}{\partial n_\beta}\delta n_\beta\right] dV, \\ &= \frac{K}{2}\iiint_V \left[\frac{\partial F}{\partial g_{\alpha\beta}}\delta\left(\frac{\partial n_\beta}{\partial \alpha}\right) + \lambda\frac{\partial R}{\partial n_\beta}\delta n_\beta\right] dV, \\ &= \frac{K}{2}\iiint_V \left[\frac{\partial F}{\partial g_{\alpha\beta}}\frac{\partial}{\partial \alpha}(\delta n_\beta) + \lambda\frac{\partial R}{\partial n_\beta}\delta n_\beta\right] dV.\end{aligned}$$

We can integrate this by parts to obtain:

$$\delta\mathcal{R} = \frac{K}{2}\left(\frac{\partial F}{\partial g_{\alpha\beta}}\delta n_\beta\bigg|_S + \iiint_V \left[-\frac{\partial}{\partial\alpha}\frac{\partial F}{\partial g_{\alpha\beta}} + \lambda\frac{\partial R}{\partial n_\beta}\right]\delta n_\beta dV\right), \tag{5.8}$$

where S is the bounding surface of V. If we assume that the surface energy of the nematic system is dominated by anchoring forces, which is typical of alignment surfaces produced by obliquely evaporated films [125, 126], then we can neglect the above surface term. Then, recalling that this must be a stationary value of $\mathcal{F}$ for arbitrary $\delta\mathbf{n}$, we obtain the following three Euler-Lagrange equations:

$$\frac{\partial}{\partial\alpha}\frac{\partial F}{\partial g_{\alpha\beta}} - \lambda\frac{\partial R}{\partial n_\beta} = 0, \qquad \text{sum over } \alpha. \tag{5.9}$$

Coupled with the constraint that $R(\mathbf{n}) = 0$, this gives four equations in the four unknowns, n_x, n_y, n_z and λ.

To solve these equations, we first need to compute F. Most papers and textbooks simply state the end results (equations (5.16) and (5.25)), but we present here a stepwise derivation for completeness. We start by expanding (5.9). The divergence term is:

$$(\nabla\cdot\mathbf{n})^2 = \left(g_{xx} + g_{yy} + g_{zz}\right)^2, \tag{5.10}$$

while the curl term is:

$$(\nabla\times\mathbf{n})^2 = \left(g_{yz} - g_{zy}\right)^2 + \left(g_{zx} - g_{xz}\right)^2 + \left(g_{xy} - g_{yx}\right)^2. \tag{5.11}$$

Summing these two pieces gives the following expression:

$$\begin{aligned}\frac{2F}{K} &= (\nabla \cdot \mathbf{n})^2 + (\nabla \times \mathbf{n})^2, \\ &= g_{\mu\mu}g_{\nu\nu} + g_{\mu\nu}g_{\mu\nu} - g_{\mu\nu}g_{\nu\mu}. \end{aligned} \tag{5.12}$$

Knowing that $\partial g_{\mu\nu}/\partial g_{\alpha\beta} = \delta_{\mu\alpha}\delta_{\nu\beta}$, where δ represents the Kronecker delta, gives:

$$\frac{\partial F}{\partial g_{\alpha\beta}} = 2(g_{\mu\mu}\delta_{\alpha\beta} + g_{\alpha\beta} - g_{\beta\alpha}). \tag{5.13}$$

We also compute $\partial R/\partial n_\beta$ as:

$$\frac{\partial R}{\partial n_\beta} = \frac{\partial n_x^2}{\partial n_\beta} + \frac{\partial n_y^2}{\partial n_\beta} + \frac{\partial n_z^2}{\partial n_\beta} = 2n_\beta. \tag{5.14}$$

We now substitute equations (5.13) and (5.14) into equation (5.9) to yield the following equations, which must be solved in order to determine the Cartesian components of the director field:

$$\frac{\partial}{\partial \alpha}(g_{\mu\mu}\delta_{\alpha\beta} + g_{\alpha\beta} - g_{\beta\alpha}) - \lambda n_\beta = 0 \quad \beta = x, y, z \tag{5.15a}$$

$$n_x^2 + n_y^2 + n_z^2 - 1 = 0 \tag{5.15b}$$

Written in vector form, as per DeGennes, these equations take the very simple form:

$$\nabla^2 \mathbf{n} = \lambda \mathbf{n}, \tag{5.16a}$$

$$\mathbf{n}^2 = 1. \tag{5.16b}$$

So, to solve for the Cartesian components of the director, we must simply solve Poisson's equation for $\mathbf{n}$ subject to the normalization constraint.

Alternatively, we can also represent $\mathbf{n}$ using spherical coordinates. Since $\mathbf{n}$ is a unit vector we have:

$$n_x = \sin\theta\cos\phi, \tag{5.17}$$

$$n_y = \sin\theta\sin\phi, \tag{5.18}$$

$$n_z = \cos\theta. \tag{5.19}$$

In this case, the normalization constraint is automatically fulfilled, and the Lagrange multiplier becomes zero. With this in mind, we first let C_θ and S_θ represent $\cos\theta$ and $\sin\theta$, and likewise for ϕ, and let θ_α and ϕ_α denote the partial derivatives of θ and ϕ with respect to α. We can then write the free energy as:

$$\begin{aligned}\frac{2F}{K} &= (\nabla\cdot\mathbf{n})^2 + (\nabla\times\mathbf{n})^2,\\ &= \theta_x^2+\theta_y^2+\theta_z^2+S_\theta^2(\phi_x^2+\phi_y^2+\phi_z^2)+2S_{2\theta}(\theta_x\phi_y-\theta_y\phi_x)\\ &\quad+2S_\theta^2C_\phi(\theta_y\phi_z-\theta_z\phi_y)-2S_\theta^2S_\phi(\theta_x\phi_z-\theta_z\phi_x).\end{aligned} \tag{5.20}$$

We see that the free energy can be written as a function of θ, $\theta_x,\theta_y,\theta_z,\phi_x,\phi_y$ and ϕ_z. Therefore, the Euler-Lagrange equations read:

$$\frac{\partial F}{\partial\theta}-\frac{\partial}{\partial x}\frac{\partial F}{\partial\theta_x}-\frac{\partial}{\partial y}\frac{\partial F}{\partial\theta_y}-\frac{\partial}{\partial z}\frac{\partial F}{\partial\theta_z}=0, \tag{5.21a}$$

$$\frac{\partial}{\partial x}\frac{\partial F}{\partial\phi_x}+\frac{\partial}{\partial y}\frac{\partial F}{\partial\phi_y}+\frac{\partial}{\partial z}\frac{\partial F}{\partial\phi_z}=0. \tag{5.21b}$$

Evaluating the terms explicitly yields:

$$\begin{aligned}\frac{\partial F}{\partial\theta} &= S_{2\theta}(\phi_x^2+\phi_y^2+\phi_z^2)+4C_{2\theta}(\theta_x\phi_y-\theta_y\phi_x)+2S_{2\theta}C_\phi(\theta_y\phi_z-\theta_z\phi_y)\\ &\quad-2S_{2\theta}S_\phi(\theta_x\phi_z-\theta_z\phi_x),\end{aligned} \tag{5.22a}$$

$$\begin{aligned}\frac{\partial}{\partial x}\frac{\partial F}{\partial\theta_x} &= 2\frac{\partial}{\partial x}(\theta_x+S_{2\theta}\phi_y-S_\theta^2S_\phi\phi_z),\\ &= 2(\theta_{xx}+S_{2\theta}\phi_{yx}+2C_{2\theta}\theta_x\phi_y-S_\theta^2S_\phi\phi_{zx}-S_\theta^2C_\phi\phi_x\phi_z-S_{2\theta}S_\phi\theta_x\phi_z),\end{aligned} \tag{5.22b}$$

$$\begin{aligned}\frac{\partial}{\partial y}\frac{\partial F}{\partial\theta_y} &= 2\frac{\partial}{\partial y}(\theta_y-S_{2\theta}\phi_x+S_\theta^2C_\phi\phi_z),\\ &= 2(\theta_{yy}-S_{2\theta}\phi_{xy}-2C_{2\theta}\theta_y\phi_x+S_\theta^2C_\phi\phi_{zy}-S_\theta^2S_\phi\phi_y\phi_z+S_{2\theta}C_\phi\theta_y\phi_z),\end{aligned} \tag{5.22c}$$

$$\begin{aligned}\frac{\partial}{\partial z}\frac{\partial F}{\partial\theta_z} &= 2\frac{\partial}{\partial z}(\theta_z-S_\theta^2C_\phi\phi_y+S_\theta^2S_\phi\phi_x),\\ &= 2(\theta_{zz}-S_\theta^2C_\phi\phi_{yz}+S_\theta^2S_\phi\phi_z\phi_y-S_{2\theta}C_\phi\theta_z\phi_y+S_\theta^2S_\phi\phi_{xz}+S_\theta^2C_\phi\phi_z\phi_x\\ &\quad+S_{2\theta}S_\phi\theta_z\phi_x),\end{aligned} \tag{5.22d}$$

$$\frac{\partial}{\partial x}\frac{\partial F}{\partial\phi_x} = 2\frac{\partial}{\partial x}(S_\theta^2\phi_x-S_{2\theta}\theta_y+S_\theta^2S_\phi\theta_z),$$

$$= 2(S_\theta^2\phi_{xx} + S_{2\theta}\theta_x\phi_x - S_{2\theta}\theta_{yx} - 2C_{2\theta}\theta_x\theta_y + S_\theta^2 S_\phi\theta_{zx} + S_\theta^2 C_\phi\theta_z\phi_x + S_{2\theta}S_\phi\theta_x\theta_z), \tag{5.22e}$$

$$\frac{\partial}{\partial y}\frac{\partial F}{\partial \phi_y} = 2\frac{\partial}{\partial y}(S_\theta^2\phi_y + S_{2\theta}\theta_x - S_\theta^2 C_\phi\theta_z),$$
$$= 2(S_\theta^2\phi_{yy} + S_{2\theta}\theta_y\phi_y + S_{2\theta}\theta_{xy} + 2C_{2\theta}\theta_x\theta_y - S_\theta^2 C_\phi\theta_{zy} + S_\theta^2 S_\phi\theta_z\phi_y - S_{2\theta}C_\phi\theta_y\theta_z), \tag{5.22f}$$

$$\frac{\partial}{\partial z}\frac{\partial F}{\partial \phi_z} = 2\frac{\partial}{\partial z}(S_\theta^2\phi_z + S_\theta^2 C_\phi\theta_y - S_\theta^2 S_\phi\theta_x),$$
$$= 2(S_\theta^2\phi_{zz} + S_{2\theta}\theta_z\phi_z + S_\theta^2 C_\phi\theta_{yz} - S_\theta^2 S_\phi\theta_y\phi_z + S_{2\theta}C_\phi\theta_y\theta_z - S_\theta^2 S_\phi\theta_{xz} - S_\theta^2 C_\phi\theta_x\phi_z - S_{2\theta}S_\phi\theta_x\theta_z). \tag{5.22g}$$

On collecting terms, one obtains the following two equations:

$$0 = S_{2\theta}(\phi_x^2 + \phi_y^2 + \phi_z^2) - 2(\theta_{xx} + \theta_{yy} + \theta_{zz}),$$
$$= S_{2\theta}|\nabla\phi|^2 - 2\nabla^2\theta, \tag{5.23a}$$

$$0 = S_\theta^2(\phi_{xx} + \phi_{yy} + \phi_{zz}) + S_{2\theta}(\theta_x\phi_x + \theta_y\phi_y + \theta_z\phi_z) + S_\theta^2(C_\phi(\theta_z\phi_x - \theta_x\phi_z) + S_\phi(\theta_z\phi_y - \theta_y\phi_z)),$$
$$= S_\theta^2\nabla^2\phi + S_{2\theta}\nabla\theta\cdot\nabla\phi + S_\theta^2(C_\phi(\nabla\theta\times\nabla\phi)\cdot\hat{\mathbf{y}} - S_\phi(\nabla\theta\times\nabla\phi)\cdot\hat{\mathbf{x}}). \tag{5.23b}$$

Notice two simplifying cases. First, if ϕ is constant, then equation (5.23b) does not apply and the gradient of ϕ vanishes, so one is simply left with:

$$\nabla^2\theta = 0. \tag{5.24}$$

Second, if instead θ is constant, then equation (5.23a) does not apply and the gradient of θ vanishes, so one has the commonly encountered result [126]:

$$\nabla^2\phi = 0. \tag{5.25}$$

Equation (5.24) will be of great importance to us in the following section. Equation (5.25) is also quite interesting, and one example in particular should be noted. Consider a liquid crystal between two plates, as in the twist configuration as shown in Figure 5.5. Let z be the direction normal to the plates, and have one plate at $z = 0$ and the other at $z = L$. If the plates can be considered

infinite in the xy-plane, then $\nabla = \partial/\partial z$ only, so equation (5.25) reads:

$$\frac{\partial^2 \phi}{\partial z^2} = 0. \tag{5.26}$$

We assume Dirichlet boundary conditions and choose the x-axis such that $\phi = 0$ at $z = 0$. We also have $\phi = \phi(L)$ at $z = L$, so the solutions to equation (5.25) are simply:

$$\phi = \frac{\phi(L)}{L} z \equiv \frac{2\pi z}{q}, \tag{5.27}$$

where we have implicitly defined the pitch of the director field, q according to:

$$q = \frac{2\pi L}{\phi(L)}. \tag{5.28}$$

Substituting this result in for $\mathbf{n}$ gives:

$$n_x = \sin\theta \cos\left(\frac{2\pi z}{q}\right), \tag{5.29a}$$

$$n_y = \sin\theta \sin\left(\frac{2\pi z}{q}\right), \tag{5.29b}$$

$$n_z = \cos\theta. \tag{5.29c}$$

We find that the director traces out a helical structure with pitch, q. If $q > 0$, the helix is right-handed, and if $q < 0$, the helix is left-handed.

Notice that one can add any integer multiple of 2π to $\phi(L)$ without physically changing the director at the boundary. This leads to a family of solutions with $q = 2\pi/(\phi_L + 2m\pi)$, where m is any integer, and $\phi_L \in (-\pi, \pi]$. To determine the correct solution, we must see which actually corresponds to a global minimum in the free energy. Under our assumptions, the free energy can be written from equation (5.20) as:

$$\frac{2F}{K} = S_\theta^2 \phi_z^2 = \frac{4\pi^2 S_\theta^2}{q^2}. \tag{5.30}$$

We see that the state with the largest $|q|$, or the smallest total twist, has the smallest distortion energy, and represents the correct solution.

Now consider the case with $\phi_L = \pi/2$, and $\theta = \pi/2$, so that the director orientation is perpendicular on the two boundaries. This represents the famous

twisted nematic phase [127]; the director traces out a quarter-helix in space. Notice that with $\theta = \pi/2$, one can add an integer multiple of π (instead of 2π) to ϕ_L and obtain equivalent boundary conditions. We find then that one can obtain two equivalent solutions with $q = \pm 4L$ for boundary values of $\pi/2$ and $-\pi/2$. In other words, the left- and right-handed solutions are degenerate, and both would be equally favored. Note also that if instead $0 < \theta < \pi/2$, then the boundary values $\pi/2$ and $-\pi/2$ are no longer equivalent, and the system picks the handedness that provides the minimum twist. In this case, $\pi/2 - \theta$ is known as the pretilt angle, and is important to prevent the system from switching between left- and right-handed twists. It also happens to be true that the performance of a twisted nematic display is often improved by increasing the twist to π or $3\pi/2$. This situation is referred to as a supertwisted nematic. But consider what happens for $\phi_L = \pi$. In this case, regardless of the pretilt, the boundary values $\phi(L) = \pi$ and $\phi(L) = -\pi$ are equivalent. Again, both chiralities, $q = \pm 2L$ are equally favored. However, one can enforce one particular handedness over the other by using chiral nematogens.

If the nematogens are chiral, then we must add a term, $(2\pi K/q_0)\mathbf{n} \cdot (\nabla \times \mathbf{n})$to the one-constant form of the Frank-Oseen free energy [128], where q_0 is called the natural pitch of the nematogen. If we again take the situation where θ is constant, and infinite substrates in the xy-plane then we can add this chiral contribution to the free energy in equation (5.20) to obtain:

$$\frac{2F}{K} = S_\theta^2 \phi_z^2 - \frac{4\pi}{q_0} S_\theta^2 \phi_z. \tag{5.31}$$

We add to this a constant term $(2\pi/q_0)^2$, which does not affect the gradients of the free energy so that we can write:

$$\frac{2F}{K} = S_\theta^2 \left(\phi_z - \frac{2\pi}{q_0} \right)^2. \tag{5.32}$$

Notice now that if one has $\mathbf{n} =$ constant, then the free energy is no longer zero. The equilibrium state for a nematic, with chiral molecules, is actually $\phi = 2\pi z/q_0$. In principle, this is similar to the twisted nematic phase, except that the pitch, q_0 is typically much smaller than the pitch in a twisted nematic, and the twist is caused by the liquid crystal itself, and not due to any boundary conditions. This phase is known as a cholesteric or a chiral nematic. In truth,

this is the phase that Reinitzer had first observed in 1888. The term cholesteric derives from the fact that the earliest chiral phases were found in derivatives of cholesterol, such as the cholesterol benzoate of Reinitzer's studies. In fact, the blue and purple colours that Reinitzer had observed were due to three-dimensional chiral nematic phases, known as blue phases [129], which act as three-dimensional photonic crystals.

For the standard cholesteric phase, the Euler-Lagrange equations are the same as the twisted nematic case ($\partial^2\phi/\partial z^2 = 0$). For the same boundary conditions as earlier, we have the same family of solutions as before:

$$n_x = \sin\theta \cos\left(\frac{2\pi z}{q}\right), \tag{5.33a}$$

$$n_y = \sin\theta \sin\left(\frac{2\pi z}{q}\right), \tag{5.33b}$$

$$n_z = \cos\theta, \tag{5.33c}$$

with $q = 2\pi/(\phi_L + 2m\pi)$. However, unlike before, the solution that is actually a minimum of the free energy is not the one with the largest $|q|$. Writing out the free energy from equation (5.32) explicitly gives:

$$\frac{2F}{K} = S_\theta^2 \left(\frac{2\pi}{q} - \frac{2\pi}{q_0}\right)^2. \tag{5.34}$$

This is a minimum when $q \sim q_0$. If m could take on any value, this would be satisfied exactly if:

$$m = \frac{L}{q_0} - \frac{\phi_L}{2\pi}. \tag{5.35}$$

Typically for cholesterics, we have $L \gg q_0$, so we find that the solution that minimizes the free energy is the one with $m = [L/q_0]$, where the square brackets denote rounding to the nearest integer. Note that the presence of a chiral nematogen allows only a helix of the same handedness as the molecule to minimize the free energy. This is how one can obtain stable supertwisted nematic arrangements.

5.3 Alignment of Nematic Liquid Crystals in GLAD Films

In order to make a useful device based on nematic liquid crystals, one must first align the nematics in a known way. In commercial devices, this is almost always done by treating a substrate (typically glass) with an alignment layer to induce known boundary conditions on $\mathbf{n}$. There are many ways to do this including rubbed polyimide [130,131], photoalignment using azo-benzenes [132] and surface relief [133]. Additionally, one can also use obliquely evaporated films, as first pointed out by Janning, in 1972 [21]. Guyon *et al.* then investigated [134] the alignment of the mesogen N-(4-methoxybenzylidene)-4-butylaniline (MBBA) on pure slanted post SiO films for all deposition angles, α. The films in question were deposited under conditions for which normal incidence films would have been 10 - 600 nm thick. Guyon discovered that for films with $\alpha < 45°$, there was no preferred orientation of the liquid crystal. For $45° \leq \alpha < 80°$, Guyon found that the orientation of the director was perpendicular to the deposition plane. In other words, he found that $\mathbf{n}||\hat{\mathbf{b}}$, the broadening vector. For $\alpha \geq 80°$, the liquid crystal was found to lie in the deposition plane, with a pretilt angle of between 20° and 30°. This behaviour above 80° corresponds with the point at which columns in a GLAD film start to become isolated, and the mesogens can infiltrate into the structure of the film. Goodman *et al.* as well as Uchida *et al.* then demonstrated [125, 126] a two-dimensional finite element approach to modeling the director field in such an arrangement using a finite element solution of equation (5.24), which we adopt here to better characterize the alignment of liquid crystals in GLAD films.

5.3.1 Finite Elements in Two-Dimensions

We imagine a case where we have GLAD columns distributed on a periodic square lattice, with period a as shown in Figure 5.6(a). Along the line XX', the GLAD film has the geometry shown in Figure 5.6(b). The columns have a diameter, d , measured in the xy-plane, a height, T^{total} and column tilt, β'. The fractional density is related to these quantities through:

$$\varrho = \pi d^2/4a^2. \tag{5.36}$$

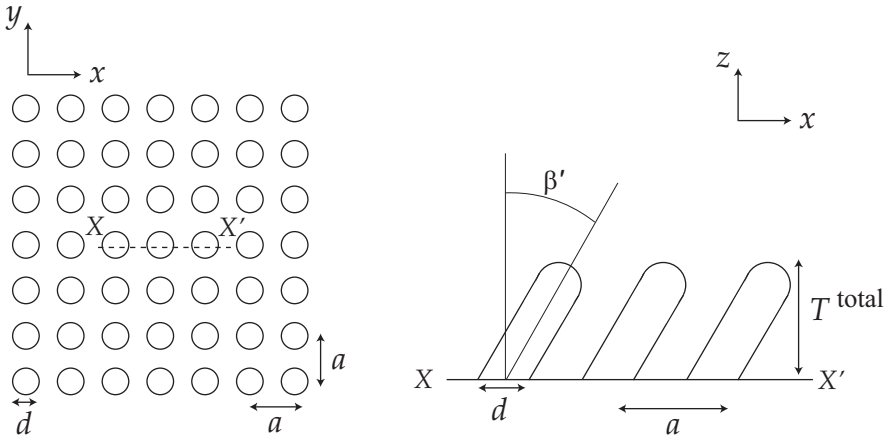

(a) Square lattice on the xy-plane

(b) Depiction of GLAD film in the xz-plane

Figure 5.6: Geometry of 2D GLAD film for finite element simulations

The shape of the top of the posts, as we shall see, is crucial to the solution to the finite element model, and can be varied. We see that there is mirror symmetry about the line XX', so along this line, there can be either no y-component of the director, implying $\phi = 0$, or the director must be in the y-direction exclusively, so that $\mathbf{n} = \hat{\mathbf{y}}$ everywhere. The latter case is representative of the situation Guyon encountered for films with $45^\circ \leq \alpha < 80^\circ$ and we will not be concerned with this case. The case for which $\phi = 0$ is much more interesting, and solving for the director is reduced to the problem of solving the two-dimensional Laplace equation on θ, as given in equation (5.24). We will solve this problem using a finite element approach with Dirichlet boundary conditions.

Nematic Defects

We must now make a comment about boundary conditions. We recall from the earlier discussion on the twisted nematic and cholesteric phases, that one can specify boundary conditions in several physically equivalent manners, that lead to different solutions to the Laplace equation. For the case at hand, we restrict θ to the range $(-\pi/2, \pi/2]$, but we must be wary of the behaviour at the (equivalent) end-points of this range. To explain the situation we consider the case of a small semicircular defect as shown in Figure 5.7. The semicircular defect is described by the function $z = f(x) = \sqrt{R^2 - x^2}$, where $R$is the radius

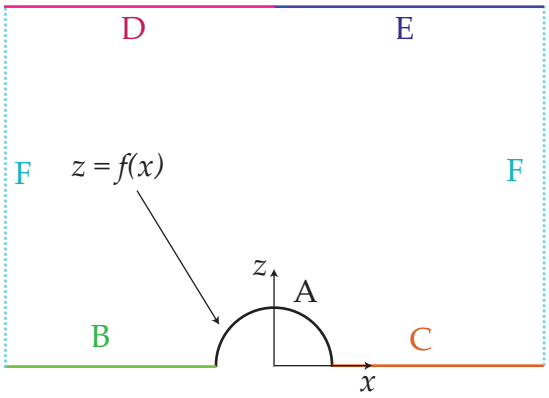

Figure 5.7: Illustration of point defects in nematic systems

of the defect. We can identify six regions (A-F) on which boundary conditions are required. On F, we can simply specify periodic boundary conditions and on B, C, D and E, we choose to specify perpendicular, or homeotropic alignment, $\theta = 0$. Along A we choose planar, or homogeneous alignment, tangent to the boundary. On A, if $\mathbf{n}$ is to lie tangent to the semicircle, then we require:

$$\tan\theta = \frac{dx}{dz} \qquad \theta = \arctan\left(\frac{-\sqrt{R^2 - x^2}}{x}\right) \tag{5.37}$$

If one solves this problem subject to these boundary conditions, one obtains the director field shown in Figure 5.8(a). Notice that by symmetry, the homeotropic boundary condition on the opposite substrate requires that, along the z-axis, $\theta = 0$. This is in conflict to the boundary condition specified along the defect. We see then that at the peak of the semicircle there is a defect in $\mathbf{n}$, known as a boojum [135, 136]. At this boojum, the director field is discontinuous; the limiting value of θ is different depending on the direction from which one takes the limit. In a 3D case, this is a very similar situation to what occurs with lines of longitude at the north or south poles. One might wonder if there a way to remove the boojum. For instance, let us consider modifying the boundary conditions. Letting $\theta = 0$ on B and D as before, we redefine $\theta = \pi$ on C and E. We also redefine the boundary condition on A. For $x < 0$, we retain $\theta = \arctan\left(-\sqrt{R^2 - x^2}/x\right)$, as before. However, for $x > 0$ we let $\theta = \arctan\left(-\sqrt{R^2 - x^2}/x\right) + \pi$. Notice that these choices ensure continuity in θ at the intersection between the defect and the substrate, as well as at the

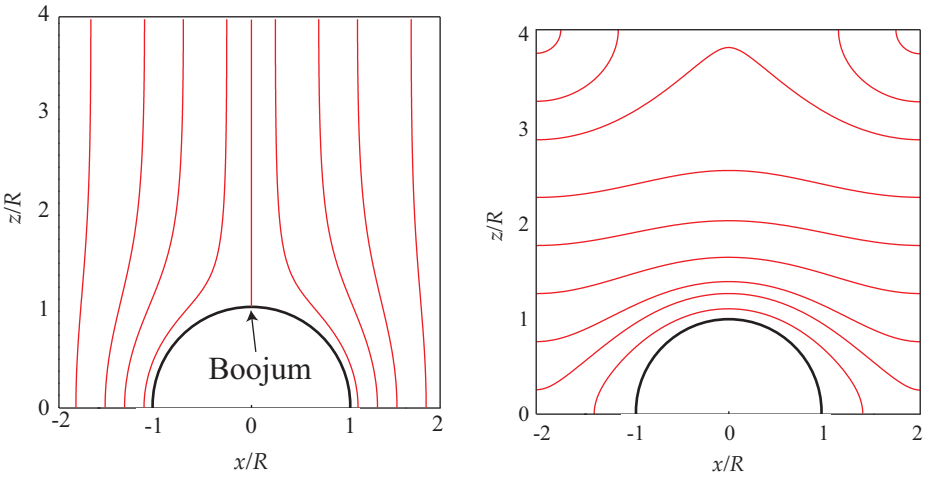

(a) Low energy configuration (b) High energy configuration

Figure 5.8: Simulated director field around a circular defect with homeotropic substrate alignment

peak of the semicircle, unlike the case before. Solving for the director field in this case yields the result shown in Figure 5.8(b). Notice that the boojum on the defect has vanished. However, the price for this change is that there is now a discontinuity in the director field on the z-axis on the upper substrate, directly above the defect. There are also additional discontinuities at the four corners of the unit cell. If one calculates the free energy of the two cases, it can be shown that the free energy in the first case is one third of that of the second case. Changing the boundary conditions further will simply generate higher energy solutions, just as it was with the twisted nematic. The lesson is again that one must be careful in specifying boundary conditions. There are a few general rules to follow. Primarily, one should always attempt to specify boundary conditions so that there are no defects along the periodic edges of the unit cell. One should then focus primarily on minimizing the magnitude of the discontinuities at sharp features. Finally, one should attempt to specify θ in the range $(-\pi/2, \pi/2]$, but this is not mandatory. However, one should only specify θ outside this range when one encounters a branch cut, similar to the one described above on the peak of the semicircular defect. With those rules in mind, we can proceed with applying these techniques to models of GLAD films.

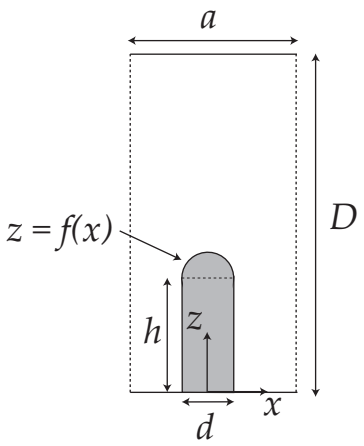

Figure 5.9: Single-substrate vertical post liquid crystal cell for finite element approach

Vertical Posts

We consider first the simple case of vertical posts, with $\beta' = 0$. To begin we consider the case where a cell is constructed using a vertical post on one edge, and a flat surface (which can be another substrate, or open air) on the other edge. The unit cell for this case is shown in Figure 5.9. The unit cell has a width of a and a height, D, and there is one vertical post structure on the bottom, The vertical post is made up of a rectangle, bordered by $x = \pm r$ and $z = 0$ and $z = h$. The top of the post is defined by a curve $z = f(x)$ on the domain $x \in [-r, r]$, and the film height is given by $T^{\text{total}} = f(0)$. Dirichlet boundary conditions are specified on the top and bottom surfaces, as well as the vertical post itself, while periodic boundary conditions are always in effect along the sides of the unit cell.

We consider first an idealized vertical post with a flat top ($f(x) = h = T^{\text{total}}$). We can specify either planar ($\theta = \pm\pi/2$) or homeotropic ($\theta = 0, \pi$) boundary conditions on the substrates, and we restrict ourselves to tangential alignment along the posts themselves. We recall from the earlier discussion that changing any boundary condition by π does not change the nature (planar, homeotropic, *etc.*) of the alignment at the surface, but it can change the configuration of molecules in the bulk. There are four possible substrate combinations (planar or homeotropic on the top and bottom surfaces), and one can obtain several different solutions for the director field, depending on the exact nature of the boundary conditions chosen. We recall from the earlier discussion

that changing the value of a boundary condition by an increment of π does not change the physical orientation of a molecule on the boundary, but can yield a completely different solution for the director field.

Figure 5.10 shows several different solutions to equation (5.25) for the director field given various boundary conditions, solved using FlexPDE (Version 5.0.20). For illustrative purposes, the film thickness was set to $h = T^{\text{total}} = 500$ nm, with a cell thickness, $D = 1000$ nm. The column diameter is $d = 100$ nm, and the column spacing is $a = 200$ nm, resulting in $\bar{\varrho} = 0.2$, which is a typical value for films deposited at $\alpha \sim 80^\circ - 85^\circ$. The results are split into four groupings, shown individually in Figures 5.10 and 5.11, each having a different combination of planar or homeotropic boundary conditions on the top and bottom surfaces. For each group, three possible solutions are shown: a homeotropic state, where molecules are vertical in the bulk of the cell, a planar state, where molecules are horizontal in the bulk of the cell, and a tilted state, where molecules adopt a slanted orientation in the bulk. These different configurations arise because of the difference in the locations of defect states in the director field, which in turn originate from $\pm\pi$ changes in the boundary conditions. The defect states are also labeled in Figure 5.10. They can either be point defects, which frequently, though not exclusively occur at sharp corners, or line defects, which occur along boundaries. In each case, we find that the lowest energy solution is always the tilted state. This state shown at the left, and the calculated free energy of the state, $\mathcal{F}$, is defined to be unity. The relative free energy of the other states are also indicated. There are a number of important conclusions to be drawn from these results. First, in each case the tilted state is actually a degenerate state. The mirror image state naturally has the exact same energy, and can be obtained by a suitable change in boundary conditions. This is similar to the twisted nematic case described earlier; neither of the two states is energetically favored. This implies that locally, one of the two degenerate cases may be preferred due to some stochastic local conditions, but nearby regions may favour the opposite state. This will result in domain boundaries, leading to effects such as optical scattering and a lack of anisotropy on larger (useful) scales. The planar and homeotropic states, by contrast are not degenerate. They have the same symmetry (about the z-axis) as the film. As a result, such a configuration would not give rise to grain boundaries, and could lead to large, monodomain samples. However, they are higher energy states

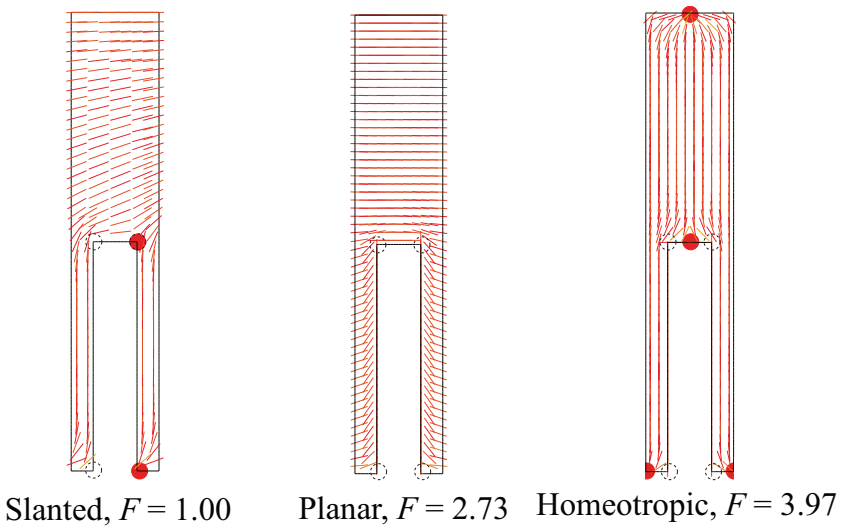

(a) Upper and lower planar alignment

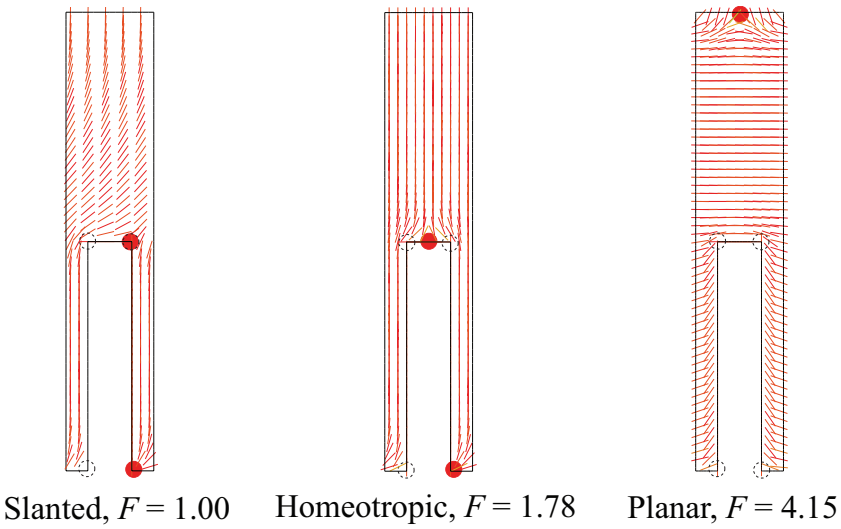

(b) Upper homeotropic and lower planar alignment

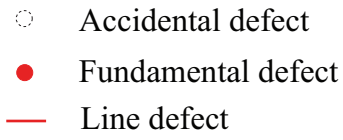

Figure 5.10: Possible director configurations for a vertical post film with different cell boundary conditions

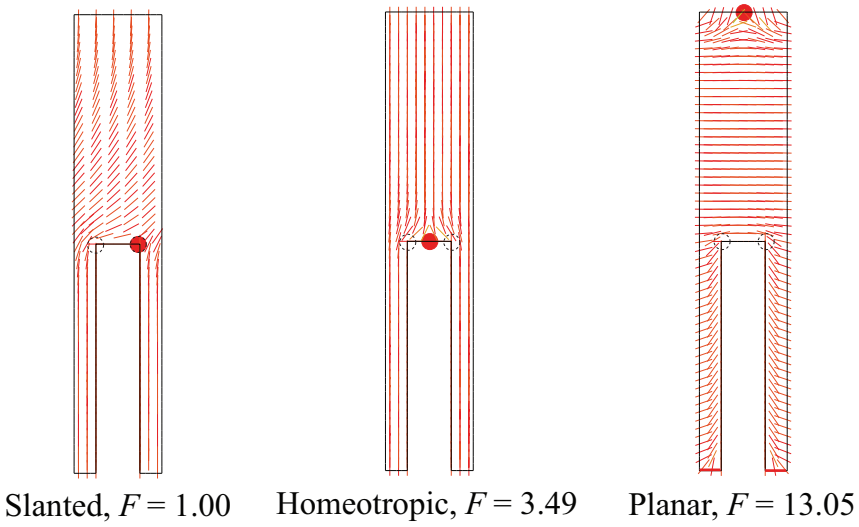

(a) Upper and lower homeotropic alignment

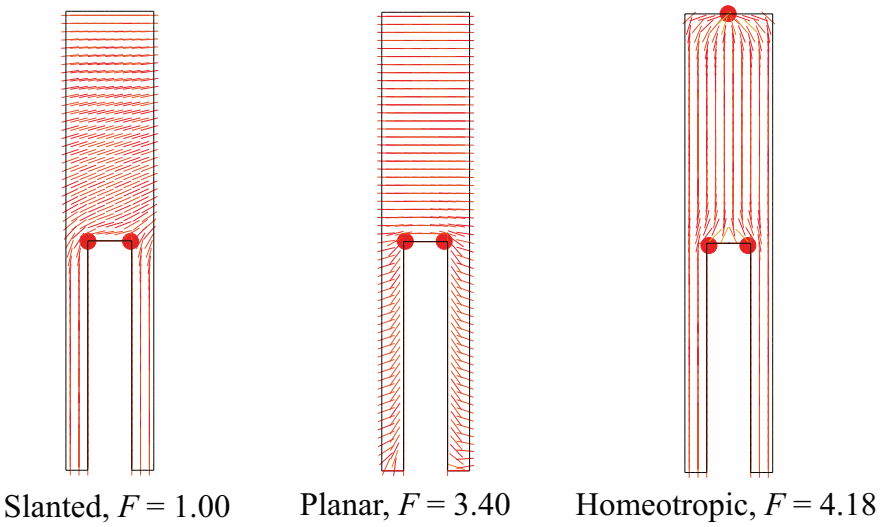

(b) Upper planar and lower homeotropic alignment

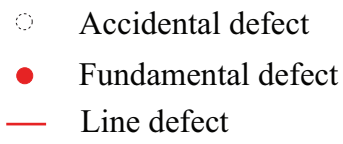

Figure 5.11: Possible director configurations for a vertical post film with different cell boundary conditions (continued)

than the tilted configuration, and are not preferred under the geometry considered here. Finally, it is of note that of the higher energy homeotropic and planar states, the state matching the alignment at the upper surface is more energetically preferred.

The distortion energies come from two sources: the continuous bend and splay distortions throughout the bulk,[5.5] as well as the localized distortions in the director field around defect states. In the above examples, most of the energy costs are associated with distortions arising due to defect states. In general, states with larger numbers of defects are more energetically unfavourable. For instance, in Figure 5.10(b), there is virtually no bulk distortion of the director field in the homeotropic cases, yet the energy of the system is higher than the tilted case, which possesses a significant splay distortion, due solely to the defect located at the center of the post. We can identify different types of defects. There are "accidental" defects, which arise due to sharp changes in the boundaries of the system. These are denoted by dotted circles in Figure 5.10. Such defects are prevalent in this model, but if the boundaries were smoothed (using a short radius, circular transition, for instance), then these defects would vanish. We will see an example of this shortly. We can also identify fundamental defects, which are defect states that can not be removed by a simple smoothing of the boundaries of the system and are identified by red circles in Figure 5.10. The boojum described earlier is an example of such a defect. In certain cases, a fundamental defect can overlap an accidental defect. Finally, there are also line defects, represented by thick red lines. An example of this can be seen in Figure 5.11(a), and the associated energy cost can be seen to be very high.

One major aspect that affects the presence and location of defects is the shape of the post. In particular, the top profile of the post, modeled by the curve $z = f(x)$ in our approach, has a major effect on the energetics of the director field. The flat profile used above was a fairly poor model, but served to illustrate the importance of boundary conditions. A much more reasonable model would be a circular top given implicitly by the equation:

$$x^2 + (z - h)^2 = r^2. \tag{5.38}$$

[5.5] There is no twist distortion in two dimensions

For tangential boundary conditions on the post, we have a similar situation as described earlier with the circular defect. The angle θ along the top of the post is given by the following:

$$\tan\theta = \frac{dx}{dz} \qquad \Rightarrow \qquad \theta = \arctan\left(\frac{h-z}{x}\right), \tag{5.39}$$

where we recall that we can always add π to θ without changing the orientation of a molecule on the surface. Note that the presence of the circular profile eliminates the sharp corner at the top of the vertical post. This results in the elimination of a number of accidental defects, which could potentially lead to different director fields being favored.

This is in fact true and an interesting case to examine. For simplicity, we relax the need for a boundary condition on the top surface, in order to determine the effect of the film on a semi-infinite sample, and consider the case where we have planar alignment along the bottom substrate. We can again find a number of states having tilted, homeotropic or planar alignment in the bulk, as shown in Figure 5.12. Notice that in this instance, we still find that a tilted state (Tilted

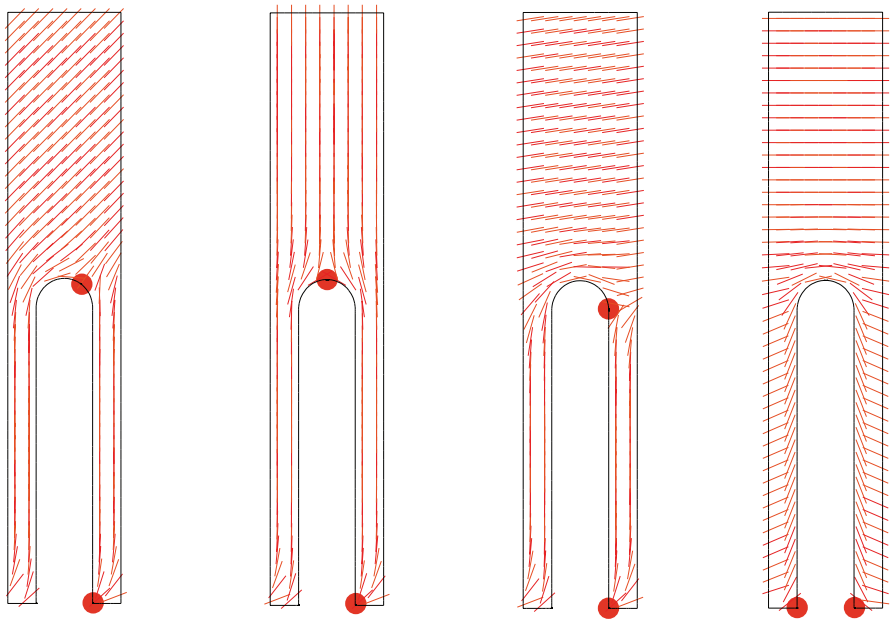

Tilted 1, $F = 1.000$ Homeotropic, $F = 1.004$ Tilted 2, $F = 1.092$ Planar, $F = 2.124$

Figure 5.12: Possible alignment configurations for a vertical post film with a circular profile, given planar boundary conditions on the lower substrate, and homeotropic alignment on the upper surface

1) has the lowest energy. This state is identically degenerate with its mirror image, and, practically, almost degenerate with the homeotropic state. However, notice that in this case, the lowest energy tilted state does not have the defect at the right hand corner of the post, but instead at an intermediate point along the rounded surface. The minimum energy state is found about 40% of the way along the surface, as measured from the peak. Placing the defect at the right hand edge of the post yields the Tilted 2 state, which is now notably a higher energy configuration than the homeotropic state, unlike the case having a flat top to the vertical post. This significant change in behaviour indicates the importance of the shape of the column when it comes to liquid crystal alignment. Rounded profiles clearly respond differently than rectangular ones, and it is probable that ellipsoidal, or asymmetric shapes will have similar effects. We also note that a planar state can also be found, but because of the significant director field curvature between the posts, the energy of this state is much higher.

As earlier, the configurations shown are distinguishable by the location of the defect states. In particular, the homeotropic and two tilted states are individual instances of the director field that results from continuously translating the defect state from the peak of the rounded surface to its right-hand edge. For the film under consideration here, with $T^{\text{total}} = 500$ nm, $a = 200$ nm and $d = 100$ nm, we have found that the lowest energy state is a (degenerate) tilted state, resulting in liquid crystal molecules oriented at $\theta_{\text{bulk}} = 45.6^\circ$. However, as the diameter of the column changes, the location of the defect that corresponds to the lowest energy state varies. As a result, the orientation of liquid crystal molecules in the bulk also changes. Figure 5.13 tracks θ_{bulk} as a function of column diameter, for a $T^{\text{total}} = 500$ nm film, maintaining an $a = 200$ nm column spacing. We find that at the lowest ratios of column diameter to column spacings, the alignment tends toward the homeotropic state, which is important, since this is non-degenerate. This behaviour is predicted for $d \lesssim 60$ nm, which corresponds to $\bar{\varrho} \lesssim 0.07$ by equation (5.36), which corresponds to deposition angles very close to 90°. However, these values must not be taken as hard predictions, as our model ignores the true three-dimensional nature of the film, the actual surface boundary of the vertical posts, as well as the boundary condition at the opposite surface from the GLAD film. Still, the important conclusion is that the molecular alignment of liquid crystals depends significantly

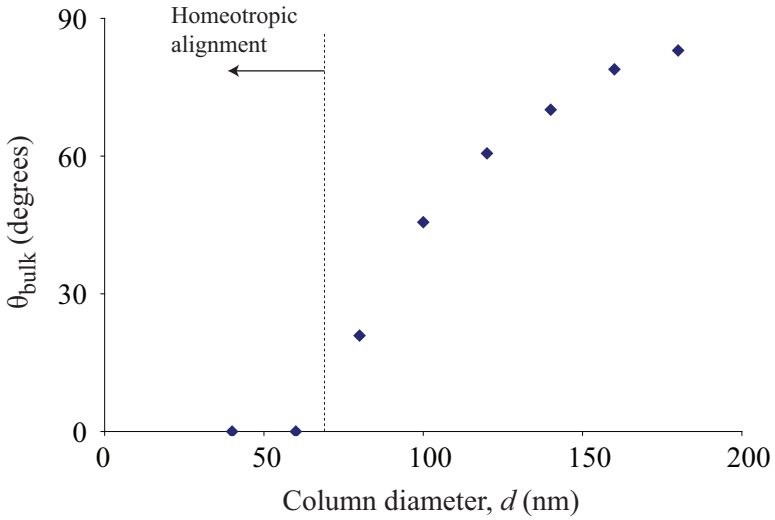

Figure 5.13: Simulated bulk liquid crystal orientation, θ_{bulk}, as a function of column diameter, d, for a $T^{total} = 500$ nm, $a = 200$ nm vertical post with a rounded surface

on the geometry of the film structure, and that for vertical posts, less dense films tend to promote single domain, homeotropic alignment.

So far, we have only considered the case of tangential boundary conditions along the GLAD film. It is certainly possible for liquid crystalline molecules to align in a different configuration. One natural option is for the molecules to align normal to the surface of the posts. However, for vertical posts, this will always result in an arrangement filled with defects because of the circular symmetry of the system. Since there is no preferred direction normal to a vertical post (in three dimensions), molecules will simply extend out radially from each post, and will inevitably encounter nearby molecules with multiple different orientations. Defect states will naturally arise because of this discontinuity in molecular alignment. The situation is different for slanted posts, however, which we consider in the following section, as well as vertical structures, such as the SBD geometry, that are not circularly symmetric.

Slanted Posts

We now seek to apply the same procedure to slanted post structures. We consider three types of slanted posts, parallel, rectangular and rounded, as depicted in Figure 5.14. The parallel and rectangular structures both reduce to

the flattened vertical post structure for $\beta' = 0$, and naturally the rounded structure reduces to the rounded vertical post structure. We wish to determine the

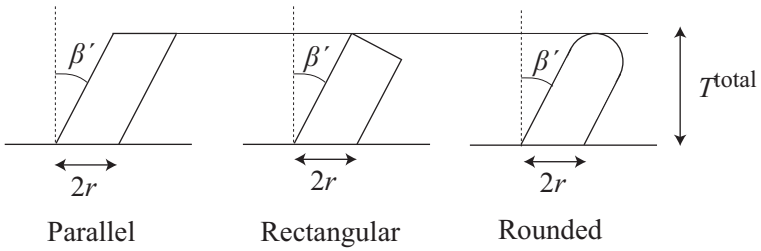

Figure 5.14: Slanted post models for finite element simulations

lowest energy configuration for each of these three structures as a function of column tilt, β'. We restrict ourselves to the case of planar alignment along the lower substrate, and remove the upper surface boundary condition to determine the influence of the slanted post film on the director alignment of a semi-infinite sample.

Let us examine the parallel system first. Three solutions for a post with $\beta' = 30°$, $a = 200$ nm, $d = 100$ nm and $T^{\text{total}} = 500$ nm are shown in Figure 5.15, along with the respective free energy of each system. Each of the three solutions shown above possesses the same fundamental defect at the bottom right of the slanted post structure, but differ in the location of the fundamental defect along the top of the post. As the defect moves, both the free energy of the director field, as well as the inclination angle, θ, of the director field far from the post are affected. The lowest energy state has the defect at the right-hand side of the post. This is the same as in the vertical post cases described above, however, the state is no longer symmetric (degenerate) with having the defect on the left-hand side, as a result of the broken symmetry of the slanted post. This is consistent with the results obtained by both Guyon and Goodman [126, 134]. The tilt of the liquid crystal molecules is in the same direction as the slanted post film, and with the parallel surface at the top of the film, the tilt is significantly larger than that of the film. As the defect moves left, the tilt of the liquid crystal molecules becomes more vertical, before ultimately tilting in the opposite direction of the post. However, without external influences, one does not expect to be able to control the location of the defect state, and should expect the lowest energy, right-side defect state, to prevail.

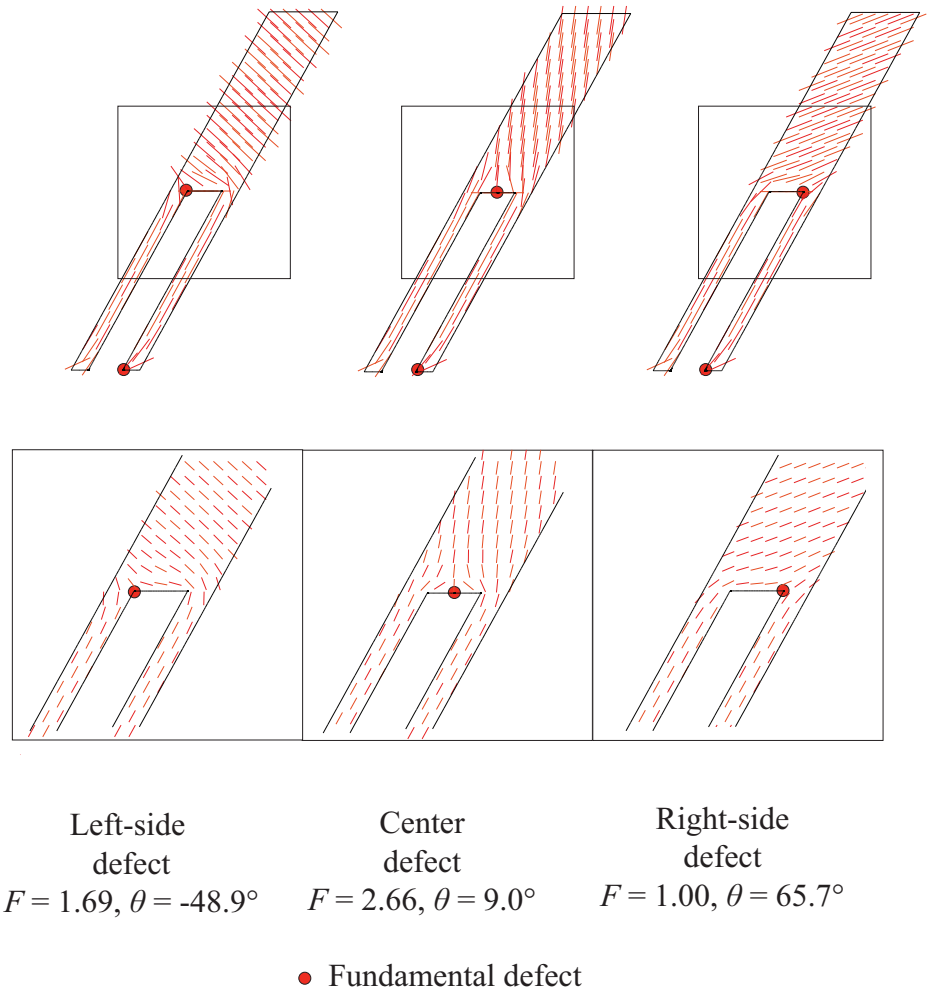

Figure 5.15: Three solutions for the director field in a slanted post configuration, with a parallel structure. Lower images are magnified versions of the boxed regions in the upper images.

The situation for the other two types of slanted post structures (which are hardly exhaustive) is quite different. The lowest energy configurations for the rectangular and rounded styles, along with a repeat of the parallel style, are illustrated in Figure 5.16, again for $\beta' = 30°$. Unlike the parallel case, the

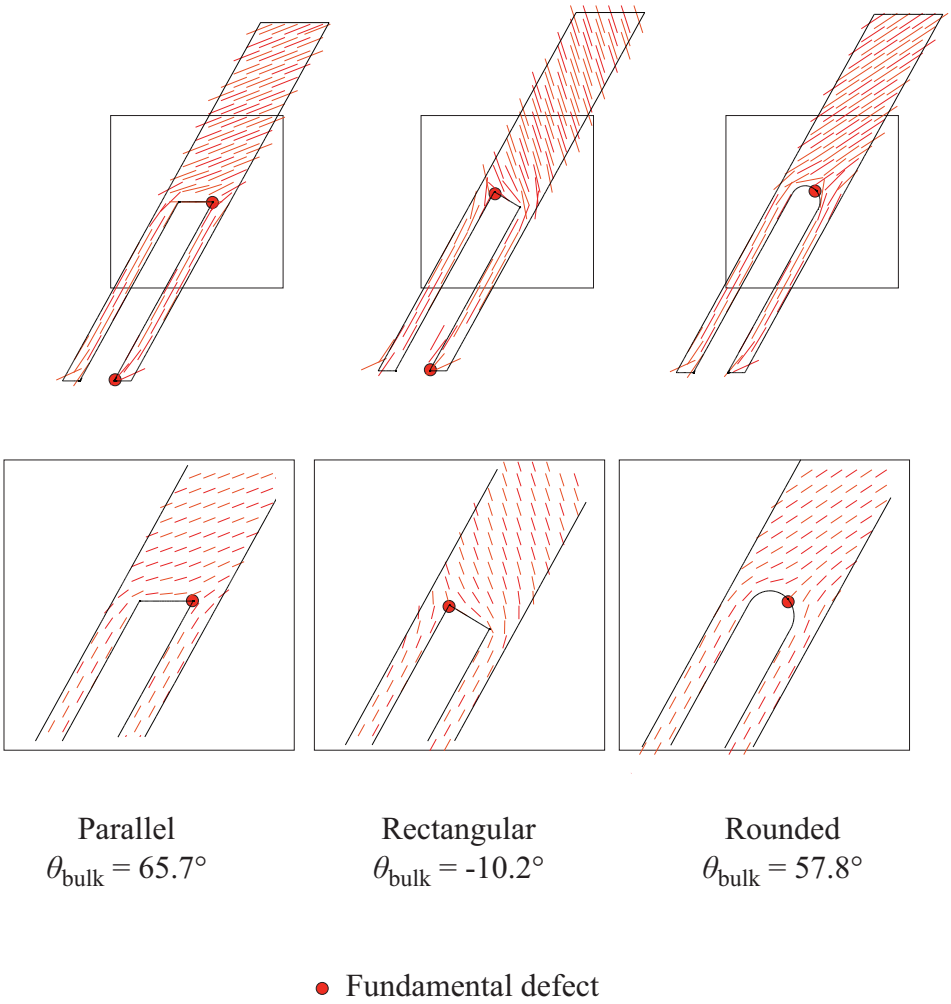

Figure 5.16: Lowest energy director field configuration for slanted post structures at $\beta' = 30°$. Lower images are magnified versions of the boxed regions in the upper images.

rectangular and rounded structures do not have a lowest energy state corresponding to a right-side fundamental defect. The lowest energy configuration for the rectangular structure is actually a left-side defect, and the alignment of liquid crystalline molecules in the bulk is opposite the direction of the slanted

posts. For the rounded structure, the lowest energy configuration possesses a defect near (but not exactly upon) the apex of the rounded surface. In this case, the liquid crystalline molecules are aligned in the same direction as the slanted post, with a value much closer to β' than observed in the parallel case. These significantly varying results reinforce just how much the top portion of the slanted post structure affects the orientation of liquid crystals in the bulk. While the rounded structure is probably the best approximation considered here to a real-world slanted post structure, the actual form of a slanted post surface is considerably more complex and variable. This variability underscores one of the greatest challenges in attempting to align liquid crystals in GLAD films.

Figure 5.17 shows the dependence of the bulk liquid crystal orientation, θ_{bulk}, as a function of the column diameter, d, for each of the parallel, rectangular and rounded structures, with $T^{\text{total}} = 500$ nm and $a = 200$ nm. We see that as the column size shrinks, θ_{bulk} approaches β'. This occurs because the influence of the top of the column is dwarfed by the influence of the slanted post itself. At the opposite extreme, as the column size approaches the column spacing, the three column structures yield vastly different results for θ_{bulk}. In particular, the parallel and rounded structures tend to promote increasing θ_{bulk} with $\theta_{\text{bulk}} \to 90^\circ$ at large column diameters, while at the same time the rectangular structure promotes decreasing values for θ_{bulk}[5.6]. These results again indicate the importance of the shape of the column in determining liquid crystal alignment, but also suggest that that effect can be mitigated somewhat by reducing the density of the film as much as possible.

Figure 5.18 shows how θ_{bulk} changes for the three slanted post structures with β'. A $d = 100$ nm, $a = 200$ nm and $T^{\text{total}} = 500$ nm structure is considered. The results again indicate the significance of the column shape. Notably, the rectangular structure exhibits much different behaviour than the rounded and parallel shapes. Though it is not obvious from the graph, in the rectangular case, the defect state begins on the left-hand side at low β', promoting negative θ_{bulk}, but slowly moves toward the right-hand side as β' increases, promoting positive θ_{bulk}. It is also worthwhile to notice that in all three cases, as β' increases, so does θ_{bulk}, presumably toward a value of 90° as $\beta' \to 90^\circ$ as

[5.6] In this case, θ_{bulk} appears to approach $-\beta'$ at large column diameters in the rectangular case, but this is purely coincidental.

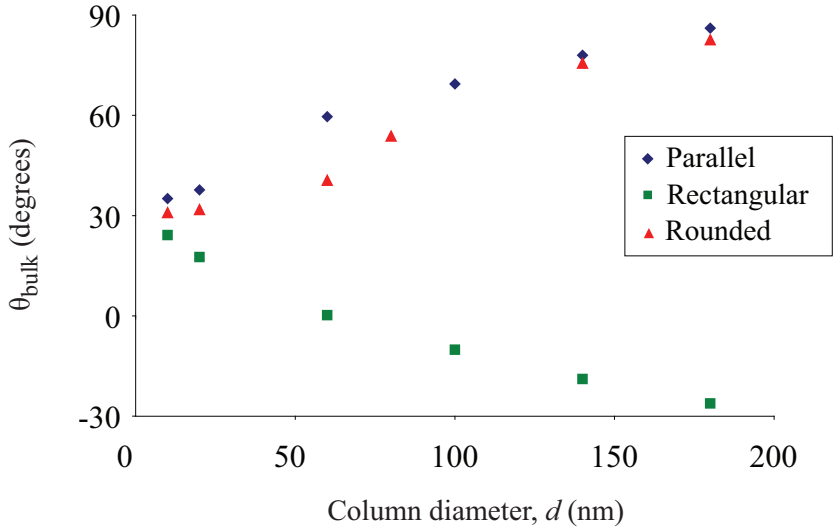

Figure 5.17: Simulated bulk liquid crystal orientation, θ_{bulk}, as a function of column diameter, d, for a $T^{total} = 500$ nm, $a = 200$ nm slanted posts

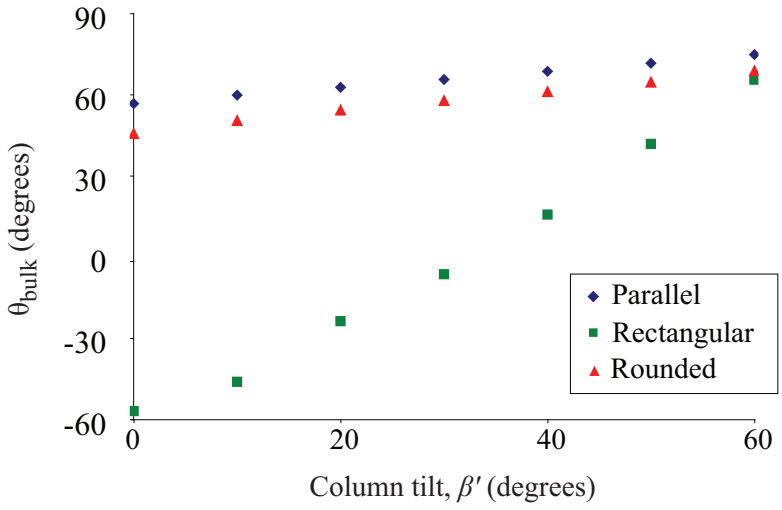

Figure 5.18: Simulated bulk liquid crystal orientation, θ_{bulk}, as a function of column tilt, β', for a $T^{total} = 500$ nm, $a = 200$ nm slanted posts

well. This result indicates that one can indeed hope to influence the orientation of liquid crystal molecules through the tilt of the GLAD film, but that the relationship between β' and θ_{bulk} is heavily dependent on a variety of factors.

Cell Structures

In addition to having a GLAD film filled with liquid crystals in open air, one can also employ a cell structure, as shown in Figure 5.19. Such a structure uses two opposing GLAD substrates to induce molecular alignment, and can be much easier to handle for experimental purposes. We can apply the finite

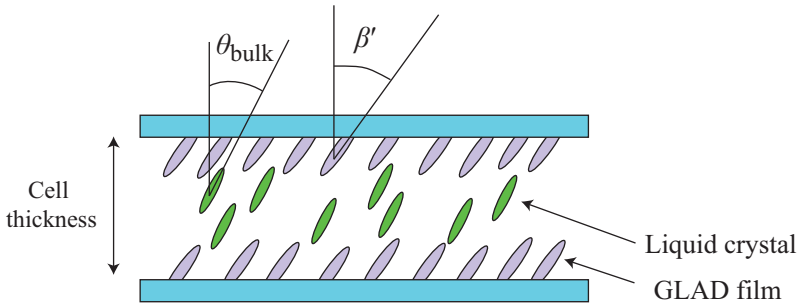

Figure 5.19: Liquid crystal cell structure, comprised of two GLAD films as substrates

element method to such a structure as well. For brevity, we restrict ourselves to slanted posts with rounded tops only, and require the system to be symmetric given a 180° rotation of the cell in the plane of the page. This ensures that the defect states are in symmetrical positions on both the top and bottom posts. Note that the cell thickness (5-100 μm) is typically one or two orders of magnitude larger than the film thickness (0.5 - 1.0 μm), and this is potentially problematic when finding numerical solutions. Fortunately, if the cell thickness is at least four times as large as the film thickness, the liquid crystal orientation in the bulk becomes independent of cell thickness. Therefore, we can model the system as having a much smaller cell thickness than in reality.

Figure 5.20(b) shows the behaviour of θ_{bulk} as a function of the tilt angle of the columns, β', for a cell structure with $a = 200$ nm, $d = 100$ nm, $T^{\text{total}} = 500$ nm and a cell thickness of 2000 nm. Figure 5.20(a) shows the behaviour of θ_{bulk} as a function of the column diameter, d, for a cell structure with $a = 200$ nm, $\beta' = 30°$, $T^{\text{total}} = 500$ nm and a cell thickness of 2000 nm. We observe that increasing β' and decreasing d both have the same effect of increasing

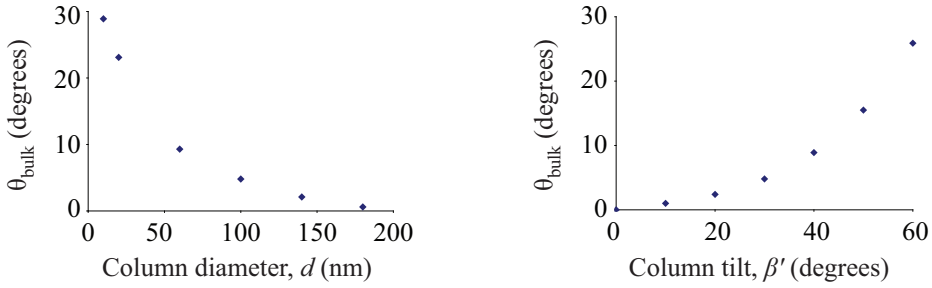

(a) θ_{bulk} as a function of d

(b) θ_{bulk} as a function of β'

Figure 5.20: Dependence of liquid crystal orientation, θ_{bulk}, on a cell structure, with $a = 200$ nm, $T^{total} = 500$ nm and a 2000 nm cell thickness

θ_{bulk}. With regards to β', this is the same behaviour that was observed in the absence of the cell structure as shown in Figure 5.18. In contrast, the behaviour with respect to d is opposite to that previously encountered, seen in Figure 5.17, where θ_{bulk} was found to increase with d outside of the cell structure. However, it should be noted that in both cases, as the column diameter approaches zero, both cases approach a state where $\theta_{bulk} = \beta'$. One final important observation is that for a vertical post film, the cell structure promotes homeotropic alignment, regardless of column diameter, unlike in the situation lacking the cell structure, as shown in Figure 5.13.

Normal Boundary Conditions

Though we have so far only considered the case where liquid crystals lie parallel to the film columns, other boundary conditions are possible. We will consider the next simplest case where liquid crystals lie perpendicular (or homeotropically) to the film surfaces. As discussed earlier, for actual vertical posts possessing rotational symmetry, solutions that are not symmetric for rotations about the vertical axis will lead to polydomain alignment experimentally. This implies that for a vertical post structure, regardless of the nature of liquid crystal alignment on the posts, the only allowable monodomain director field is vertical alignment through the bulk. However, for vertical structures that are not rotationally symmetric, such as vertical films fabricated using serial bideposition, this restriction does not apply due to the broken symmetry of such a system.

Figure 5.21 shows the lowest energy director field configurations for a ver-

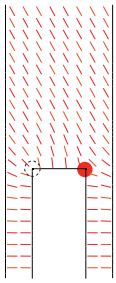

(a) Flat surface, $d = 100$ nm

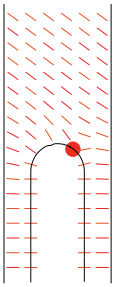

(b) Rounded surface, $d = 100$ nm

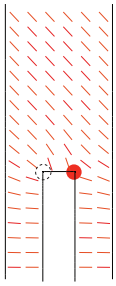

(c) Flat surface, $d = 60$ nm

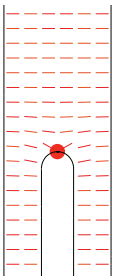

(d) Rounded surface, $d = 60$ nm

Figure 5.21: Alignment of liquid crystals on vertical structures with homeotropic boundary conditions

tical structure having parallel and rounded surfaces. Parallel boundary conditions are specified on the lower substrate, and a semi-infinite sample is assumed (no boundary condition on the upper substrate). We show the results for two values of the column width, $d = 60$ and $d = 100$ nm. We retain the same values for the other variables as employed earlier ($a = 200$ nm, $T^{\text{total}} = 500$ nm). We notice a few interesting results. With the flat surface, for both the wider and the thinner columns, a degenerate solution (equal to its mirror image) is the lowest energy state, and possesses one accidental and one fundamental defect on the corners of the vertical structure. This results in tilted liquid crystals in the bulk, having $\theta_{\text{bulk}} = \pm 30.0^\circ$ for $d = 100$ nm and $\theta_{\text{bulk}} = \pm 44.4^\circ$ for $d = 60$ nm. Qualitatively, this is very similar to the results obtained earlier, given vertical posts with tangential boundary conditions. With the rounded structure, we see one fundamental defect whose location changes as a func-

tion of column width. For the wider column, the defect state corresponding to the lowest energy is off-center, resulting in a degenerate state, with tilted liquid crystals throughout the bulk ($\theta_{\text{bulk}} = \pm 54.8^\circ$). However, for the thinner column, the defect state is centered on the post, generating a non-degenerate state, with planar liquid crystal alignment through the bulk. Again, this is similar to the results we obtained given tangential alignment. However, we do notice that the bulk alignment for thinner columns is planar, as opposed to vertical/homeotropic. This is not an allowed state for rotationally symmetric vertical posts, so we would only expect the planar alignment to be present for vertical film structures lacking rotational symmetry.

We can move on to consider slanted structures, and focus on the three structures described earlier (parallel, rectangular and rounded). Figure 5.22 shows the lowest energy director configurations for the three structure types, for films with $\beta' = 30^\circ$, $d = 100$ nm, $a = 200$ nm and $T^{\text{total}} = 500$ nm. We find that

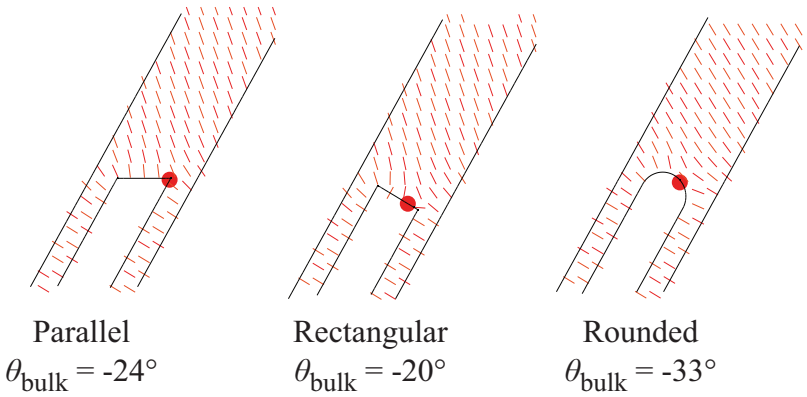

Figure 5.22: Lowest energy director field configuration for slanted posts ($\beta' = 30^\circ$, $d = 100$ nm, $a = 200$ nm and $T^{\text{total}} = 500$ nm) having normal boundary conditions

in each case, θ_{bulk} is negative, owing to fundamental defects located predominantly on the right hand sides of the slanted post structures. The negative θ_{bulk} implies that for liquid crystals that align normal to the GLAD columns, the bulk alignment is in the direction opposite the tilt of the film. This is in contrast to the tangential alignment case, where liquid crystals would tilt predominantly (though not exclusively) in the same direction as the film columns, as seen in Figure 5.17.

Figures 5.24 and 5.23 show the dependence of θ_{bulk} on the column tilt, β', and the column width, d, for rectangular, parallel and rounded slanted post

structures, with normal boundary conditions. For the most part, increasing β'

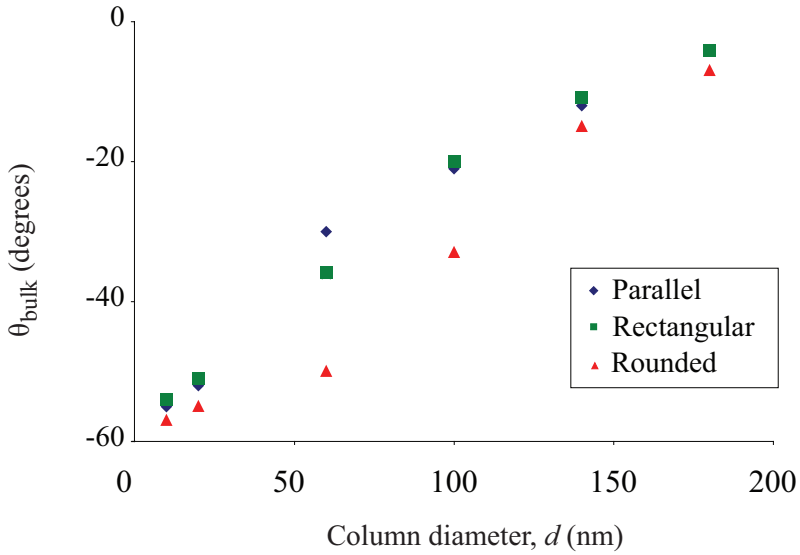

Figure 5.23: Bulk liquid crystal orientation, θ_{bulk}, as a function of column diameter, d, for a $T^{total} = 500$ nm, $a = 200$ nm slanted posts, with normal boundary conditions

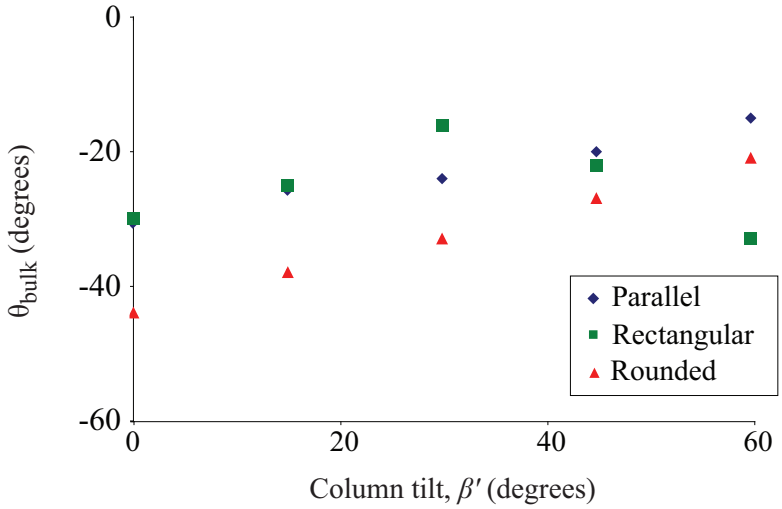

Figure 5.24: Bulk liquid crystal orientation, θ_{bulk}, as a function of column tilt, β', for a $T^{total} = 500$ nm, $a = 200$ nm slanted posts, with normal boundary conditions

and increasing d both have the same effect of moving θ_{bulk} from large negative values toward vertical alignment ($\theta_{bulk} = 0$). For small values of d, the shape of

the column is negligible and the bulk alignment is governed by β'. As a result, at these small values of d, the bulk liquid crystal alignment approaches $\beta' - \theta_{\text{bulk}}$. At the other extreme, as d approaches the intercolumn spacing, a, θ_{bulk} tends toward vertical alignment. As a function of β', the general trend is that as β' increases, θ_{bulk} also increases. This is sensible as one would expect that as $\beta' \to 90^\circ$, the bulk alignment of liquid crystals should approach being vertical. However, as the predicted behaviour of the rectangular structure suggests, this is not a universal result and, not unexpectedly given previous discussions, is dependent on the film's structure.

Finally, we wish to examine the behaviour of θ_{bulk} in a cell structure having normal boundary conditions. Again, we restrict ourselves to the analysis of a rounded structure, for brevity. We again model the cell structure as having a cell thickness of 2000 nm, and consider films with $a = 200$ nm and $T^{\text{total}} = 500$ nm. The dependence of θ_{bulk} on d for a film with $\beta' = 30^\circ$ is shown in Figure 5.25(a), while the dependence of θ_{bulk} on β' for a film with $d = 100$ nm is shown in Figure 5.25(b). The behaviour of θ_{bulk} in both of these cases is identical to that observed given tangential boundary conditions, as shown in Figure 5.20, except the data has been offset by -90°. We see that for a vertical structure, the cell structure induces planar alignment (which is degenerate for a rotationally symmetric vertical post), and that as β' increases, the liquid crystals rotate toward vertical alignment. We also see that as d increases from zero, liquid crystal in the bulk tend to move from being aligned perfectly perpendicular to the posts, and adopt planar alignment ($\theta_{\text{bulk}} \to -90^\circ$) as d approaches the intercolumn spacing, a.

We must always remember that the results exhibited by these simulated director field are hardly quantitatively accurate, and are unable to be used to make quantitative predictions of real world situations. These models ignore many real-world non-idealities including the precise shape of the columns, the three-dimensional nature of the films, surface roughness, surface energy contributions from the sample edges and the stochastic distribution of film columns. Consequently, the results seen here should be taken as guidelines used to generate a sensible picture of how liquid crystal molecules are interacting with GLAD films and to identify plausible trends and effects owing to different film parameters.

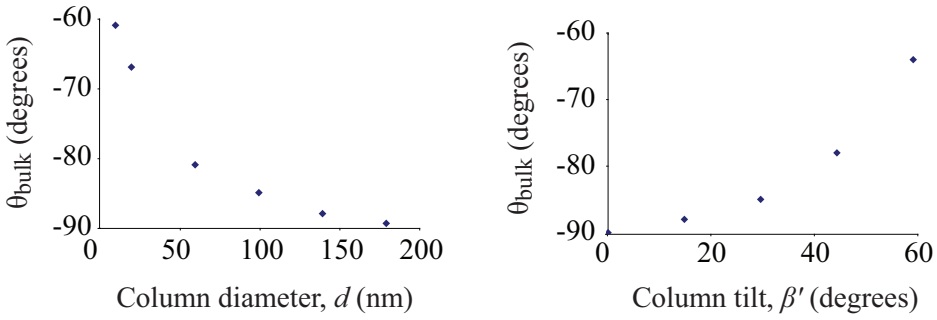

(a) θ_{bulk} as a function of d

(b) θ_{bulk} as a function of β'

Figure 5.25: Dependence of liquid crystal orientation, θ_{bulk}, on a cell structure, with $a = 200$ nm, $T^{\text{total}} = 500$ nm and a 2000 nm cell thickness, using normal boundary conditions

5.4 Experimental

We now look to examine the real-world interaction between GLAD films and liquid crystals. Specifically, we wish to try and determine the orientation of a variety of liquid crystal types in various SiO_2 GLAD film structures and how to control that orientation by varying the specifics of the structure using the deposition techniques described in Chapter 2. We seek to do this in order to modify the properties of the resulting hybrid system, in an attempt to create devices with optical properties that are not achievable via solid films alone.

5.4.1 Liquid Crystalline Materials

For the experiments described here, reactive and non-reactive liquid crystalline materials were used, all obtained from Merck, via collaborators at the Eindhoven University of Technology. Their chemical compositions are shown in Figure 5.26. The non-reactive mesogens are polar cyanobi- or cyanotriphenyls, and are the components of the liquid crystal mixture, E7. This mixture is the only non-reactive liquid crystal that we employed in our experiments. E7 is comprised of 51% 5CB, 25% 7CB, 16% 8OCB and 8% T15, and has a nematic to isotropic temperature of $T_{NI} = 60.5^{\circ}$C. E7 exists in the nematic phase at room temperature, and for this reason must always be fabricated in a cell structure. Sample fabrication details will be discussed shortly.

Of the four reactive mesogens, C3M and C6M are non-polar diacrylates, and serve as cross-linking species that form polymer networks. C6BP and

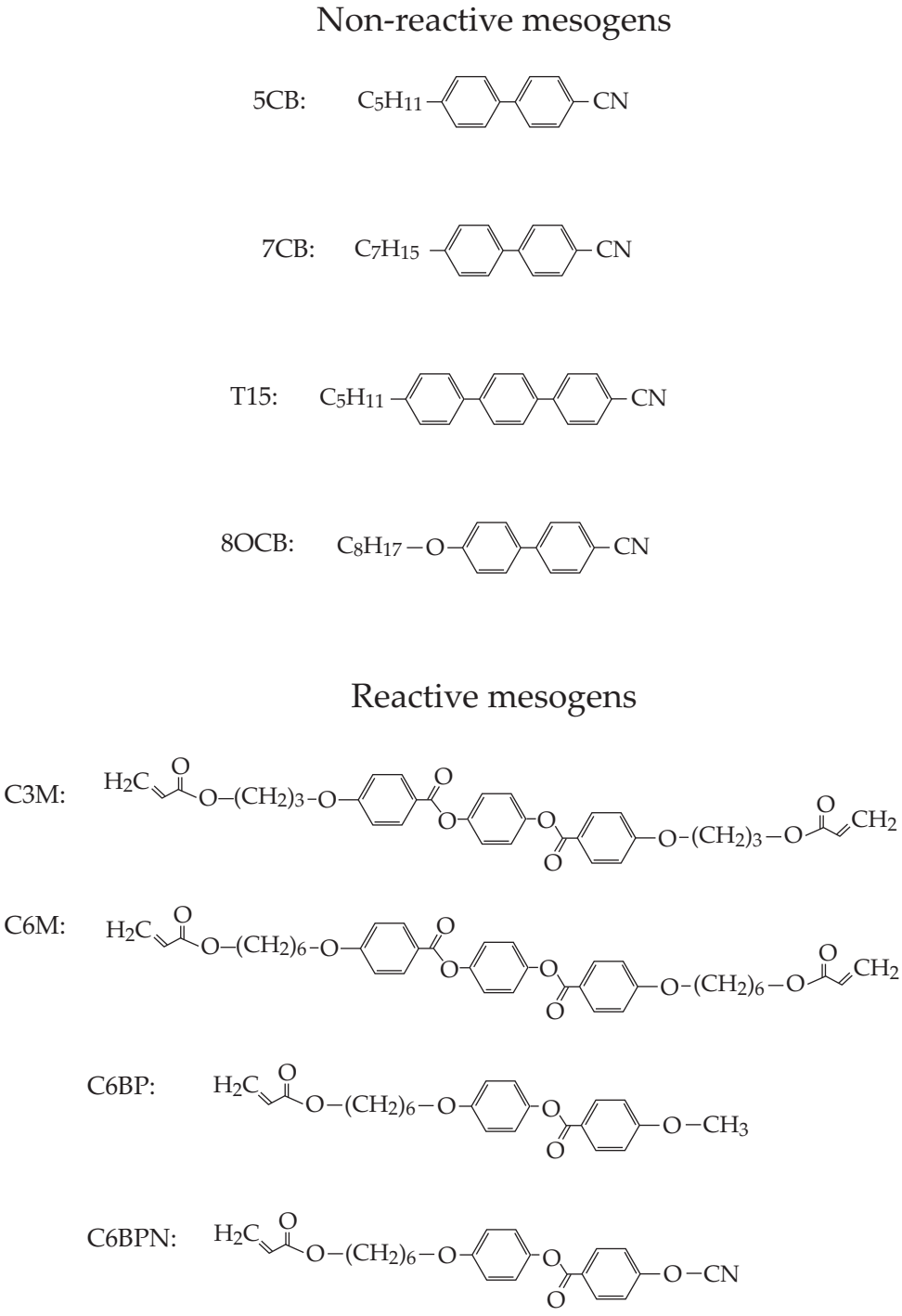

Figure 5.26: Molecular structure of various nematogens.

C6BPN are non-polar and polar monoacrylates, respectively. These molecules exist in polymer networks as side-chain elements. These reactive mesogens are all crystalline at room temperature, but the cross-linkers, C3M and C6M, exhibit nematic phases at elevated temperatures ($\gtrsim 50^{\circ}$C) in their pure form, or in mixtures. C6BPN and C6BP do not have nematic phases in their pure form, and do not form liquid crystal networks, so must be used in a mixture with one or more of the cross-linking species. If the material is then polymerized while it is in the nematic phase, a polymer network will form, as illustrated in Figure 5.27, freezing in the anisotropic properties of the nematic. This allows us to fabricate samples that are open to the air without the need of a cell structure. Polymerization is accomplished using the photoinitiator, Irgacure 184

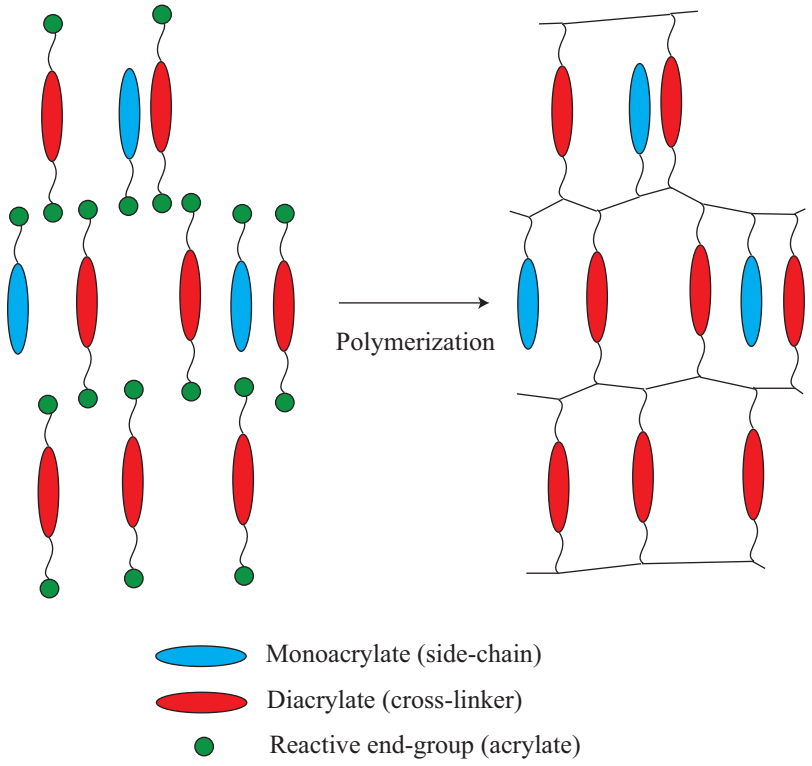

Figure 5.27: Liquid crystal network formed by polymerization of reactive mesogens

(Ciba Specialty Chemicals), illustrated in Figure 5.28. This molecule releases a free radical when illuminated by ultraviolet light, which then initiates the free radical polymerization. The polymerization reaction must take place in an

inert atmosphere and we must simultaneously ensure that the temperature of the sample is sufficiently high so as to maintain the liquid crystal mixture in the nematic phase. For these reasons, polymerization is frequently done in an enclosed box filled with N_2 gas, containing a temperature-controlled heating stage as well as a transparent lid in order to allow incident UV light.

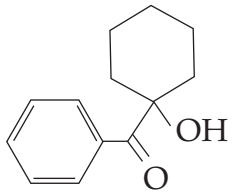

Figure 5.28: Irgacure 184 photoinitiator

Finally, in many of our experiments we incorporate absorbing and/or fluorescent dyes. The dyes we employ are anisotropic in shape, and have two important properties. First, because of their shape anisotropy, these dye molecules will tend to align with the liquid crystals in a predictable manner. Second, these dyes exhibit anisotropic absorption, known as dichroism. Optical absorption in a material can be treated by replacing the refractive index, n, of the material by a complex quantity, $\tilde{n} = n + ik$, where the imaginary component, k, is known as the extinction coefficient and is indicative of how much light is absorbed by the material at a given wavelength. As we know, many materials exhibit birefringence, characterized by having different values of n for different incident polarization states. Similarly, dichroism is characterized by a material having different values of k for incident polarization states, meaning that different polarizations of light are absorbed in different amounts. For all the dyes used here, the dichroism is uniaxial, meaning that the dye has an extraordinary axis, and light polarized along that axis is absorbed to a much higher degree than light polarized normal to that axis. Two dyes are used in our experiments. The first is a custom dye, which we denote as D1, shown in Figure 5.29, that was synthesized at Philips Research Laboratories and obtained from collaborator Prof. Dirk Broer (Eindhoven University of Technology). The second dye is Lumogen Yellow 170 (BASF). This dye is also fluorescent, and is the subject of most of the experiments of the following chapter. The absorbance ($-\log_{10}(\text{Transmission})$) for these two dyes, parallel to and perpendicular to the absorption axis are shown in Figure 5.30. These results were measured by mix-

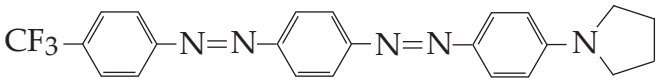

Figure 5.29: Dichroic dye, D1

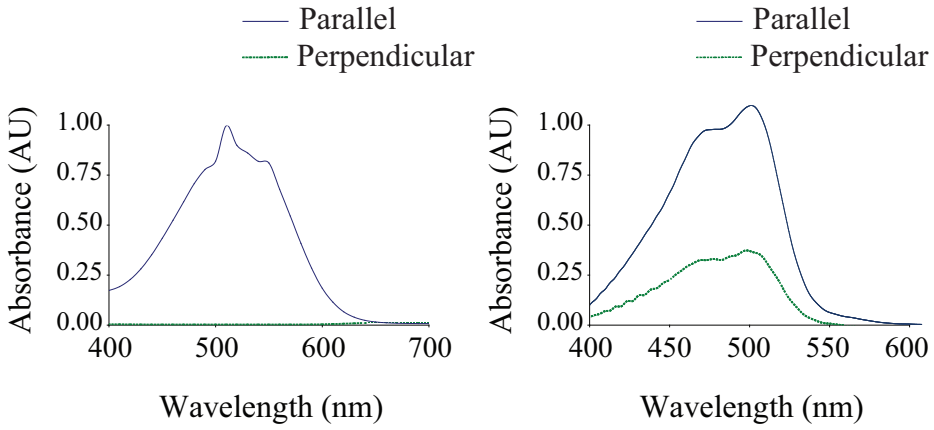

(a) D1 (b) Yellow 170

Figure 5.30: Dichroic ratio of dyes used to determine liquid crystal alignment

ing the dye into E7 at a small concentration ($\sim 1-2$ wt. %) and infiltrating that mixture into a commercial liquid crystal cell, in which E7 is known to adopt a planar orientation. We find that the absorption axis of the dye is parallel to the (constant) director orientation of the E7 molecules and measure the absorption of light parallel to and perpendicular to that axis at normal incidence.

We see that the D1 dye has a very strong dichroism extending between about 400-650 nm. Light polarized along the absorption axis is absorbed more than 10 times as much as light polarized perpendicular to the axis. The Lumogen Yellow 170 dye exhibits moderate dichroism between about 400-550 nm, where light polarized along the absorption axis is absorbed 2.5-3 times as much as light polarized perpendicular to the axis. We will return to the experimental application of these dyes shortly.

5.4.2 Sample Fabrication

In order to fabricate samples with liquid crystals infiltrated into GLAD films, two approaches can be used. The first of these is spin coating, which is typically employed when using reactive liquid crystals. This approach is straightfor-

ward. The desired liquid crystal mixture is either dissolved in an appropriate solvent or heated into the isotropic phase. The mixture is then spread across an empty GLAD film, making sure that the liquid crystal mixture adequately wets the whole film. The sample is then spun at high speed (1000 - 5000 rpm), jettisoning excess material and evaporating the solvent. The spin speed is chosen to obtain the desired film thickness. After spinning, one is then left with a film infiltrated with the liquid crystal material. If needed, the sample can then be polymerized according to the procedure outlined above. While fairly straightforward, this approach does have a number of drawbacks. After spinning, one is typically left with and overburden of liquid crystalline material above the surface of the GLAD film. This overburden is typically on the order of microns thick, and can be very difficult to eliminate. As indicated by the earlier simulations, paying special attention to the relevant situation depicted in Figure 5.10, this situation can potentially result in a difficult to predict distortion of the nematic director field in the overburden region. This is hard to characterize and can potentially be detrimental to a film's performance. Another issue is that the reactive liquid crystal mixtures are often solid at room temperature. While the material can be melted prior to their application on the spin coater, during spinning, the material will often cool below the melting point and crystallize. One can heat the sample after coating in order to melt the liquid crystal, but this difficulty can potentially affect the repeatability of the fabrication approach. Finally, when using solvents to aid in spin coating, after coating, residual amounts of solvent may still remain in the film, which can affect liquid crystal properties. Additionally, the evaporation of solvent from the film has been known to cause damage to the film, occasionally termed the "nano-carpet" effect [137, 138].

The alternative approach is to infiltrate liquid crystals into a cell structure such as the one illustrated in Figure 5.19. A cell is fabricated by taking two substrates, each coated with an alignment layer (GLAD or otherwise), and pressing those two substrates together. Between the two substrates should be placed some form of spacer. Silica spheres of a known diameter are commonly employed, but simple scotch or kapton tape can be used as well if the cell thickness is not critical. The substrates are then glued together, leaving a unsealed "fill port" for infiltration. Once prepared, the liquid crystalline material should be placed on the fill port, and capillary action will draw the liquid into the cell.

This step should be done at as high a temperature as possible to reduce the viscosity of the mixture, and to promote uniform filling. Solvents should not be employed whatsoever. However for reactive species, the temperature can not be raised too high, as thermally induced polymerization can occur. As a rule of thumb, one should not use temperatures in excess of about 90°C. In order to maintain uniform temperatures across a sample, filling is often best done in an oven[5.7], as opposed to on a hot plate, for example.

5.4.3 Results

In order to optically characterize the alignment of liquid crystals in GLAD films, one often relies on measurements of a film's birefringence and dichroism. Experimentally, dichroism is the simplest to measure, as it simply requires comparing the transmission of different polarization states of light. Measurement of birefringence is more complicated, and this is especially true when needing to compensate for the optical effects of the GLAD film itself. Consequently, all of the results presented here have been obtained by identifying a film's dichroic properties.

Alignment in SiO_2 Films

We first seek to examine the alignment of reactive and non-reactive mesogens in GLAD films by examining their behaviour in cell structures. We are curious as to whether different liquid crystal mixtures align in similar or different manners in a given film, as well as how changes in the film parameters affect alignment. We also wish to examine if the alignment can be modified by chemically treating the film surface (prior to liquid crystal infiltration). We choose to study cell structures because these structures promote uniform liquid crystal alignment in the bulk of the cell, rather than spin coated films, which have distortion in the bulk owing to the boundary conditions imposed by the open air.

We considered six film structures, given in Table 5.1. All were deposited at $\alpha = 85^\circ$ to a thickness, $T^{\text{total}} = 250$ nm out of SiO_2 (99.9% purity, from Cerac, Inc.). Films were deposited on 1×1 inch, B270 glass substrates (Howard Glass)

[5.7] One useful technique is to leave necessary tools such as pipettes in the oven as well, so the mixture does not crystallize when coming in contact with room temperature objects.

using electron beam evaporation at deposition pressures between 0.3 mPa to 0.7 mPa. The film structures were fabricated according to the algorithms described in Chapter 3, with $P = 23$ nm, $\delta = 2$ nm and $p_v = 5$ nm. Table 5.1 also lists the values of a and $-\bar{b}^2$ as obtained from Chapter 3, as well as the measured column tilt, β'. We recall that films with $-\bar{b}^2 > 0$ broaden preferentially in the direction normal to the column tilt, while films with $-\bar{b}^2 < 0$ broaden in the same plane as the column tilt. We assemble these substrates into cell structures, using 80 μm kapton tape as spacers.

Table 5.1: Film samples used to determine liquid crystal alignment

Label	Structure	a	$-\bar{b}^2$	β' (degrees)
A	Spin-pause (vertical post)	0.0	0.0	0
B	Spin-pause (slanted post)	1.0	1.0	43
C	Zig-zag	0.6	1.0	20
D	Spin-pause	0.6	0.6	18
E	Zig-zag (serial bideposition)	0	1.0	10
F	Phisweep	0.6	-0.2	35

We choose to investigate the behaviour of the following four different liquid crystal/dichroic dye mixtures:

1. E7/D1 (99.5/0.5), $T_{NI} = 60.5°$C

2. C3M/C6BPN/Yellow 170/Irgacure 184 (49.5/49.5/0.5/0.5), $T_{XN} = 70°$C, $T_{NI} = 95°$C

3. C3M/C6BP/Yellow 170/Irgacure 184 (49.5/49.5/0.5/0.5), $T_{XN} = 37°$C, $T_{NI} = 90°$C

4. C3M/C6M/Yellow 170/Irgacure 184 (78.4/19.6/1/1), $T_{XN} = 55°$C, $T_{NI} = 115°$C

Transition temperatures were measured by visual inspection of each mixture on a temperature controlled stage. In order to fill the cell structures, cells were placed in an oven at $80 - 85°$C for 15-30 minutes, and the liquid crystal mixture was allowed to fill the cell by capillary action, as described above. Once filled,

the E7 samples are fully fabricated, however one step remains for the reactive mixtures. Following filling, the reactive mixtures must be cured to freeze in the liquid crystal character. This is done by placing the samples on a hot plate set above the crystal to nematic transition temperature, and illuminating with UV light for 5 minutes. For simplicity in polymerizing multiple samples at once, this is typically performed at $75 - 80°$C. Once cured, this completes the fabrication process for the reactive mixtures. In all cases we were able to obtain cells with large regions possessing scatter-free transmission, implying the presence of single domain alignment.

Finally, we also investigate the effect of chemically treating the surface of the film to be hydrophobic, and ask how that affects liquid crystal alignment. This was done using vapour phase functionalization to fluorinate the SiO_2 films [139], which are hydrophilic as-deposited (contact angle $< 5°$), prior to cell fabrication. The procedure to do this is straightforward. Substrates are reactively ion etched (RIE) in an O_2 plasma (80 sccm, 150 mtorr, 5 min) in order to hydroxylate the film surface. Films are then placed in a desiccator for 24 hours, along with 1 mL of the precursor, trichloro(3,3,3-trifluoro-propyl) silane. Contact angles post functionalization are in the $90° - 100°$ range.

In order to examine the alignment of the liquid crystals in the cell, we probe the dichroism in two ways. First, we simply measure the optical transmittance of linear polarized light at normal incidence, and rotate the incident polarization state through a full 180°, as illustrated in Figure 5.31(a). We track the orientation of polarized light by the variable ϕ_{beam}. For $\phi_{\text{beam}} = 0°$, the beam is polarized so that it is perpendicular to the tilting plane of the film columns. Recalling the notation from Chapter 2, we would say that the light is polarized along the y-axis. For $\phi_{\text{beam}} = 90°$, the light is polarized parallel to the posts themselves; we say it is x-polarized. The transmittance of the system shown in Figure 5.31(a) is shown in Figure 5.31(b). The angle at which the transmittance is a minimum corresponds to the case where the polarization state is parallel to the absorption axis of the dichroic molecules, and in turn to the director of the liquid crystal molecules. For liquid crystal alignment in the plane of the posts (xz), like that discussed in the earlier simulations, we expect to find $\phi_{\text{beam}} = 90°$. Alignment along the y-direction is described by $\phi_{\text{beam}} = 0°$ or 180°. Other values indicate that liquid crystals are aligned along some intermediate direction, which may be a result of asymmetries in the film structure or

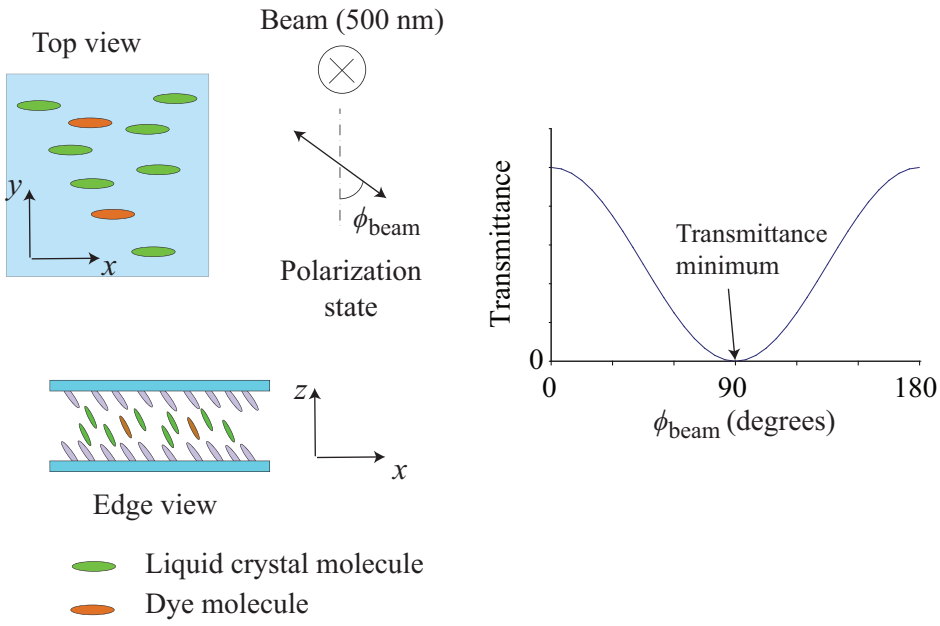

(a) Measurement setup (b) Typical transmittance result

Figure 5.31: Examining liquid crystal orientation by identifying the in-plane orientation of dichroic molecules

misalignment of opposing substrates arising either from a fabrication error, or from non-uniformities in columnar growth direction, as discussed in Chapter 2.

We can now attempt to determine the orientation angle, θ_{bulk} of the liquid crystals. To do this, the dichroism is probed in a second way, illustrated in Figure 5.32. Knowing the in-plane orientation of the liquid crystals from the first measurement, the sample is now rotated by an angle, θ_{sample}, in that plane. Light is incident on the sample, polarized either in the plane of rotation (transverse magnetic, $\parallel$), or normal to it (transverse electric, $\perp$). On contact with the glass substrate, the light bends according to Snell's law. It then bends again as light enters the liquid crystal portion of the cell, but as an approximation, we will neglect this effect because of the close index matching between the liquid crystal and the glass substrate ($n \sim 1.5$). As the light travels through the cell, the two polarization states will be differently absorbed due to the dye. The ratio of the absorbance of the $\parallel$ state to the $\perp$ state is known as the dichroic ratio, and we track this quantity as a function of θ_{sample}. The predicted behaviour is shown in Figure 5.33. We can identify a value for θ_{bulk} by looking for maxima

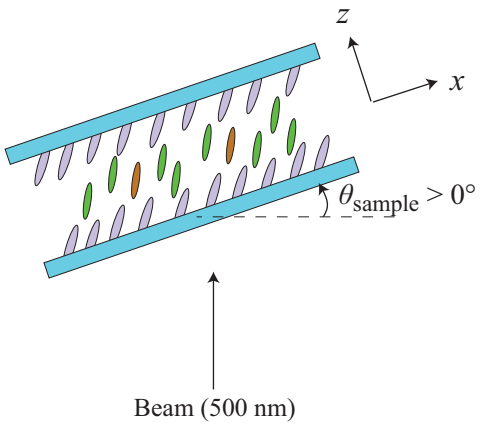

Figure 5.32: Setup for determining θ_{bulk} through dichroism measurements at non-normal incidence

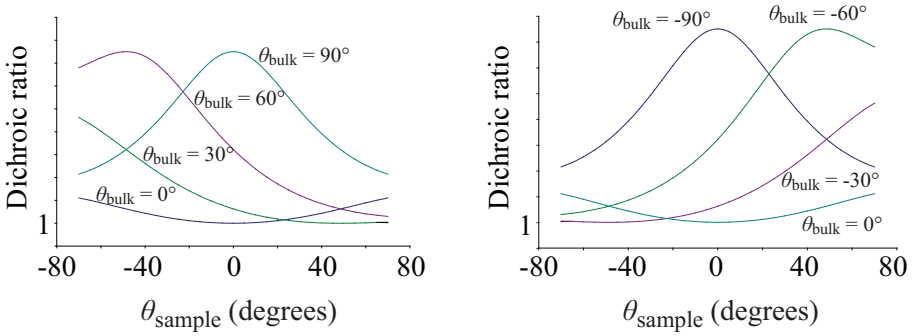

(a) $\theta_{bulk} > 0°$ (b) $\theta_{bulk} < 0°$

Figure 5.33: Predicted dichroic ratio as a function of θ_{sample} for samples with different θ_{bulk} on glass substrates with $n = 1.5$

or minima in the dichroic ratio as a function of θ_{sample}. Maxima occur when light is traveling in the cell perpendicular to the absorption axis, while minima (at a dichroic ratio equal to unity) occur when light is traveling along the absorption axis. To obtain θ_{bulk} from θ_{sample} in the case of an observed minimum, one must simply take the value of the θ_{sample} and convert to the angle of propagation in the sample via Snell's law and take that result as θ_{bulk}. When a maximum is obtained, one must convert θ_{sample} via Snell's law, then add or subtract 90°, ensuring that the result is in the range $[-90°, 90°]$. That result is equal to θ_{bulk}. Finally, notice that this implies that samples with $\theta_{\text{bulk}} > 0$ have minima at positive values of θ_{sample}, and maxima at negative values, while the opposite is true for films with $\theta_{\text{bulk}} < 0$. In this work, for simplicity and for brevity, we restrict this second measurement approach to those films which demonstrated liquid crystal alignment along GLAD columns, as obtained from the first measurement technique.

Figure 5.34 shows the measurement results for the in-plane orientation of the four liquid crystal mixtures in cells made from each of the six film structures, both with and without surface functionalization. The size of the data points is indicative of the measurement uncertainty. Figure 5.35 show the results for θ_{bulk} for the same samples. Because the x-axis represents the individual mixtures, the lines joining the data should be primarily interpreted as a guide to the eye. The mixtures are listed, from left to right, in order of decreasing molecular polarity. E7 and C6BPN are strongly polar because of the presence of cyano groups at the end of the molecules, while C6BP, C3M and C6M have no such polar groups. The data is somewhat difficult to interpret, but is important to understand in order to comprehend how different liquid crystals are interacting with the film. We must examine both Figure 5.34 and 5.35 simultaneously to have the proper picture of what is going on. We recall first that a result of $\phi_{\text{beam}} = 90°$ implies alignment in the plane of the posts, while a result of 0° or 180° implies alignment perpendicular to the post structures. Other results can imply several possibilities. Cells exhibiting near vertical alignment can exhibit any value for ϕ_{beam}, but the difference in signal between maximum and minimum will be very small. Vertical alignment can be confirmed using the test for θ_{bulk}. If this is not the case, then it is likely that the sample promotes some more complicated form of alignment, which cannot be deduced at this time. In cases where we have alignment perpendicular to

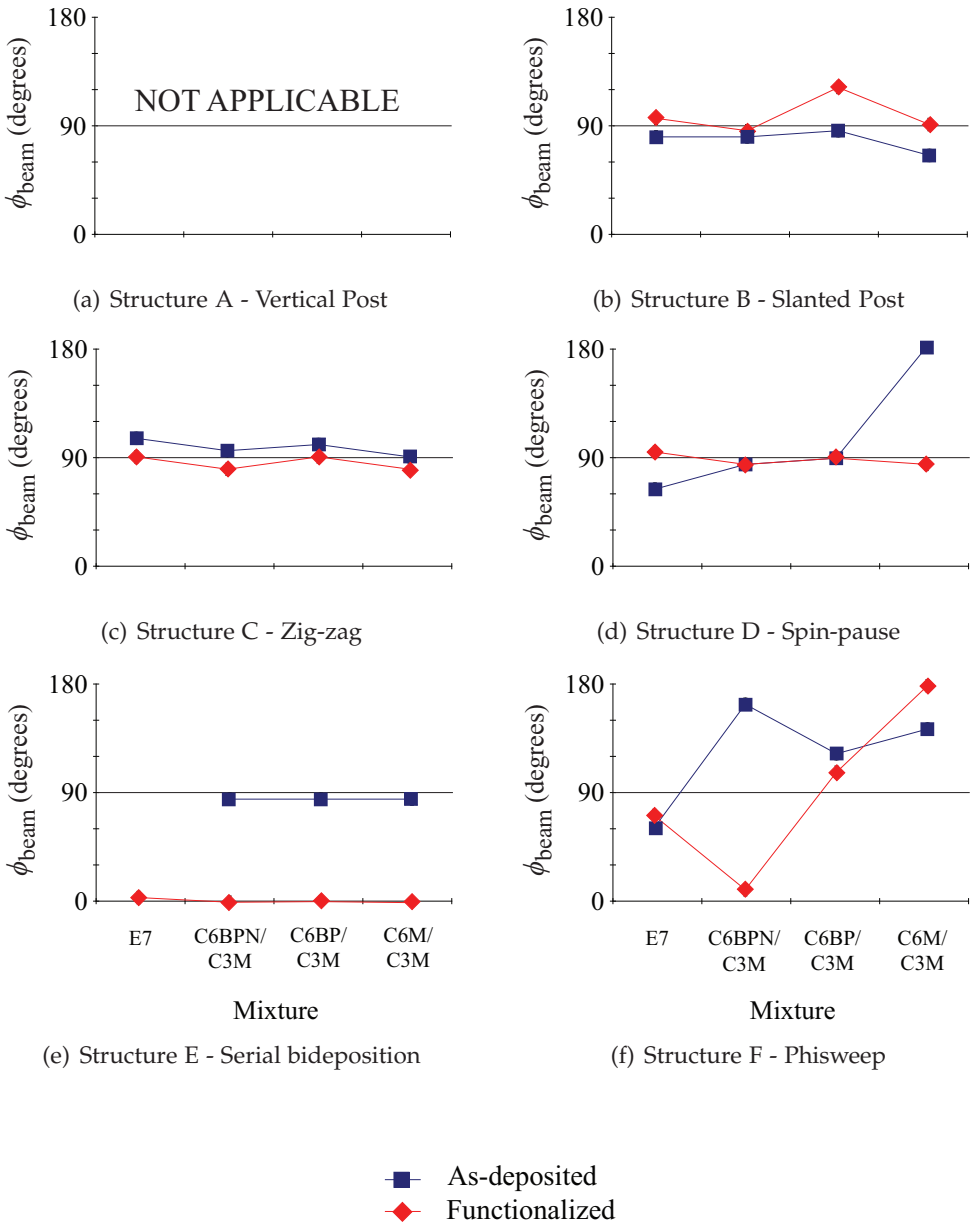

(a) Structure A - Vertical Post

(b) Structure B - Slanted Post

(c) Structure C - Zig-zag

(d) Structure D - Spin-pause

(e) Structure E - Serial bideposition

(f) Structure F - Phisweep

Figure 5.34: Measurements of in-plane orientation of liquid crystals, ϕ_{beam}, for all six film types as-deposited and functionalized

the film columns, we expect $\theta_{\text{bulk}} = 0^\circ$ by symmetry. If this is not the case, we again have a complicated alignment that can not easily be determined.

The vertical post, structure type A, is considered first. The in-plane results are omitted in Figure 5.34(a) since these results do not indicate anything valuable, as the measurement setup and the film samples have the same circular symmetry. This is not true, however, of the results for θ_{bulk}. We see that for E7, the alignment is vertical, having $\theta_{\text{bulk}} = 0^\circ$. This corresponds to the situation depicted in Figure 5.20(b) for $\beta' = 0^\circ$ and is a nice result. At the same time, we find that the reactive mesogens all have $\theta_{\text{bulk}} = \pm 90^\circ$. This corresponds to the result predicted in Figure 5.25(b). Earlier we remarked that such a result would be degenerate for circularly symmetric vertical posts, and would lead to polydomain alignment. However, as we know from Chapter 2, vertical posts are rarely truly vertical, and possess some structural asymmetry (*e. g.* non-zero β', ξ'). These asymmetries can induce non-degenerate, monodomain alignment, which appears to be the case here. These results give us our first important result, which is that E7 appears to experience tangential boundary conditions in as-deposited SiO_2 posts, while the reactive mesogens used here exhibit normal boundary conditions under the same environment. Curiously, despite the similarity between E7 and C6BPN, the mixture containing the latter species followed the trend of the other reactive species. Post surface functionalization, we find that the behaviour of E7 flips completely, and adopts the same behaviour as the reactive mesogens in the as-deposited case. This gives the important result that the boundary conditions applied to E7 switch upon fluorination of the SiO_2 columns. This could potentially be used as a way to micropattern alignment surfaces, to yield regions of both vertical and perpendicular molecular orientation. The results for the reactive species is not quite as clear. The mixtures containing C6BP and C6BPN appear to be unchanged post functionalization, while the C3M/C6M mixture adopts nearly vertical orientation. It is not clear why the different mixtures have such different responses, but we do clearly see that at least on some level, the orientation of the reactive mesogens can also be controlled by surface functionalization. We state, cautiously, that to some extent, fluorination of the film structure has the opposite effect on non-polar molecules as compared to polar molecules.

Structures B, C and D all have some moderate column tilt, and moderate broadening normal to the column tilt plane ($-\bar{b}^2 > 0$), and can be discussed

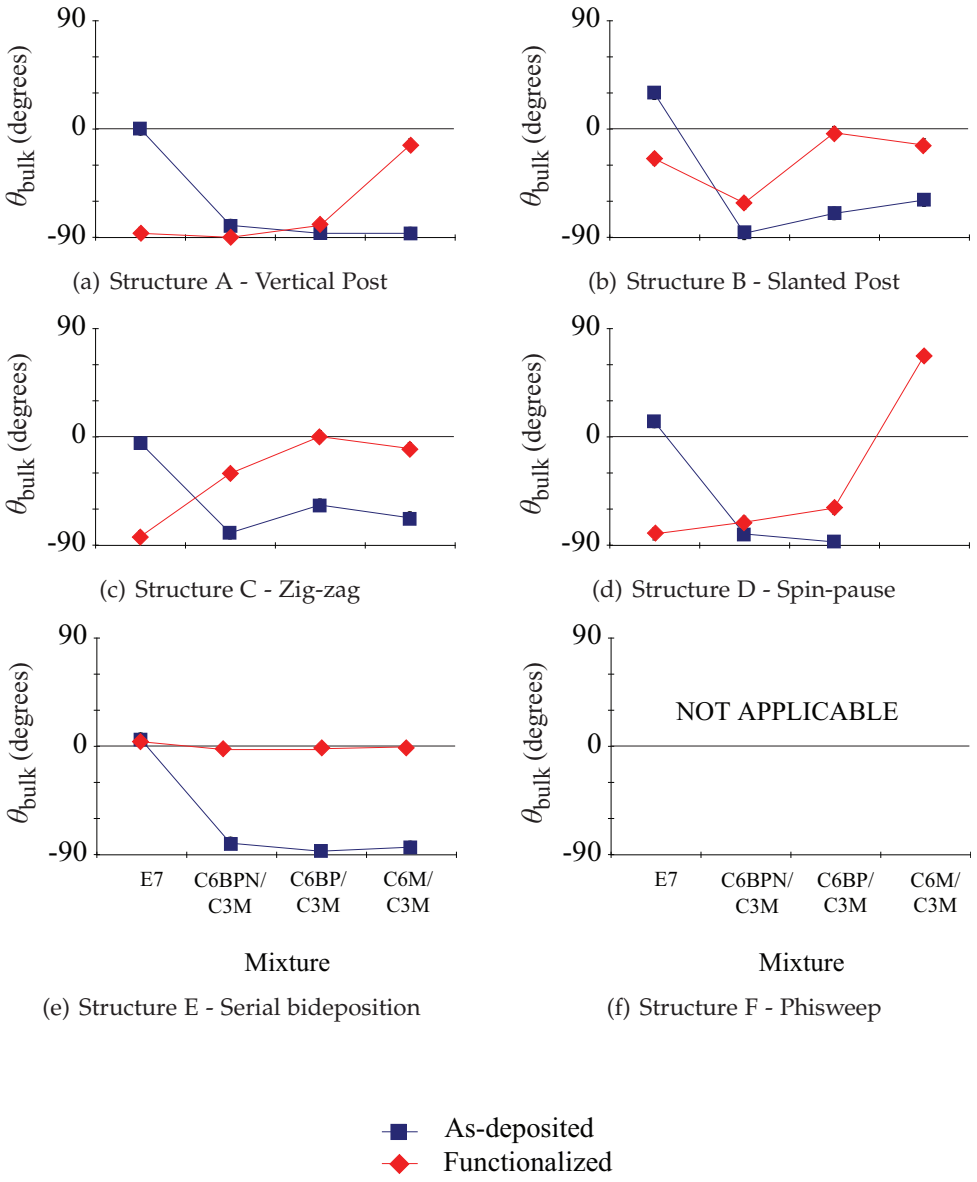

Figure 5.35: Measurements of bulk liquid crystal orientation, θ_{bulk}, for all six film types as-deposited and functionalized

together. For the most part, in all of these cases, both functionalized and not, $\phi_{\text{beam}} \approx 90^\circ$ is obtained, implying that liquid crystal alignment takes place in the plane of the film columns, as understood using the finite element approach from earlier. One noticeable exception to this rule is the C3M/C6M mixture infiltrated into an as-deposited cell made from structure D ($a = 0.6$ spin-pause), where alignment perpendicular to the film columns was obtained. Other than this point though, this gives the nice result that for films with $-\bar{b}^2 > 0$, liquid crystals align in the plane of the columns. However, the molecular orientation, θ_{bulk}, is strongly dependent on the molecular species involved. For E7 with as-deposited films, we see that θ_{bulk} is usually positive, and slightly less than β'. Again, this is perfectly consistent with Figure 5.20(b), further indicating that E7 does experience tangential alignment in as-deposited SiO_2 films. Upon functionalization, E7 adopts negative values for θ_{bulk}, often close to -90°, consistent with Figure 5.25(b). The reactive mesogens act quite differently than E7, but together have very similar behaviour. In as-deposited films, the reactive species adopt large, negative values of θ_{bulk}, consistent with normal boundary conditions on the film surface. Post functionalization, these species still yield negative values for θ_{bulk}, but they have all moved closer to zero degrees (vertical alignment). This precise behaviour was not observed in any of the cell structures considered earlier and it is not entirely clear what is occurring. It is observed, however, that as in the vertical post case, functionalization causes the molecular alignment to change from having purely normal boundary conditions on the surface of the film, to having characteristics resembling tangential alignment. A plausible explanation is that in the case of the reactive mesogens, fluorination of the film promotes tangential alignment, but is simply not capable of causing a full switch in the alignment behaviour, unlike the E7 case. We hypothesize, then, that fluorination causes the reactive species to align at some intermediate point between normal and tangential alignment, and that perhaps alternative functionalization approaches may be able to induce a complete switch. Figure 5.36 shows that this is a plausible explanation by illustrating that the lowest energy director configuration in a cell structure with boundary conditions rotated 10° from normal causes θ_{bulk} to increase significantly.

Structure E is a serially bideposited structure. This is a prime example of a vertical structure that lacks rotational symmetry, and it exhibits some interest-

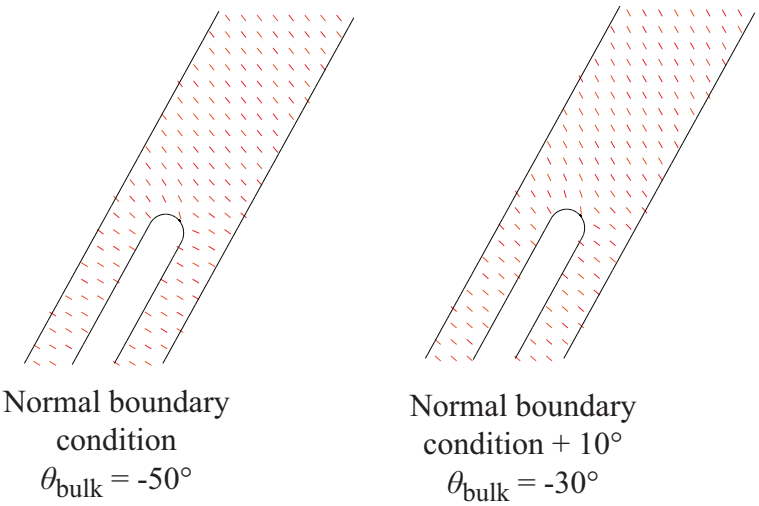

Figure 5.36: Increase in θ_{bulk} by rotating the boundary condition along the film surface by 10° from normal toward tangential alignment

ing results for liquid crystal alignment. Considering E7 first, no value for ϕ_{beam} is shown because we find that θ_{bulk} is 0°, meaning that values for ϕ_{beam} are immaterial. This means that just like in the vertical post case, E7 aligns vertically, with tangential boundary conditions on the film. The reactive species, on the other hand all have $\phi_{beam} = 90°$, implying that the molecules align along the x-axis, perpendicular to the broadening vector, which is along $\hat{\mathbf{y}}$, as recalled from Chapter 3. This is consistent with all previous observations. After functionalization, however, something interesting happens. It is observed that all the liquid crystal species have $\phi_{beam} = 0°$ and $\theta_{bulk} = 0°$, meaning that the molecules are aligning parallel to the broadening vector, along the y-axis. This situation is depicted in Figure 5.37. This behaviour is interesting, but difficult to explain. For some reason, after functionalization it is energetically favorable to align along the parallel, broadened grooves of the SBD structure. This is similar to what E7 does in GLAD films fabricated at lower α, but absent any surface functionalization. It is likely that the correct resolution has to do with contributions to the elastic energy arising from the three dimensional structure of the film, which is quite significant in SBD structures. To examine this, one would need to solve the full three-dimensional problem specified by equations (5.16) or (5.23), which will not be done here.

Structure F, the PhiSweep structure further hints at the complexity that the three-dimensional nature of GLAD films can induce. This film is characterized

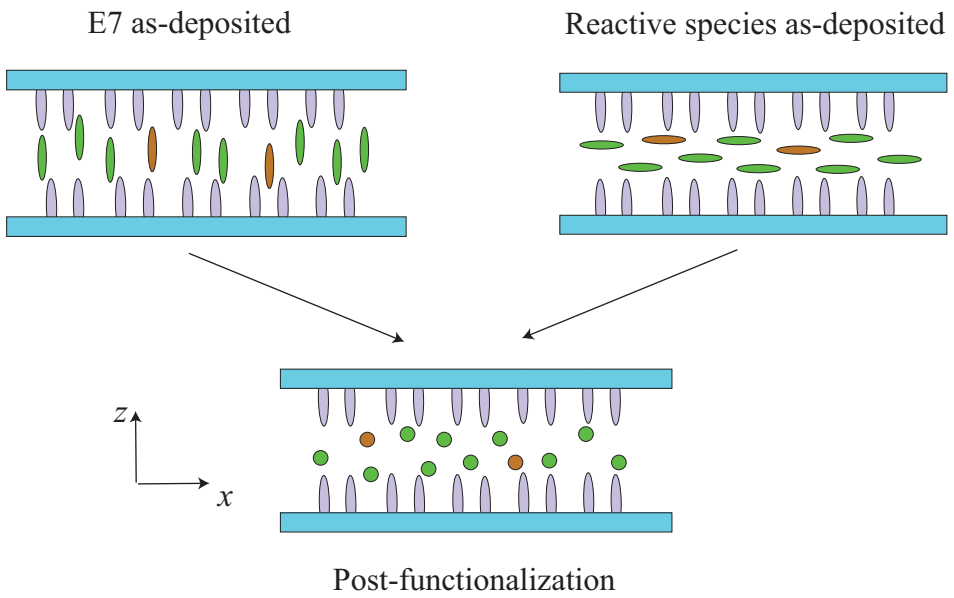

Figure 5.37: Alignment of liquid crystals in an SBD film pre- and post-functionalization

by having $-\bar{b}^2 < 0$, implying that the broadening vector is along the x-axis. Prior to functionalization, none of the mixtures are found to align either along the posts, or perpendicular to them. The other structures did not exhibit any of these strange features, and the main difference between this structure and all the previous ones is the broadening direction of the film columns. It appears that broadening along the y-axis, which is the usual case, seems to promote liquid crystal alignment in the xz-plane. For tangential alignment, perhaps the extrusion of the film columns along the y-axis provides a platform on which liquid crystal molecules can "lie down" in an energetically favourable manner. For normal alignment, the large extruded surface may cause the vast majority of liquid crystals to align perpendicularly, which may explain why that is the energetically favourable state. However, when broadening takes place along the x-axis, the large extruded surface is now parallel to, and symmetric about the xz-plane. This causes both a potential degeneracy problem, as well as affects the alignment dynamic. Molecules that typically prefer tangential alignment may start to wrap around the post, causing ϕ_{beam} to take on values other than 90°. For molecules that typically prefer normal alignment, they still may prefer this, but now the dominant surface is in the xz-plane so that this alignment results in molecular orientation at a variety of angles. Functionalizing the film

does nothing to further explain this scenario, as no discernable pattern can be observed post-functionalization. This may be a result of potentially degenerate states dominating this film structure, with no overt preference for monodomain alignment. As a result of the ambiguity in the results of the in-plane molecular alignment, results for θ_{bulk} are of no use, and are omitted from Figure 5.35.

The results of this section are quite illuminating. We find that for as-deposited films, with normal broadening ($-\bar{b}^2 > 0$), E7 tends to align parallel to film columns, while reactive mesogens tend to align normal to the columns. When the film is fluorinated and made hydrophobic, E7 tends to adopt normal boundary conditions, while the reactive mesogens adopt more tangential characteristics, but do not fully make the transition like E7 does. We also see that certain structures, particularly those with strong features in the third-dimension (normal to the xz-plane), can generate strange and unpredictable alignment configurations. Since these films are often employed because of their unique nature, it would be of great use to better understand how liquid crystals orient themselves in these situations. This would likely require a three-dimensional finite element model of the director field surrounding a GLAD film, and would likely be a challenging and complex problem, but it is likely one that needs to be resolved in order to ultimately be able to employ GLAD films for more sophisticated alignment purposes.

Liquid Crystal Alignment in a Layered Film

To this point, it has been assumed that liquid crystals fully infiltrate the pores of a GLAD film, and align to the columnar structure. It is also known from the finite element simulations that the upper surface has a dominant influence on the bulk orientation of the liquid crystal through the film. However, one of the advantages of using GLAD films for liquid crystal alignment is the fact that layered structures can potentially induce different molecular alignment at different film thicknesses, such as has been observed for E7 infiltrated into helical GLAD films [81]. This would allow a GLAD film to alter the orientation of liquid crystal molecules throughout the entire thickness of a cell, rather than being used to induce alignment from substrate surfaces. However, the exact nature of the alignment in layered structures is somewhat unclear, and confirmation that liquid crystal alignment takes place throughout such a film was desired.

To determine this, the layered slanted post/vertical post structure seen in Figure 5.38(a) was used. Two of these films were used to form a cell structure, using kapton tape as the spacer. The cell was then filled by a mixture of 99:1, E7 and D1, as was a control cell, made using two vertical post structures. We examined the degree of polarization, given by the Stokes parameter

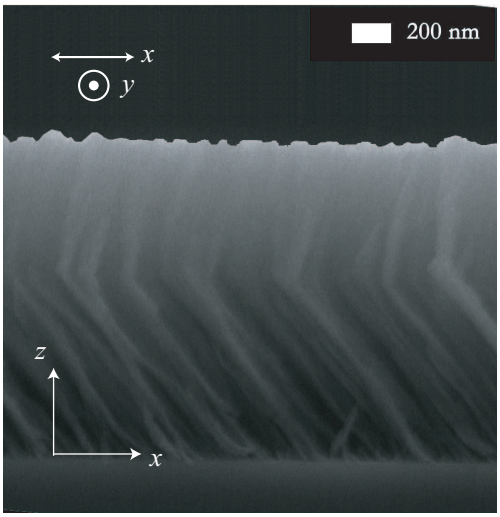

(a) Layered GLAD film

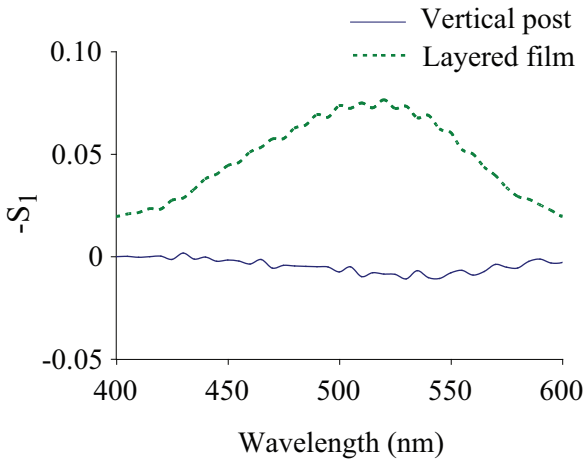

(b) Layered GLAD film

Figure 5.38: Proof of complete infiltration of liquid crystals in porous GLAD films

S_1 as in equation (4.68). For the vertical post cell, we know that E7 adopts vertical alignment in such a structure. Therefore, it is expected that there will

be no difference in transmission between x- and y-polarized light ($S_1 = 0$). If, in the layered structure, liquid crystal alignment only occurs at the top of the film, then we would expect the same result. If, however, there is alignment throughout the film, we would expect to find that x-polarized light is strongly absorbed, and the transmitted light will be preferentially y-polarized. Consequently, we would expect S_1 to be negative for wavelengths in the absorption band of D1. Figure 5.38(b) shows $-S_1$ as a function of wavelength for both cell structures. It is clear that we have $-S_1 > 0$ over the absorption range of the D1 dye, which clearly indicates that liquid crystal alignment takes place throughout the entirety of a film. We also have $S_1 \sim 0$ for the vertical post structure, consistent with all previous observations. Slight deviations from $S_1 = 0$ are likely due to small asymmetries in the vertical post structure.

5.5 Conclusions

This chapter has hopefully illustrated both the simultaneously interesting and frustrating world of liquid crystals. Liquid crystalline materials are unique, diverse and have a host of amazing properties. This chapter barely touches on the surface on the science and the applications of these special materials. But while liquid crystals can be used for a number of amazing applications, they do not yield their secrets easily. A map, or a picture of what is going on is of crucial importance. For instance, one of the initial goals of this research was to take a porous version of the S-shaped structure outlined in the previous chapter and infiltrate it with liquid crystals to try and generate a device with linear polarization selectivity, similar to the circular polarization selectivity achieved by Robbie *et al.* with helical films. The use of liquid crystals to achieve this goal would have added the possibility of dynamic switching, which is simply not possible for the static film described in the previous chapter. However, despite a number of attempts, no useful results could be obtained. Moreover, the results that were obtained did not provide clues as to what was going wrong at all. It was not until the twilight of this thesis research that a model for the alignment of liquid crystals in GLAD films was obtained, and could be used to interpret what would have been otherwise difficult to understand results. This is a significant contribution and serves as a nice extension of the contributions of previous researchers, and will hopefully provide a nice starting point for fu-

ture researchers interested in the potential of three-dimensional liquid crystal alignment in GLAD films. The model allowed us to understand the measurable differences between liquid crystals aligning parallel to or perpendicular to GLAD film columns, and how best to identify which situation was present. Another significant aspect to the model is the ability to predict what features of the film geometry are likely to contribute to favourable or unfavourable alignment conditions. For instance, though fabricating a dynamic linear polarizer proved impossible due to a lack of time, the finite element model suggests ways to potentially create success in the future, for instance, by attempting to reduce the width of the film columns to create the most favourable situation for tangential alignment through a layered structure. The model presented here is still woefully incomplete. Several situations were encountered that the model could not explain, and it omits a host of pertinent features, notably the lack of consideration of any three-dimensional effects. However, these are shortcomings that can be addressed and incorporated into the model if needed. Earlier chapters espoused the benefit of simple models, even in fairly well-understood systems; this chapter reminds us how essential the need is for even the most simplistic of models in systems where it is not at all clear what in the world is happening.

Chapter 6

GLAD-Based Luminescent Solar Concentrators

"The most exciting phrase to hear in science, the one that heralds the new discoveries, is not 'Eureka!' (I found it) but 'That's funny...' " – Isaac Asimov

6.1 Introduction

This chapter details the use of GLAD films toward the fabrication of luminescent solar concentrators [140, 141] (LSCs). The work in this chapter was initially intended to investigate the performance of LSCs that made use of luminescent liquid crystalline polymer networks, with tilted alignment provided by GLAD films, as described in the previous chapter. It was unclear whether tilted alignment would improve device performance, as compared to more standard designs, that employed only planar (lying down) or homeotropic (standing up) liquid crystal alignment [142], and the use of GLAD films represented an easy method with which to obtain repeatable, tilted systems. However, it was rapidly determined that the action of the GLAD/liquid crystal material system had a number of interesting and advantageous effects, that were ultimately ascribed to strong anisotropic scattering, which remains a poorly understood and poorly studied topic with respect to GLAD films. As a result, while the original vision of this work was initially to simply compare the effects of tilted

alignment to non-tilted alignment in LSC design, the results instead ended up focused predominantly on the improved performance arising from anisotropic scattering from the GLAD/LC system. This work therefore contributes to LSC design by demonstrating one potentially useful manner in which to improve the performance of an LSC, but more importantly illustrates the need to better understand anisotropic scattering behaviour in GLAD films, as a means to either exploit or reduce these effects as a particular situation would call for.

6.2 Luminescent Solar Concentrator Operation

The basic principle of operation for an LSC is shown in Figure 6.1. A thin,

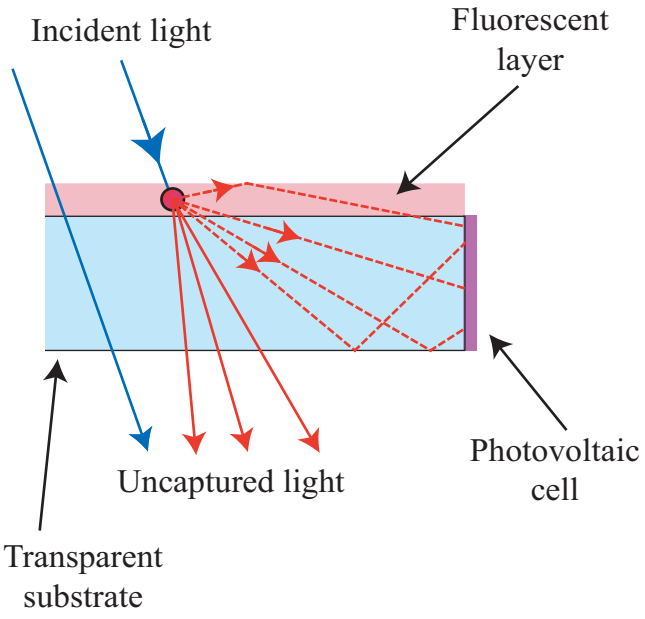

Figure 6.1: Operation of a luminescent solar concentrator

fluorescent film is deposited on a cheap, transparent substrate, typically made of glass, or a polymer such as polycarbonate, or poly(methyl methacrylate) (PMMA). Incident solar radiation is absorbed and reradiated by the fluorescent film, where the reradiated light is Stokes shifted to redder wavelengths as compared to the incident light. Some of that incident light is captured into a waveguide mode of the transparent substrate, whereupon it is guided to one of the substrate edges. A photovoltaic cell can be placed at one or more edges of the device in order to capture the light, and convert it to electricity.

One potential application of LSCs is to act as a low-cost solar collector for use in photovoltaic energy generation [143]. The application is as follows. On the input surface, the LSC captures dN_{in} photons per unit time in the wavelength range $\lambda \rightarrow \lambda + d\lambda$. At a given output surface, dN_{out} photons are emitted per unit time in the same range. If we assume a square substrate with an edge length, L, and a thickness, D, the input area over which solar energy is collected by the LSC is L^2, while the output area is given by $4LD$, if one considers all four edges simultaneously, or just LD if one considers a single output edge. We can relate the number of photons in $\lambda \rightarrow \lambda + d\lambda$ to dI, the irradiance in $\lambda \rightarrow \lambda + d\lambda$, via I_λ, the irradiance per unit wavelength. If we consider only a single output edge, then by conservation of energy, the relationship between dN_λ and dI_λ at the input and at the output is given by:

$$dN_{\text{in}} = \frac{I_{\lambda_{\text{in}}} L^2 \lambda d\lambda}{hc} = \frac{P_{\lambda_{\text{in}}} \lambda d\lambda}{hc}, \tag{6.1}$$

$$dN_{\text{out}} = \frac{I_{\lambda_{\text{out}}} LD\lambda d\lambda}{hc} = \frac{P_{\lambda_{\text{out}}} \lambda d\lambda}{hc}. \tag{6.2}$$

Here, c is the speed of light, and h is Planck's constant. P_λ is the input or output power, and is useful since it is a quantity that can be measured experimentally with relative ease. The external quantum efficiency, η_{EQE}, of the device is given by ratio of output photons to the ratio of input photons:

$$\eta_{\text{EQE}} = \frac{\int_\lambda dN_{\lambda_{\text{out}}}}{\int_\lambda dN_{\lambda_{\text{in}}}} = \frac{\int_\lambda P_{\lambda_{\text{out}}} \lambda d\lambda}{\int_\lambda P_{\lambda_{\text{in}}} \lambda d\lambda} \tag{6.3}$$

The action of the LSC is to take N input photons from an area, $A_{\text{in}} = L^2$, and convert them to $\eta_{\text{EQE}} N$ output photons over an area $A_{\text{out}} = LD = A_{\text{in}} \frac{D}{L} = A_{\text{in}}/G$. Here, we have defined the quantity $G = \frac{L}{D}$ as the geometric gain. We also define the power efficiency, η, of the system as:

$$\eta = \frac{P_{\text{out}}}{P_{\text{in}}} \tag{6.4}$$

In order to determine the cost-effectiveness of an LSC, we consider two cases. Case 1 is covers an area A_{in} with a photovoltaic cell. Case 2 covers an area A_{in} with an LSC/photovoltaic combination, characterized by the parameters G and η_{EQE}. If the cost of a photovoltaic cell, C, is assumed to be proportional to

its area (with a proportionality constant, k), and we assume that the cost of the LSC is negligible, then the cost per unit power of these two approaches is then equal to:

$$C_1 = \frac{kA_{\text{in}}}{P_{\text{in}}}, \tag{6.5}$$

$$C_2 = \frac{kA_{\text{out}}}{P_{\text{out}}} = \frac{kA_{\text{in}}}{GP_{\text{out}}} = \frac{C_1}{\eta G} \tag{6.6}$$

We see that the LSC is only a cost-effective solution if $\eta G > 1$. This is the break even case (for a zero-cost LSC), but in principle we want both η and G to be as large as possible for the most cost efficiency. It is relatively simple to increase G by reducing the substrate thickness, and a large G can somewhat compensate for a small η. However, this is only partially true, as a low η will require a much larger physical area to be covered. We shall show that this requirement is a significant challenge, and it is possible that LSCs will fail to be viable in this application.

A second, more likely application of the LSC technology is not to compete directly with photovoltaic electricity generation, but to be integrated in smart, or self-powered windows [144]. Smart windows are active windows that can be electrically switched between transparent state, and opaque or scattering states. There are a variety of methods to create such windows, many of which are based on liquid crystal and/or dichroic materials. LSCs have the potential to be of great utility in these applications as various designs would allow the fluorescent layer to either operate in the infrared, or to possess a neutral tint, which would not impede the usual application of a smart window. In such a situation, the integrated LSC would absorb incident sunlight (or other ambient light), and provide power for the electrical switching of the smart window. Coupled with an energy storage device, this would allow for easy-to-install self-contained smart windows, requiring no external wiring or batteries. In this situation, it is the transparency of the device that is paramount, not the efficiency.

6.3 Luminescent Solar Concentrators Based on Polymeric Liquid Crystals

The LSCs of interest use a liquid crystalline polymer host material doped with fluorescent guest molecules as the fluorescent coating on top of polycarbonate or PMMA substrates. The fluorescent dye we use is the dichroic Lumogen Yellow 170, introduced in the previous chapter. As with the optical absorption, the fluorescence of the dye is also anisotropic. The molecule possesses a transition dipole moment [35], which reradiates light in a dipolar fashion. Dipoles emit radiation predominantly along directions normal to the transition moment, and no light radiates along the axis of the transition moment itself. If we visualize the fluorescent molecule as a uniaxial ellipsoid, and assume, plausibly [145], that the preferential extinction direction, and the transition dipole moment are parallel to the long axis of the molecule, then the properties of anisotropic optical absorption and fluorescence are summarized in Figure 6.2. We illustrate

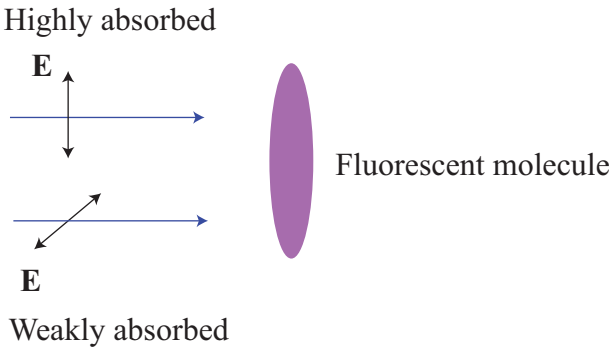

(a) Dichroism of an ellipsoidal molecule

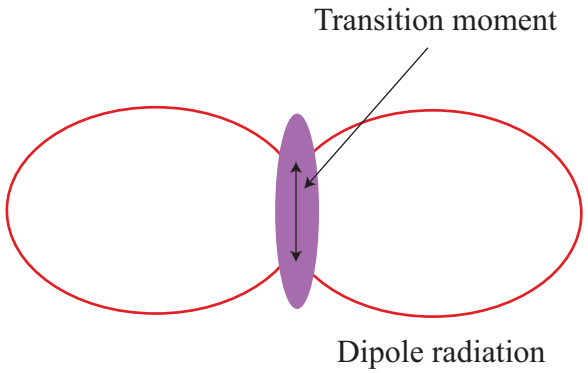

(b) Radiation of an ellipsoidal molecule

Figure 6.2: Dichroic absorption and radiation of a fluorescent molecule

here that light polarized along the axis of the molecule is preferentially absorbed, while light polarized normal to that axis is more weakly absorbed. As well, reradiated light is emitted preferentially normal to the molecular long axis, with no emission taking place along the molecular axis itself.

As we saw in the previous chapter, dye molecules can be dissolved into liquid crystalline materials and will align so that the molecular long axis is parallel to the director of the liquid crystal host. By aligning the fluorescent molecules appropriately, one can exert control over the direction of reradiated light. Carefully chosen orientations of the dye molecules can lead to both higher LSC efficiencies due to the capture of additional light in waveguiding modes, as well as differences in the amount of collected light at each of the four edges of the LSC. This phenomenon was recognized by Verbunt *et al.* [145], who used a planar polymeric liquid crystal layer comprised of C3M and C6M, with various fluorescent dyes as guest molecules, as illustrated in Figure 6.3. The researchers

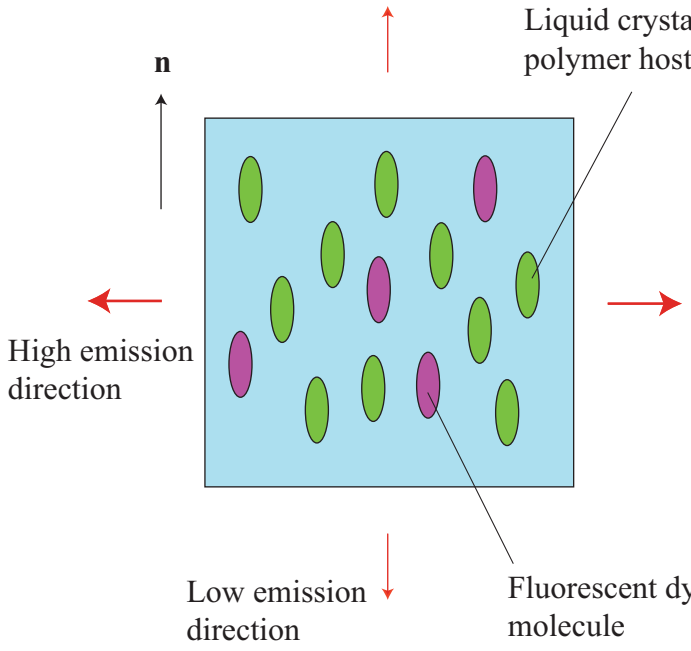

Figure 6.3: Illustration of preferred emission in an aligned polymeric liquid crystal-based LSC

found that the collected light along the edges normal to the molecular axes of the dye molecules was up to 60% greater than the collected light on the remaining two edges. This allows for the placement of photovoltaic cells on only two

edges as opposed to four, significantly reducing the overall cost of the device. Placing mirrors or scattering layers on the other two edges can further increase the amount of light collected.

The original motivation for using GLAD in this approach was to use these films to try and orient the liquid crystalline molecules, and, in turn, the fluorescent molecules at different angles off the substrate, in an effort to try and emit light preferentially into guided modes. However, as the following sections will show, the true interaction between the liquid crystals and the GLAD films for this application is quite complicated, and ultimately points to a large deficiency in understanding how light propagates through highly porous GLAD films.

6.4 Experimental

6.4.1 Experimental Procedure

To examine the feasibility of using GLAD films in the application of LSCs, a number of SiO_2 films were chosen. Films were deposited on $30 \times 30 \times 3$ mm^3 poly-methylmethacrylate (PMMA) substrates at $\alpha = 85^\circ$ ($G = 10$). Deposition was done using electron beam evaporation at deposition pressures between 0.3 mPa to 0.7 mPa. The films were fabricated using the spin-pause algorithm with $f = 0.8, 0.9$ and 1.0 resulting in films having $\beta' = 30.0^\circ, 35.8^\circ$ and 39.0° respectively. Films were deposited to thickness, T^{total} ranging from $1 - 5$ μm. For the fluorescent polymer, a similar C3M/C6M mixture to that described in the previous chapter was employed:

- C6M/C3M/Yellow 170/Irgacure 184 (78.8/19.7/1.0/0.5)

To coat the samples, the liquid crystal mixture was heated to approximately 80 °C, spread on the empty sample, and spun at $1500 - 2500$ rpm. The sample was quickly placed on an enclosed hot plate held at 57 °C, just above the crystalline to nematic transition temperature, and cured under ultraviolet light for $5 - 10$ minutes in an N_2 atmosphere. Based on the previous chapter, the liquid crystal orientation is expected to be oriented in the direction opposite the column tilt, and some bulk distortion is expected, owing to the energetics of the film/air boundary. Once cured, the samples are mechanically and chemically robust, which is a potential advantage of this application over many other potential applications involving GLAD. The final film thickness is measured by scraping

a small section of the film away with a razor blade, and using optical profilometry to measure the height from the substrate to the top of the film. In all cases, the final thickness is greater than the initial GLAD thickness, typically by $1-3$ μm.

In order to measure the performance of the GLAD-based LSC, the sample was illuminated by an AM1.5 solar simulator at normal incidence on a black background. The irradiance spectrum of the lamp is shown in Figure 6.4. The

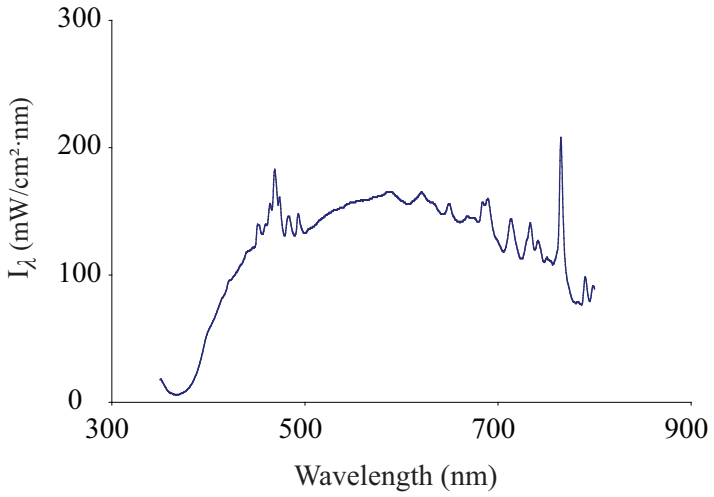

Figure 6.4: Power spectrum of the AM1.5 solar simulator

figure shows the incident irradiance per unit wavelength of the lamp, over the range $350-800$ nm, measured across a 1 cm^2 area. The integral of the curve represents the total irradiance of the light source, and is equal to 54.6 mW/cm^2. For the 9 cm^2 substrates used in this study, this equates to a total input power of $P_{\text{in}} = 491.4$ mW. While illuminated, the output from a single edge is measured by placing the edge of the sample at the input port to an integrating sphere (Labsphere, Inc.). The input port is designed to match the dimensions of the substrate edge to ensure that no stray light enters the sphere, and that only light from the very edge of the substrate (and none from the top) enters the sphere. The sphere is equipped with a photopic detector (SDA-050-P-RTA-CX) and a spectrometer, and can measure the output power per unit wavelength of the sample.

6.4.2 Results

Figure 6.5 shows the measured $P_{\lambda_{out}}$ for five different scenarios over the 350 – 800 nm spectral range. At the bottom of the graph, we see the output power

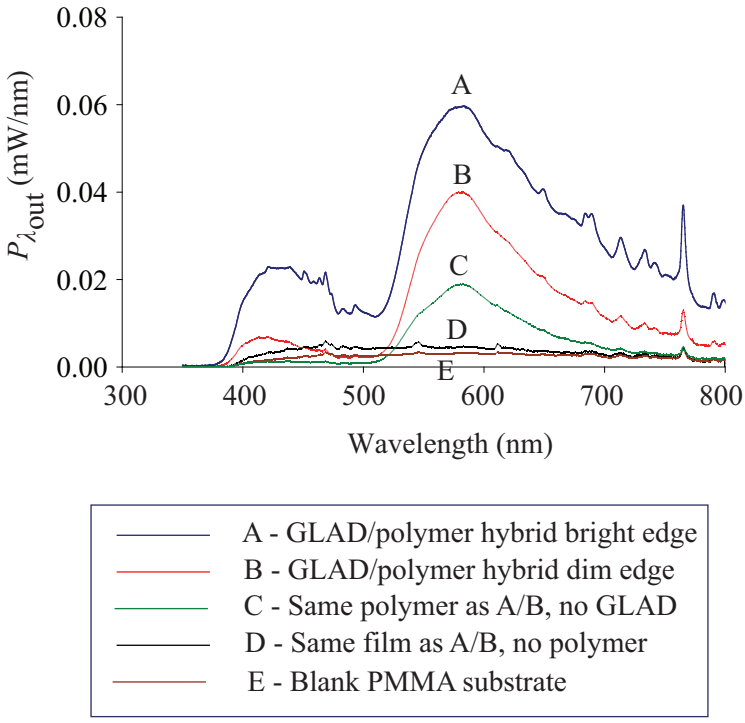

Figure 6.5: Comparison of light output for several different samples (P_{in} = 491.4 mW)

spectrum for a bare PMMA substrate (sample E). Because of a small amount of scattering and leakage, some light is coupled into the sphere by the bare substrate. Just above this, the light coupled in by an as-deposited GLAD film (sample D) is shown, and exhibits a marginal increase in output power. Sample C is a standard LSC, using liquid crystals aligned using a rubbed layer of polyvinyl alcohol. Otherwise, fabrication of this sample followed the same procedure as for the GLAD-based LCs. We see that this device couples a significant amount of light into the output. Very little light is coupled in between 350 – 500 nm, corresponding closely to the absorption region of the Yellow 170 dye. Most of the light is coupled in between 500 – 750 nm, corresponding to the fluorescent

region of the dye. Samples A and B are the same sample, but represent the output from opposing edges. We will discuss the difference between these two edges shortly. For the time being, notice that both of these edges output the most amount of light, more than any of the other control samples. Additionally, while most of the output light is coupled out between $500 - 750$ nm, these samples, particularly sample A, still couple out a significant amount of light at lower wavelengths. We will see later that this corresponds to scattered light, which is a huge reason for the performance of these devices. Figure 6.6 show photographs of a number of these samples under AM1.5 illumination, in which one can visually see the difference in light output.

Table 6.1 lists the total output power, $P_{\text{out}} = \int_{\lambda} P_{\lambda_{\text{out}}} d\lambda$, as well as the power efficiency, for these 5 samples. The table also lists the transmission losses, reported as the total (specular and diffuse) transmittance of each sample, measured using a Shimadzu UV-Vis spectrophotometer. We see that the overall efficiency is quite poor. The quantity, ηG, is also quite small, attaining only 0.3 in the best performing case, still a significant amount below the break even point of unity. One major reason for this is because of how much light is transmitted straight through the film. In each case, approximately 80% or more of the incident light is not coupled into the system to begin with. Additional sources of loss include losses due to reflection, estimated at approximately $(5 - 10\%)$, losses to the Stokes shift during absorption and re-emission, and light that is coupled into the LSC, but leaves through some other pathway (scattered out, reabsorbed and re-emitted outward, emitted from a different edge). Some of these concerns can be addressed, for instance by making the film thicker to increase absorption, by placing the device on a white background in order to reflect light back into the system, and by placing mirrors or scatterers on the other edges of the sample. Still, there are many hurdles to overcome with the design, and it appears that it will be difficult to fabricate a cost-efficient device. However, the use of the GLAD film appears to significantly increase the light output, and is a very encouraging feature.

That said, there are a number of interesting properties of these devices to examine. Figure 6.7 shows the difference in the light output on the four edges of the substrate for $\beta' = 35.8^{\circ}$ samples of varying thickness, of which sample A/B above is the thickest member. The figure also has a top-down view of a typical sample, indicating the definition of the four sides. The side labeled

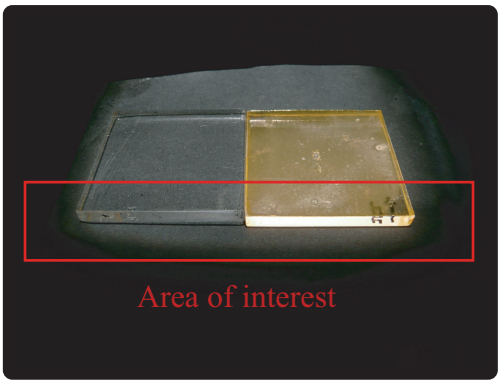

(a) Left: Sample E (blank substrate); Right: Sample A ("front" side GLAD-based LSC)

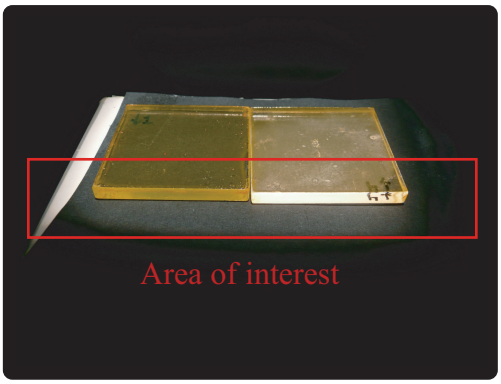

(b) Left: Sample C (traditional LSC); Right: Sample A ("front" side GLAD-based LSC)

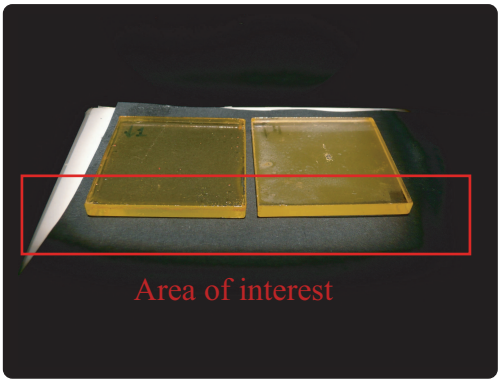

(c) Left: Sample C (traditional LSC); Right: Sample B ("back" side GLAD-based LSC)

Figure 6.6: Photographs of different LSC samples under AM1.5 illumination (taken at an angle of $\sim 30°$)

Table 6.1: Luminescent solar concentrator film samples ($P_{\text{in}} = 491.4$ mW)

Label	Description	$P_{\lambda_{\text{out}}}$ (mW)	η	Transmission loss
A	6.5 μm thick film, $\beta' = 35.8°$, bright edge	14.65	0.0298	0.793
B	6.5 μm thick film, $\beta' = 35.8°$, dim edge	4.46	0.009	0.797
C	5 μm film, same polymer as A/B, no GLAD	2.59	0.005	0.941
D	Same GLAD film as A/B, no polymer	1.46	0.003	0.784
E	Blank PMMA substrate	1.01	0.002	0.922

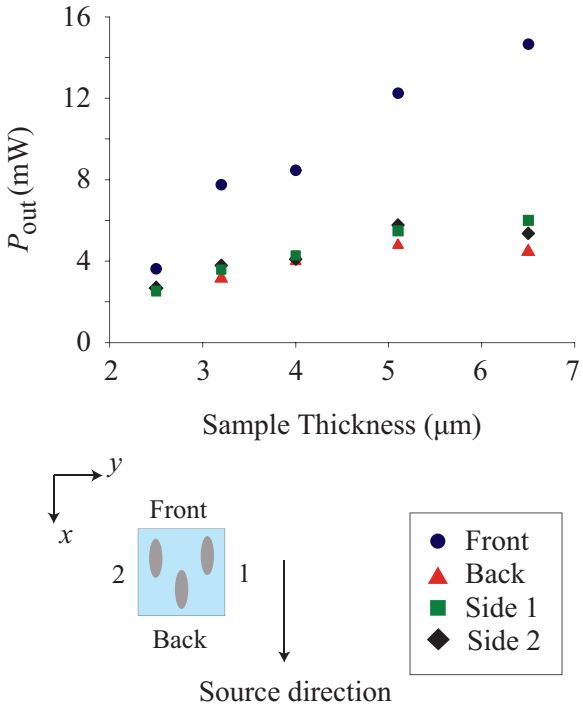

Figure 6.7: Comparison of light output for the four edges of sample A/B ($P_{in} = 491.4$ mW)

"back" is the side closest to the deposition source, during paused segments of the spin-pause algorithm. As a result, film columns grow toward the "back" edge, and point away from the "front" edge. The x- and y-axes are labeled as well, consistent with previous chapters, in order to help visualize the situation. Sides 1 and 2 are symmetric, and their labeling is somewhat arbitrary. The results are quite interesting. The "front" edge couples out significant amount more power than the other sides, by a factor of $2-3$, with the ratio increasing steadily with film thickness. As expected, there is no discernable difference in the output between sides 1 and 2, but the output from the "back" side is marginally less. This ordering of the output power, with the "back" side outputting the least amount, the "front" side emitting the most, with sides 1 and 2 in the middle was consistently observed in all measured samples. This is a very interesting result, as the strong output from a single edge could potentially reduce the cost of a GLAD-based LSC system by restricting the placement of photovoltaic cells to that edge only, and attempting to redirect light propagating toward the other three edges, back into the system toward the "front" edge.

Figure 6.8 shows the light output as a function of sample thickness for films with $\beta' = 30.0°, 35.8°$ and $39.0°$. This figure illustrates the unusually strong

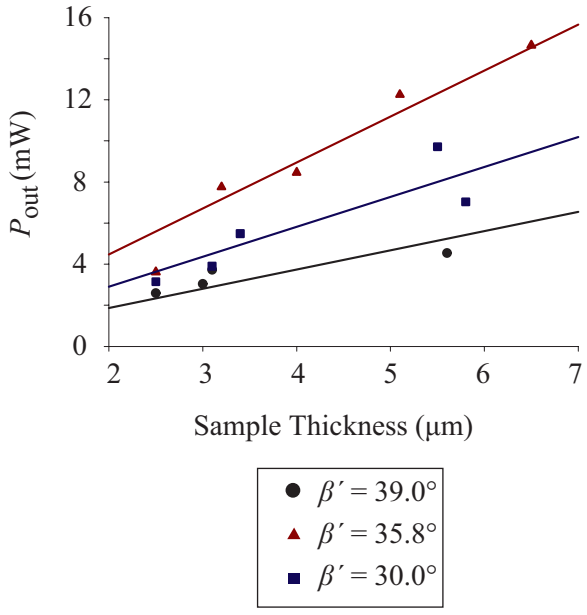

Figure 6.8: Comparison of light output for samples with different β'

dependence of the output power on the liquid crystal column tilt. Strange as well is the fact that there appears to be a local maximum in the light output for $\beta' = 35.8°$, as opposed to having a monotonic relationship with β'. It is unclear why the system behaves in this manner, and why it is so sensitive to small changes in β'. In fact, these differences in β' are not far removed from the expected differences in β' that would be observed from non-uniformity issue, as described in Chapter 2. However, the strong dependence on β' hints at the next result, which indicates that the increase in light output has less to do with the liquid crystal nature of the polymer, but more to do with interesting scattering behaviour that occurs when polymers are introduced into a GLAD film.

Figure 6.9 shows the output power obtained from two new device designs (labeled F and G). We use the same type of GLAD film as previously: a 6.5 μ m, $\beta' = 35.8°$ SiO_2 spin-pause design. However, in this case, we infiltrate the film with two, non-fluorescent species. For sample F, we merely spun coat the film with isotropic polystyrene, dissolved in xylene. For sample G, we used the same liquid crystal mixture and fabrication process described above, but simply removed the Yellow 170 dye. We see that in both cases the light output is very significant. In fact, the polystyrene sample has $P_{\text{out}} = 12.3mW$, which is almost as high as the best performing GLAD-based concentrators that do include fluorescence. The liquid crystal sample has $P_{\text{out}} = 4.7mW$, which is comparable to the output from many of the traditional LSC structures that do not employ GLAD. Additionally, though we do not show it here, the magnitude of the output light from each of the edges follows the same order as mentioned earlier, depicted in Figure 6.7. Figure 6.10, which shows pictures of samples F and G, can be examined to try and determine what exactly is going on. We see in Figure 6.10(a), that the polystyrene sample is very cloudy and scatters most of the light incident on it. However, rather than scatter this light uniformly straight through the sample, it appears to scatter the light preferentially toward the "front" edge of the device. This behaviour occurs at all wavelengths, which results in very similar spectra for the output power shown in Figure 6.9, and the input power shown in Figure 6.4. It is important to note that it is the combination of the polystyrene and the GLAD film is required to achieve this. Neither an empty GLAD film (as shown in Figure 6.5) nor a polystyrene film (which can have no preferred directionality) on their own can cause this

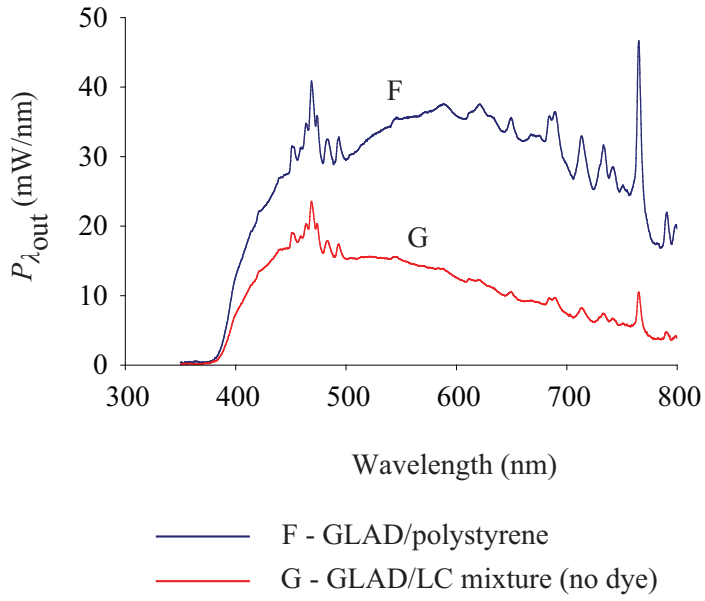

Figure 6.9: Comparison of light output for two samples with no fluorescent dye present

directional scattering. This is a very interesting result and suggests that GLAD films infiltrated with a variety of species may have very interesting scattering properties. In fact it is likely that this scattering is at least as important as the fluorescence in driving light to the output of the GLAD-based LSC's. Additionally, the behaviour of sample G is also very interesting. As seen in Figure 6.10(b), the device out-couples a reasonable amount of light. However, unlike the polystyrene sample, sample G retains most of its specular transmission, and does not appear cloudy at all. However in order to be out-coupling light, it must be scattering it, as there is no other possible mechanism with which to accomplish this. Interestingly then, sample G acts as a scattering element, but maintains a high degree of transparency. It is also colourless, and for this reason it is reasonable to think of using such a device in a smart window capacity, as discussed earlier. In this case, the amount of output power and the cost-efficiency of the device are not primary constraints (though are certainly still important), but rather it is the ability to out-couple light for power generation, while still maintaining a window-like appearance that is important.

Unfortunately, one of the major hurdles with trying to employ this GLAD-

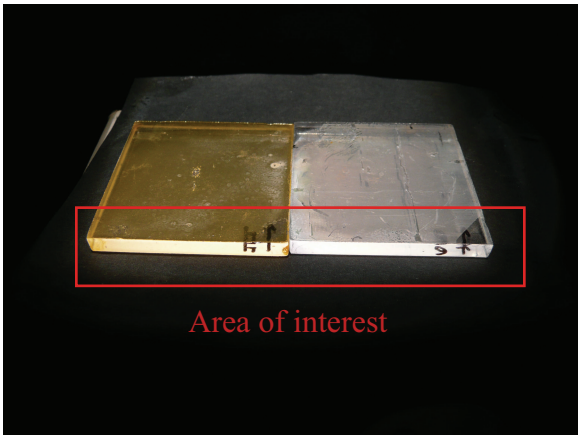

(a) Left: Sample A ("front" side, GLAD-based LSC); Right: Sample F ("front" side, polystyrene concentrator)

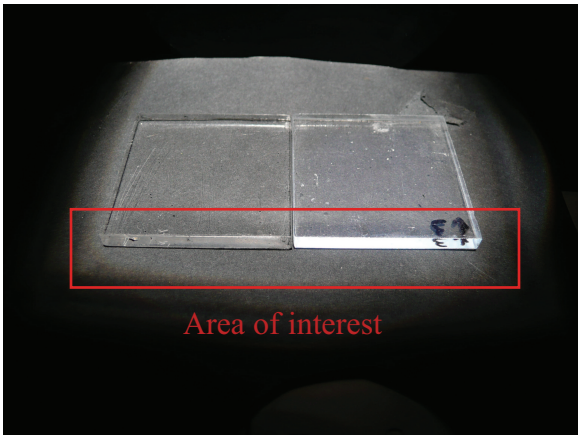

(b) Left: Sample E (blank substrate); Right: Sample G ("front" side, GLAD-based concentrator lacking fluorescent dye)

Figure 6.10: Comparison photographs of concentrator designs lacking fluorescent dyes, under AM1.5 illumination

based technology in any capacity is that the effect does persist over long distances. New samples were fabricated on $5 \times 5 \times 0.5$ cm^3 PMMA substrates in order to gauge the potential to scale these devices to larger dimensions. An experiment is set up so that incident light is blocked from the input surface of the film using opaque masks, except for in a 1 cm region as shown in Figure 6.11. The exposed region extends from $d - 1$ cm to d, and we measure the output power when only that strip of the sample is exposed to the light source. Figure 6.12 shows how the out-coupled power decreases with distance from the output edge for different LSC designs. We see that in the GLAD-based LSC, both

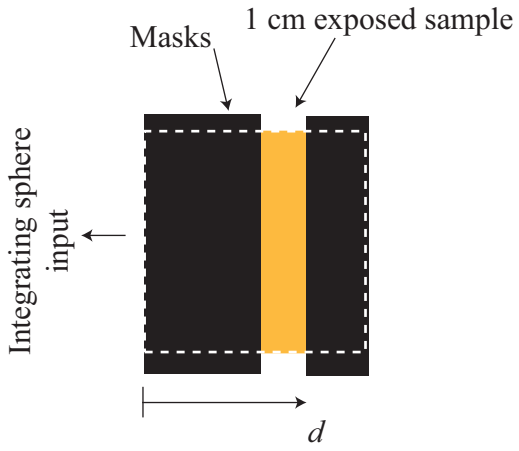

Figure 6.11: Experimental setup for measuring the dependence of output power on the distance from the sample edge

with and without fluorescent polymer present, the amount of power gained from the GLAD coating quickly drops off, and it appears as though the GLAD approach will offer no benefit beyond about 10 cm away from the edge. Figure 6.13 shows the dependence on the out-coupled power for the GLAD LSC employing liquid crystals with the fluorescent dye. We see that the drop off is most significant for the high-output "front" edge, but there is a mild decrease along the remaining edges as well. Unfortunately, it is not currently known how to mitigate this problem, and until it can be solved, it is not likely that this technology will be useful, except for by perhaps slightly increasing light collection along the outer edges of a larger concentrator device. Hopefully, with a greater future understanding of how GLAD films scatter light, and how that scattering is affected by media infiltrated into the film's pores, researchers will be able to design a device in a way that can be scaled to larger sizes, and

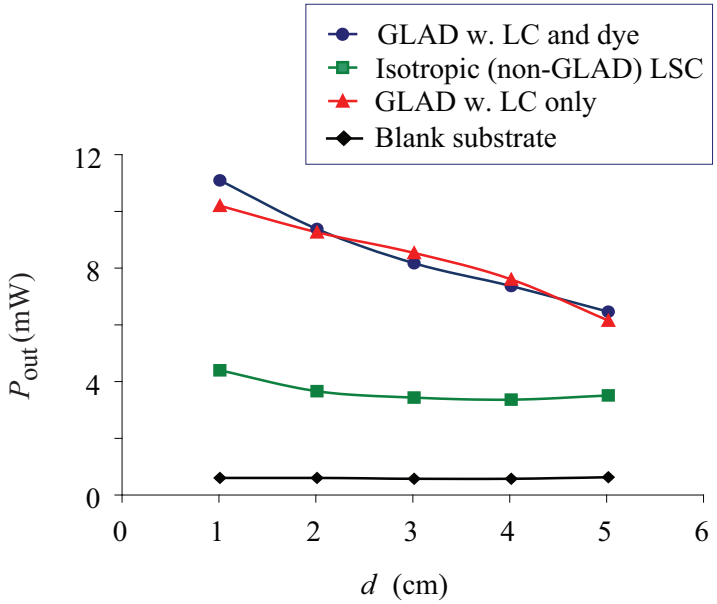

Figure 6.12: Amount of out-coupled power as a function of distance from the substrate edge for different LSC designs

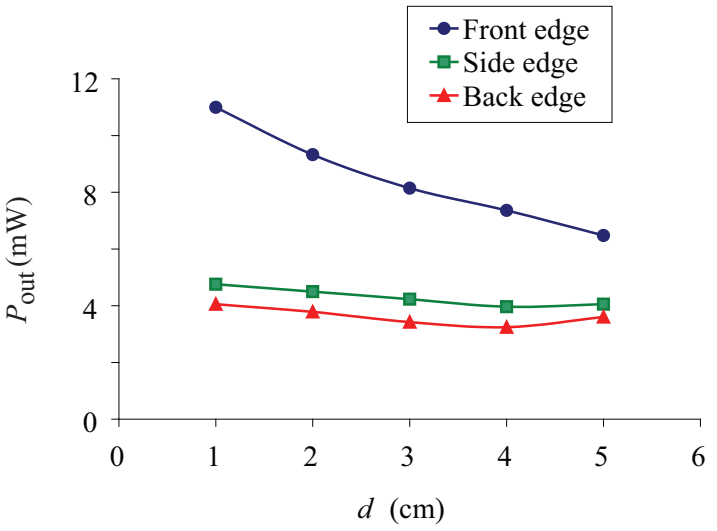

Figure 6.13: Amount of out-coupled power as a function of distance from the substrate edge for different sides of a GLAD-based LSC

that could potentially make use of some of the interesting properties described here.

6.5 Conclusions

Unfortunately, this chapter did not yield the most positive results. That said, it is worth mentioning that it is encouraging to see that LSCs based on GLAD do have a number of advantages over more traditional LSCs, and they do significantly increase the ability to harvest light in a concentrator approach. And while GLAD may not be the ideal candidate for pursuing this line of research, it does appear that controlled scattering could be a very productive and beneficial method of increasing the out-coupling of light in LSCs. Major problems that would need to solved would include determining the optimum composition of scattering layers (scatterer shape, appropriate materials, etc.) as well as a way to solve the drop-off problem and find a way to scale this approach up to much larger device sizes. Though the work described in this chapter was begun with the intention of controlling the emission of light by controlling molecular orientation, it appears that the major result was the discovery of very strange directional scattering behaviour in films that combine GLAD and various polymer species. This behaviour only occurs when the constituent components are brought together, and the reasons for it are still unclear. Directional scattering appears to be useful, at least on small scales in solar concentrator applications, and it is only for lack of time that this phenomenon was not further investigated. Scattering in GLAD films, even absent guest materials, is already a poorly understood problem, and deserves some serious attention. The appearance of interesting behaviour when the voids of a GLAD film are filled makes the attention doubly deserved.

Chapter 7

Conclusions

"I may not have gone where I intended to go, but I think I have ended up where I needed to be." – Douglas Adams

7.1 Summary

The major contributions of this thesis are in Chapters 2 to 6, which we will summarize here briefly. Possible directions for future research are also indicated.

Chapter 2 contains what is probably the most useful work in this thesis and presents a model useful, in some form, to virtually all researchers involved in GLAD. The material builds upon earlier fundamental studies of GLAD growth in order to answer a number of important engineering questions, ultimately related to scalability and commercialization. The work unifies two quantities in particular, β' (through E) and $\bar{\varrho}$ (through c) as crucially important characteristics of a given film material, and illustrates how a great number of important film properties can be deduced if those quantities are known. The major results in this chapter include the ability to predict film thickness and film density, as well as the columnar orientation for arbitrary GLAD algorithms, applicable in a wide variety of cases. Knowing how these quantities varies over a substrate enables one to predict how much other important parameters, such as optical constants or conductivity, *etc.* will vary under a host of different condi-

tions. Moving forward, there remains a number of avenues for future research. Modifying the model to handle changing substrate temperatures is likely to be fruitful and very informative. Additional subtleties can also be tackled, such as dealing with larger area sources, and dealing with scattered vapour flux, due to residual pressure in the deposition chamber. Finally, modifying the model to handle non-planar substrates is likely a very important direction to pursue, as this may be highly relevant for large scale production.

Chapter 3 and Chapter 4 have similar themes. Chapter 3 provides a framework to predict the optical properties of a variety of possible GLAD structures, knowing, again, only a select few material properties. This framework is built on a combination of previous work into understanding the optical properties of porous dielectric thin films as well as previous work describing the connection between film growth algorithms and film geometry. A number of important new results were obtained by bringing these two research directions together. Again, the column tilt and the film density show their importance, as do the birefringence and the bulk refractive index of the deposited materials. The model is used to correctly predict the existence of several interesting optical features, notably a slanted uniaxial film, as well as film structures possessing negative in-plane birefringence. Chapter 4 takes inspiration from liquid crystals and the results from Chapter 3 to create and refine a robust reflective linear polarizer for use at normal incidence. Future work related to these chapters will likely follow one of two directions. The first is to simply catalog the physical properties (density, column tilt) of as many materials as possible to serve as a database from which designers can choose the ideal materials for given applications. The second avenue is to actually design and fabricate new optical devices by choosing both appropriate materials and appropriate film geometries to yield the required optical properties. Additionally the results of Chapter 2 and 3 can be combined to create gradients in film properties, which may be inherently useful from a device perspective, or may simply be used as a combinatorial approach to identify ideal designs. The work in this chapter may also be useful for refining existing designs, as it was for the S-shaped film in Chapter 4.

Chapter 5 introduced the use of GLAD films as alignment materials for liquid crystals and examined the history and physics behind nematic liquid crystals. The major goal of the work in this chapter was to expand upon the

important, but not yet fully understood work of previous researchers. The major contribution of the work was a two-dimensional finite element model based on an elastic continuum theory capable of accurately predicting a number of experimental features of a variety of GLAD/liquid crystal hybrid systems. The presentation of the model, and the dissemination of results pertaining to the alignment of a variety of reactive and non-reactive mesogens in several GLAD film structures should allow future researchers to move on to more complex systems and models to fully exploit the potential of GLAD as a three-dimensional scaffold for liquid crystal alignment. There remains a significant number of directions for future research in this area. Extending the finite element model to three-dimensions is an obvious suggestion as is trying to obtain a greater understanding of the anchoring conditions that lead to various boundary conditions at the film surface. There is also a virtually infinite number of combinations of film material, liquid crystal material, film structure and surface chemistry that can be explored to search through to find ones that lead to specific molecular orientations or reliable liquid crystal alignment in three-dimensions. This latter condition would very much be the "holy grail" of this research topic. Finally, patterning a substrate with different film structures or film surface chemistry could provide a new method of micropatterned alignment which could be of great interest.

Finally, Chapter 6 introduced the concept of the luminescent solar concentrator. The use of GLAD films to align fluorescent liquid crystal polymers for this application proved to be promising on the small scale, and exhibited some significant improvements in concentrating light as compared to concentrators fabricated without GLAD. Perhaps more importantly, it was determined that a significant portion of the effect owed itself to a curious form of directional scattering that is only observed when a suitable GLAD film host is paired with a suitable polymer guest. This reinforces the notion that scattering effects in GLAD films is currently seriously underinvestigated, and should be a major focus of research in the near future, regardless of any specific connection to luminescent solar concentrator effects. The ability to introduce directional scattering, and to be able to control the degree and direction of this scattering through simple changes in film geometry, film material or by adding material into the pores of the film indicates that this is a system that is potentially rife with interesting effects and that possesses a huge number of variables that

could be adjusted. Because of the richness of this system, the prevalence of scattering at high deposition angles and the small number of reported results in the literature, it is likely that research into the optical scattering of GLAD films would be very worthwhile and relevant to most researchers in the field.

7.2 Final Words

And with that, we have reached the end. There is not a great deal to say that hasn't already been said, so I'd like to abandon the formality of the previous chapters to say a few things. I'd first like to thank you, reader, if you've made it this far, for being interested in my work. And if you are on my defense committee and were forced to sit through this whole thing, my sincerest apologies. Seriously though, I do hope this work has been useful, or at the very least, interesting. Writing this thesis has required an accumulation of over five years worth of reading, experimenting, surviving numerous frustrations, squeezing under deadlines, and waiting for those wonderful moments where things just made sense. It has been a great adventure that I'd repeat again if I had the choice, though it might be nice to do things in the correct order the second time around. I encourage any students reading this to keep a positive attitude when things are not working, or are not making sense. Be sure to ask your peers and your colleagues for help, and don't be afraid to take the time to take a step back and try and get a new perspective on your problems. Often it makes the biggest difference. Some final words of advice to any of you still reading:

- Don't wait until the night before/day of important deadlines to get things done. Definitely don't do this over and over again for the duration of your studies.
- Jump at any opportunities you get, even if they seem a bit intimidating. Successfully tackling an intimidating goal is one of the greatest feelings in the world.
- There are some sites on the internet that will consume way too much of your time if you let them. This effect gets more serious for every grad student in the nearby vicinity. Grad students also seem to have a gravitational attraction to other grad students. You have been warned.

- To paraphrase Paul McCartney, show the people who love you the same amount of love in return. And make sure you thank them for putting up with you being cranky while you were scrambling to write your thesis.
- Whatever you do, have fun! Otherwise you are doing it wrong.

This has been an incredible learning experience, and I look forward to whatever comes next. Thanks for reading.

Nick Wakefield

References

[1] B. A. Movchan and A. V. Demchishin. Study of the structure and propoerties of thick vacuum condensates of nickel, titanium, tungsten, aluminum oxide and zirconium oxide. *Fizika Metallov i Metallovedenie*, 28:653–660, 1969.

[2] R. Messier. Revised structure zone model for thin film physical structure. *Journal of Vacuum Science & Technology A: Vacuum, Surfaces, and Films*, 2(2):500, 1984.

[3] M. Kupsta. *Advanced Methods for GLAD Thin Films*. PhD thesis, University of Alberta, 2010.

[4] W. F. Smith and J. Hashemi. *Foundations of Materials Science and Engineering*. McGraw-Hill, 4th edition, 2006.

[5] D. O. Smith, M. S. Cohen, and G. P. Weiss. Oblique-Incidence Anisotropy in Evaporated Permalloy Films. *Journal of Applied Physics*, 31(10):1755, 1960.

[6] X. Xiao, G. Dong, J. Shao, H. He, and Z. Fan. Optical and electrical properties of SnO2:Sb thin films deposited by oblique angle deposition. *Applied Surface Science*, 256(6):1636–1640, January 2010.

[7] Y. Levy, M. Jurich, and J. D. Swalen. Optical properties of thin layers of SiOx. *Journal of Applied Physics*, 57(7):2601, 1985.

[8] Y. Taga. Recent progress of nanotechnologies of thin films for industrial applications. *Materials Science and Engineering: C*, 15(1-2):231–235, August 2001.

[9] A. Kundt. Ueber Doppelbrechung des Lichtes in Metallschichten, welche durch Zerstäuben einer Kathode hergestellt sind. *Annalen der Physik und Chemie*, 263(1):59–71, 1886.

[10] I. Hodgkinson, Qi Hong Wu, and Simon Collett. Dispersion Equations for Vacuum-Deposited Tilted-Columnar Biaxial Media. *Applied Optics*, 40(4):452, 2001.

[11] D. J. Poxson, F. W. Mont, M. F. Schubert, J. K. Kim, and E. F. Schubert. Quantification of porosity and deposition rate of nanoporous films grown by oblique-angle deposition. *Applied Physics Letters*, 93(10):101914, 2008.

[12] J. M. Nieuwenhuizen and H. B. Hannstra. No Title. *Philips Technical Review*, 27:87, 1966.

[13] R Tait, T Smy, and M Brett. Modelling and characterization of columnar growth in evaporated films. *Thin Solid Films*, 226(2):196–201, April 1993.

[14] S. Lichter and J. Chen. Model for columnar microstructure of thin solid films. *Physical Review Letters*, 56(13):1396–1399, 1986.

[15] K. M. Krause, M. T. Taschuk, K. D. Harris, D. A. Rider, N. G. Wakefield, J. C. Sit, J. M. Buriak, M. Thommes, and M. J. Brett. Surface area characterization of obliquely deposited metal oxide nanostructured thin films. *Langmuir*, 26(6):4368–76, March 2010.

[16] A. L. Elias, K. D. Harris, and M. J. Brett. Fabrication of Helically Perforated Gold, Nickel, and Polystyrene Thin Films. *Journal of Microelectromechanical Systems*, 13(5):808–813, October 2004.

[17] J. J. Steele, Michael T. Taschuk, and Michael J. Brett. Nanostructured Metal Oxide Thin Films for Humidity Sensors. *IEEE Sensors Journal*, 8(8):1422–1429, August 2008.

[18] L. W Bezuidenhout and M. J Brett. Ultrathin layer chromatography on nanostructured thin films. *Journal of Chromatography A*, 1183(1-2):179–85, March 2008.

[19] M. D. Fleischauer, Jing Li, and M. J. Brett. Columnar Thin Films for Three-Dimensional Microbatteries. *Journal of The Electrochemical Society*, 156(1):A33, 2009.

[20] G. K. Kiema, M. J. Colgan, and M. J. Brett. Dye sensitized solar cells incorporating obliquely deposited titanium oxide layers. *Solar Energy Materials and Solar Cells*, 85(3):321–331, January 2005.

[21] J. L. Janning. Thin film surface orientation for liquid crystals. *Applied Physics Letters*, 21(4):173, 1972.

[22] S. Woo and C. K. Hwangbo. Optical Anisotropy of TiO 2 and MgF 2 Thin Films Prepared by Glancing Angle Deposition. *Journal of the Korean Physical Society*, 49(5):2136–2142, 2006.

[23] W. A. Crossland and J. H. Morrissy. Tilt angle measurements of nematic phases of cyano-biphenyls aligned by obliquely evaporated films. *Journal of Physics D: Applied Physics*, 9:2001–2014, 1976.

[24] G. A. Niklasson, C. G. Granqvist, and O. Hunderi. Effective medium models for the optical properties of inhomogeneous materials. *Applied Optics*, 20(1):26, January 1981.

[25] D Aspnes. Optical properties of thin films. *Thin Solid Films*, 89(3):249–262, March 1982.

[26] T. C. Choy. *Effective Medium Theory: Principles and Applications*. Oxford University Press, 1st edition, 1999.

[27] D. Stroud. The effective medium approximations: Some recent developments. *Superlattices and Microstructures*, 23(3-4):567–573, March 1998.

[28] D. J. Griffiths. *Introduction to Electrodynamics*. Prentice Hall, third edition, 1999.

[29] D. E. Aspnes. Local-field effects and effective-medium theory: A microscopic perspective. *American Journal of Physics*, 50:704, 1982.

[30] R. Becker and F. Sauter. *Electromagnetic fields and interactions*. Dover Publications, 1982.

[31] G. W. Milton. *The Theory of Composites*. Cambridge University Press, first edition, 2002.

[32] C. Kittel. *Introduction to Solid State Physics*. John Wiley & Sons, seventh edition, 1996.

[33] R. M. A. Azzam. Propagation of partially polarized light through anisotropic media with or without depolarization: A differential 4 4 matrix calculus. *Journal of the Optical Society of America*, 68(12):1756, December 1978.

[34] R. M. A. Azzam. *Mueller-matrix ellipsometry: a review*, volume 3121. SPIE, 1997.

[35] E. Hecht. *Optics*. Addison Wesley, fourth edition, 2001.

[36] J. Gospodyn and J. Sit. Characterization of dielectric columnar thin films by variable angle Mueller matrix and spectroscopic ellipsometry. *Optical Materials*, 29(2-3):318–325, November 2006.

[37] D. W. Marquardt. An Algorithm for Least-Squares Estimation of Nonlinear Parameters. *SIAM Journal on Applied Mathematics*, 11(2):431, 1963.

[38] N. G. Wakefield and J. C. Sit. On the uniformity of films fabricated by glancing angle deposition. *Journal of Applied Physics*, 109(8):084332, 2011.

[39] K. Robbie, L. J. Friedrich, S. K. Dew, T. Smy, and M. J. Brett. Fabrication of thin films with highly porous microstructures. *Journal of Vacuum Science & Technology A: Vacuum, Surfaces, and Films*, 13(3):1032, May 1995.

[40] K. Robbie and M. J. Brett. Sculptured thin films and glancing angle deposition: Growth mechanics and applications. *Journal of Vacuum Science & Technology A: Vacuum, Surfaces, and Films*, 15(3):1460, May 1997.

[41] R. Messier and A. Lakhtakia. Sculptured thin films – II. Experiments and applications. *Materials Research Innovations*, 2(4):217–222, January 1999.

[42] K. Robbie, M. J. Brett, and A. Lakhtakia. Chiral sculptured thin films. *Nature*, 384(6610):616–616, December 1996.

[43] M. M. Hawkeye and M. J. Brett. Glancing angle deposition: Fabrication, properties, and applications of micro- and nanostructured thin films. *Journal of Vacuum Science & Technology A: Vacuum, Surfaces, and Films*, 25(5):1317, 2007.

[44] K. Robbie, G. Beydaghyan, T. Brown, C. Dean, J. Adams, and C. Buzea. Ultrahigh vacuum glancing angle deposition system for thin films with controlled three-dimensional nanoscale structure. *Review of Scientific Instruments*, 75(4):1089, 2004.

[45] M. T. Taschuk, M. M. Hawkeye, and M. J. Brett. Glancing Angle Deposition. . In *Handbook of Deposition Technologies for Films and Coatings*. Elsevier, 2010.

[46] M. Ohring. *Materials Science of Thin Films*. Academic Press, 2nd edition, 2002.

[47] K. Robbie, G. Beydaghyan, T. Brown, C. Dean, J. Adams, and C. Buzea. Ultrahigh vacuum glancing angle deposition system for thin films with controlled three-dimensional nanoscale structure. *Review of Scientific Instruments*, 75(4):1089, 2004.

[48] K. D. Harris, D. Vick, T. Smy, and M. J. Brett. Column angle variations in porous chevron thin films. *Journal of Vacuum Science & Technology A: Vacuum, Surfaces, and Films*, 20(6):2062, 2002.

[49] T. Motohiro and Y. Taga. Thin film retardation plate by oblique deposition. *Applied Optics*, 28(13):2466–82, July 1989.

[50] R. Messier, T. Gehrke, C. Frankel, V. C. Venugopal, W. Otano, and A. Lakhtakia. Engineered sculptured nematic thin films. *Journal of Vacuum Science & Technology A: Vacuum, Surfaces, and Films*, 15(4):2148, July 1997.

[51] S. R. Kennedy, M. J. Brett, O. Toader, and S. John. Fabrication of Tetragonal Square Spiral Photonic Crystals. *Nano Letters*, 2(1):59–62, January 2002.

[52] K. Robbie, J. C. Sit, and M. J. Brett. Advanced techniques for glancing angle deposition. *Journal of Vacuum Science & Technology B: Microelectronics and Nanometer Structures*, 16(3):1115, May 1998.

[53] M. O. Jensen and M. J. Brett. Porosity engineering in glancing angle deposition thin films. *Applied Physics A*, 80(4):763–768, June 2004.

[54] D.-X. Ye, T. Karabacak, B. K. Lim, G.-C. Wang, and T.-M. Lu. Growth of uniformly aligned nanorod arrays by oblique angle deposition with two-phase substrate rotation. *Nanotechnology*, 15(7):817–821, July 2004.

[55] C. Buzea, K. Kaminska, G. Beydaghyan, T. Brown, C. Elliott, C. Dean, and K. Robbie. Thickness and density evaluation for nanostructured thin films by glancing angle deposition. *Journal of Vacuum Science & Technology B: Microelectronics and Nanometer Structures*, 23(6):2545, 2005.

[56] J.J. Steele, J.P. Gospodyn, J.C. Sit, and M.J. Brett. Impact of morphology on high-speed humidity sensor performance. *IEEE Sensors Journal*, 6(1):24–27, February 2006.

[57] D. Schmidt, B. Booso, T. Hofmann, E. Schubert, A. Sarangan, and M. Schubert. Monoclinic optical constants, birefringence, and dichroism of slanted titanium nanocolumns determined by generalized ellipsometry. *Applied Physics Letters*, 94(1):011914, 2009.

[58] A. C. van Popta, J. C. Sit, and M. J. Brett. Optical properties of porous helical thin films. *Applied Optics*, 43(18):3632–9, June 2004.

[59] K. Kaminska, T. Brown, G. Beydaghyan, and K. Robbie. Vacuum evaporated porous silicon photonic interference filters. *Applied Optics*, 42(20):4212–9, July 2003.

[60] C. Patzig and B. Rauschenbach. Temperature effect on the glancing angle deposition of Si sculptured thin films. *Journal of Vacuum Science & Technology A: Vacuum, Surfaces, and Films*, 26(4):881, 2008.

[61] M.R. Kupsta, M.T. Taschuk, M.J. Brett, and J.C. Sit. Overcoming cap layer cracking for glancing-angle deposited films. *Thin Solid Films*, 519(6):1923–1929, January 2011.

[62] K. M. Krause and M. J. Brett. Spatially Graded Nanostructured Chiral Films as Tunable Circular Polarizers. *Advanced Functional Materials*, 18(20):3111–3118, October 2008.

[63] I. Hodgkinson and Q. H. Wu. Serial bideposition of anisotropic thin films with enhanced linear birefringence. *Applied Optics*, 38(16):3621–5, June 1999.

[64] D.-X. Ye, Y.-P. Zhao, G.-R. Yang, Y.-G. Zhao, G.-C. Wang, and T.-M. Lu. Manipulating the column tilt angles of nanocolumnar films by glancing-angle deposition. *Nanotechnology*, 13(5):615–618, October 2002.

[65] K. D. Harris, A. C. van Popta, J. C. Sit, D. J. Broer, and M. J. Brett. A Birefringent and Transparent Electrical Conductor. *Advanced Functional Materials*, 18(15):2147–2153, August 2008.

[66] P. C. P. Hrudey, M. A. Martinuk, M. A. Mossman, A. C. van Popta, M. J. Brett, T. D. Dunbar, J. S. Huizinga, and L. A. Whitehead. Application of transparent nanostructured electrodes for modulation of total internal reflection. *Proceedings of SPIE*, 6647:66470A–66470A–12, 2007.

[67] V. Leontyev, N. G. Wakefield, K. Tabunshchyk, J. C. Sit, M. J. Brett, and A. Kovalenko. Selective transmittance of linearly polarized light in thin films rationally designed by FDTD and FDFD theories and fabricated by glancing angle deposition. *Journal of Applied Physics*, 104(10):104302, 2008.

[68] S. R. Kennedy and M. J. Brett. Porous broadband antireflection coating by glancing angle deposition. *Applied Optics*, 42(22):4573–9, August 2003.

[69] J.-Q. Xi, M. F. Schubert, J. K. Kim, E. F. Schubert, M. Chen, S.-Y. Lin, W. Liu, and J. A. Smart. Optical thin-film materials with low refractive index for broadband elimination of Fresnel reflection. *Nature Photonics*, 1:176–179, February 2007.

[70] M. Jensen and M. Brett. Square spiral 3D photonic bandgap crystals at telecommunications frequencies. *Optics Express*, 13(9):3348–54, May 2005.

[71] M. M. Hawkeye, R. Joseph, J. C. Sit, and M. J. Brett. Coupled defects in one-dimensional photonic crystal films fabricated with glancing angle deposition. *Optics Express*, 18(12):13220–6, June 2010.

[72] I. Hodgkinson, Q. H. Wu, and J. Hazel. Empirical equations for the principal refractive indices and column angle of obliquely deposited films of tantalum oxide, titanium oxide, and zirconium oxide. *Applied Optics*, 37(13):2653–9, May 1998.

[73] J. Wang, J. Shao, and Z. Fan. Extended effective medium model for refractive indices of thin films with oblique columnar structure. *Optics Communications*, 247(1-3):107–110, March 2005.

[74] A. C. van Popta, J. Cheng, J. C. Sit, and M. J. Brett. Birefringence enhancement in annealed TiO2 thin films. *Journal of Applied Physics*, 102(1):013517, 2007.

[75] D.-X. Ye, Y.-P. Zhao, G.-R. Yang, Y.-G. Zhao, G.-C. Wang, and T.-M. Lu. Manipulating the column tilt angles of nanocolumnar films by glancing-angle deposition. *Nanotechnology*, 13(5):615–618, October 2002.

[76] M. O. Jensen and M. J. Brett. Periodically Structured Glancing Angle Deposition Thin Films. *IEEE Transactions On Nanotechnology*, 4(2):269–277, March 2005.

[77] G. Beydaghyan, K. Kaminska, T. Brown, and K. Robbie. Enhanced birefringence in vacuum evaporated silicon thin films. *Applied Optics*, 43(28):5343–9, October 2004.

[78] D. Gish, M. Summers, and M. Brett. Morphology of periodic nanostructures for photonic crystals grown by glancing angle deposition. *Photonics and Nanostructures - Fundamentals and Applications*, 4(1):23–29, February 2006.

[79] B. Szeto, P. C. P. Hrudey, J. Gospodyn, J. C. Sit, and M. J. Brett. Obliquely deposited tris(8-hydroxyquinoline) aluminium (Alq 3) biaxial thin films with negative in-plane birefringence. *Journal of Optics A: Pure and Applied Optics*, 9(5):457–462, May 2007.

[80] M. M. Hawkeye and M. J. Brett. Narrow bandpass optical filters fabricated with one-dimensionally periodic inhomogeneous thin films. *Journal of Applied Physics*, 100(4):044322, 2006.

[81] K. Robbie, D. J. Broer, and M. J. Brett. Chiral nematic order in liquid crystals imposed by an engineered inorganic nanostructure. *Nature*, 399(June):764–766, 1999.

[82] J. M. Garcia-Martin, R. Alvarez, P. Romero-Gomez, A. Cebollada, and A. Palmero. Tilt angle control of nanocolumns grown by glancing angle sputtering at variable argon pressures. *Applied Physics Letters*, 97(17):173103, 2010.

[83] J. B. Sorge and M. J. Brett. Film morphology modification in ion-assisted glancing angle deposition. *Thin Solid Films*, 519(4):1356–1360, December 2010.

[84] N. G. Wakefield, J. B. Sorge, M. T. Taschuk, L. W. Bezuidenhout, M. J. Brett, and J. C. Sit. Control of the principal refractive indices in biaxial metal oxide films. *Journal of the Optical Society of America A*, 28(9):1830, August 2011.

[85] J. B. Sorge, A. C. van Popta, J. C. Sit, and M. J. Brett. Circular birefringence dependence on chiral film porosity. *Optics Express*, 14(22):10550–7, October 2006.

[86] I. Hodgkinson and Q. H. Wu. Birefringent thin-film polarizers for use at normal incidence and with planar technologies. *Applied Physics Letters*, 74(13):1794, 1999.

[87] A. C. van Popta, K. R. van Popta, J. C. Sit, and M. J. Brett. Sidelobe suppression in chiral optical filters by apodization of the local form birefringence. *Journal of the Optical Society of America A*, 24(10):3140–3149, 2007.

[88] D. W. Berreman. Optics in Stratified and Anisotropic Media: 4 4-Matrix Formulation. *Journal of the Optical Society of America*, 62(4):502, April 1972.

[89] M. Born and E. Wolf. *Principles of Optics*. Cambridge University Press, seventh edition, 2005.

[90] B. E. A. Saleh and M. C. Teich. *Fundamentals of Photonics*. Wiley-Interscience, second edition, 2007.

[91] R. B. Meyer. Piezoelectric Effects in Liquid Crystals. *Physical Review Letters*, 22:918–921, 1969.

[92] R. B. Meyer. Effects of Electric and Magnetic Fields on the Structure of Cholesteric Liquid Crystals. *Applied Physics Letters*, 12(9):281, 1968.

[93] D. W. Berreman and T. J. Scheffer. Bragg Reflection of Light from Single-Domain Cholesteric Liquid-Crystal Films. *Physical Review Letters*, 25(9):577–581, August 1970.

[94] D. Berreman and T. Scheffer. Reflection and Transmission by Single-Domain Cholesteric Liquid Crystal Films: Theory and Verification. *Molecular Crystals and Liquid Crystals*, 11(4):395–405, November 1970.

[95] S. Mori, H. Teraguchi, J. Yamakita, and K. Rokushima. Analysis of wave diffraction in a periodically bent nematic liquid crystal. *Journal of the Optical Society of America A*, 7(8):1562, August 1990.

[96] H. L. Ong and R. B. Meyer. Electromagnetic wave propagation in a periodically bent nematic liquid crystal. *Journal of the Optical Society of America*, 73(2):167, February 1983.

[97] J. C. Sit, D. J. Broer, and M. J. Brett. Alignment and switching of nematic liquid crystals embedded in porous chiral thin films. *Liquid Crystals*, 27(3):387–391, March 2000.

[98] S. R. Kennedy, J. C. Sit, D. J. Broer, and M. J. Brett. Optical activity of chiral thin film and liquid crystal hybrids. *Liquid Crystals*, 28(12):1799–1803, December 2001.

[99] A. L. Elias and M. J. Brett. Polymeric helices with submicron dimensions for MEMS devices (Invited Paper). In *Proceedings of SPIE*, volume 5836, pages 41–55. SPIE, 2005.

[100] A. L. Elias, M. J. Brett, M. E. Sousa, S. J. Woltman, G. P. Crawford, C. W. M. Bastiaansen, and D. J. Broer. Template induced chiral ordering in nematic liquid crystalline materials: A deuterium nuclear magnetic resonance study. *Journal of Applied Physics*, 99(11):116105, 2006.

[101] G. Crawford, M. Vilfan, J. Doane, and I. Vilfan. Escaped-radial nematic configuration in submicrometer-size cylindrical cavities: Deuterium nuclear-magnetic-resonance study. *Physical Review A*, 43(2):835–842, January 1991.

[102] H. Desmet, K. Neyts, and R. Baets. Modeling nematic liquid crystals in the neighborhood of edges. *Journal of Applied Physics*, 98(12):123517, 2005.

[103] M. Kleman and O. D. Lavrentovich. Topological point defects in nematic liquid crystals. *Philosophical Magazine*, 86(25-26):4117–4137, September 2006.

[104] H. Matthias, S. L. Schweizer, R. B. Wehrspohn, and H. S. Kitzerow. Liquid crystal director fields in micropores of photonic crystals. *Journal of Optics A: Pure and Applied Optics*, 9(9):S389–S395, September 2007.

[105] T. J. Sluckin, D. A. Dunmur, and H. Stegemeyer. *Crystals That Flow*. Taylor & Francis, 2004.

[106] O. Lehmann. Uber fliessende krystalle. *Zeitschrift für Physikalische Chemie*, 4:462–472, 1889.

[107] H. Kawamoto. The History of Liquid-Crystal Displays. *Proceedings of the IEEE*, 90(4):460–500, 2002.

[108] P. G. de Gennes and J. Prost. *The Physics of Liquid Crystals*. 1995.

[109] H. Dai. Characteristics of LCoS Phase-only spatial light modulator and its applications. *Optics Communications*, 238(4-6):269–276, August 2004.

[110] H. Finkelmann, H.J. Kock, and G. Rehage. Investigations on Liquid Crystalline Polysiloxanes. *Die Makromolekulare Chemie, Rapid Communications*, 2(4):317–322, 1981.

[111] C. L. van Oosten, C. W. M. Bastiaansen, and D. J. Broer. Printed artificial cilia from liquid-crystal network actuators modularly driven by light. *Nature Materials*, 8(8):677–82, August 2009.

[112] K. D. Harris, C. W. M. Bastiaansen, J. Lub, and D. J. Broer. Self-assembled polymer films for controlled agent-driven motion. *Nano Letters*, 5(9):1857–60, September 2005.

[113] P. Van Konynenburg, S. Marsland, and J. McCoy. Solar radiation control using NCAP liquid crystal technology. *Solar Energy Materials*, 19(1-2):27–41, 1989.

[114] Y. Ide and Z. Ophir. Orientation development in thermotropic liquid crystal polymers. *Polymer Engineering & Science*, 23(5):261–265, 1983.

[115] M. W. Matsen. Unifying Weak- and Strong-Segregation Block Copolymer Theories. *Macromolecules*, 29:1091–1098, January 1996.

[116] Barrett. Introduction to Liquid Crystals (http://barrett-group.mcgill.ca/teaching/liquid_crystal/LC01.htm).

[117] T. J. Sluckin. The liquid crystal phases: physics and technology. *Contemporary Physics*, 41:37–56, 2000.

[118] H. Takezoe and Y. Takanishi. Bent-Core Liquid Crystals: Their Mysterious and Attractive World. *Japanese Journal of Applied Physics*, 45(No. 2A):597–625, February 2006.

[119] P. J. Collings. *Liquid Crystals*. Princeton and Oxford, 2nd edition, 2002.

[120] L. Onsager. The effects of shape on the interaction of colloidal particles. *Annals of the New York Academy of Sciences*, 51(4):627–659, May 1949.

[121] P. Yeh and C. Gu. *Optics of Liquid Crystal Displays*. John Wiley & Sons, 2nd edition, 2010.

[122] B. Jerome. Surface effects and anchoring in liquid crystals. *Reports on Progress in Physics*, 391, 1991.

[123] C. W. Oseen. The theory of liquid crystals. *Transactions of the Faraday Society*, 29(140):883, 1933.

[124] F. C. Frank. On the theory of liquid crystals. *Discussions of the Faraday Society*, 25:19, 1958.

[125] T. Uchida, M. Ohgawara, and M. Wada. Liquid Crystal Orientation on the Surface of Obliquely-Evaporated Silicon Monoxide with Homeotropic Surface Treatment. *Japanese Journal of Applied Physics*, 19(No. 11):2127–2136, November 1980.

[126] L.A. Goodman, J.T. McGinn, C.H. Anderson, and F. DiGeronimo. Topography of obliquely evaporated silicon oxide films and its effect on liquid-crystal orientation. *IEEE Transactions on Electron Devices*, 24:795–804, July 1977.

[127] M. Schadt. Voltage-dependent optical activity of a twisted nematic liquid crystal. *Applied Physics Letters*, 18(4):127, 1971.

[128] M.P. Allen. Calculating the helical twisting power of dopants in a liquid crystal by computer simulation. *Physical Review E*, 47(6):4611–4614, 1993.

[129] P. Etchegoin. Blue phases of cholesteric liquid crystals as thermotropic photonic crystals. *Physical Review E*, 62:1435–1437, July 2000.

[130] D. Berreman. Solid Surface Shape and the Alignment of an Adjacent Nematic Liquid Crystal. *Physical Review Letters*, 28(26):1683–1686, June 1972.

[131] J. Stöhr, M. G. Samant, A. Cossy-Favre, J. Díaz, Y. Momoi, S. Odahara, and T. Nagata. Microscopic Origin of Liquid Crystal Alignment on Rubbed Polymer Surfaces. *Macromolecules*, 31(6):1942–1946, March 1998.

[132] M. Schadt, K. Schmitt, V. Kozinkov, and V. Chigrinov. Surface-Induced Parallel Alignment of Liquid Crystals by Linearly Polymerized Photopolymers. *Japanese Journal of Applied Physics*, 31(Part 1, No. 7):2155–2164, July 1992.

[133] J. C. Jones. Novel bistable liquid crystal displays based on grating alignment. *Proceedings of SPIE*, 3955:84–93, 2000.

[134] E. Guyon, P. Pieranski, and M. Boix. On different boundary conditions of nematic films deposited on obliquely evaporated plates. *Letters in Applied Engineering Sciences*, 1:19–24, 1973.

[135] G. E. Volovik and O. D. Lavrentovich. Topological dynamics of defects: boojums in nematic drops. *Zhurnal Eksperimentalnoi i Teoreticheskoi Fiziki*, 85:1997–2010, 1983.

[136] P. Poulin and D. Weitz. Inverted and multiple nematic emulsions. *Physical Review E*, 57(1):626–637, January 1998.

[137] J.-G. Fan, D. Dyer, G. Zhang, and Y.-P. Zhao. Nanocarpet Effect: Pattern Formation during the Wetting of Vertically Aligned Nanorod Arrays. *Nano Letters*, 4(11):2133–2138, November 2004.

[138] J. K. Kwan and J. C. Sit. The use of ion-milling to control clustering of nanostructured, columnar thin films. *Nanotechnology*, 21(29):295301, July 2010.

[139] S. Tsoi, E. Fok, J. C. Sit, and J. G. C. Veinot. Surface Functionalization of Porous Nanostructured Metal Oxide Thin Films Fabricated by Glancing Angle Deposition. *Chemistry of Materials*, 18(22):5260–5266, October 2006.

[140] J. S. Batchelder, A. H. Zewail, and T. Cole. Luminescent solar concentrators. 1: Theory of operation and techniques for performance evaluation. *Applied Optics*, 18(18):3090–3110, September 1979.

[141] J. S. Batchelder, A. H. Zewail, and T. Cole. Luminescent solar concentrators. 2: Experimental and theoretical analysis of their possible efficiencies. *Applied Optics*, 20(21):3733–3754, November 1981.

[142] M. G. Debije, P. P. C. Verbunt, B. C. Rowan, B. S. Richards, and T. L. Hoeks. Measured surface loss from luminescent solar concentrator waveguides. *Applied Optics*, 47(36):6763–8, December 2008.

[143] L. H. Slooff, E. E. Bende, A. R. Burgers, T. Budel, M. Pravettoni, R. P. Kenny, E. D. Dunlop, and a. Büchtemann. A luminescent solar concentrator with 7.1% power conversion efficiency. *physica status solidi (RRL) - Rapid Research Letters*, 2(6):257–259, December 2008.

[144] M. G. Debije. Solar Energy Collectors with Tunable Transmission. *Advanced Functional Materials*, 20(9):1498–1502, April 2010.

[145] P. P. C. Verbunt, A. Kaiser, K. Hermans, C. W. M. Bastiaansen, D. J. Broer, and M. G. Debije. Controlling Light Emission in Luminescent Solar Concentrators Through Use of Dye Molecules Aligned in a Planar Manner by Liquid Crystals. *Advanced Functional Materials*, 19(17):2714–2719, September 2009.